

Springer Theses

Recognizing Outstanding Ph.D. Research

Lina K. Blusch

The Siamese-Twin Porphyrin and Its Copper and Nickel Complexes: A Non-Innocent Twist

 Springer

Springer Theses

Recognizing Outstanding Ph.D. Research

For further volumes:
<http://www.springer.com/series/8790>

Aims and Scope

The series “Springer Theses” brings together a selection of the very best Ph.D. theses from around the world and across the physical sciences. Nominated and endorsed by two recognized specialists, each published volume has been selected for its scientific excellence and the high impact of its contents for the pertinent field of research. For greater accessibility to non-specialists, the published versions include an extended introduction, as well as a foreword by the student’s supervisor explaining the special relevance of the work for the field. As a whole, the series will provide a valuable resource both for newcomers to the research fields described, and for other scientists seeking detailed background information on special questions. Finally, it provides an accredited documentation of the valuable contributions made by today’s younger generation of scientists.

Theses are accepted into the series by invited nomination only and must fulfill all of the following criteria

- They must be written in good English.
- The topic should fall within the confines of Chemistry, Physics, Earth Sciences, Engineering and related interdisciplinary fields such as Materials, Nanoscience, Chemical Engineering, Complex Systems and Biophysics.
- The work reported in the thesis must represent a significant scientific advance.
- If the thesis includes previously published material, permission to reproduce this must be gained from the respective copyright holder.
- They must have been examined and passed during the 12 months prior to nomination.
- Each thesis should include a foreword by the supervisor outlining the significance of its content.
- The theses should have a clearly defined structure including an introduction accessible to scientists not expert in that particular field.

Lina K. Blusch

The Siamese-Twin Porphyrin and Its Copper and Nickel Complexes: A Non-Innocent Twist

Doctoral Thesis accepted by
the Georg-August-University Göttingen, Germany

 Springer

Author

Dr. Lina K. Blusch
Institute of Inorganic Chemistry
Georg-August-University Göttingen
Göttingen
Germany

Supervisor

Prof. Dr. Franc Meyer
Institute of Inorganic Chemistry
Georg-August-University Göttingen
Göttingen
Germany

ISSN 2190-5053

ISBN 978-3-319-01673-3

DOI 10.1007/978-3-319-01674-0

Springer Cham Heidelberg New York Dordrecht London

ISSN 2190-5061 (electronic)

ISBN 978-3-319-01674-0 (eBook)

Library of Congress Control Number: 2013946220

© Springer International Publishing Switzerland 2013

This work is subject to copyright. All rights are reserved by the Publisher, whether the whole or part of the material is concerned, specifically the rights of translation, reprinting, reuse of illustrations, recitation, broadcasting, reproduction on microfilms or in any other physical way, and transmission or information storage and retrieval, electronic adaptation, computer software, or by similar or dissimilar methodology now known or hereafter developed. Exempted from this legal reservation are brief excerpts in connection with reviews or scholarly analysis or material supplied specifically for the purpose of being entered and executed on a computer system, for exclusive use by the purchaser of the work. Duplication of this publication or parts thereof is permitted only under the provisions of the Copyright Law of the Publisher's location, in its current version, and permission for use must always be obtained from Springer. Permissions for use may be obtained through RightsLink at the Copyright Clearance Center. Violations are liable to prosecution under the respective Copyright Law. The use of general descriptive names, registered names, trademarks, service marks, etc. in this publication does not imply, even in the absence of a specific statement, that such names are exempt from the relevant protective laws and regulations and therefore free for general use.

While the advice and information in this book are believed to be true and accurate at the date of publication, neither the authors nor the editors nor the publisher can accept any legal responsibility for any errors or omissions that may be made. The publisher makes no warranty, express or implied, with respect to the material contained herein.

Printed on acid-free paper

Springer is part of Springer Science+Business Media (www.springer.com)

Parts of this thesis have been published in the following journal articles:

“The Siamese-Twin Porphyrin: A Pyrazole-Based Expanded Porphyrin Providing a Bimetallic Cavity” L. K. Frensch, K. Pröpper, M. John, S. Demeshko, C. Brückner, F. Meyer, *Angew. Chem.* **2011**, *123*, 1456–1460; *Angew. Chem. Int. Ed.* **2011**, *50*, 1420–1424.

“Siamese-Twin Porphyrin: A Pyrazole-Based Expanded Porphyrin of Persistent Helical Conformation” L. K. Blusch, Y. Hemberger, K. Pröpper, B. Dittrich, F. Witterauf, M. John, G. Bringmann, C. Brückner, and F. Meyer, *Chem. Eur. J.* **2013**, *19*, 5868–5880.

“Hidden Non-Innocence in an Expanded Porphyrin: Electronic Structure of the Siamese-Twin Porphyrin’s Dicopper Complex in Different Oxidation States” L. K. Blusch, K. E. Craigo, V. Martin-Diaconescu, E. Bill, A. B. McQuarters, S. Dechert, S. DeBeer, N. Lehnert, F. Meyer, DOI: [10.1021/ja406176e](https://doi.org/10.1021/ja406176e).

*Believe those who are seeking the truth.
Doubt those who find it.*

André Guide

Supervisor's Foreword

The highly impressive dissertation by Mrs. Blusch describes, for the first time, the formal fusion of two porphyrin-like chromophores into an expanded porphyrin dubbed Siamese-twin porphyrin, whereby the fusion points are pyrazole moieties. The design of expanded porphyrins has become a key topic in contemporary porphyrin chemistry. This is because these systems contribute to the general understanding of the factors controlling the conformation of larger π -conjugated oligopyrrolic macrocycles, and particularly how structural and conformational effects modulate and interconvert aromatic/anti-aromatic/non-aromatic conjugated π -systems.

The Siamese-twin porphyrin structure was long sought-after, but all previous attempts had been unsuccessful and it was only once Mrs. Blusch became involved that this novel expanded porphyrin could firstly be made. The availability of this unprecedented type of macrocycle now opens up an entirely new field of study. As described in this thesis, physicochemical investigations (using multi-nuclear, 1D and 2D NMR spectroscopy, UV-vis spectroscopy, and mass spectrometry) characterize the connectivity of the macrocycle and support the conclusions derived with respect to macrocycle conformation, the electronic coupling of the two near-isolated π -conjugated systems present in the macrocycle, its acid/base properties, and its conformational flexibility. The intrinsically helimeric (chiral) conformation of the twin porphyrin was shown spectroscopically as well as by single crystal diffractometry and rationalized using computational studies.

One more and major aspect of the twin-porphyrins is evaluated: the Siamese-twin porphyrin contains two pseudoplanar $\{N_4\}$ porphyrin-like coordination sites that each can accommodate a transition metal ion. Once metalated, the twin-porphyrin features a bimetallic complex in which the metals are bridged by two pyrazoles. Mrs. Blusch prepared the homobimetallic nickel(II) and copper(II) complexes as well as the heterometallic nickel(II)/copper(II) analog and characterized them by X-ray diffractometry, spectro-electrochemistry, cyclic voltammetry, SQUID magnetometry, X-ray absorption, and MCD spectroscopy, some of this in collaboration with specialty groups. Much of the investigations were focused on defining the degree of electronic coupling of the two metal centers and the involvement of the non-innocent ligand framework in redox events. An unusual ferromagnetic coupling of the two adjacent pyrazolate-bridged copper(II) ions and a sequence of multiple redox processes were found, whereby initial oxidations

appear to be largely ligand-based. This now offers exciting prospects for exploiting novel metal–metal as well as metal–ligand cooperativity effects when activating and transforming substrates at the metalated Siamese-twin porphyrin.

28 February 2013, Göttingen

Prof. Dr. Franc Meyer

Acknowledgments

At the beginning I would like to thank my mentor Prof. Franc Meyer for his support, the scientific freedom combined with his precious guidance and advice, for this challenging and versatile project and the supply of several analytical devices and funding. Further, I would like to thank him for the possibility to participate at national and international conferences, the introduction to the scientific community, and the opportunity to do research at the University of Connecticut in Prof. Brückner's laboratory. With respect to this, I also would like to thank Prof. Christian Brückner for his support, the good collaboration, his expertise in porphyrin chemistry, and the possibility to accommodate me in his laboratory. Special thanks are accredited to Prof. Ulf Diederichsen for being my correferent and writing several endorsements for scholarship application processes.

I further would like to thank all my collaborators, who are Yasmin Hemberger, Franziska Witterauf, Prof. Gerhard Bringmann, Dr. Eckhard Bill, Prof. Nicolai Lehnert, Kevin Pröpper, Birger Dittrich, Prof. Serena DeBeer, and Dr. Vlad Martin-Diaconescu for the good communication and teamwork.

I gratefully acknowledge the funding of the "Fonds der Chemischen Industrie" and the DAAD without whom the fruitful international experiences would not have been realized.

I thank the people from the analytic laboratories, the mass spectrometry division, Dr. Michael John, and Wolfgang Zolke from the NMR spectroscopy division Dr. Claudia Stückl for measuring several EPR spectra and the scientific discussions and my bachelor students and all other students who supported me in the laboratory. Thank to Adam, Kai, Andreas, and Jörg for the wonderful atmosphere in our common laboratory. I thank Anne, Adam, Kai, Antonia, Sven, Anett, Michael, Les, Jill, Michelle, Victoria, Esther, and Kristian for correcting parts of the present Ph.D. work and the whole Meyer group for the pleasant atmosphere throughout my Ph.D. time.

Finally, I thank my husband for being my husband and his strong support in any way and also my family for their continuous support.

Contents

1	General Introduction	1
1.1	Porphyryns	1
1.1.1	Natural Porphyrins	2
1.1.2	Synthetic Porphyrins	6
1.2	Expanded Porphyrins	10
1.2.1	Aromaticity in Large Systems	11
1.2.2	Complexes of Expanded Porphyrins	13
1.2.3	Applications	15
1.3	Oxidoreductase Enzymes	16
1.3.1	Monooxygenases	16
1.4	Pyrazole: A Common Motif in Dinuclear Complexes	17
	References	19
2	Objective	23
	Reference	24
3	Route to the Siamese-Twin Porphyrin	25
3.1	Cyclization Strategies	26
3.2	Synthesis of Building Blocks	27
3.2.1	The Pyrazole Precursor	27
3.2.2	The Pyrrole Precursor	29
3.2.3	Pyrrole/Pyrazole Hybrids	30
3.2.4	Dipyrromethane/Dipyromethene Units	32
3.3	Cyclization Reactions	32
3.3.1	Route A	33
3.3.2	Route B	33
3.3.3	Route C	34
3.4	Oxidation Reaction Toward the Siamese-Twin Porphyrin	37
	References	40
4	Siamese-Twin Porphyrin LH₄	41
4.1	The Twist	41
4.1.1	NMR Spectroscopy	41

4.1.2	Solid-State Structure and UV-Vis Spectroscopy	45
4.1.3	Origin of the Twist	47
4.1.4	Aromaticity	47
4.2	pH Dependency	49
4.2.1	NMR Spectroscopy	50
4.2.2	UV-Vis Spectroscopy	54
4.2.3	DFT Calculations	56
4.3	Chiral Resolution	56
4.4	Redox Properties	62
	References	64
5	Nickel and Copper Complexes	67
5.1	Comparison of Optical Properties	70
5.2	Dicopper(II) Complex LCu_2	71
5.2.1	Solid-State Structure	71
5.2.2	Magnetic Properties	73
5.2.3	MCD Spectroscopy	78
5.2.4	Chiral Resolution	81
5.3	Mono- and Di-Nickel(II) Complexes LH_2Ni and LNi_2	81
5.3.1	Solid-State Structures	81
5.3.2	pH Dependency	85
5.3.3	MCD Spectroscopy	87
5.3.4	Chiral Resolution	88
5.4	Heterobimetallic Copper(II) Nickel(II) Complex $LCuNi$	88
5.4.1	Magnetic Properties	88
	References	91
6	Redox Properties	93
6.1	Dicopper Complex	95
6.1.1	Electrochemical Oxidation/Reduction	97
6.1.2	Chemical Oxidation	98
6.1.3	Localization of the Redox Center in LCu_2^+	100
6.1.4	Localization of the Redox Center in LCu_2^{2+}	102
6.2	Mono- and Di-Nickel Complexes	107
6.2.1	Electrochemical Oxidation/Reduction	108
6.2.2	Chemical Oxidation	110
6.2.3	Localization of the Redox Center in LNi_2^+	111
6.3	Copper Nickel Complex	117
6.3.1	Electrochemical Oxidation/Reduction	118
6.3.2	Chemical Oxidation	120
6.3.3	Localization of the Redox Center in $LCuNi^+$	120
6.3.4	Localization of the Redox Center in $LCuNi^{2+}$	122
	References	124

7 Summary and Outlook	127
8 Experimental Section	129
8.1 Instruments and Materials	129
8.2 Ligand Synthesis	132
8.2.1 3,5-Bis-(hydroxy(phenyl)methyl)-4-phenyl- 1 <i>H</i> -pyrazole (13)	132
8.2.2 3,5-Bis-(chloro(phenyl)methyl)-4-phenyl- 1 <i>H</i> -pyrazole hydrochloride (7)	133
8.2.3 3,5-Bis-(1 <i>H</i> -pyrrole-2-yl-benzyl)-1 <i>H</i> -pyrazole (24a)	133
8.2.4 3,5-Bis-(3,4-diethyl-1 <i>H</i> -pyrrole-2-yl-benzyl)- 1 <i>H</i> -pyrazole (24b)	134
8.2.5 3,5-Bis-(3,4-diethyl-5-formyl-1 <i>H</i> -pyrrole-2- yl-benzyl)-1 <i>H</i> -pyrazole (25)	135
8.2.6 Siamese-twin Porphyrinogen 6d	136
8.2.7 Siamese-twin Porphyrin LH ₄	137
8.2.8 Siamese-twin Porphyrin LH ₆ ²⁺	138
8.3 Complex Synthesis	139
8.3.1 Siamese-twin Porphyrin Dicopper(II) Complex LCu ₂	139
8.3.2 Siamese-twin Porphyrin Dinickel(II) Complex LNi ₂	140
8.3.3 Siamese-twin Porphyrin Mononickel(II) Complex LH ₂ Ni	141
8.3.4 Siamese-twin Porphyrin Copper(II) Nickel(II) Complex LCuNi	142
8.3.5 General Procedure Toward LM ₂ ⁺	143
8.3.6 General Procedure Toward LM ₂ ²⁺	143
References	144
Appendix	147
Scientific Contributions	153
Curriculum Vitae	155
Index	157

Abbreviations

AM1	Austin model 1
antiferro	Antiferromagnetic
Bn	Benzyl
BP86	Becke–Perdew-1986
Bz	Benzoyl
CA	Chloranil
CD	Circular dichroism
COSY	Correlation spectroscopy
CT	Charge transfer
CV	Cyclic voltammetry
D	Donor atom
DBU	1,8-Diazabicyclo[5.4.0]undec-7-ene
DDQ	2,3-Dichloro-5,6-dicyano-1,4-benzoquinone
DFc	Decamethylferrocene
DFT	Density functional theory
DMF	Dimethylformamide
DMSO	Dimethylsulfoxide
EDG	Electron donating group
EPR	Electron paramagnetic resonance
ESI	Electrospray ionization
Et	Ethyl
EWG	Electron withdrawing group
ex	Exchange
EXAFS	Extended X-ray absorption fine structure
Fc	Ferrocene
ferro	Ferromagnetic
h	Hour
HMBC	Heteronuclear multiple-bond correlation
HOMO	Highest occupied molecular orbital
HPLC	High pressure liquid chromatography
HR	High resolution
IAM	Independent atom model
IBX	2-Iodoxybenzoic acid
IR	Infrared

IV	Intervalence
LC	Liquid chromatography
lcp	Left circular polarized
LL	Ligand-to-ligand
LUMO	Lowest unoccupied molecular orbital
m. p.	Melting point
Me	Methyl
min	Minute
MM	Metal-to-metal
MRI	Magnetic resonance imaging
MS	Mass spectrometry
NIR	Near infrared
NLO	Non-linear optics
NMR	Nuclear magnetic resonance
NOE	Nuclear overhauser effect
OAc	Acetate
OEP	Octaethylporphyrin
PDT	Photodynamic therapy
Ph	Phenyl
ppm	Parts per million
PS	Polystyrene
py	Pyridine
pyr	Pyrrole
pz	Pyrazole
r. t.	Room temperature
rcp	Right circular polarized
sMMO	Soluble methane monooxygenase
SQUID	Superconducting quantum interference device
SVP	Split valence polarization
SWV	Square wave voltammetry
t	Total
TEMPO	2,2,6,6-Tetramethyl-1-piperidinyloxy
TFA	Trifluoroacetic acid
TLC	Thin layer chromatography
TPP	Tetraphenylporphyrin
UV-vis	Ultraviolet-visible
VTVH	Variable temperature variable field
XAS	X-ray absorption spectroscopy
ZFS	Zero field splitting

Chapter 1

General Introduction

Porphyrins are planar aromatic macrocycles and ubiquitous in nature [1]. Their monometallic complexes are involved in many key processes of life, such as: respiration and photosynthesis [2–4]. Since their discovery, these exceptional systems stimulated enormous interest. Their isolation and subsequent total synthesis shed light on their constitution and function and in turn this research was rewarded with several nobel prizes [5]. With the synthetic procedures in hand, a range of synthetic modifications [6] were made viable utilizing the attachment of various backbone residues, replacement of subheterocyclic units and the expansion of the core structure. The latter opens a completely new subfield of porphyrinoids: the class of expanded porphyrins [7–11]. These higher analogs of porphyrins are excellent candidates to study fundamental questions of aromaticity [12, 13] and with their larger cavities they provide ligand scaffolds capable of supporting late transition metal or even bimetallic complexes [14–16]. Sessler, Osuka, Kim, Latos-Grazynski, Chandrashekar and Vogel pioneered the field, which has developed rapidly within the last 40 years.

In the present work, a novel expanded porphyrin system with biomimetic elements is introduced: the Siamese-twin porphyrin [17]. Inspired by the mechanisms of cytochrome P450 and the bimetallic active center of methane monooxygenase [3, 4], it was designed to combine their motifs and to yield fascinating redox properties.

1.1 Porphyrins

After the short introduction, the porphyrinic macrocycle is now described in more detail (Fig. 1.1). Pyrrole, as the basic unit of porphyrins, is an aromatic five-membered nitrogen heterocycle and belongs to the group of azoles [18, 19]. Due to its six π -electrons distributed over five atoms, pyrroles are π -excessive and therefore good π -donors. Its new nomenclature of arabic numbers is not consistently used. Particularly, in porphyrin chemistry, the old greek letters are common, because they retain its validation when pyrrole is part of the porphyrinic scaffold.

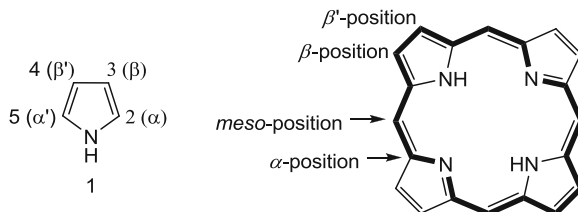
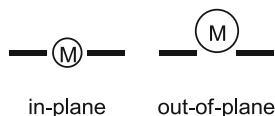


Fig. 1.1 *Left:* Pyrrole labeled according to the old (*Greek letters*) and new (*Arabic numbers*) nomenclature; *Right:* Chemical structure of the porphyrin system with labeling and the highlighted 18 π -electrons counting conjugation pathway (Sect. 1.2.1)

Fig. 1.2 Different possibilities of metal complexation by porphyrin ring systems depending on the metal ion size



Porphyrin consists of all together four pyrrole units that are linked between their α -positions via methine bridges, also denoted as *meso* carbon atoms. Porphyrins are planar and have an extended π -system, in which only 18 out of 24 π -electrons contribute to the delocalized “conjugation pathway” which is highlighted in Fig. 1.1. Due to their delocalized system, the highest occupied molecular orbital (HOMO)–lowest unoccupied molecular orbital (LUMO) gap shrinks and light absorption is seen in the visible region, which explains their intense colors. Porphyrins show characteristic absorption at around 400 nm with an extinction coefficient of around $10^5 \text{ M}^{-1} \text{ cm}^{-1}$, the so called Soret-band [20, 21].

In its twice deprotonated form, porphyrins are tetradentate chelating ligands offering a rigid, square planar cavity (radius of 0.6 – 0.7 Å) [2]. Only with metal ions of distinct size in-plane coordination modes can be formed (Fig. 1.2) [22, 23]. With larger metal ions complexes can only be formed adopting an out-of-plane coordination mode. A change of the metal oxidation or spin state can introduce a geometry flip due to the change of the metal ion’s size.

1.1.1 Natural Porphyrins

The most famous natural porphyrins are heme and chlorophyll (Fig. 1.3). The first is an iron porphyrin complex, which is part of many active sites of different proteins, such as hemoglobin and cytochrome P450. Chlorophyll is a magnesium porphyrin complex which is indispensable for photosynthesis [3]. In photosynthesis light energy is converted to chemical energy stored as glucose (Scheme 1.1).

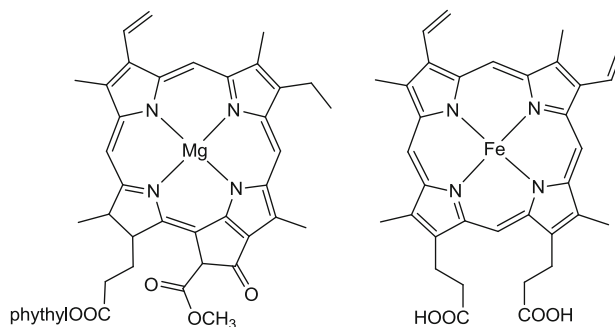
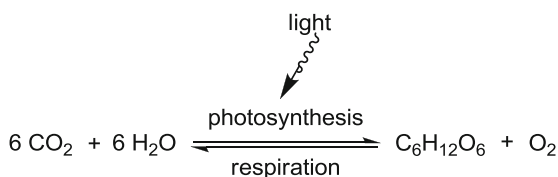


Fig. 1.3 Chlorophyll *b* (left) and the heme-*b* unit (right) [4]

Scheme 1.1 Connection of photosynthesis and respiration. In photosynthesis light energy is stored in form of glucose ($C_6H_{12}O_6$). Heterotrophs consume this energy via respiration



Chlorophyll

Chlorophyll consists of a chlorine ring, which is a β,β' -hydrated porphyrin although the aromatic 18 π -electron conjugation pathway is preserved (Fig. 1.3, left) [2, 24]. The aliphatic phytyl side chain can be understood as an anchor to connect the system to the hydrophobe thylakoid membrane within the chloroplasts, the location of photosynthesis. The magnesium ion bound by the chlorine scaffold fits perfectly in the porphyrinic cavity, is redox inactive and favors an octahedral coordination sphere. Hence, additional axial binding results in a neat arrangement of the chlorophylls, which is crucial for their activity in light-harvesting. Therefore, the carbonyl groups of chlorophyll act as lone-pair donors and rigidify the array additionally. Besides chlorophyll, also diverse carotenoids, phycoerythrins and phycocyanins are among the antenna pigments, which belong to the light-harvesting complex to cover almost the whole spectrum of light. The green color of chloroplasts appears from the left-over wavelengths, that were not absorbed. The energy absorbed by the antenna pigments is funneled to the reactive center, the photosystem, which again consist of two chlorophylls. These get oxidized and become cationic π -radicals (Fig. 1.4) which is the initial step needed for chemical energy storage—the charge separation. Thus, porphyrins are redox-active, which can be denoted as non-innocent behavior.

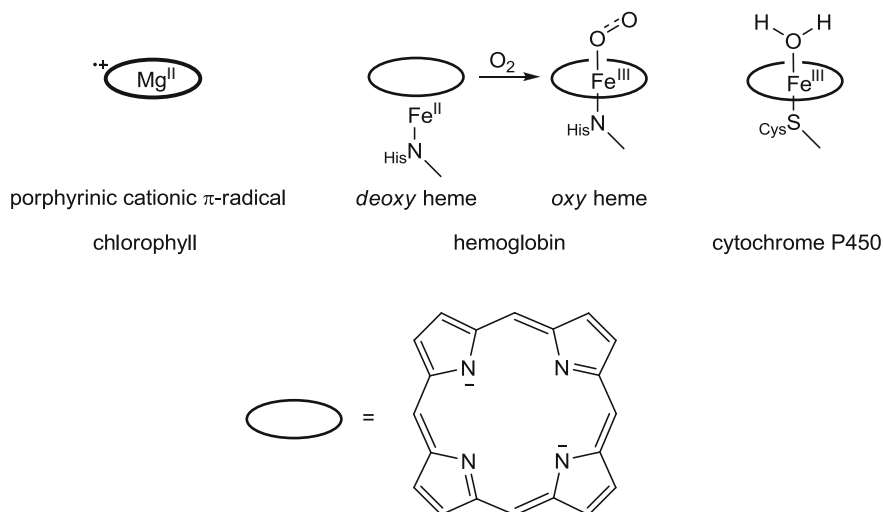


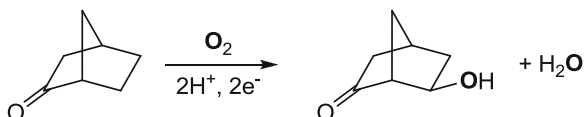
Fig. 1.4 Relevant intermediate of chlorophyll after light excitation (porphyrinic cationic π -radical), the transformation of the heme-*b* unit in hemoglobin from its *deoxy* to its *oxy* form and the resting state of the heme-unit in cytochrome P450

Hemoglobin

Respiration describes the reverse reaction of photosynthesis, in which oxygen and the stored chemical energy is consumed e.g. by vertebrates, which thus are heterotrophs (Scheme 1.1). The consumption of oxygen takes place in muscle tissue, and therefore the oxygen transport within the body has to be regulated. Hemoglobin is an oxygen carrier, found in blood of vertebrates as well as in some bacteria and plants [4]. Hemoglobin is not only responsible for the supply of O_2 to the tissue but also for the removal of the produced CO_2 . If hemoglobin contains O_2 , the prefix *oxy* is commonly used. When O_2 is not bound the prefix *deoxy* is used. Depending on the creature, hemoglobin can be found as monomers, dimers, tetramers or higher weight assemblies concerning their quaternary structure [24]. Binding of O_2 to one subunit positively affects the affinity of the remaining subunits toward oxygen—a phenomenon known as cooperativity [25–27]. Due to this mechanism, the solubility of O_2 in blood is increased 30-fold compared to its solubility in plain water [2].

In its *deoxy* form hemoglobin carries high spin Fe^{II} , which is relatively large (ionic radius; 0.78 Å) and is coordinated in an out-of-plane mode with an axial histidine ligand (Fig. 1.4) [4]. Upon binding of O_2 , a redox reaction takes place in which high spin Fe^{II} gets oxidized to low spin Fe^{III} while dioxygen is bound as O_2^- , a superoxide [28]. The change in oxidation state and in turn the switch between high spin and low spin results in a size change of the ion. Low spin Fe^{II} (ionic radius: 0.55 Å) is much smaller and flips right into the cavity

Fig. 1.5 Campher oxidation catalyzed by cytochrome P450_{cam} [4]



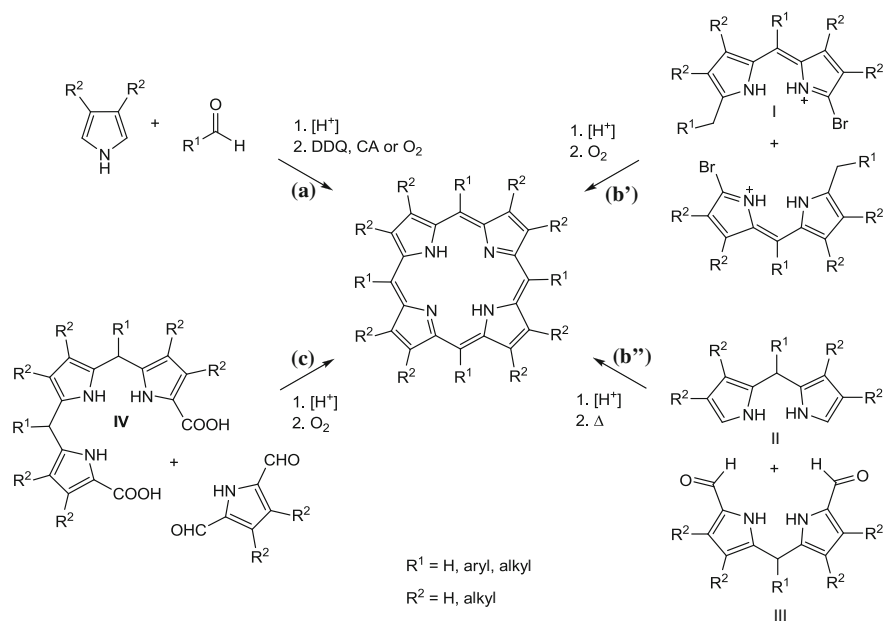
simultaneously pulling its axial bound histidine ligand toward the center of the cavity. This accounts for a structural change that affects the remaining subunits (cooperativity) [29]. Hence, hemoglobin demonstrates descriptively the different coordination modes of porphyrins depending on the size of the metal ion.

Cytochromes

Cytochromes also consist of a heme unit. Among the class of cytochromes, some are responsible for electron transport, while cytochrome c oxidase and cytochrome P450 catalyze redox reactions [2]. Their different reactivity arises mainly from their protein surrounding which determines the occupation of the axial heme positions. While in cytochromes functioning as electron carriers both axial positions are permanently occupied and no substrate binding is allowed, in cytochrome c oxidase and cytochrome P450 only one permanent axial ligand is provided by the protein scaffold. Cytochrome c oxidase is part of the complicated respiratory chain and catalyzes the final reduction step of dioxygen, also referred to as dioxygen activation. Here, dioxygen is converted to two water molecules.

The active center of cytochrome P450 consists of a heme-*b* unit (Fig. 1.3), exactly as in hemoglobin but carries an axial cysteine instead of a histidine ligand. Cytochrome P450 is a monooxygenase and mediates oxidation of small organic molecules with dioxygen. This gets reduced, whereupon one oxygen atom gets inserted into the substrate and simultaneously the second becomes a water molecule (Fig. 1.5 and Sect. 1.4). All P450-enzymes are metabolizing endogeneous substrates via oxidation and regulate the decontamination of xenobiotics [2]. Cytochrome P450 is able to catalyze the hydroxylation of saturated carbon-hydrogen bonds (Fig. 1.5), the epoxidation of double bonds, the oxidation of heteroatoms and dealkylation reactions and the oxidations of aromatics [30]. Its high reactivity but low substrate specificity requires a tight activity control. In the resting state, the two axial positions are generally blocked with a proximal cysteine ligand and a labile-bound water molecule (Fig. 1.4).

Porphyrins and their complexes are colorful and inevitably needed for life and thus are described as “Pigments of Life” [31]. Because their discovery as well as their functional and structural determination marked cornerstones, several nobel prizes were awarded, e.g. to Willstätter (constitution elucidation of chlorophyll), Fischer (total synthesis of heme), Woodward (total synthesis of chlorophyll), etc. [5, 32].



Scheme 1.2 Different strategies for porphyrin syntheses: **a** Rothemund synthesis, **b'** Fischer synthesis, **b''** [2 + 2] Macdonald synthesis and **c** [3 + 1] Macdonald synthesis. For **b''** and **c**, R^1 for the fusion points in the synthesized porphyrin corresponds to a hydrogen atom [9]

1.1.2 Synthetic Porphyrins

The first synthetic approaches towards porphyrins started in the 1930s. Fischer and Rothemund almost simultaneously reported on the synthesis of a porphyrin [33–35]. Overall, three fundamental synthetic routes toward porphyrins have been developed, in which a cyclization step to build the not yet oxidized macrocyclic arrangement (porphyrinogen) is always followed by the oxidation of the ring (Scheme 1.2) [6]:

- (a) The most popular way is the acid-catalyzed Rothemund synthesis where the pyrrole building block attacks the desired aldehyde's carbon atom. An equimolar ratio of the two is needed to yield the porphyrinogen. Subsequent oxidation with air or with commonly used proton coupled oxidants such as chloranil (CA) or 2,3-dichloro-5,6-dicyano-*p*-benzoquinone (DDQ), gives the desired highly symmetric (D_{4h}) porphyrin. Eventually, the reaction conditions were slightly modified by Lindsey toward milder conditions so that porphyrins carrying functional groups were accessible [36].
- (b) The [2 + 2] self-condensation of two dipyrromethenes **I** in e.g. boiling formic acid (Fischer route; Scheme 1.2, (b')) is limited to centrosymmetrically substituted porphyrins due to scrambling effects. The use of acid sensitive

dipyrromethanes **II** was not successful until Macdonald (Scheme 1.2, (b')) discovered that α -formylated dipyrromethanes **III** readily undergo a [2 + 2] condensation reaction with an α -dicarboxylic or α -unsubstituted moiety in good yields [37], but still the same symmetry restrictions are apparent as in Fischer's route.

- (c) Macdonalds approach was expanded to the so called [3 + 1] strategy. Here, the ability to selectively functionalize a porphyrin in one unit is given. Demanding is hence the synthesis of the tripyrrolic building block **IV**. The tripyrrane **IV** usually carries two carboxylic acid substituents in its α -positions and is then condensed with a monopyrrolic diformylated precursor [9].

Each method has its advantages and depending on the desired symmetry and later application, a suitable synthetic approach can be chosen. A general drawback in porphyrin synthesis is the low yields obtained in the cyclization reaction [6], which also explains the demand for improved synthetic strategies. Due to the manifold synthetic strategies, a variety of synthetic porphyrins were prepared (Fig. 1.6). Tetraphenylporphyrin (TPP) is a *meso*-modified system, while octaethylporphyrin (OEP) is modified in its β -positions. Further porphyrins with extended π -systems such as **V** were synthetically made viable [38].

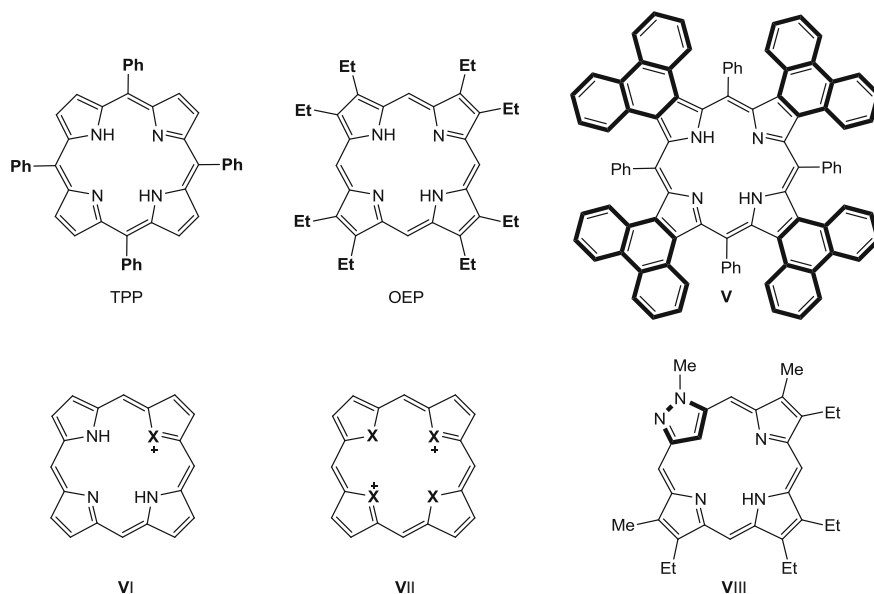
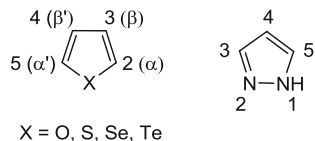


Fig. 1.6 Different porphyrin modifications: Variations of the substitution pattern: tetraphenylporphyrin (TPP), octaethylporphyrin (OEP), tetraphenyltetraphenanthroporphyrin **V**, and core-modified porphyrins (*meso* and β -residues are omitted for clarity) with one **VI** ($X = S, O, Se$ or Te) or four heteroatoms **VII** ($X = S, O$ or Se), and the first porphyrin incorporating a pyrazole unit **VIII**. Modifications are highlighted in bold. [38–44, 46]

Fig. 1.7 Furan (X = O), thiophene (X = S), selenophene (X = Se), tellurophene (X = Te) and 1*H*-pyrazole (right)



Apart from modifications in the substitution pattern Latos-grazynski and Vogel contributed pioneering work to the field of core-modified porphyrins, where pyrrole was (partially) substituted by furan (X = O), thiophene (X = S), selenophene (X = Se) or tellurophene (X = Te) (Fig. 1.6) [39–44]. These are all pyrrole analogous, five-membered heterocycles incorporating another heteroatom than nitrogen (Fig. 1.7) [19]. In contrast, pyrazole is a diazole. Its five-membered heterocycle carries two adjacent nitrogen atoms. The second nitrogen atom is slightly basic and pyrazole's reactivity resembles the one of pyrrole [45]. Lash et al. were the first realizing the synthesis of a pyrrole/pyrazole based porphyrin framework **VIII** [46]. With this enormous library of porphyrin systems, syntheses of manifold main group and transition metal complexes could be realized [22].

Porphyrin Assemblies

The expansion of the π -system is interesting due to the smaller HOMO–LUMO gap and hence a red-shifted Soret band. Expanded π -systems may furthermore serve as functional dyes, as ligands for a variety of metal complexes (Sect. 1.2.2) or to mimic photosynthesis. The expansion itself can be addressed differently, e.g. the substitution pattern can be modified as in **V** or the core structure can be expanded as in the expanded porphyrins (Sect. 1.2). The third method is discussed in this chapter: the assembly of several porphyrin units via covalent and non-covalent linkage, which then become supramolecular systems [47].

The first covalently linked porphyrin **IX** was published in 1972 and was named a doubleporphyrin (Fig. 1.8) [48]. Since then various systems, e.g. **X**, were built where up to five porphyrins were covalently linked [49, 50]. Only conjugated linkers were chosen to guarantee a complete conjugation and thus a smaller HOMO-LUMO gap leading to a red-shifted absorption.

Using the axial vacant positions, further cross-linking between different porphyrin complexes was achieved [51]. Therefore backbone substituents are modified in this way such that σ -donor atoms were incorporated, which then induce the axial binding (Fig. 1.8, **XI**). For axially linked supramolecular systems zinc often is the preferred metal. Zinc is similar to magnesium, the bound metal in chlorophyll, as it has a closed shell. Thus, zinc is redox-inert and its *d*-orbital splitting is not affected by ligand field stabilizing energy. These macromolecular porphyrin arrays are self-assembling systems and their ability to biomimic the convoluted process of photosynthesis is under investigation [52, 53].

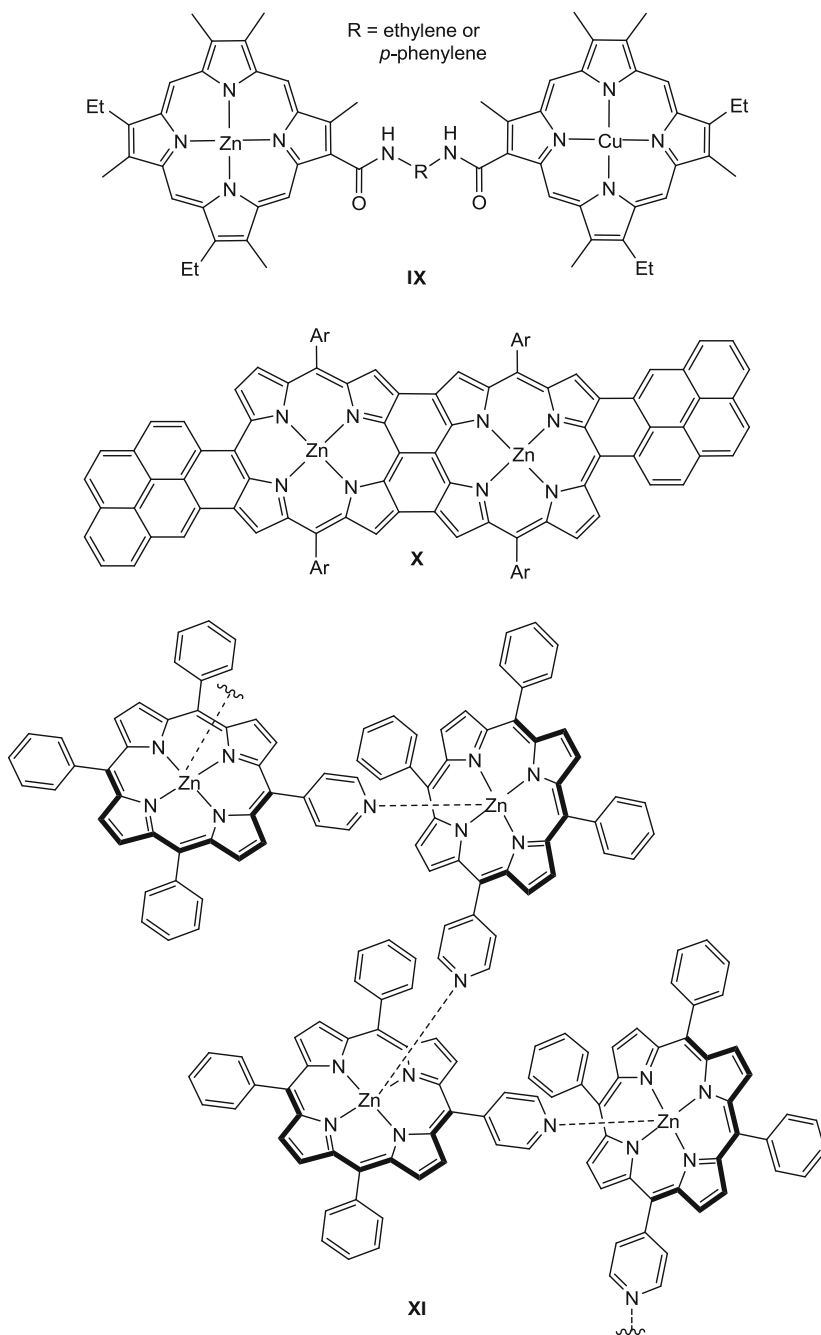


Fig. 1.8 Macromolecular assemblies of porphyrins linked via different units [48, 50, 51]

1.2 Expanded Porphyrins

Besides linking different porphyrin units, an enlargement of the π -system can also be realized by expanding the core itself, in the so called expanded porphyrins. Expanded porphyrins are artificial analogs of porphyrins, which consist of minimal 17 atoms within the internal ring [9]. The resulting cavity is larger than that of porphyrins, thus complexes with later transition metals and even bimetallic complexes can be formed [14, 15]. The cavity and π -system size can be tailored varying the amount, type or the connectivity of the heterocyclic subunits. Woodward discovered the first expanded porphyrin, sapphyrin **XII**, serendipitously in 1966 (Fig. 1.9) [54, 55]. Since then the field exploded and a multitude of different expanded porphyrins are currently available. Expanded porphyrins are named after their core-size: five-pyrrolic systems are called pentaphyrins **XII**, six-pyrrolic systems hexaphyrins **XIII**, seven-pyrrolic systems heptaphyrins **XIV**, eight-pyrrolic systems octaphyrins **XV**, and so on (Fig. 1.9). The largest expanded porphyrin synthesized is composed of 18 pyrrolic units and is referred to as octadecaphyrin [56]. In addition to different core sizes due to a varying amount of

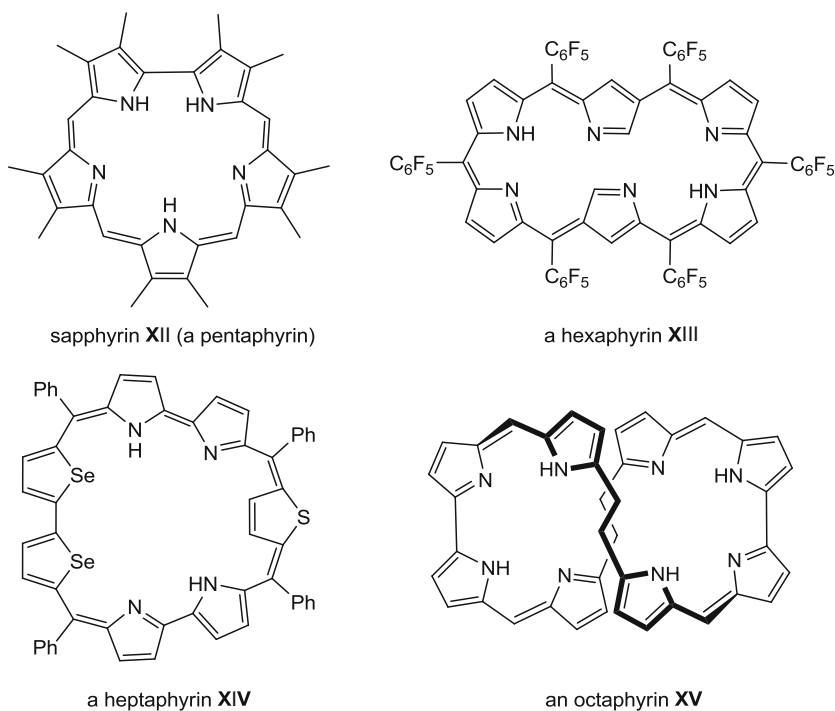


Fig. 1.9 Structural diversity in expanded porphyrins. β -ethyl groups in **XV** are omitted for reasons of clarity [11, 63–65, 101]

pyrrolic units, the linkage between them can either be direct, via a methine bridge or a longer alkyl chain (Fig. 1.9). This is usually indicated in parentheses which follow the name, where the number represents the amount of carbon atoms between each heterocyclic unit [19]. The different numbers are separated via a dot, which marks the heterocyclic unit. The number of π -electrons within the conjugation pathway is prefixed in square brackets, which completes the name to [57–59] hexaphyrin(1.1.1.1.1.1) for the **XIII**-core.

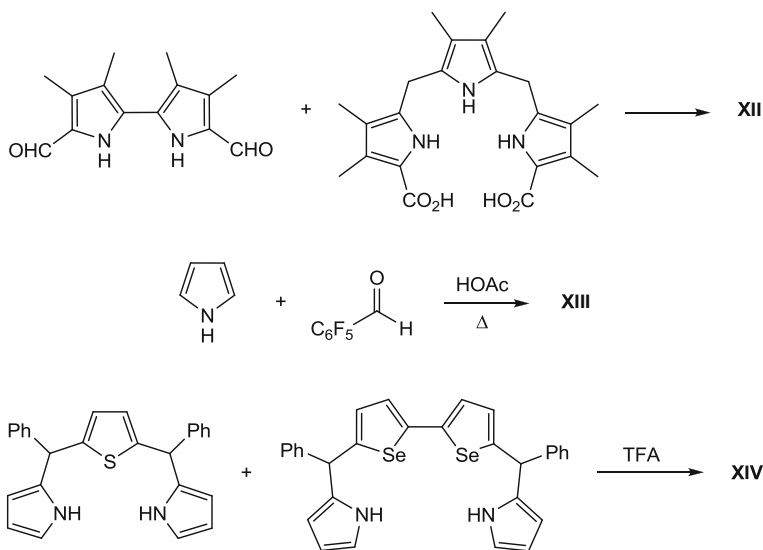
Except all-aza expanded porphyrins (only pyrrole) also core-modified expanded porphyrins are present as in porphyrins, e.g. **XIV**. Expanded porphyrins can exhibit *normal* conformations when all heteroatoms point inward, such as **XII** and **XV**. When heteroatoms point to the outside as the one thiophene unit in **XIV**, it is called *inverted*. In structure **XIII**, two pyrrole units are incorporated into the macrocycle via an α,β -connection, which is referred to as *N-confused*. All mentioned factors, plus the substitution pattern in β - and *meso*-positions, affect the actual geometry. Pentaphyrins and hexaphyrins are mainly planar, except when extremely bulky substituents are involved which force the system into a ruffled or twisted conformation. As octaphyrins, most heptaphyrins exhibit a figure-eight structure [7]. However, a universal structure cannot be derived, because solvent, temperature, protonation, oxidation and metal complexation immensely influence the geometry [60–62].

For the syntheses of expanded porphyrins mono-, bi-, tri- and tetra-pyrrolic fragments are basic building blocks. Depending on the desired connectivity, namely the number of heterocycles, methine bridges and the substitution pattern, appropriate building blocks have to be chosen. Three general synthetic strategies are applied for the syntheses of expanded porphyrins: Macdonald-type condensations, Rothmund condensations or oxidative coupling reactions.

The synthesis of sapphyrin **XII** follows a Macdonald-type [3 + 2] condensation [11] while in the synthesis of hexaphyrin **XIII** pyrrole and an aldehyde are condensed according to the Rothmund approach with low yields of 15 % [63] (Scheme 1.3). Heptaphyrin **XIV** can be synthesized following the oxidative coupling of unformulated tripyrranes and tetrapyranes, in which distinct pyrrole units were replaced via thiophene and selenophene [64]. Octaphyrin **XV** was synthesized using a Macdonald-type [2 + 2 + 2 + 2] condensation [65].

1.2.1 Aromaticity in Large Systems

Aromaticity describes the delocalization of π -electrons and stabilizes the system [66]. It is solely observed when distinct conditions are met: only systems which are planar and cyclic, have conjugated double bonds and obey Hückel's rule ($4n + 2$ π -electrons) are considered aromatic according to Hückel while $4n$ π -electrons are considered antiaromatic. The classic Hückel's aromaticity concept is derived from small molecules of only one sort of atoms. Heilbronner evolved a different concept of aromaticity which is named Möbius aromaticity due to the Möbius stripe [67].



Scheme 1.3 Varieties in the syntheses of expanded porphyrins: Macdonald-type approach toward sapphyrin **XII**, Rothemund-type approach toward hexaphyrin **XIII** and oxidative coupling reaction toward **XIV** [11, 63, 64]

A Möbius stripe is best constructed by taking a stripe of paper, twist it by 180° and join the ends. Heilbronner proposed that $4n$ π -electronic Möbius stripes are aromatic while $4n + 2$ π -electrons are antiaromatic [68].

Expanded porphyrins are extremely large systems and ideal partners to highlight the rules of aromaticity [12]. Especially hexaphyrin systems are suitable examples due to the easy two electron switch of [26] to [28] hexaphyrin (Fig. 1.10) [69, 70]. The conjugation pathway, which was already mentioned earlier in this work (Sect. 1.1), was defined by the annulene model dating back to the 1960s, which is a useful tool for aromaticity in molecules larger than benzene [71]. A conjugation pathway is present within the π -system when the following criteria are met:

- Passes through all subunits and encompasses the macrocycle.
- Can be represented by two resonance structures.
- Does not involve charge separation.

In general, the aromatic character cannot be quantified using a single criterion. Structural evidence for aromaticity is found by the observation of equal bond lengths along the conjugation pathway due to delocalized single and double bonds. Theoretical studies usually further fortify the assignment revealing the energy stabilization gained by aromaticity.

In nuclear magnetic resonance (NMR) experiments diatropic ring currents dramatically influence the chemical shifts of the inner and outer protons

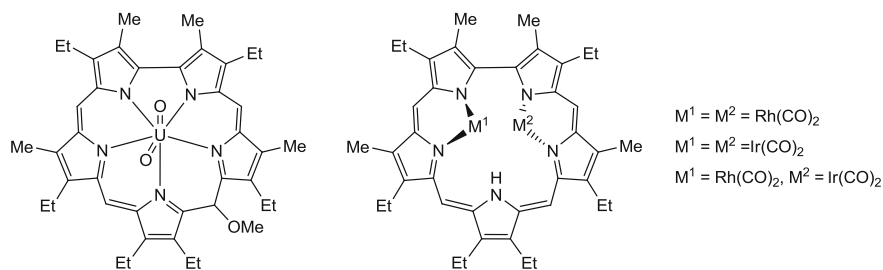


Fig. 1.12 Mono- and bi-metallic complexes of sapphyrin [73, 74]

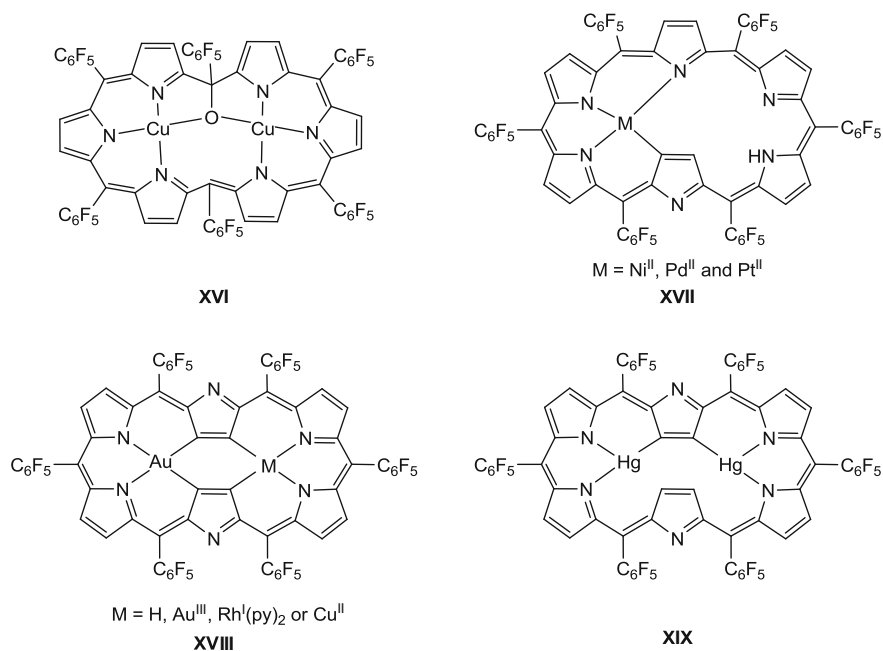


Fig. 1.13 Mono and bimetallic complexes of [26] hexaphyrin [75, 77, 78, 102]

in the square planar complexation. The molecule exhibits a gable structure and is non-planar. Thus, in some cases metal complexation comes along with yet not understood ligand reactions [75]. [26] hexaphyrin reacted with group 10 metal(II) acetates to primarily form mononuclear complexes (**XVII**).

In the monogold, digold and the hetero-bimetallic gold/copper, gold/silver and gold/rhodium complexes (**XVIII**), [26] hexaphyrin carries two inverted pyrrole units, offering two square planar N_2C_2 donor sets for complexation. The digold complex is nearly planar. Rhodium captured two additional pyridine residues to complete its desired octahedral coordination sphere [76, 77]. In the homobimetallic

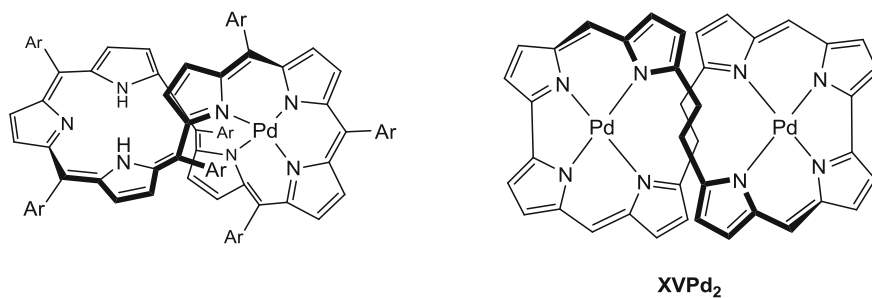


Fig. 1.14 Exemplarily chosen metal complexes of hepta- and octa-pyrin [79, 80]

mercury complex (**XIX**), mercury is bound only via an N_2C donor set leaving one vacant side [78]. For all metalation products summarized in Fig. 1.13, the same [26] hexapyrin as starting material was used, consequently distortion and inversion is solely originated from complexation (Fig. 1.13).

Additionally, metal complexes of heptapyrins and octapyrins were reported (Fig. 1.14). Under the retention of the organic scaffold of heptapyrin, only monometallic complexes were feasible [79]. With **XV**, the dipalladium complex was published [80]. Both chosen metal complexes depicted in Fig. 1.14 exhibit a figure-eight structure.

1.2.3 Applications

Expanded porphyrins are useful materials to back up the concept of aromaticity and prepare late transition metal or bimetallic complexes (Sects. 1.2.1 and 1.2.2). Even though expanded porphyrins are non-natural products, some are biologically compatible. Since low energy radiation is sufficient for excitation of expanded porphyrins and due to their observed red-shift they can be directly addressed in body's tissue while radiation does not excite biologically relevant porphyrins. This is used in photodynamic therapy (PDT) of tumors [16, 81, 82] and magnetic resonance imaging (MRI). In general terms, PDT uses a tumor localizing light-absorbing dye which upon radiation gets excited to its triplet state and converts triplet oxygen to singlet oxygen. That is cell toxic and initiates the destruction of unwanted tissue, such as carcinomas [83].

Further expanded porphyrins were proven useful for anion recognition with sapphyrin as the pioneer [84, 85]. Here, it was found that in its protonated form, sapphyrins are capable of binding halide and phosphate anions. However, other expanded porphyrins in their protonated and their neutral form showed affinity toward anions.

Many expanded porphyrins possess pronounced non-linear optical (NLO) properties [86, 87], which are desirable properties for use in optoelectronics [88].

Expanded porphyrins have greater thermal stability compared to typical organic chromophores, their extended π -conjugated macrocyclic ring gives large NLO effects and chemical modification of their backbone results in subtle variation in their physical properties.

1.3 Oxidoreductase Enzymes

As was already mentioned in [Sect. 1.1.1](#), porphyrin-containing enzymes play an important role in nature. It was shortly discussed that in respiration glucose gets oxidized using dioxygen and the chemically stored energy is released. Because oxidation in general is an energy releasing process and energy is needed for life, oxidation of small organic molecules is an attractive reaction. Dioxygen, with a percentage of 21 % in air, is always present and thus an interesting and cheap source for oxidation reactions.

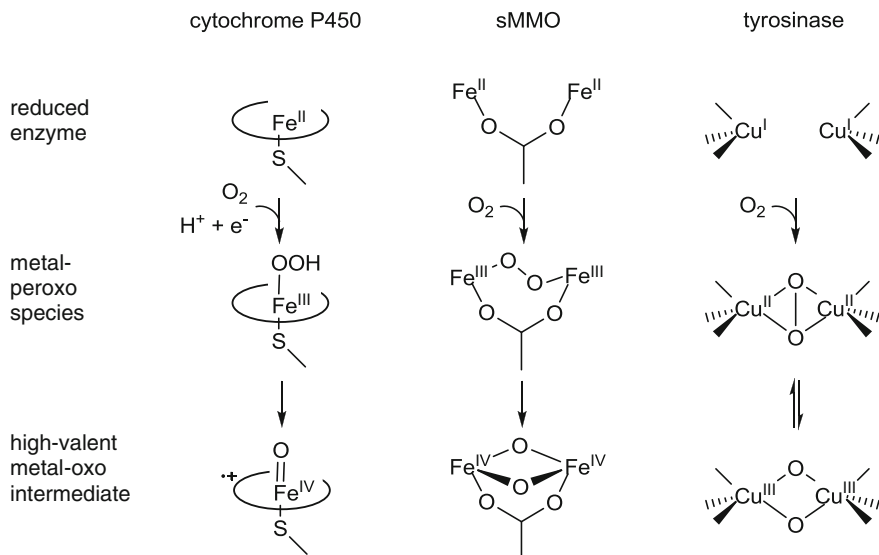
The consumption of the ambient dioxygen is not as simple as one may assume. Dioxygen is a triplet molecule while most organic molecules, so is glucose, are singlets and thus direct oxidation is usually spin-forbidden [4]. The dioxygen activation results in a redox-state change from 0 to -2 per oxygen atom, which is a four electron consuming process that rarely occurs in one concerted step in non-catalyzed reactions. Enzymes with their often paramagnetic metal based active centers help to overcome the spin-forbiddance and the difficulties of a four electron reduction process.

The final step of oxygen activation in the respiratory chain is catalyzed by the porphyrin-based enzyme cytochrome *c* oxidase. In oxidase enzymes the two oxygen atoms become water molecules. In contrast, cytochrome P450 is a monooxygenase, where one out of the two oxygen atoms is transferred to the organic substrate [2]. The residual oxygen atom becomes a water molecule. In dioxygenases, both oxygen atoms are transferred to the organic substrate.

1.3.1 Monooxygenases

Cytochrome P450 has a mononuclear heme-*b* core with Fe^{II} bound in its resting state. Upon reaction with dioxygen, two out of four electrons are provided by the redox state change from Fe^{II} to the high-valent Fe^{IV} , which is formed as an intermediate. The oxidation of the porphyrin system toward the cationic π -radical further contributes one electron, while the fourth electron has to be delivered from an electron transferring reagent (Scheme 1.4).

Besides the porphyrin-based monometallic active center in cytochrome P450, two monooxygenase enzymes with bimetallic active centers need to be mentioned, the soluble methane monooxygenase (sMMO) and tyrosinase. While sMMO is an iron based enzyme, tyrosinase has a dinuclear copper center [2]. The two iron



Scheme 1.4 Comparison of the key steps of the three introduced monooxygenases: cytochrome P450, sMMO and tyrosinase. The high-valent dicopper species was only observed in model complexes [2, 90–92]

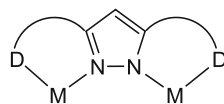
metals in sMMO are bridged via a carboxylate ligand [89]. The four electrons are here simply provided by a redox-state change from Fe^{II} to Fe^{IV} for both metal ions. In tyrosinase, first a two electron reduction of dioxygen to peroxide occurs which then reacts with the substrate. The exact mechanism has not yet been resolved [90–92]. Besides its monooxygenase activity, tyrosinase can also act as a dioxygenase.

In summary, among others, nature uses two different principles to provide the overall four electrons for dioxygen activation in monooxygenase enzymes: Either one metal center and the redox-active porphyrin ligand are involved or a bimetallic center, in which the latter bares the advantage that no additional electron sources are required. In a schematic drawing the three different presented monooxygenases and their key steps in oxygen activation are compiled (Scheme 1.4). In all key steps, high-valent metal species are formed.

1.4 Pyrazole: A Common Motif in Dinuclear Complexes

Bioinorganic chemistry tries to learn from nature by understanding it. In a simple approach, the active centers of metalloenzymes are tried to be modeled in their first coordination sphere with low molecular weight complexes [93, 94]. For mimicking dinuclear centers pyrazoles were shown to be a good replacement for

Fig. 1.15 Typical pyrazolate based bimetallic complex motif, *D* donor atom



the often observed carboxylate bridge. In its deprotonated form, pyrazolate is singly negatively charged and additional to its σ -donor function offers an enhanced π -donor function. Furthermore, side arms in its 3 and 5 position with donor atoms (*D*) can easily be attached and thus the coordination motif individually tailored. Diverse dinuclear complexes can be designed exhibiting the motif depicted in Fig. 1.15 [95]. By changing the lengths of the side arms, the metal–metal separation can be tuned within the range observed for carboxylate bridged systems.

Pyrazolate bridges in dinuclear complexes mediate cooperative effects due to its conjugated nature. The phenomena of cooperativity was introduced in hemoglobin, in which the binding of dioxygen to one subunit enhanced the affinity of the remaining subunits toward dioxygen. On a lower molecular level as in dinuclear pyrazolate-bridged complexes, magnetic exchange interactions are observed such that the spin orientation of the first metal ion influences the spin orientation of the second metal ion. Synergistic electronic effects enhance the reducing power in dinuclear systems [96, 97]. Using dinuclear complexes as catalysts, cooperativity is noticeable in the sense that the substrate can be preorganized on one metal center while the actual transformation takes place at the second.

Besides pyrazole-based complexes of the motif depicted in Fig. 1.15, several macrocyclic pyrazole-based ligands and dinuclear complexes of these were isolated [95]. Brooker et al. prepared a bimetallic macrocyclic pyrazolate-based dicopper complex **XX**, in which extra Schiff-base nitrogen atoms are provided [98]. Navarro and co-workers published the first pyrazole based cryptand-type ligand **XXI** in 1995 along with di- and tetra-nuclear silver(I), copper(II) and zinc(II) complexes [99]. Katsiaouni from our group synthesized macrocyclic pyrazole-based Schiff-base ligands **XXII** with a cavity too small to built dinuclear complexes (Fig. 1.16) but represent the first examples of pyrrole/pyrazole hybrid macrocycles to date [100].

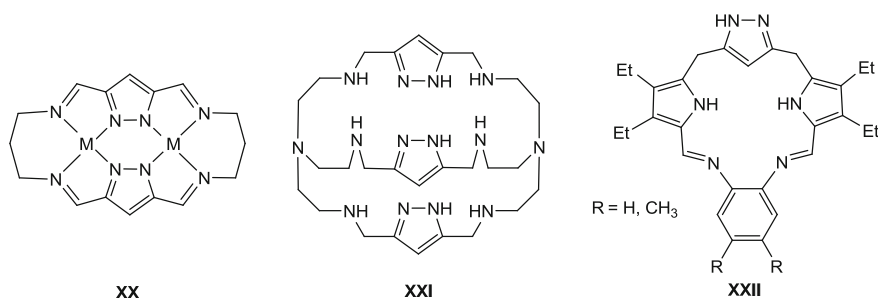


Fig. 1.16 Examples of non-aromatic macrocyclic 3,5-functionalized pyrazolate-based ligands [98–100]

References

1. D. Dolphin, *The Porphyrins* (Academic Press, New York, 1978)
2. W. Kaim, B. Schwederski, *Bioanorganische Chemie*, 4th edn. (B. G. Teubner, Wiesbaden, 2005)
3. A. Messerschmidt, R. Huber, K. Poulos, K. Wieghardt, *Handbook of Metalloproteins* (John Wiley & Sons Inc, Chichester, 2001)
4. I. Bertini, H.B. Gray, E.I. Stiefel, J.S. Valentine, *Biological Inorganic Chemistry* (University Science Books, Sausalito, 2007)
5. http://www.nobelprize.org/nobel_prizes/chemistry/laureates/
6. K.M. Kadish, K.M. Smith, R. Guilard, *The Porphyrin Handbook*, vol. 1 (Academic Press, San Diego, 2000)
7. S. Saito, A. Osuka, *Angew. Chem. Int. Ed.* **50**, 4342–4373 (2011)
8. M. Stępień, N. Sprutta, L. Latos-Grażyński, *Angew. Chem. Int. Ed.* **50**, 4288–4340 (2011)
9. J.L. Sessler, A. Gebaur, S.J. Weghorn, in *The Porphyrin Handbook*, vol. 2, ed. by K.M. Kadish, K.M. Smith, R. Guilard (Academic Press, San Diego, 2000), pp. 1–413
10. J.L. Sessler, D. Seidel, *Angew. Chem. Int. Ed.* **42**, 5134–5175 (2003)
11. A. Jasat, D. Dolphin, *Chem. Rev.* **97**, 2267–2340 (1997)
12. Z.S. Yoon, A. Osuka, D. Kim, *Nat. Chem.* **1**, 113–122 (2009)
13. A. Osuka, S. Saito, *Chem. Commun.* **47**, 4330–4339 (2011)
14. J.L. Sessler, A.E. Vivian, D. Seidel, A.K. Burrell, M. Hoehner, T.D. Mody, A. Gebauer, S.J. Weghorn, V. Lynch, *Coord. Chem. Rev.* **216–217**, 411–434 (2001)
15. J.L. Sessler, E. Tomat, *Acc. Chem. Res.* **40**, 371–379 (2007)
16. J.L. Sessler, G. Hemmi, T.D. Mody, T. Murai, A. Burrell, S.W. Young, *Acc. Chem. Res.* **27**, 43–50 (1994)
17. L.K. Frensch, K. Pröpper, M. John, S. Demeshko, C. Brückner, F. Meyer, *Angew. Chem. Int. Ed.* **50**, 1420–1424 (2011)
18. T. Eicher, S. Hauptmann, *The Chemistry of Heterocycles* (WILEY-VCH, Weinheim, 2003)
19. M. Stępień, L. Latos-Grażyński, in *Topics in Heterocyclic Chemistry*, vol. 19, ed. by R.R. Gupta (Springer, Heidelberg, 2009), pp. 83–153
20. L.R. Milgrom, *The Colours of Life: An Introduction to the Chemistry of Porphyrins and Related Compounds* (Oxford University Press, Oxford, 1997)
21. M. Gouterman, in *The Porphyrins*, vol. 3, ed. by D. Dolphin (Academic Press, New York, 1978), pp. 1–165
22. C.M. Lemon, P.J. Brothers, B. Boitrel, *Dalton Trans.* **40**, 6591–6609 (2011)
23. O.Q. Munro, J.C. Bradley, R.D. Hancock, H.M. Marques, F. Marsicano, P.W. Wade, *J. Am. Chem. Soc.* **114**, 7218–7230 (1992)
24. D. Voet, J.G. Voet, C.W. Pratt, A. Beck-Sickinger, *Lehrbuch der Biochemie* (Wiley VCH Verlag GmbH, Weinheim, 2010)
25. J. Monod, J. Wyman, J.-P. Changeux, *J. Mol. Biol.* **12**, 88–118 (1965)
26. W.A. Eaton, E.R. Henry, J. Hofrichter, A. Mozzarell, *Nat. Struct. Mol. Biol.* **6**, 351–358 (1999)
27. M.F. Perutz, G. Fermi, B. Luisi, B. Shaanan, R.C. Liddington, *Acc. Chem. Res.* **20**, 309–321 (1987)
28. J.J. Weiss, *Nature* **202**, 83 (1964)
29. M.F. Perutz, *Nature* **228**, 726–734 (1970)
30. B. Meunier, S.P. de Visser, S. Shaik, *Chem. Rev.* **104**, 3947–3980 (2004)
31. A.R. Battersby, *Nat. Prod. Rep.* **17**, 507–526 (2000)
32. A.F. Holleman, N. Wiberg, *Lehrbuch der Anorganischen Chemie*, 102nd edn. (Walter de Gruyter, Berlin, 2007)
33. H. Fischer, W. Gleim, *Liebigs Ann. Chem.* 1936, 521, 157–160
34. P.J. Rothmund, *J. Am. Chem. Soc.* 1935, 57, 2010–2011
35. P. Rothmund, *J. Am. Chem. Soc.* 1936, 58, 625–627

36. J.S. Lindsey, I.C. Schreiman, H.C. Hsu, P.C. Kearney, A.M. Marguerettaz, *J. Org. Chem.* **52**, 827–836 (1987)
37. G.P. Arsenault, E. Bullock, S.F. MacDonald, *J. Am. Chem. Soc.* **82**, 4384–4389 (1960)
38. H.-J. Xu, J. Mack, A.B. Descalzo, Z. Shen, N. Kobayashi, X.-Z. You, K. Rurack, *Chem.-Eur. J.* **17**, 8965–8983 (2011)
39. L. Latos-Grazynski, J. Lisowski, M.M. Olmstead, A.L. Balch, *J. Am. Chem. Soc.* **109**, 4428–4429 (1987)
40. L. Latos-Grazynski, E. Pacholska, P.J. Chmielewski, M.M. Olmstead, A.L. Balch, *Angew. Chem. Int. Ed.* **34**, 2252–2254 (1995)
41. L. Latos-Grazynski, E. Pacholska, P.J. Chmielewski, M.M. Olmstead, A.L. Balch, *Inorg. Chem.* **35**, 566–573 (1996)
42. E. Vogel, P. Röhrig, M. Sicken, B. Knipp, A. Herrmann, M. Pohl, H. Schmickler, J. Lex, *Angew. Chem. Int. Ed.* **28**, 1651–1655 (1989)
43. E. Vogel, W. Haas, B. Knipp, J. Lex, H. Schmickler, *Angew. Chem. Int. Ed.* **27**, 406–409 (1988)
44. E. Vogel, C. Fröde, A. Breihan, H. Schmickler, J. Lex, *Angew. Chem. Int. Ed.* **36**, 2609–2612 (1997)
45. T.L. Gilchrist, *Heterocyclic Chemistry*, 3 edn. (Pearson Education, New Delhi, 1997)
46. T.D. Lash, A.M. Young, A.L. Von Ruden, G.M. Ferrence, *Chem. Commun.* 6309–6311 (2008)
47. J.-M. Lehn, *Supramolecular Chemistry: Concept and Perspectives* (Wiley VCH, Weinheim, 1995)
48. F.P. Schwarz, M. Goutermann, Z. Muljiani, D.H. Dolphin, *Bioinorg. Chem.* **2**, 1–32 (1972)
49. V.V. Diev, K. Hanson, J.D. Zimmerman, S.R. Forrest, M.E. Thompson, *Angew. Chem. Int. Ed.* **49**, 5523–5526 (2010)
50. H. Shinokubo, A. Osuka, *Chem. Commun.* 1011–1021 (2009)
51. I. Beletskaya, V.S. Tyurin, A.Y. Tsivadze, R. Guilard, C. Stern, *Chem. Rev.* **109**, 1659–1713 (2009)
52. M.R. Wasielewski, *Chem. Rev.* **92**, 435–461 (1992)
53. T.S. Balaban, P. Marek, R. Hedderich, *Nanotechnik* **06** (2006)
54. U.K. R.B. Woodward (Sheffield, 1966)
55. V.J. Bauer, D.L. J. Clive, D. Dolphin, J.B. P. III, F.L. Harris, M.M. King, J. Loder, S.W. C. Wang, R.B. Woodward, *J. Am. Chem. Soc.* **105**, 6429–6436 (1983)
56. Y. Tanaka, J.-Y. Shin, A. Osuka, *Eur. J. Org. Chem.* 1341–1349 (2008)
57. K.M. Kadish, K.M. Smith, R. Guilard, *The Porphyrin Handbook*, vol. 3 (Academic Press, Diego, 2000)
58. H. Brand, J. Arnold, *Coord. Chem. Rev.* **140**, 137–168 (1995)
59. P.J. Brothers, *J. Porphyrins Phthalocyanines* **6**, 259–267 (2002)
60. J.-Y. Shin, K.S. Kim, M.-C. Yoon, J.M. Lim, Z.S. Yoon, A. Osuka, D. Kim, *Chem. Soc. Rev.* **39**, 2751–2767 (2010)
61. R. Misra, T.K. Chandrashekar, *Acc. Chem. Res.* **41**, 265–279 (2008)
62. M.-C. Yoon, P. Kim, H. Yoo, S. Shimizu, T. Koide, S. Tokuji, S. Saito, A. Osuka, D. Kim, *J. Phys. Chem. B*, **115**, 14928–14937 (2011)
63. M.G. P.M. S. Neves, R.M. Martins, A.C. Tome, A.J. D. Silvestre, A.M. S. Silva, V. Felix, J.A. S. Cavaleiro, M.G. B. Drew, *Chem. Commun.* 385–386 (1999)
64. V.R.G. Anand, S.K. Pushpan, A. Srinivasan, S.J. Narayanan, B. Sridevi, T.K. Chandrashekar, R. Roy, B.S. Joshi, *Org. Lett.* **2**, 3829–3832 (2000)
65. E. Vogel, M. Bröring, J. Fink, D. Rosen, H. Schmickler, J. Lex, K.W.K. Chan, Y.-D. Wu, D.A. Plattner, M. Nendel, K.N. Houk, *Angew. Chem. Int. Ed.* **34**, 2511–2514 (1995)
66. J. Clayden, N. Greeves, S. Warren, P. Wothers, *Organic Chemistry* (Oxford University Press, New York, 2001), pp. 151–180
67. E. Heilbronner, *Tetrahedron Lett.* **5**, 1923–1928 (1964)
68. N. Jux, *Angew. Chem. Int. Ed.* **47**, 2543–2546 (2008)
69. M. Suzuki, A. Osuka, *Chem. Commun.* 3685–3687 (2005)

70. T. Koide, K. Youfu, S. Saito, A. Osuka, *Chem. Commun.* 6047–6049 (2009)
71. F. Sondheimer, R. Wolovsky, Y. Amiel, *J. Am. Chem. Soc.* **84**, 274–284 (1962)
72. J.A.N.F. Gomes, R.B. Mallion, *Chem. Rev.* **101**, 1349–1384 (2001)
73. A.K. Burrell, M.J. Cyr, V. Lynch, J.L. Sessler, *J. Chem. Soc., Chem. Commun.* 1710–1713 (1991)
74. J.L. Sessler, M.J. Cyr, A.K. Burrell, *Synlett* **1991**, 127–134 (1991)
75. S. Shimizu, V.G. Anand, R. Taniguchi, K. Furukawa, T. Kato, T. Yokoyama, A. Osuka, *J. Am. Chem. Soc.* **126**, 12280–12281 (2004)
76. S. Mori, A. Osuka, *Inorg. Chem.* **47**, 3937–3939 (2008)
77. S. Mori, A. Osuka, *J. Am. Chem. Soc.* **127**, 8030–8031 (2005)
78. A. Mori, S. Shimizu, J.-Y. Shin, A. Osuka, *Inorg. Chem.* **46**, 4374–4376 (2007)
79. T. Yoneda, S. Saito, H. Yorimitsu, A. Osuka, *Angew. Chem. Int. Ed.* **50**, 3475–3478 (2011)
80. A. Werner, M. Michels, L. Zander, J. Lex, E. Vogel, *Angew. Chem. Int. Ed.* **38**, 3650–3653 (1999)
81. D.J. Magda, Z. Wang, N. Gerasimchuk, W. Wei, P.J. Anzenbacher, J.L. Sessler, *Pure Appl. Chem.* **76**, 365–374 (2004)
82. T.D. Mody, J.L. J. Sessler, *Porphyrins Phthalocyanines* **5**, 134–142 (2001)
83. M. Ochsner, *Arzneimittelforschung* **47**, 1185–1194 (1997)
84. J.L. Sessler, S. Camiolo, P.A. Gale, *Coord. Chem. Rev.* **240**, 17–55 (2003)
85. J.L. Sessler, M. Cyr, H. Furuta, v. Kral, T. Mody, T. Morishima, M. Shionoya, S. Weghorn, *Pure Appl. Chem.* **65**, 393–398 (1993)
86. J.L. Sessler, S. Weghorn, *Expanded, Contracted & Isomeric Porphyrins* (Pergamon Press, New York, 1997)
87. R. Misra, R. Kumar, T.K. Chandrashekar, C.H. Suresh, A. Nag, D. Goswami, *J. Am. Chem. Soc.* **128**, 16083–16091 (2006)
88. K.M. Kadish, K.M. Smith, R. Guilard, *The Porphyrin Handbook*, vol. 6 (Academic Press, San Diego, 2000)
89. C.E. Tinberg, S.J. Lippard, *Acc. Chem. Res.* **44**, 280–288 (2011)
90. J.A. Halfen, S. Mahapatra, E.C. Wilkinson, S. Kaderli, V.G. Young, L. Que, A.D. Zuberbühler, W.B. Tolman, *Science* **271**, 1397–1400 (1996)
91. L.M. Mirica, X. Ottenwaelder, T.D. P. Stack, *Chem. Rev.* **104**, 1013–1046 (2004)
92. M.J. Henson, P. Mukherjee, D.E. Root, T.D. P. Stack, E.I. Solomon, *J. Am. Chem. Soc.* **121**, 10332–10345 (1999)
93. A.L. Gavrilova, B. Bosnich, *Chem. Rev.* **104**, 349–384 (2004)
94. R.H. Holm, P. Kennepohl, E.I. Solomon, *Chem. Rev.* **96**, 2239–2314 (1996)
95. J. Klingele, S. Dechert, F. Meyer, *Coord. Chem. Rev.* **253**, 2698–2741 (2009)
96. B. Bosnich, *Inorg. Chem.* **38**, 2554–2562 (1999)
97. D.G. McCollum, B. Bosnich, *Inorg. Chim. Acta* **270**, 13–19 (1998)
98. D.J. de Geest, A. Noble, B. Moubaraki, K.S. Murray, D.S. Larsen, S. Brooker, *Dalton Trans.* 467–475 (2007)
99. M. Kumar, V.J. Arán, P. Navarro, *Tetrahedron Lett.* **36**, 2161–2164 (1995)
100. S. Katsiaouni, S. Dechert, C. Brückner, F. Meyer, *Chem. Commun.* 951–953 (2007)
101. A. Srinivasan, T. Ishizuka, A. Osuka, H. Furuta, *J. Am. Chem. Soc.* **125**, 878–879 (2003)
102. S. Mori, S. Shimizu, R. Taniguchi, A. Osuka, *Inorg. Chem.* **44**, 4127–4129 (2005)

Chapter 2

Objective

It was shown, that nature is using the enzymes introduced in Sect. 1.3 to catalyze the activation of dioxygen, which is a four electron reduction. In the active center of cytochrome P450, two electrons are provided by the redox-state change of one Fe^{II} to Fe^{IV} . The third electron is generated by the participation of the porphyrin ligand which becomes a cationic π -radical. The fourth electron is provided by an electron transferring reagent. The active center of cytochrome P450 only provides three out of four needed electrons, methane monooxygenase with its advantageous bimetallic active center is able to provide all four.

A system combining the two principles of a redox-active bimetallic unit [1] and a non-innocent porphyrinic macrocycle would be of particular interest with regards to redox chemistry and oxygenase activity. A framework as the one depicted in Fig. 2.1 seems to be worthwhile. This arrangement can be interpreted as the fusion of two N_4 coordination sites and belongs to the substance class of expanded porphyrins. It consists of four pyrrole and two pyrazole units connected via methine carbon atoms. The connectivity pattern resembles two porphyrins joined at the hip, which tempted us to call it the Siamese-twin porphyrin. This naming is descriptive of the framework structure but shall not evoke any implications about the presence of porphyrinic conjugation pathways inherent to this system.

The first objective of this work was to accomplish the synthesis of the Siamese-twin porphyrin scaffold. Investigations concerning the geometry and aromaticity are of interest, to compare these with porphyrin data. Because expanded porphyrins are known to react sensitively toward pH changes, protonation studies will be performed and their influence on geometry will be investigated. However, with respect to the biomimetic inspiration, also the redox chemistry of the Siamese-twin porphyrin itself should be investigated with the help of electrochemical methods.

From a coordination chemist's perspective, this system is a strong chelating ligand capable of binding two metals in close proximity. While the outcome of metalation reactions of expanded porphyrins is not always predictable, especially seen in first-row transition metal complexation of hexaphyrins, an N_4 donor set is advantageous. Thus, after completing the synthesis of the Siamese-twin porphyrin, the second objective is to synthesize homo- and hetero-bimetallic complexes and

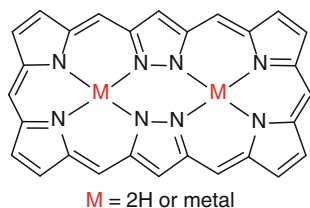
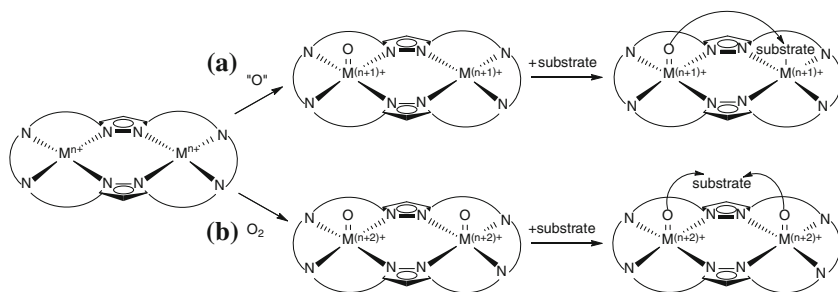


Fig. 2.1 Scaffold of the Siamese-twin porphyrin



Scheme 2.1 The Siamese-twin porphyrin as a catalyst in assumed oxygenation reactions: **a** with monooxygenase activity. **b** with dioxygenase activity. The possible non-innocence of the ligand system is neglected in this scheme

to understand their ground states and further investigate their redox behavior. This knowledge is necessary to predict their behavior in catalysis.

The future goal is to catalyze oxygenation reactions of small organic molecules using these complexes. Several mechanisms are possible thinking of the bimetallic cavity: either only one metal is involved in the oxygen activation, while the substrate may be preorganized by coordination to the vacant metal side (monooxygenase activity, Scheme 2.1a) or both metals are forming high-valent metal-oxo species in their active intermediate to transfer the two oxygen atoms to the substrate (dioxygenase activity, Scheme 2.1b).

Reference

1. D.G. McCollum, B. Bosnich, *Inorg. Chim. Acta.* **270**, 13–19 (1998)

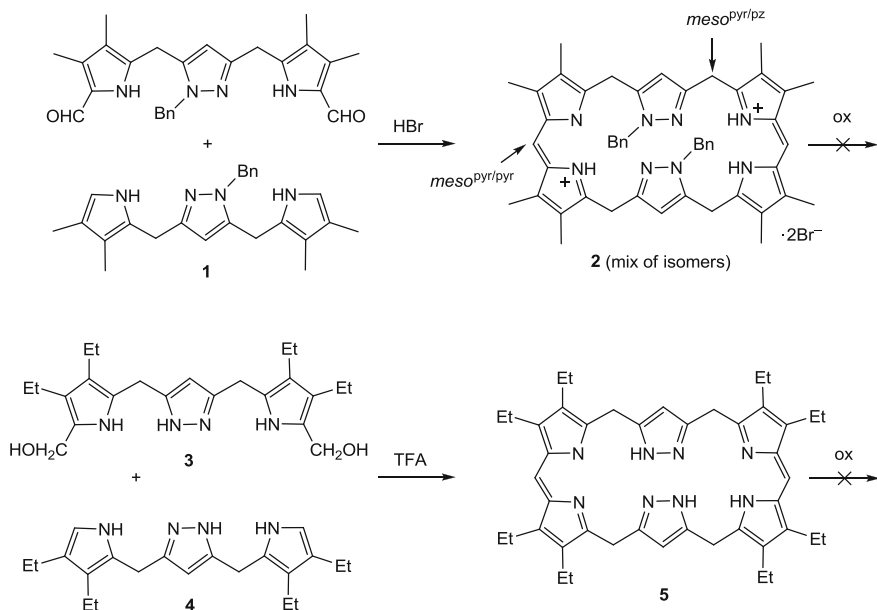
Chapter 3

Route to the Siamese-Twin Porphyrin

I am not the first to conceive the structure of the Siamese-twin porphyrin. Already Lind and Katsiaouni spent some effort to succeed in the synthesis of the described framework [1, 2]. Two main factors stymied progress in Lind's 1987 dissertation: Firstly, the route to the key intermediate **1** was only feasible protecting the pyrazole-*N*1 with a benzylic protective group (Bn). However, its cleavage remained unsuccessful. The cyclization toward the Siamese-twin porphyrinogen **2** was still conducted, obtaining a mixture of regioisomers which could not be separated. Secondly, the following oxidation step of the left sp^3 hybridized carbon atoms failed (Scheme 3.1) Katsiaouni also faced the latter problem and could not establish a reliable oxidation strategy.

Both pursued a [3 + 3]-Macdonald type approach using pyrrole/pyrazole hybrids (**1**, **3**, **4**; Scheme 3.1), which are similar to a tripyrrane in the [3 + 2] approach in the saphyrin synthesis (Sect. 1.2) and the [3 + 1] approach in porphyrin synthesis (Sect. 1.1.2). Katsiaouni chose an alternative route to avoid the need of a pyrazole protective group. As Lindsey, Katsiaouni further reduced the keto function to alcohol **3** to subsequently run the cyclization step toward **5** [3]. As in Lind's observation, oxidation success was limited to *meso* carbon atoms between two pyrrole units ($meso^{pyr/pyr}$ with pyr = pyrrole; Scheme 3.1).

Because both previous studies reported problems in the oxidation attempts of the carbon atoms between pyrrole and pyrazole units ($meso^{pyr/pz}$ with pz = pyrazole), our strategy was to implement phenyl groups in these positions by choosing a suitable pyrazole building block. An increased driving force toward the completely oxidized macrocycle is anticipated because introduction of the phenyl groups enhances the π -system. Bulky substituents in the backbone are further favored to avoid inversion of the pyrazole units by steric hindrance and to indeed provide the desired N_4 coordination motif for each pocket.



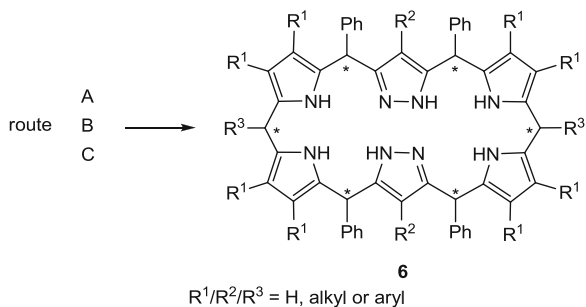
Scheme 3.1 Lind's (*top*) and Katsiaouni's (*bottom*) attempt toward the Siamese-twin porphyrin scaffold

3.1 Cyclization Strategies

Based on Lind's and Katsiaouni's strategy of a [3 + 3] type cyclization reaction, different routes were developed for the work in hand. In this chapter, only the initial cyclization to the macrocyclic arrangement (porphyrinogen **6**, Scheme 3.2) is discussed while the oxidation-debate is held for Sect. 3.4.

There are three conceivable pathways to approach the cyclization to the Siamese-twin porphyrinogen **6**, route A–C (Fig. 3.1, Scheme 3.2). In route A, which differs from Lind's, Katsiaouni's and common (expanded) porphyrin synthetic strategies, two dipyrromethanes/dipyrromethenes are converted with an appropriate

Scheme 3.2 Cyclization reaction to the Siamese-twin porphyrinogen



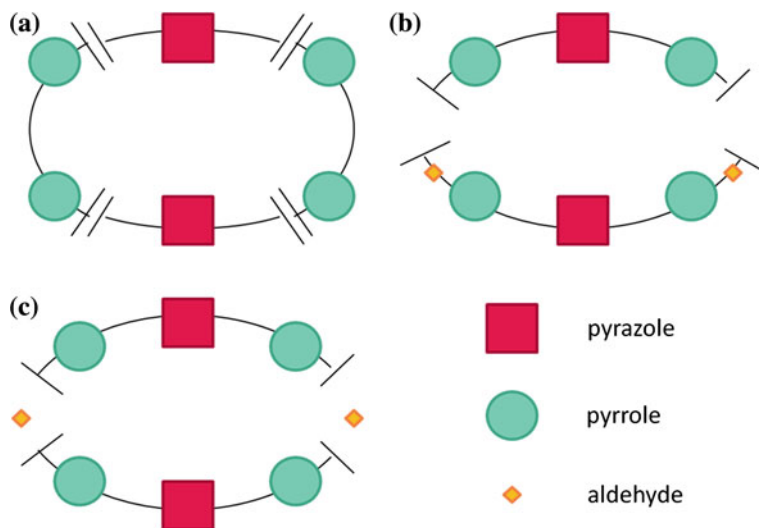


Fig. 3.1 En route to the Siamese-twin porphyrinogen: synthetic cyclization strategies

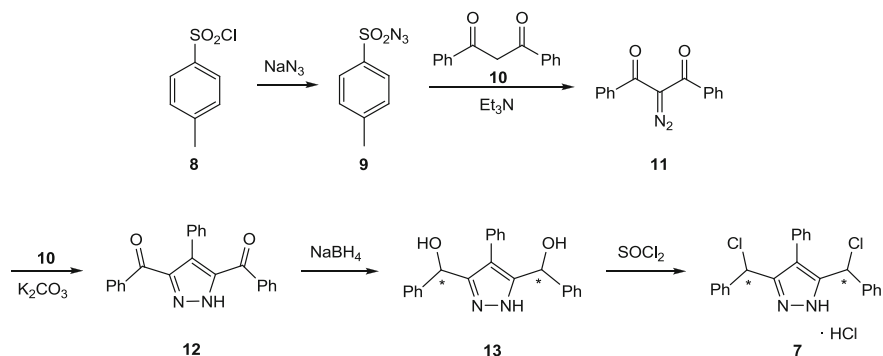
pyrazole moiety. Route B is analogous to A [3 + 3] Macdonald-type condensation step and was already applied by Lind and Katsiaouni. Route C follows A [3 + 3] condensation with free aldehydes.

3.2 Synthesis of Building Blocks

To accomplish the synthesis of the macrocyclic Siamese-twin porphyrinogen **6** (Scheme 3.2) according to the proposed routes A–C, multiple building blocks are required. For all routes a reactive pyrazole building block is needed. This can be converted with suitable pyrrole units to a pyrrole/pyrazole hybrid as the tripyrrane analog for pathways B and C, which additionally has to be formylated in its α -position for route B. For a, special dipyrrromethane/dipyrrromethene units are of interest. A variety of aldehydes are commercially available. Thus, prior to the investigation of the cyclization reactions A–C, suitable pyrazole, pyrrole, dipyrrromethane and dipyrrromethene building blocks have to be chosen and synthesized.

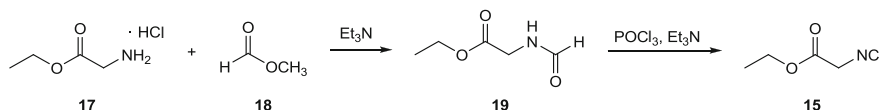
3.2.1 The Pyrazole Precursor

Profiting from Lind's and Katsiaouni's observations, phenyl groups introduced in the *meso*^{pyr/pz} positions were considered beneficial for facilitating the final oxidation step, thus a pyrazole unit is chosen with phenyl groups attached to the side

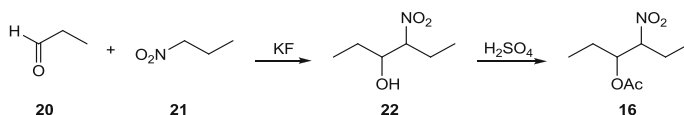


Scheme 3.3 Synthesis of the activated pyrazole precursor **7** [4–8]

arms. Hence, to synthesize the desired Siamese-twin porphyrin scaffold 3,5-bis-(chloro(phenyl)-methyl)-4-phenyl-1*H*-pyrazole hydrochloride (**7**) was chosen as the pyrazol building block (Scheme 3.3). Its side arms allow reactivity via a nucleophilic substitution and provide phenyl groups on the later *meso*^{pyr/pz} carbon atoms. The additional phenyl group in position 4 of the pyrazol is helpful to avoid *inverted* conformations. Its five step synthesis was published by Sachse (until **12**) [4] and was further developed during my diploma thesis (**13** and **7**, Scheme 3.3) [5, 6]. **7** was synthesized via the reaction of *p*-toluenesulfonyl chloride (**8**) with sodium azide to yield the temperature sensitive *p*-toluenesulfonyl azide (**9**) [7]. This was used to introduce a diaza group in the double α -position of the dibenzoylmethane (**10**) [8]. The reaction of **10** and **11** led to the desired pyrazole precursor **12**. The keto function introduces reactivity at the carbonyl atom but requires further activation. Therefore, sodium borohydride was added to reduce the keto to a hydroxyl group. To increase the leaving group character [9], this group was replaced by a chloride by stirring **13** with SOCl_2 for three days. Decomposition products of SOCl_2 (HCl and SO_2) led to protonation and yielded the hydrochloride **7**. This along with residual SOCl_2 complicated the following conversions. Hence, redissolving **7** three times in toluene and subsequent removal under reduced pressure helped to remove the residual SOCl_2 but still rendered the molecule in its protonated form. Because water is the product of the neutralization reaction, neutralization of **7** is hindered due to its water sensitivity. Attempts to neutralize **7** by stirring in anhydrous CH_2Cl_2 over Na_2CO_3 and MgSO_4 minimized the yield drastically without gaining reinsurance about the success of neutralization, because NH signals were not observed in the ^1H NMR spectrum. That is why **7** was used in its protonated form. The sp^3 hybridized positions were designed to be highly reactive toward nucleophilic attacks due to chloride as a good leaving group and its double benzylic nature. With reduction from **12** to **13**, the molecule turned chiral (chiral centers are marked with an asterisk) and a mixture of enantiomers and diastereomers is present in **13** and **7**. Because the stereogenic carbon atoms are supposed to act as *meso* carbon atoms later, and thus methine carbon



Scheme 3.4 Synthetic route to ethylisocyanoacetate (**15**) [11]



Scheme 3.5 Synthetic route to 4-acetoxy-3-nitrohexane (**16**) [12]

atoms, there is no need to apply enantioselective synthetic strategies. However, chirality complicated ^1H NMR spectra of the intermediates.

3.2.2 The Pyrrole Precursor

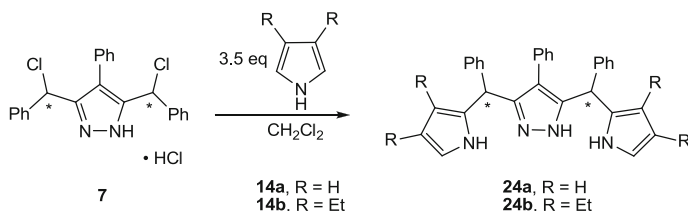
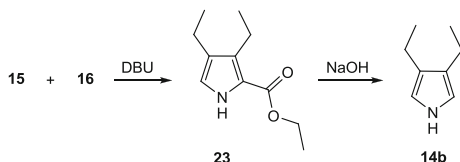
As pyrrole units, pyrrole (**14a**, Fig. 1.1) and 3,4-diethylpyrrole (**14b**) were used (Scheme 3.6). **14a** in comparison to **14b** reduces the steric demand in the latter Siamese-twin porphyrin and is commercially available. **14b** on the other hand prevents a possible nucleophilic attack in the β -positions and enhances the solubility in organic solvents. But unfortunately it is not commercially available: a well-working seven step synthesis is literature-known [10–11].

To build 3,4-diethylpyrrole, ethylisocyanoacetate [10] (**15**) (2 steps) and 4-acetoxy-3-nitrohexane [11] (**16**) (2 steps) had to be synthesized. Therefore, glycine ethylester hydrochloride (**17**) was deprotonated with triethylamine to induce a nucleophilic attack from the then deprotonated **17** on the carbonyl atom of **18** (Scheme 3.4). To the formed *N*-formylglycine ethylester (**19**) was added triethylamine and phosphorylchloride to convert the amide to an isonitrile group. The obtained brownish crude product could be purified via distillation. Ethylisocyanoacetate (**15**) tends to decompose and has to be stored under inert atmosphere and cooling.

For the synthesis of 4-acetoxy-3-nitrohexane (**16**), propanal (**20**), 1-nitropropane (**21**) and potassium fluoride were dissolved in isopropanol to form **22**. **22** was distilled and the purified product was reacted with sulfuric acid and acetic anhydride to convert the hydroxyl group to an acetate. **16** was obtained after fractional distillation and had to be stored at low temperature (Scheme 3.5).

Letting **16** react with DBU, the acetate protecting group was cleaved and 3-nitro-3-hexene was formed. Addition of **15** gave ethyl-3,4-diethylpyrrole-2-carboxylate (**23**). After decarboxylation the needed pyrrole block **14b** was obtained.

Scheme 3.6 Synthetic route to 3,4-diethylpyrrole (**14b**) [12]



Scheme 3.7 Synthesis of the pyrrole/pyrazole hybrids **24a** and **b** [5]

3.2.3 Pyrrole/Pyrazole Hybrids

Based on the pyrroles **14a/b** and pyrazole **7**, the two different pyrrole/pyrazole hybrids (**24a/b**) are in reach (Scheme 3.7). Coupling of the activated pyrazole building block **7** and the pyrrole units **14a/b** via a nucleophilic attack of pyrrole's free α -position on the activated chiral carbon atoms was induced. Reactions had to be carried out under anhydrous conditions. **7** was dissolved in anhydrous CH_2Cl_2 and an excess of **14a** or **14b** was added; then it was stirred for 2 h. The reaction was monitored via thin layer chromatography (TLC) which could be stained using bromine.

The products **24a/b** were purified using column chromatography. The eluent [*n*-hexane/ethylacetate (EtOAc)] for **24a** had to be much more polar than for **24b**. In the case of **24a** solubility problems in the eluent were observed resulting in yields lower than 20 %. Also the practicability in further reactions as starting material is affected due to the bad solubility in organic solvents—except DMSO. **24b** did not show any of these problems. Yields higher than 40 % are within an acceptable range. One byproduct was identified as the monosubstituted pyrazole [5].

Not only the purification, but also the analysis with ^{13}C NMR spectroscopy of **24a** was hindered due to its bad solubility. ^1H NMR spectra were recorded in DMSO (Fig. 3.2). Besides many low field shifted signals due to the phenyl groups, characteristic shifts of the pyrrolic protons at 5.82, 5.91 and 6.61 ppm were observed. A characteristic signal at 5.32 ppm is present, which arises from the benzylic protons. Two broad resonances at 10.50 and 12.55 ppm were observed for the NH^{pyr} and NH^{pz} supported by the reduced exchange of these protons due to the good hydrogen-bond acceptor DMSO. For **24b**, ^1H NMR spectra were recorded in CD_2Cl_2 , where a multitude of signals is evoked by the mixture of diastereomers. The expected ethyl triplets and quartets appear as multiplets in the

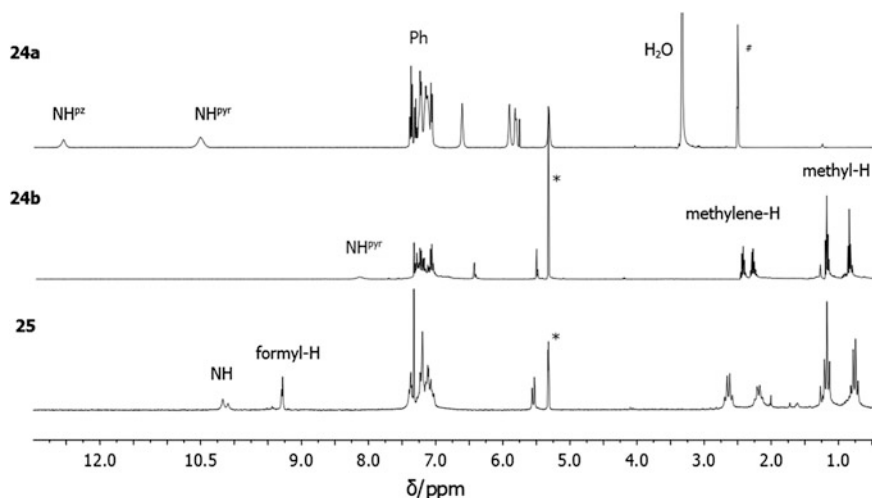
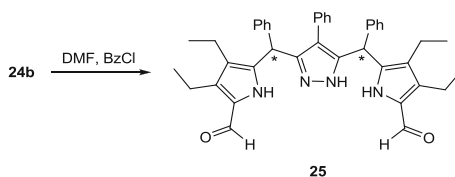


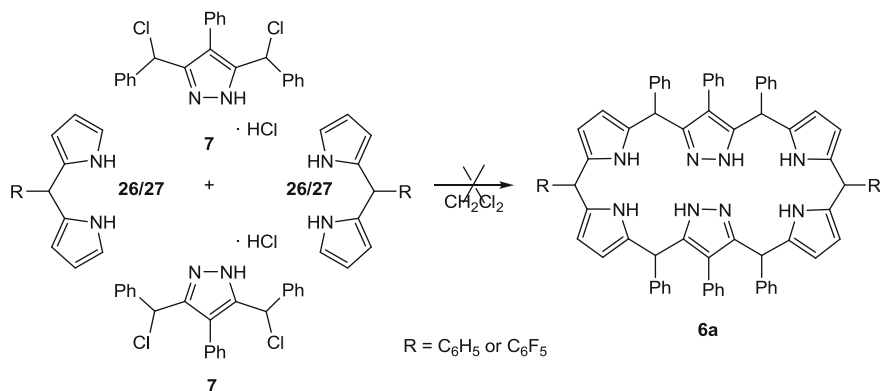
Fig. 3.2 ^1H NMR spectra (400 MHz, CD_2Cl_2 , *) of **24b** and **25**, and of **24a** (300 MHz, $\text{DMSO}-d_6$, #)

Scheme 3.8 Synthesis of 3,5-bis-(3,4-diethyl-5-formyl-1*H*-pyrrole-2-yl-benzyl)-1*H*-pyrazole (**25**)



range of 0.77–0.90 ppm and 1.14–1.20 ppm (CH_3 groups) and from 2.20 to 2.32 and 2.37 to 2.48 ppm (CH_2 groups). Comparing this spectrum to the ^1H NMR spectrum of **24a**, only one pyrrole signal for the free α -position at 6.42 ppm was detected. The benzylic CH groups resonate at 5.50 ppm and only one broad NH^{pyr} signal at 8.10 ppm was observed, most likely because the good hydrogen-bond acceptor DMSO was replaced by CD_2Cl_2 as NMR solvent.

With these, the basic building blocks for route C are available. For route B, **24b** was further modified in its α -position via formylation. According to Katsiaouni's experience, the use of DMF and benzoylchloride (BzCl) as formylating reagents turned out to be most promising. Using DMF and BzCl as reagents gave **25** (Scheme 3.8) in pathetic yields of 23 %. The ^1H NMR spectrum of **25** revealed a new signal at 9.29 ppm referring to carbonyl protons (Fig. 3.2), while compared to **24b** the signal at 6.42 ppm referring to the free α -position disappeared. ^{13}C NMR spectroscopy additionally confirmed the formation of **15** with a resonance at 177 ppm—a typical shift for carbonyl carbon atoms [12], as well as the carbonyl bands at 1625 cm^{-1} in the IR spectrum [13].



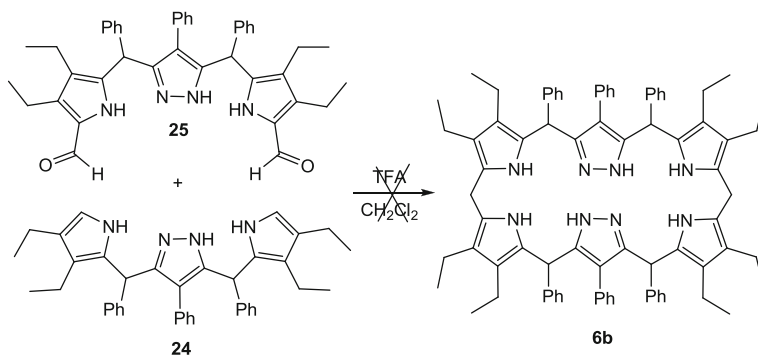
Scheme 3.10 Chemical reaction to the Siamese-twin porphyrinogen following route A

3.3.1 Route A

The symbols from the analogy in Fig. 3.1 transferred into chemical formulas leads to the reaction mechanism shown in Scheme 3.10. The activated pyrazole **7** (5 mg, 116 μmol) was dissolved in anhydrous CH₂Cl₂ (5 mL) and cooled with an ice bath. One equivalent of the dipyrrometha(e)ne unit (2.6 mg for **26** or 3.6 mg for **27**; 0.116 μmol) was added slowly and the mixture was stirred up to two days while the progress of the reaction was monitored via TLC and ESI–MS. According to ESI–MS neither for **26** nor for **27** a conversion to the desired macrocycle **6a** was detected. The absence of starting material points to decomposition. Since **7** could not be neutralized the acid sensitive **26** most likely decomposed. For **27** ¹⁹F NMR spectroscopy was applied but confirmed the first result. Both dipyrrometha(e)ne building blocks contain sterically not-demanding substituents in 2- and 6- positions of the aryl ring. Literature shows that the use of unhindered dipyrrometha(e)nes results in more extensive scrambling in porphyrin synthesis, which probably prevented a successful conversion [23].

3.3.2 Route B

Given the unsatisfying yield of **25** in the additional formylation step, route B is not appealing but was performed nevertheless (Scheme 3.11). Therefore, TFA, formylated **25** and pyrrole/pyrazole hybrid **24b** were converted in an equimolar ratio using stock solutions of **24b** and **25** (100 mM) and of TFA (1 M) in CH₂Cl₂. 200 μL of each pyrrole/pyrazole hybrid solution was combined with 20 μL TFA solution. The reaction progress was monitored via TLC and the first ESI mass spectrum was measured after 2 h—no product signal was observed even after three days of stirring.



Scheme 3.11 Synthetic approach via route B

3.3.3 Route C

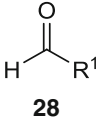
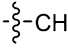
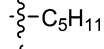
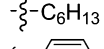
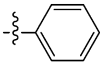
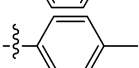
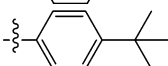
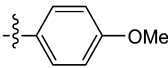
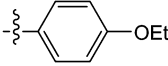
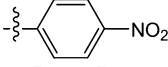
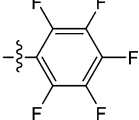
First screening experiments were performed using **24b** due to its enhanced solubility and different aldehydes were tested. 100 mM stock solutions of the chosen aldehydes $R^1\text{CHO}$ (**28**) and the pyrrole/pyrazole building block **24b** were prepared. TFA was used as a 1 M solution.

Small scale reactions of 10 mg of **24b** (179.6 μL of the stock solution) with TFA (18 μL of the stock solution, 1 eq), the corresponding aldehyde (179.6 μL of the stock solution, 1 eq) and additional 1.5 mL CH_2Cl_2 were run and the mixture was stirred for 1 h under the exclusion of light. For reaction control ESI-MS was used.

Ethanal, hexanal and heptanal were tested as alkylic aldehydes and benzaldehyde, 4-methylbenzaldehyde, 4-^tbutylbenzaldehyde, 4-methoxybenzaldehyde, 4-ethoxybenzaldehyde, 4-nitrobenzaldehyde and pentafluorobenzaldehyde as arylc aldehydes (Table 3.1). While alkyl chains are electron donating groups (EDG), the arylc residues were either EDG or electron withdrawing groups (EWG). Usually, EWG enhance the aldehyde's reactivity toward a nucleophilic attack. Counter to intuition, solely for hexanal, heptanal, benzaldehyde, 4-methylbenzaldehyde and 4-^tbutylbenzaldehyde, which all have EWG as R^1 , MS evidence was found as a signal of $[\text{MH}^+]$ (Table 3.1). ESI mass spectra signals were compared checking their relative signal heights whereat the highest peak was set to 100 %. With benzaldehyde (**28Ph**) and 4-methylbenzaldehyde the main product was found to be the desired macrocycle. With 4-methoxy and 4-ethoxybenzaldehyde the formation of the macrocycle cannot reliably be proven, as a peak was observed probably of the composition $[\text{M}]^+$ and $[\text{M}-1]^+$. For all other conversions no macrocyclic fragment was detected.

28Ph is commercially available, commonly used in porphyrin synthesis and gave the most promising results according to ESI-MS investigations. Hence, the following work concentrates on conversions with **28Ph**. In further screening experiments the reaction conditions using **28Ph** and **24b** were optimized

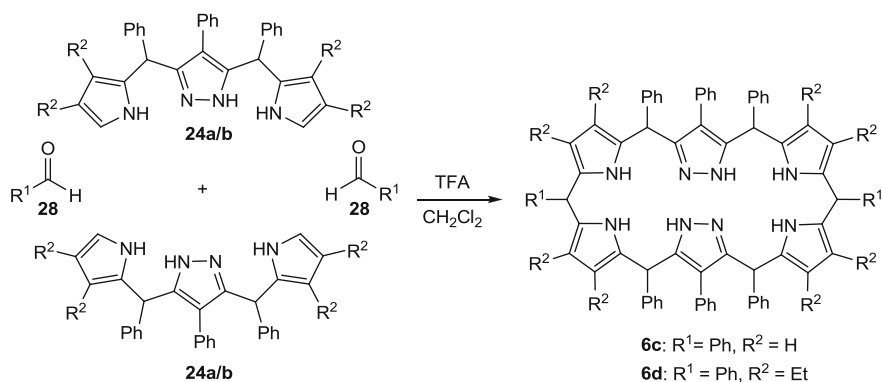
Table 3.1 Overview of all tested aldehydes

	R ¹ =	Elemental formula	Calc. mass	Meas. mass (rel. to 100 %)
 28		C ₈₂ H ₈₈ N ₈	1184.7132	not detected
		C ₉₀ H ₁₀₄ N ₈	1296.8384	1297.8(17.0 %)
		C ₉₂ H ₁₀₈ N ₈	1324.8697	1325.7(39.7 %)
		C ₉₂ H ₉₂ N ₈	1308.7445	1309.7(100 %)
		C ₉₄ H ₉₆ N ₈	1336.7758	1337.7(100 %)
		C ₁₀₀ H ₁₀₈ N ₈	1420.8697	1421.7(28.3 %)
		C ₉₄ H ₉₆ N ₈ O ₂	1368.7656	1368.7(6.3 %)
		C ₉₆ H ₁₀₀ N ₈ O ₂	1396.7969	1395.7(3.9 %)
		C ₉₂ H ₉₀ N ₁₀ O ₄	1398.7147	not detected
		C ₉₂ H ₈₂ F ₁₀ N ₈	1488.6731	not detected

(Scheme 3.12). TFA, BF₃·OEt₂ and *p*-toluenesulfuric acid were investigated as acids, each with 0.1, 1 and 10 equivalents in reference to **24b**. After 15 min, 1, 2 and 3 h a sample was taken and examined by ESI–MS. After evaluation of all screening experiments, a 1:1:1 ratio of TFA : **28Ph** : **24b** and a reaction time of 2 h were found to be optimal.

Knowing the optimal conditions from conversions of **24b**, the cyclization was run using the pyrrole/pyrazole building block **24a** (Scheme 3.12). **24a** was dissolved in one drop of DMSO to mediate the solubility in CH₂Cl₂. All other reaction parameter remained constant. The formation of the macrocycle **6c** could be confirmed via ESI–MS and high resolution (HR) mass spectrometry with a composition of C₇₆H₆₁N₈ for [MH⁺] (Fig. 3.3), but could not be isolated. HRMS measurements were performed for **6d** as well and indicated a composition of C₉₂H₉₃N₈ for [MH⁺], which unequivocally confirmed its successful formation (Fig. 3.3). **6d** was purified using silica column chromatography and a *n*-hexane/EtOAc eluent. **6d** was eluted first as a pale yellow substance. Size exclusion chromatography (Sephadex in CH₂Cl₂) was used for further purification.

6d is a mixture of minimum 64 stereoisomers with its six chiral carbon atoms (2ⁿ stereoisomers, n = number of stereo centers) [24]. In its ¹H NMR spectrum



Scheme 3.12 Synthetic approach via route C

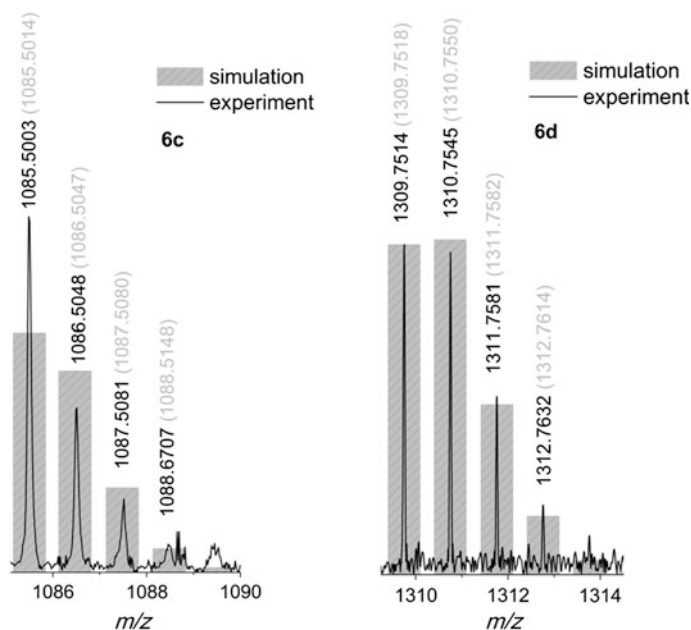


Fig. 3.3 ESI-HRMS (CH_2Cl_2 , MeCN) of compound **6c** (left) and **6d** (right) with simulated isotopic distribution (gray bars)

multiplets are seen due to numerous stereoisomers (Fig. 3.4). The spectrum fits perfectly with 24 CH_3 protons, 16 CH_2 protons, 6 CH protons and 40 phenylic protons while NH resonances are not resolved. The magnitude of the phenylic protons is a little higher than expected because of the residual proton signal of CDCl_3 (resonance at 7.26 ppm) within the integrated area. The UV-vis spectrum of

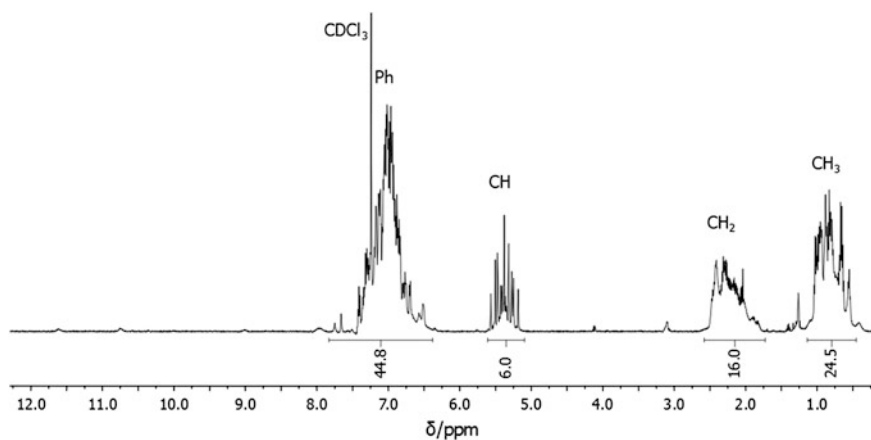


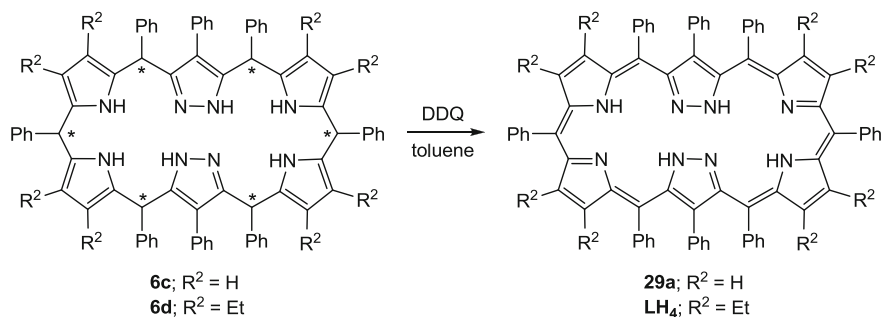
Fig. 3.4 ^1H NMR spectrum (500 MHz, CDCl_3 , 25 $^\circ\text{C}$) of **6d**. Copyright Wiley–VCH Verlag GmbH & Co. KGaA. Reproduced with permission [6]

pale yellow **6d** gives an extinction coefficient of $1250 \text{ M}^{-1}\text{cm}^{-1}$ (Fig. 4.6, Table 4.1, Sect. 4.1.2). The attempt to grow crystals of **6d** was abandoned rapidly due to the presence of a plethora of stereoisomers.

3.4 Oxidation Reaction Toward the Siamese-Twin Porphyrin

The porphyrinogens **6c** and **6d** were successfully synthesized, but the bottle neck in previously reported synthetic approaches toward the Siamese-twin porphyrin was the final oxidation step. It was proceeded with the challenging oxidation of **6c** and **6d**. All sp^3 hybridized carbon atoms within the core structure are supposed to get oxidized to sp^2 hybridized carbon atoms. Ergo, the removal of eight hydrogen atoms gives the fully oxidized macrocycle **LH₄** and **29a** (Scheme 3.13).

Air exposure over several weeks already proved the possibility of forming **LH₄**, which could be ascertained via ESI-MS. This was never reported in any previous work. Our theory of facilitating the oxidation process by introducing phenyl groups in the *meso*^{pyr/pz} positions was proven true! Oxidation upon simple exposure to air lasts too long and at no time a complete conversion was observed. Chemically imitating the success, FeCl_3 , CA and DDQ were used. While FeCl_3 worked for Lash et al. to oxidize **VIII** in its *meso*^{pyr/pz} position, CA and DDQ are ordinarily used in porphyrin chemistry (Sect. 1.1.2). Refluxing an excess of DDQ with **6c** (unpurified) or **6d** in toluene turned out successful (Scheme 3.13). The reaction time had to be watched carefully not to exceed 15 min. because then decomposition reactions initiated. Reaction control via TLC is recommended. HRMS spectra of **LH₄** and **29a** fit well to their simulation (Fig. 3.5). The purification of



Scheme 3.13 Oxidation toward macrocycle **LH₄** and **29a**

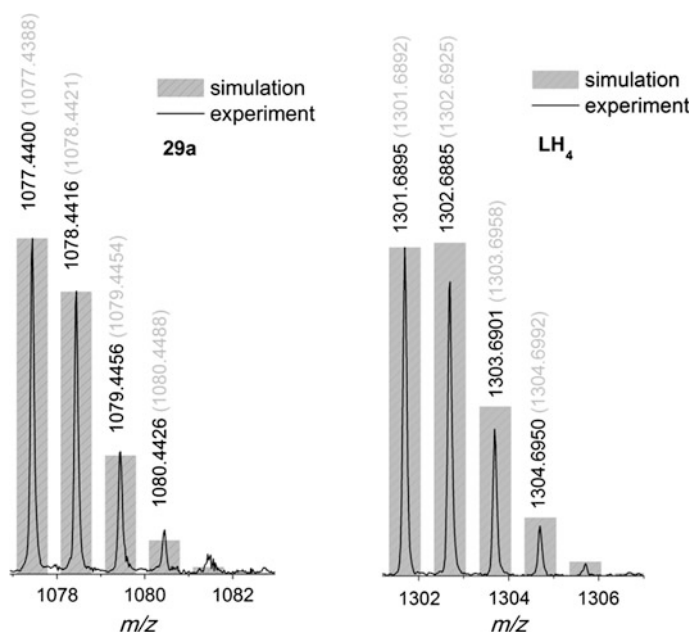
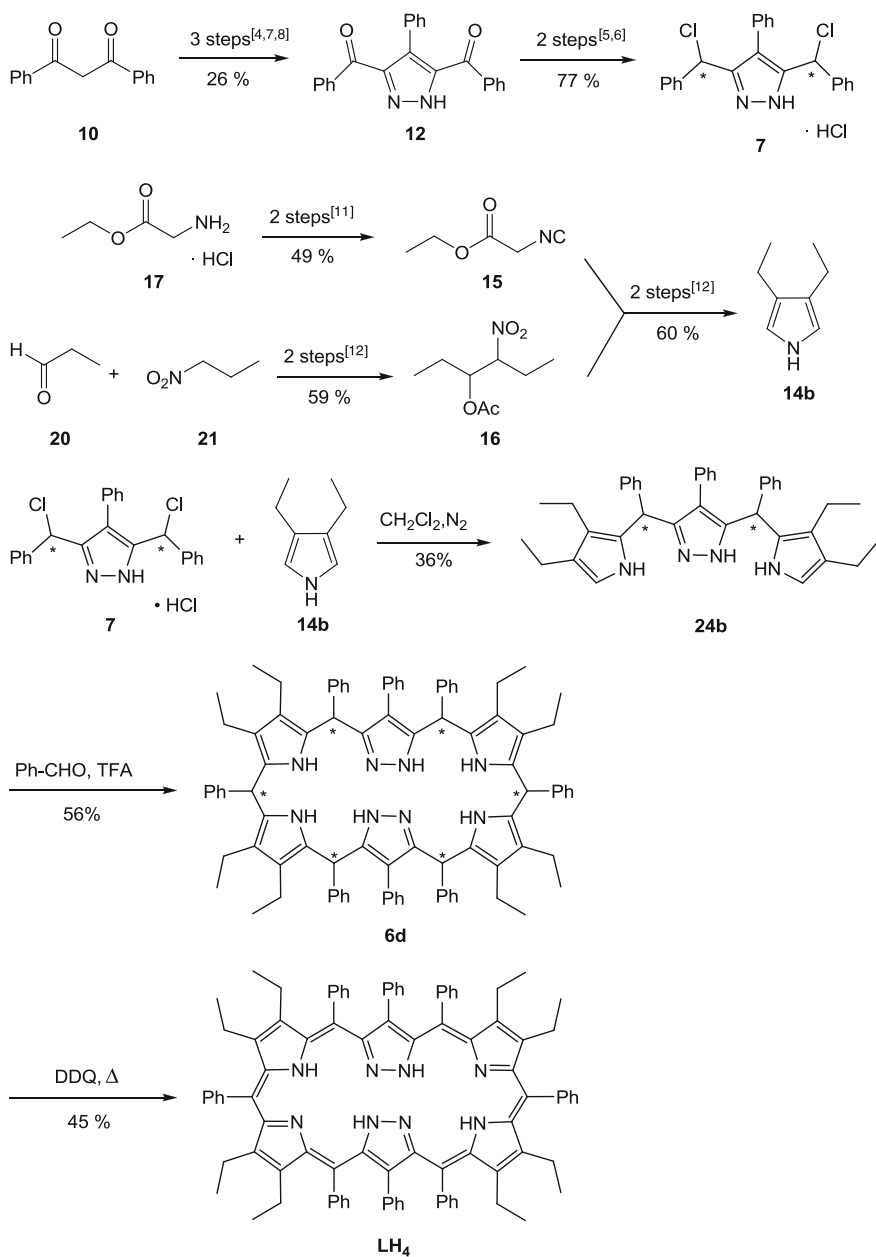


Fig. 3.5 HRMS (CH₂Cl₂, MeCN) of compound **29a** (left) and **LH₄** (right) with simulated isotopic distribution (gray bars)

LH₄ was done via silica column chromatography with *n*-hexane/EtOAc as eluent. Redissolving **LH₄** in minimal amounts of acetone, exposing it to the ultra sonic bath and subsequent filtering led to further purification (yields of 30–50 %). Purification of **29a** was not feasible even after oxidation. Attempts to convert **29a** with metal salts to finally isolate its complexes failed as well.

Scheme 3.14 Synthesis of the Siamese-twin porphyrin LH₄

In summary, the Siamese-twin porphyrin (**LH₄**) was attained via route C in a demanding fourteen-step synthesis. Even though overall low yields stymied progress to some extent, **LH₄** can reliably be reproduced. Scheme 3.14 presents a final overview of the synthetic approach:

References

1. E. J. Lind, Ph.D.: *Synthesis of the Tetrapyrrolic Macrocycle Octaazatetrahydro (1.5.1.5) Platyrin* (Michigan State University, East Lansing, 1987)
2. S. Katsiaouni, Ph.D.: *Neuartige Pyrrol/Pyrazol-Bausteine für die Synthese von Hybrid-Makrozyklen, azyklischen Ligandsystemen und bimetallischen Komplexen* (Georg-August-Universität Göttingen, 2007)
3. P.D. Rao, S. Dhanalekshmi, B.J. Littler, J.S. Lindsey, *J. Org. Chem.* **65**, 7323–7344 (2000)
4. A. Sachse, L. Penkova, G. Noel, S. Dechert, O.A. Varzatskii, I.O. Fritsky, F. Meyer, *Synthesis* **5**, 800–806 (2008)
5. L.K. Frensch, *Diploma: Synthese von Pyrrol/Pyrazol-Hybrid-Bausteinen als Vorstufen zum Doppelporphyrin* (Georg-August-Universität, Göttingen, 2008)
6. L.K. Frensch, K. Pröpper, M. John, S. Demeshko, C. Brückner, F. Meyer, *Angew. Chem. Int. Ed.* **50**, 1420–1424 (2011)
7. K.C. Majumdar, S. Mondal, *Synlett* **18**, 2851–2855 (2008)
8. O. Meth-Cohn, E. Vuorinen, T.A. Modro, *J. Org. Chem.* **54**, 4822–4827 (1989)
9. H.G.O. Becker, R. Beckert, G. Domschke, E. Fanhänel, W.D. Habicher, P. Metz, D. Pavel, K. Schwetlick, *Organikum*, 21st edn. (Wiley-VCH, Weinheim, 2001)
10. G.D. Hartman, L.M. Weinstock, *Org. Synth.* **6**, 620 (1988)
11. J.L. Sessler, A. Mazaffari, M.R. Johnson, *Org. Synth.* **9**, 242 (1998)
12. H.-O. Kalinowski, S. Berger, S. Braun, *Carbon 13 NMR Spectroscopy* (Wiley, Weinheim, 1998)
13. E. Riedel, *Moderne Anorganische Chemie*, 3rd edn. (de Gruyter, Berlin, 2009)
14. K.M. Kadish, K.M. Smith, R. Guilard, *The Porphyrin Handbook*, vol. 1 (Academic Press, San Diego, 2000)
15. R.W. Boyle, C. Brückner, J. Posakony, B.R. James, D. Dolphin, *Org. Synth.* **76**, 287–290 (1999)
16. L. Yu, K. Muthukumar, I.V. Sazanovich, C. Kirmaier, E. Hindin, J.R. Diers, P.D. Boyle, D.F. Bocian, D. Holton, J.S. Lindsey, *Inorg. Chem.* **42**, 6629–6647 (2003)
17. G.R. Geier, J.S. Lindsey, *J. Chem. Soc. Perkin Trans.* **2**, 677–686 (2001)
18. G.R. Geier, J.S. Lindsey, *J. Chem. Soc. Perkin Trans.* **2**, 687–700 (2001)
19. G.R. Geier, B.J. Littler, J.S. Lindsey, *J. Chem. Soc. Perkin Trans.* **2**, 701–711 (2001)
20. G.R. Geier, B.J. Littler, J.S. Lindsey, *J. Chem. Soc. Perkin Trans.* **2**, 712–718 (2001)
21. G.R. Geier, J.A. Riggs, J.S. Lindsey, *J. Porphyr. Phthalocyanines* **5**, 681–690 (2001)
22. G.R. Geier, Y. Ciringh, F. Li, D.M. Haynes, J.S. Lindsey, *Org. Lett.* **2**, 1745–1748 (2000)
23. B.J. Littler, Y. Ciringh, J.S. Lindsey, *J. Org. Chem.* **64**, 2864–2872 (1999)
24. J. Clayden, N. Greeves, S. Warren, P. Wothers, *Organic Chemistry* (Oxford University Press, New York, 2001)

Chapter 4

Siamese-Twin Porphyrin LH₄

4.1 The Twist

After the development of a reliable synthetic strategy and the proof of the exact elemental composition of the Siamese-twin porphyrin, several analytical methods were applied to examine the connectivity and geometry of LH₄.

4.1.1 NMR Spectroscopy

First of all free-base LH₄ was investigated by NMR spectroscopy. At room temperature, the spectrum is broadened beyond interpretation while under cooling to 248 K an optimum resolution is gained (Fig. 4.1). At this temperature, at least some conformational dynamics are hemstringed. Counterintuitively, at lower temperatures the signals broaden again pointing to further conformational flexibility. Unless otherwise indicated, NMR experiments were all conducted at 248 K. CD₂Cl₂ was chosen as solvent because its residual proton signal does not overlap with any signals of the investigated compound.

The ¹H NMR spectrum at 248 K of LH₄ shows only four distinct triplets with an overall intensity of 24 protons at chemical shifts of 0.40, 0.44, 0.54 and 0.55 ppm, each representing two CH₃ groups (Figs. 4.1 and 4.2). In the range of 0.78–2.07 ppm six multiplets are visible with an intensity ratio of 2:2:4:4:2:2, which refers to overall 16 protons matching the amount of CH₂ protons. The phenyl resonances between 6.03 and 7.92 ppm integrate to 40 and the two downfield signals (11.40 and 13.36 ppm) each to two. The latter two readily exchange with MeOD-*d*₄ and thus refer to NH^{pyr} and NH^{pz}.

The presence of only four triplets and two downfield signals hints at a C₂ symmetry inherent to LH₄ in solution but that does not give answer to the appearance of multiple signals between 0.78 and 2.07 ppm. The ¹H¹H-COSY spectrum explains this observation (Fig. 4.1): we are dealing with diastereotopic CH₂ groups. This effect was already observed e.g. for hexadecaethyl[32]octaphyrin

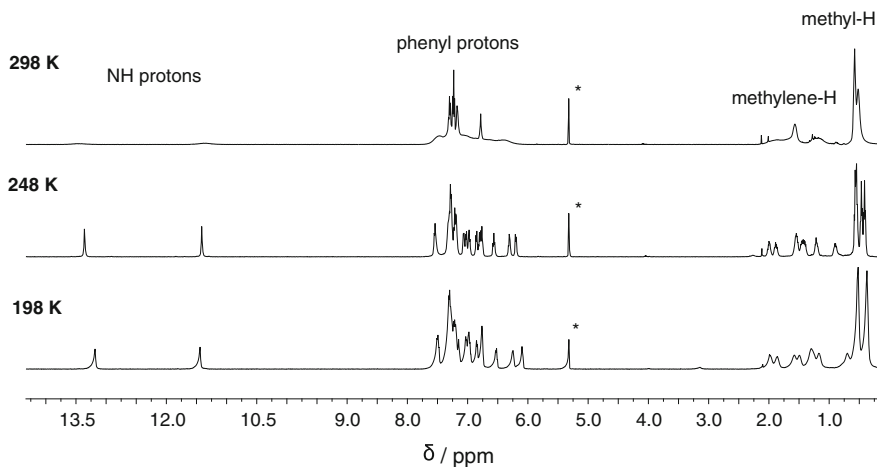


Fig. 4.1 Temperature-dependent ¹H NMR spectra (500 MHz, CD₂Cl₂) of LH₄ at 298 K, 248 K and 198 K. The residual solvent signals are marked with asterisks

XV—a highly twisted molecule that also possesses ethyl groups in its β-pyrrole positions [1, 2] and thus also LH₄ has to be twisted. The twisted geometry evokes different chemical environments for the two CH₂ protons resulting in diastereotopic signals. Each multiplet at 1.34–1.46 and 1.47–1.61 ppm refers to two protons according to integration. The assignment of CH₂ groups to the corresponding CH₃ groups is visualized in Fig. 4.2 and was additionally proven by NOESY (Fig. 4.3, left). NOESY cross signals originate from dipolar coupling through space and thus give information about the distance of atoms. Cross signals only appear within a maximum atom distance of 5 Å [4]. The two protonated nitrogen atoms NH^{pyr} and NH^{pz} exhibit cross peaks at low temperatures (Fig. 4.3, right) and consequently face each other, which rules out the possibility of inverted pyrrole or pyrazole rings. With that, already the first synthetic goal is confirmed. The connectivity of LH₄ mirrors the desired ligand design to provide twice an N₄ donor set for metal complexation.

Porphyrinic NH protons usually resonate in the negative ppm range because of large diatropic ring currents resulting from its aromatic nature (Sect. 1.2.1) while peripheral β and meso proton signals show their resonances in the downfield region at 8–10 ppm and 10–11 ppm, respectively [5]. In antiaromatic systems paratropic ring currents shift inner NH signals toward the downfield region, as observed in some expanded porphyrins. Osuka and Mori reported NMR studies on an antiaromatic monogold(III)hexaphyrin **XVIII** complex (Fig. 1.13), where the NH protons of the metal-free pocket resonate at 25 ppm [6].

The NH chemical shifts of 11–14 ppm observed here are a little higher than free pyrrole NH resonances but within the range of expectations [7, 8]. Also peripheral ethyl and phenyl groups experience anticipated chemical shifts. In this context, neat evaluation of the chemical shifts provides the first evidence for a system

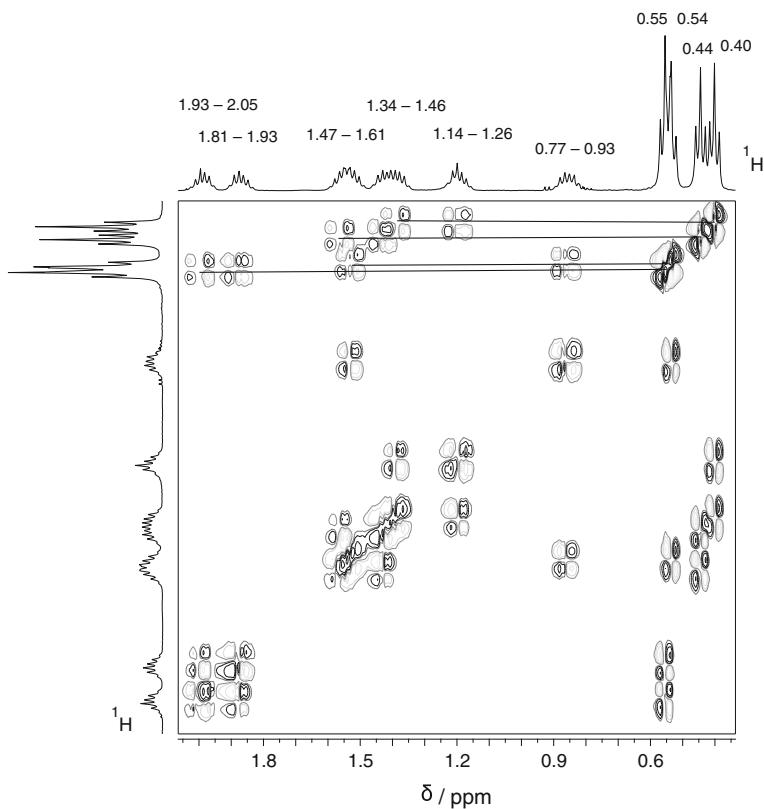


Fig. 4.2 ^1H - ^1H -COSY spectrum (500 MHz, CD_2Cl_2 , 248 K) of **LH₄**. Cross peak assignment is visualized with black lines. Copyright Wiley-VCH Verlag GmbH & Co. KGaA. Reproduced with permission [3]

which behaves neither aromatic nor antiaromatic according to Hückel's and Möbius' concepts of aromaticity.

The $^1\text{H}^{15}\text{N}$ -HMBC experiment is an indirect 2D method with much higher sensitivity to detect ^{15}N , but only via coupling to protons. Besides 1J , 2J and 3J couplings, sometimes long range couplings or H-bonds are detected with coupling constants much smaller than 1J (typically around 7 Hz). The cross-peak intensity is directly proportional to the coupling constant [4].

In **LH₄**, it is obvious that the two signals at 11.40 and 13.36 ppm refer to NH atoms but $^1\text{H}^{15}\text{N}$ -HMBC spectroscopy helps to assign them to the NH^{pyr} ($^1J = 95$ Hz) and NH^{pz} ($^1J = 107$ Hz), respectively (Fig. 4.4) [7, 8]. Apart from these two resonances, one basic imine-type pyrrole at -130.2 ppm N^{pyr} signal and one pyrazole imine nitrogen N^{pz} ($^2J = 7$ Hz) signal at -69.6 ppm are detected. The four ^{15}N signals thus confirm the overall C_2 symmetry of the molecule.

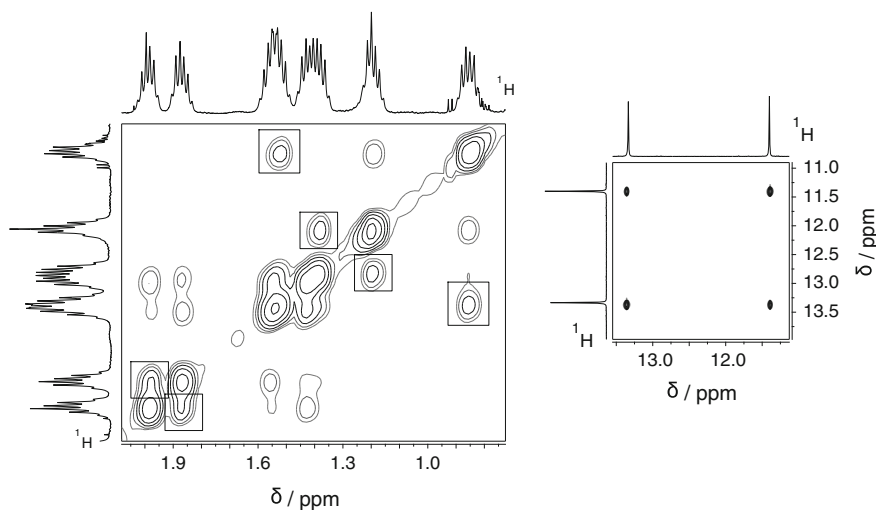


Fig. 4.3 NOESY spectrum (500 MHz, CD₂Cl₂, 243 K, $\tau_{\text{mix}} = 0.5$ s) of **LH₄**: alkyl region (*left*) and zoom into the downfield NH region (*right*). NOE cross peaks are highlighted

In summary, information gained from NMR spectroscopy suggests a twisted, not-inverted and non-aromatic structure in solution, but does not reveal more detailed information about the 3D structure. Therefore, X-ray analysis was performed.

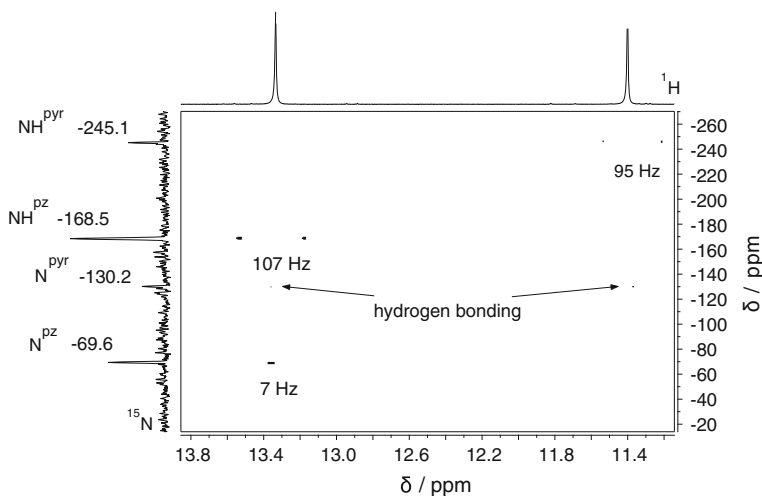


Fig. 4.4 ¹H-¹⁵N-HMBC spectrum (500 MHz, CD₂Cl₂, 248 K) of **LH₄**

4.1.2 Solid-State Structure and UV–Vis Spectroscopy

A mixture of stereomers usually prevents crystallization. As after the oxidation from **6d** to **LH₄** no chiral carbon atoms are left, crystallization attempts were performed. **LH₄** is soluble in all nonpolar organic solvents. Best crystallization results were obtained via slow evaporation of a saturated solution of **LH₄** in acetone with small amounts of TFA. The recorded data were resolved in the non-chiral space group *P1* (Fig. 4.5). Integrated solvent molecules, and disorders of these and the phenyl and ethyl groups complicated the analysis. The data are reminiscent of recorded protein structures as more than 800 atoms per asymmetric unit give an enormous size of the cell unit. An R value of 11 % is therefore justifiable.

The quality of the data did not allow for a localization of hydrogen atoms and, due to several incorporated TFA molecules the amount of counterions could not be determined. Protonation studies discussed later (Sect. 4.2) reveal **LH₄** to be the dicationic species **LH₆²⁺** under the used conditions. As expected, all heterocyclic

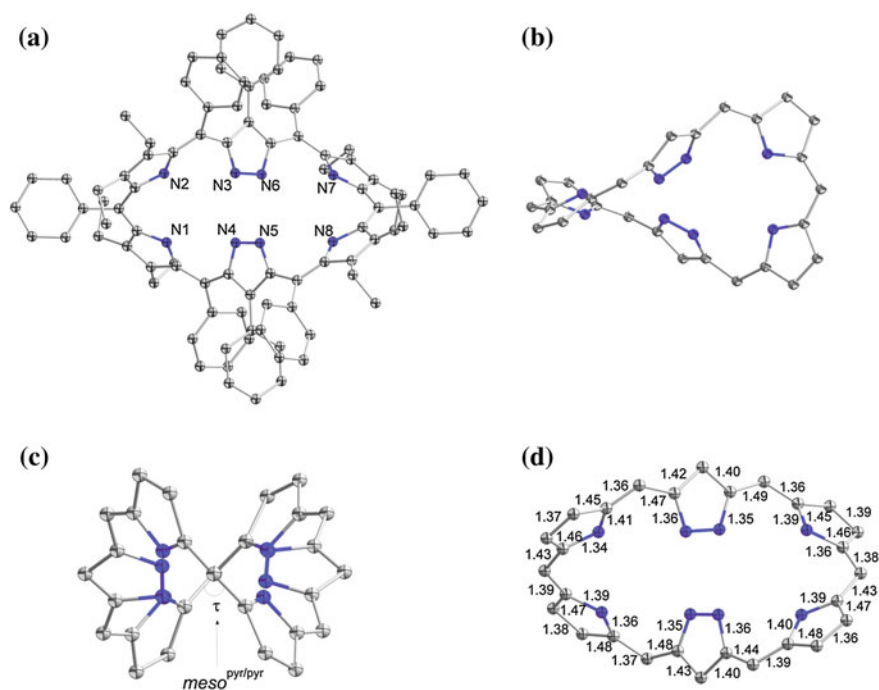


Fig. 4.5 X-ray structure of **LH₆²⁺** (*P* helix), all hydrogen atoms and residual solvent molecules were omitted for clarity. **a** whole molecule inclusive labeling, **b** side view—additionally all ethyl and phenyl groups were omitted, **c** view along the *meso*^{pyr/pyr} to *meso*^{pyr/pyr} axis and definition of the angle τ , **d** bond lengths in Å. Copyright Wiley–VCH Verlag GmbH & Co. KGaA. Reproduced with permission [3]

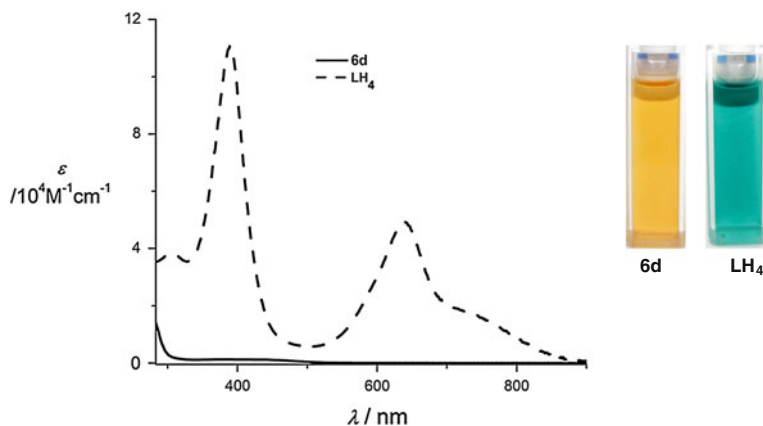


Fig. 4.6 Left: UV-vis spectra of **6d** and **LH₄** in CH₂Cl₂. Right: Photographs of **6d** and **LH₄** in a UV-vis cuvette

nitrogen atoms point inward (Fig. 4.5). X-ray analysis is in line with NMR data not only with respect to the orientation of the azoles. X-ray analysis shows **LH₆²⁺** to be highly twisted with a dihedral angle between the two N1–N2–N3–N4 and N5–N6–N7–N8 mean planes of 41° (Fig. 4.5b). The twisting implies helical chirality and the two enantiomeric *P* and *M* helices are present as a racemic mixture in the crystal. Looking from one *meso*^{pyr/pyr} carbon atom between two pyrrole units to the second a torsion angle τ can be defined which is approximately $\pm 86^\circ$ or $\pm 87^\circ$ differing for both sides, with a helical pitch of 10.73 Å (*meso*^{pyr/pyr} to *meso*^{pyr/pyr} distance) (Fig. 4.5c). The obvious *C*₂ symmetry of the **LH₆²⁺** core structure in Fig. 4.5, c is broken by the various arrangements of ethyl and phenyl groups and not depicted solvent molecules and thus is not of crystallographic nature.

In aromatic porphyrins, the neighboring C–C bonds are equal in length [9]. The corresponding bond lengths in **LH₆²⁺** differ, however, showing an alternating short-long pattern (shortest bond of 1.36 Å versus longest bond of 1.48 Å; Fig. 4.5d) which points to a conjugated, but not delocalized π -system. The bond lengths found here match the data reported for single bonds between two *sp*²-hybridized carbon atoms (1.47 Å) and normal double bonds (1.34 Å) [10].

This finding is consistent with the optical properties of **LH₄**. The UV-vis spectrum of the intensively greenish **LH₄** shows extinction coefficients lower than porphyrins (Fig. 4.6, Table 4.1). The spectrum shows its most intense band at 390 nm with an extinction coefficient of $11 \cdot 10^4 \text{ M}^{-1} \text{ cm}^{-1}$ and a less intense band at 639 nm with a slight shoulder at 734 nm. No Soret band and an absence of multiple Q-bands further fortifies the non-aromatic structure. The UV-vis spectrum of **LH₄** reminds of UV-vis spectra of tetrapyrrolic, non-aromatic relatives of porphyrins [12]. There is an enormous increase in the extinction coefficients when comparing the absorption spectra of **6d** and **LH₄** (about 100 times higher) due to conjugation.

Table 4.1 Absorption maxima and extinction coefficients listed for 6d, LH₄, and TPP

	6d	LH ₄	TPP [11]
λ/nm ($\epsilon/10^4\text{M}^{-1}\text{cm}^{-1}$)	390 (0.1)	307 (3.9)	418 (37.2)
	438 (0.1)	390 (11)	468 (1.55)
		639 (4.9)	512 (1.68)
		734 (1.7)	542 (0.88)
			588 (0.67)
			643 (0.42)

4.1.3 Origin of the Twist

In general, porphyrins are planar. Deviations from planarity were observed with (a) bulky substituents, especially when all β - and *meso*-positions are occupied, (b) complexation of very small or large metal ions such as Ni^{II} and Ag^{II}, respectively, (c) incorporation of “straps” or “basket handles” between peripheral substituents or (d) axial ligand binding in complexes [13]. In expanded porphyrins distortion is common. Hexaphyrin is mainly planar—but can exhibit a figure-eight conformation when bulky substituents in *meso* and/or β -positions are present [14]. Higher analogs of hexaphyrin, as heptaphyrins and octaphyrins usually exhibit distorted structures (Sect. 1.2).

The β -unsubstituted **29a** would be a perfect reference to LH₄ to draw conclusions about the origin of the twist. Because of the reduced bulk **29a** was thought to be less twisted. DFT calculations with the ORCA package [15] were carried out for LH₄, **29a**, **29b** (only ethyl groups) and **29c** (no residues at all) (Fig. 4.7). While **29b** with its β -ethyl groups resembles OEP, **29a**, in which all *meso* positions are occupied with phenyl substituents, resembles TPP. Atom coordinates were obtained from first guess structures drawn in ChemDraw3D. Coordinates were first optimized with the semi-empirical Austin Model 1 (AM1) [16, 17] and then refined using the Becke–Perdew-1986 functional (BP86) [18, 19] and SVP basis sets [20].

DFT calculations for LH₄, **29a**, **29b** and **29c** were performed for their neutral states. The lack of ethyl groups (Fig. 4.7b) leads to marginal changes toward planarity which is demonstrated by the overlay of the two core structures of **29a** and LH₄ (Fig. 4.7e). The lack of phenyl groups on the contrary results in a completely planar geometry (Fig. 4.7c and d). Comparison of LH₄, **29a**, **29b** and **29c** reveals that the torsion is caused by steric repulsion of the bulky backbone induced by the required phenyl groups.

4.1.4 Aromaticity

The non-aromatic nature of LH₄ was proven by NMR and UV–vis spectroscopy and X-ray analysis. The twisted geometry interdicts Hückel aromaticity, but still

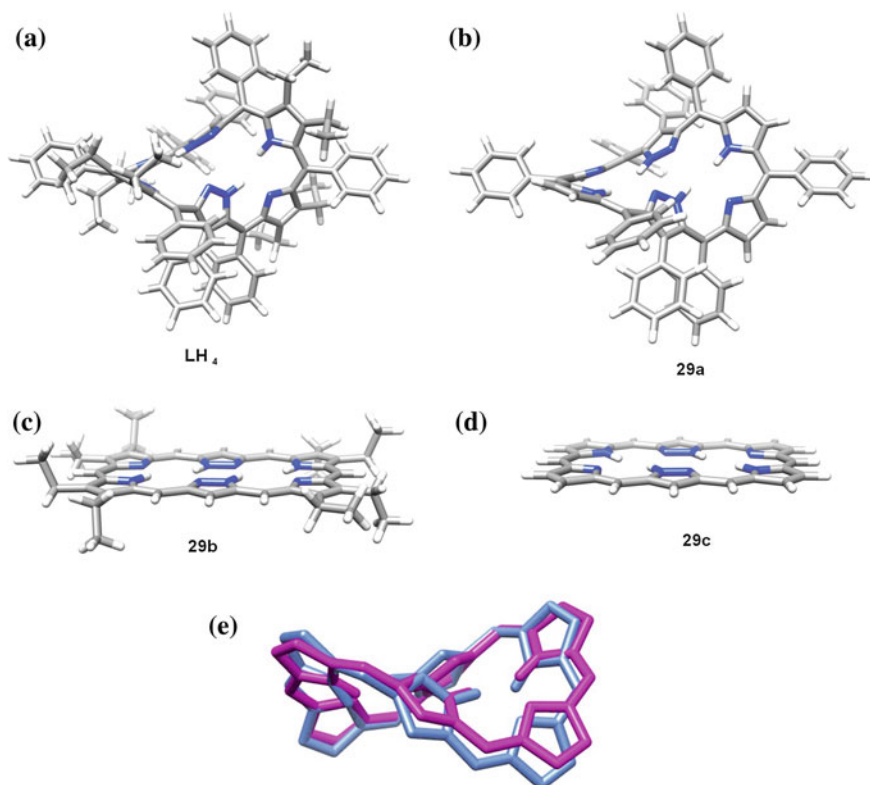


Fig. 4.7 DFT calculations on LH_4 (a), $29a$ (b), $29b$ (c) and $29c$ (d). e Overlay of xyz coordinates of LH_4 (blue) and $29a$ (pink), in which all peripheral residues are omitted for clarity. In all, hydrogen atoms were omitted for clarity. Geometry optimizations were carried out with the ORCA package. The BP86 functional and SVP basis sets were used. Copyright Wiley-VCH Verlag GmbH & Co. KGaA. Reproduced with permission [3]

allows Möbius aromaticity (Sect. 1.2.1). The analysis of the conjugation pathway will shed light on the non-aromatic behavior of LH_4 .

Following the conjugation pathway in LH_4 it is interrupted by the pyrazole unit and instead of one closed pathway it consists of two independent conjugation pathways (Fig. 4.8). With that, already the first criterion for aromaticity applying the annulene model, which is that the conjugation pathway has to pass through all subunits and encompass the macrocycle, is not fulfilled. Already Lash et al. observed the breaking of the conjugation pathway by the pyrazole unit in the pyrazole-based porphyrin **VIII** (Fig. 1.6), [21].

Initially it was thought of a $[26]\text{LH}_2$ scaffold (Fig. 4.8). $[26]\text{LH}_2$, as its name suggests, consists of 26 π -electrons following the conjugation pathway and could exhibit Möbius antiaromaticity keeping the twist in mind. With a different substitution pattern leading to a planar geometry $[26]\text{LH}_2$ could obey Hückel's rule

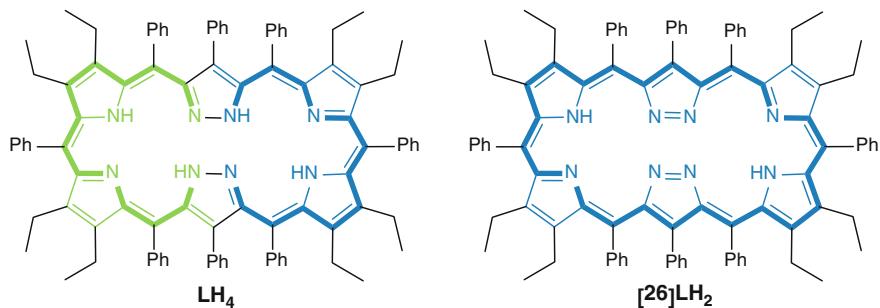


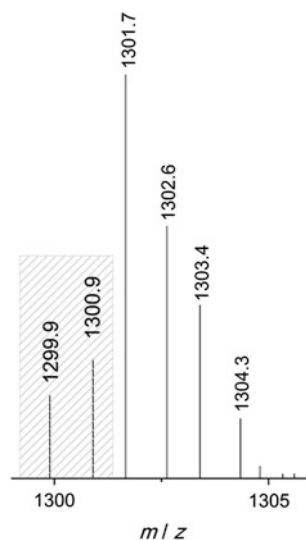
Fig. 4.8 Conjugation pathway of **LH₄** and **[26]LH₂**

and turn aromatic. However, all oxidation attempts failed, despite many different oxidizing agents were tested: DDQ, CA, FeCl₃, KMnO₄, O₂, IBX, H₂O₂, Br₂, Ag₂O and TEMPO. Only when using DDQ a mass peak of 1299.9 was observed (Fig. 4.9, [MH⁺] = 1299.7) once, but a HRMS measurement was not performed and an exact assignment of the isotopic pattern is hindered due to overlapping mass peaks of **LH₄**.

4.2 pH Dependency

Porphyrins are known to be strongly pH sensitive and to undergo a significant color change upon protonation [22]. Many studies have been performed investigating the behavior of various expanded porphyrins upon protonation. A switch in

Fig. 4.9 ESI(+) MS spectrum of **LH₄** and probably **[26]LH₂**. Signals of the two are overlapping, but the gray part marks the ones of the higher oxidized **[26]LH₂**



geometry (figure-eight ↔ planar) and thereby in aromaticity (Möbius ↔ Hückel, aromatic or antiaromatic) was reported for heptaphyrins and octaphyrins [23–25]. In line with this, significant color changes and breaking of intramolecular hydrogen bonds were observed [26–28].

Also the Siamese-twin porphyrin is an excellent candidate for protonation studies. The excess of TFA under crystallization conditions and the imine nitrogen atoms present in the neutral form suggest high sensitivity of LH₄ toward protonation. Potentiometric investigations were impossible due to minor solubility in water or water/DMSO mixtures—a necessity to obtain reliable pK_A values. Thus NMR and UV-vis spectroscopy were the methods of choice.

4.2.1 NMR Spectroscopy

Once the ¹H NMR spectrum of LH₄ was fully understood (Sect. 4.1.1) an exact pH titration using TFA as acid was performed. TFA is advantageous as in its deprotonated state it does not give any resonances in a proton spectrum and is soluble in CD₂Cl₂. A stock solution of TFA in CD₂Cl₂ (500 mM) was prepared. The titration was followed at r.t. (300 MHz spectrometer instrument) and at 248 K (500 MHz spectrometer instrument). At each step, 0.25 equivalents TFA were added and the spectra were measured after the completion of the protonation reaction. For discussion of the pH titration only selected spectra are depicted in Fig. 4.10, which represent the low temperature measurements. Particularly the downfield region justifies a closer inspection (Fig. 4.10, bottom). With addition of TFA, the intensity of the two NH resonances at 11.40 and 13.36 ppm (NH^{PVT}, NH^{PZ}) decreases while a range of new signals appear. After the addition of one equivalent of TFA, overall ten signals are observed in the downfield region. The assignment of all species was possible using NOESY (Fig. 4.11). NOESY experiments were performed at 198 K to suppress cross peaks from proton exchange leaving only cross peaks originated from dipolar coupling (Sect. 4.3). Clearly, three independent species can be assigned: the starting material LH₄ (a), the monoprotonated species LH₅⁺ (b) and the dicationic species LH₆²⁺ (c) (Figs. 4.10 and 4.11). They balance in a temperature-dependent equilibrium which shifts toward the monoprotonated species at lower temperatures.

Besides the previous two NH resonances from LH₄, signals at 11.52, 13.26 and 15.36 ppm refer to the twice protonated species LH₆²⁺. This can be deduced by comparison with the spectrum after the addition of two equivalents TFA in Fig. 4.10. The amount of NH signals is suggestive of a C₂ symmetry in LH₄ as well as in LH₆²⁺. The five signals at 9.05, 10.34, 13.53, 14.28 and 14.96 ppm derive from the monoprotonated species LH₅⁺ where no symmetry is inherent. The structural formula of the different protonated species and their symmetry axes are depicted in Fig. 4.13.

Extensive NMR studies were performed for LH₄ after the addition of 1 equivalent TFA. Zooming into the most interesting downfield region, all three

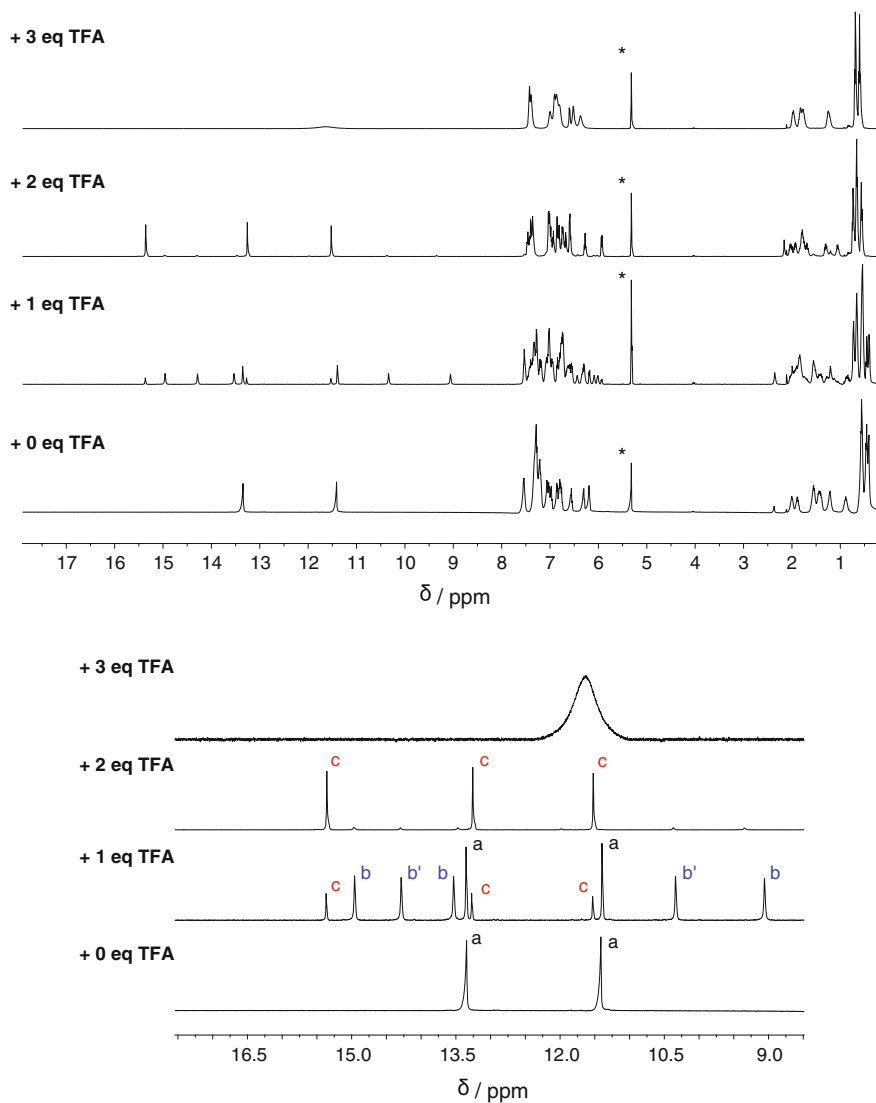


Fig. 4.10 ^1H NMR spectra of the pH titration of LH_4 with TFA (500 MHz, CD_2Cl_2) at 248 K. The amount of equivalents of TFA is mentioned in the spectra. *Bottom* Zoom into the downfield region. The residual proton signal of CD_2Cl_2 is marked with an asterisk. Copyright Wiley-VCH Verlag GmbH & Co. KGaA. Reproduced with permission [3]

species can be presented in one spectrum due to their coexistence even though the upfield region shows overlapping alkyl and aryl signals. Signals referring to LH_4 (a), were already discussed in Sect. 4.1.1 According to the $^1\text{H}^{15}\text{N}$ -HMBC spectrum the more basic imine nitrogen atom N^{pyr} gets protonated first to give LH_5^+

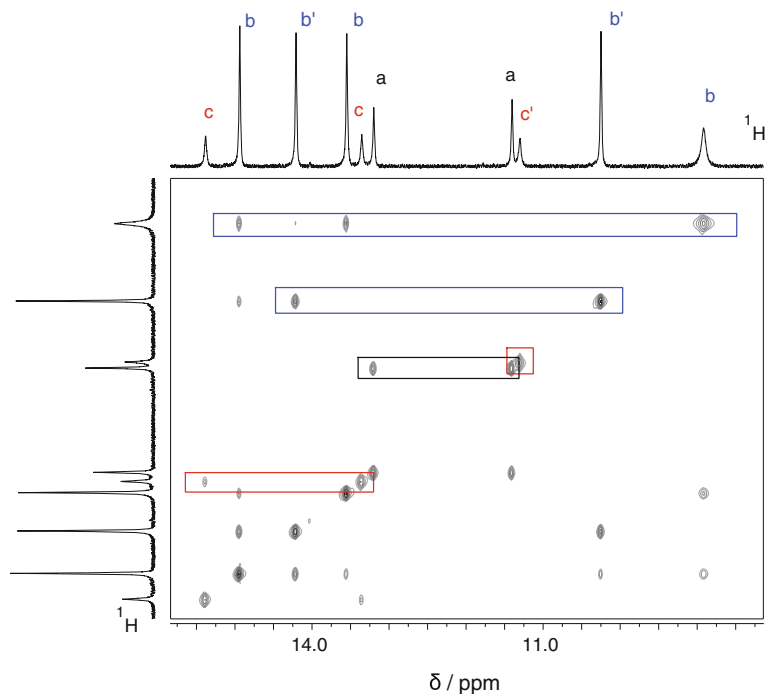


Fig. 4.11 NOESY spectrum (500 MHz, CD₂Cl₂, 198 K) of LH₄ after addition of one equivalent TFA. The Arabic letters indicate the signals arising from LH₄ (a), LH₅⁺ (b) and LH₆²⁺ (c). b' and c' refer to the non-protonated pocket of LH₅⁺ and LH₆²⁺, respectively. Copyright Wiley-VCH Verlag GmbH & Co. KGaA. Reproduced with permission [3]

(Fig. 4.12). This extra NH^{pyr} proton appears at 9.05 ppm, while the protons resonating at 10.34/13.53 and at 14.28/14.96 can be assigned to the formerly protonated NH^{pyr} and NH^{pz} respectively. Also the NOESY spectrum (Fig. 4.11) clearly reveals the presence of two distinct pockets: The three NH protons belonging to the protonated pocket (labeled b) give intense cross peaks, so do the two NH protons belonging to the non-protonated pocket (labeled b'). Thus, the molecule LH₅⁺ exhibits no symmetry at all. ¹H¹⁵N-HMBC cross peaks due to hydrogen bonding were also observed for LH₅⁺ and the H-bond pattern is visualized in Figs. 4.12 and 4.13.

In LH₆²⁺ the protonation takes place in the already protonated pocket at the remaining imine-nitrogen atom to give a C₂-symmetric compound with three NH resonances. The resonances at 11.52 and 13.26 ppm could be assigned to two distinct NH^{pyr} and the one at 15.36 ppm to NH^{pz}, each of an intensity of two.

¹³C NMR spectroscopy enabled us to exactly locate the apparent C₂ symmetry axis in LH₄ and LH₆²⁺: While the ¹³C NMR spectrum of LH₄ shows exactly one signal for each two carbon atoms, in the spectrum of LH₆²⁺ three additional carbon signals (two quaternary and one tertiary carbon) are visible. Integration showed that four quaternary signals at 102.9 and 103.6 ppm for C^{meso} and at 136.9 and

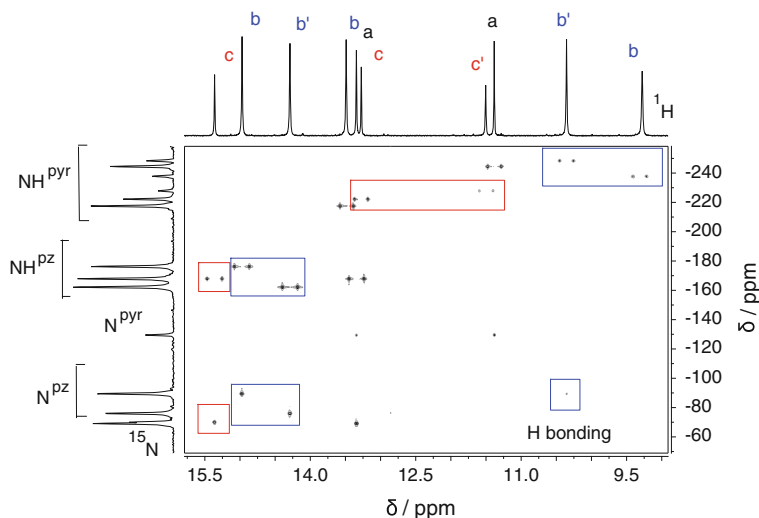


Fig. 4.12 $^1\text{H}^{15}\text{N}$ -HMBC spectrum (500 MHz, CD_2Cl_2 , 248 K) of LH_4 after addition of one equivalent TFA. Copyright Wiley-VCH Verlag GmbH & Co. KGaA. Reproduced with permission [3]

138.2 for C^{ipso} each belong to a single carbon atom (Fig. 4.13). The same is valid for the two tertiary C^{para} atoms which separately resonate at 128.1 and 128.8 ppm. Therefore, these six carbon atoms must lie on the C_2 axis as this is the only way that they can be magnetically inequivalent. This is also confirmed by the absence of a detectable NOE cross peak between the inequivalent NH^{pyr} protons showing they belong to different pockets (Fig. 4.11). The two NH^{pz} protons must be oriented toward the same pocket as they show NOE cross peaks only with the downfield NH^{pyr} signal.

As soon as an excess of TFA was present a fast exchange between all NH and TFA protons took place and only one broad downfield signal is observed (spectrum at the level of 3 equivalents of TFA, Fig. 4.10), because scrambling is accelerated and becomes efficiently averaged on the NMR time scale (Fig. 4.14). The same effect was observed by increasing the temperature as the exchange becomes so fast that one combined signal for TFA and NH^{pz} was observed and a second one for NH^{pyr} . These two resonances coincide at 248 K. For high-temperature NMR experiments, a second sample was prepared using deuterated tetrachloroethane as NMR solvent which has a higher boiling point than CD_2Cl_2 (419 K) [29]. The change of the solvent itself results in marginal alterations of the chemical shifts in the alkyl and aryl region.

With an excess of TFA, pseudo- D_2 symmetry is observed, meaning that only one quarter of the molecule is chemically inequivalent (Fig. 4.14). Thus only two triplets for the CH_3 groups at 0.66 (12H) and 0.73 ppm (12H) and the corresponding diastereotopic CH_2 groups at 1.19–1.40 (4H), 1.71–1.90 (8H) and 1.91–2.08 ppm (4H) are visible.

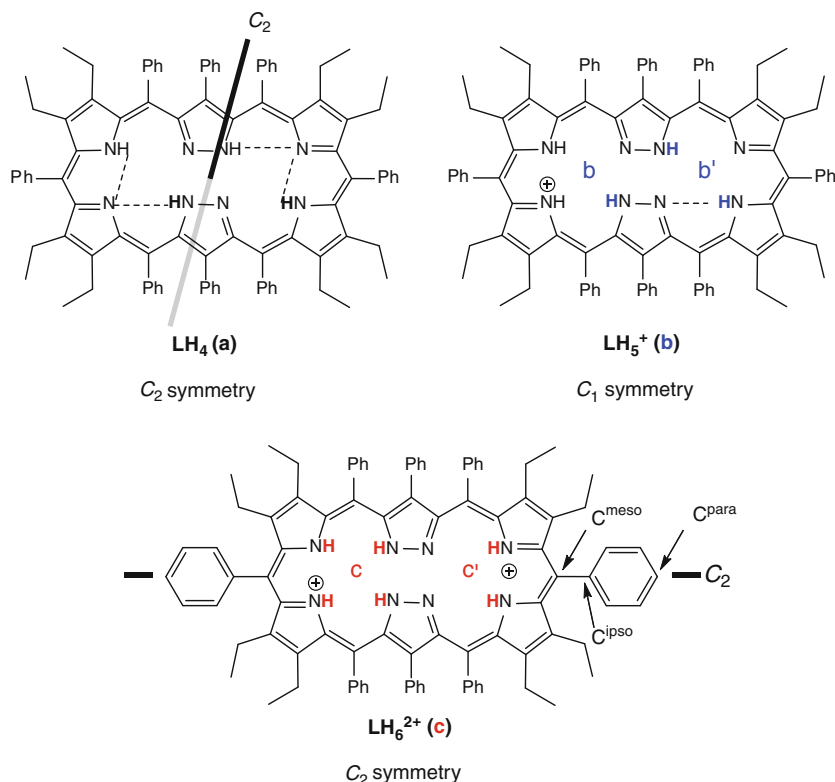


Fig. 4.13 NMR spectroscopically derived structures and H-bond pattern in the three protonation stages of LH_4 . Copyright Wiley–VCH Verlag GmbH & Co. KGaA. Reproduced with permission [3]

4.2.2 UV–Vis Spectroscopy

Large differences in the UV–vis spectra of porphyrinic compounds are observed upon protonation due to a conformational reorganization [22]. Even though hydrogen bonds have to be broken and the conformational flexibility is affected, in the present system (Sect. 4.2.1) only subtle color changes upon protonation of LH_4 were observed—almost invisible for the human eye (Fig. 4.15, right). While porphyrins undergo enormous color changes upon protonation, the behavior of LH_4 once more reminds more of non-aromatic porphyrin analogs than of porphyrins [12, 30]. The pH titration was done with a 100 mM stock solution of TFA in CH_2Cl_2 . Consistent with the NMR experiment, until the addition of approximately two equivalents of TFA changes in the UV–vis spectrum were observed (Fig. 4.15, left and Table 4.2). The fact that exactly 2.25 equivalents were added can be ascribed to titration inaccuracy. From LH_4 to LH_6^{2+} the extinction

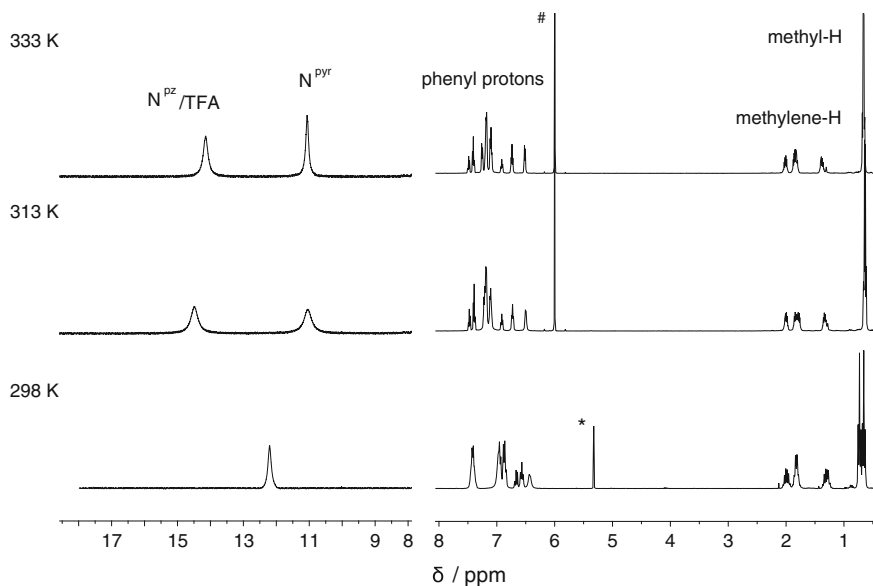


Fig. 4.14 ^1H NMR spectra of LH_4 with an excess of TFA measured at variable temperatures. The residual solvent proton signals are marked with an asterisk (CD_2Cl_2) or number sign ($\text{C}_2\text{D}_4\text{Cl}_4$). It was zoomed into the downfield region to highlight the changes. Copyright Wiley-VCH Verlag GmbH & Co. KGaA. Reproduced with permission [3]

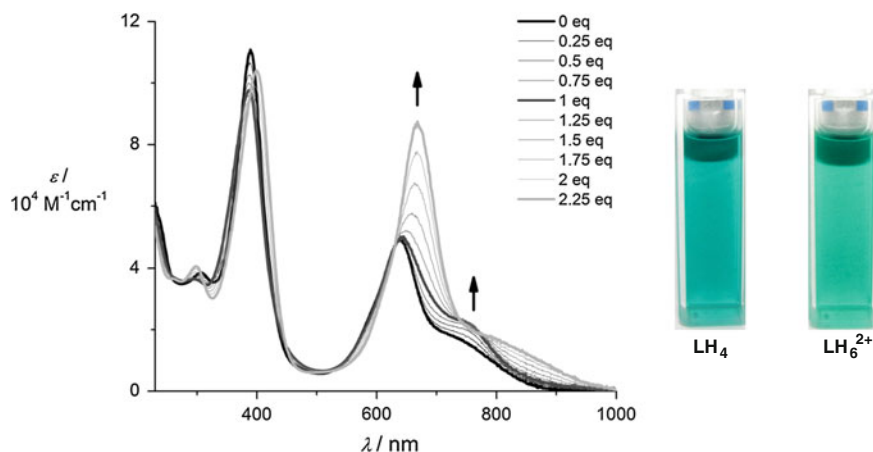


Fig. 4.15 pH titration of LH_4 with TFA followed using UV-vis spectroscopy. Copyright Wiley-VCH Verlag GmbH & Co. KGaA. Reproduced with permission [3]

coefficient at 390 nm decreases and a marginal red-shift is observed to 400 nm. Main changes occur in the range from 550 to 900 nm. The absorption band at 639 nm almost doubles its extinction coefficient and is red-shifted to 668 nm with

Table 4.2 Absorption maxima and extinction coefficients (ϵ) listed for LH₄ and its protonated form LH₆²⁺

	LH ₄	LH ₆ ²⁺
λ/nm ($\epsilon/10^4\text{M}^{-1}\text{cm}^{-1}$)	307 (3.9)	298 (4.1)
	390 (11)	400 (10)
	639 (4.9)	668 (8.7)
	734 (1.7)	795 (1.8)

a shoulder at 795 nm. As known from NMR experiments, the spectrum after the addition of one equivalent of TFA represents a mixture of LH₄, LH₅⁺ and LH₆²⁺.

NMR and UV–vis spectroscopy confirmed the presence of the dicationic species LH₆²⁺ in solution when the sample was exposed to an excess of TFA. Because such a solution is the starting point in the crystallization attempt (Sect. 4.1.2), the obtained solid-state structure is anticipated to represent LH₆²⁺.

4.2.3 DFT Calculations

Besides the geometry optimizations for the free base LH₄ and 29c in Sect. 4.1.3, now also their protonated forms LH₆²⁺ and 29cH₂²⁺ are investigated to study the influence of protonation on geometry. Protonation was assumed to take place at the imine-pyrrole nitrogen atoms as was known from NMR experiments. First atom coordinates were obtained from ChemDraw 3D structures. Calculations were carried out using the ORCA package [15] with a BP86 functional [18, 19] and an SVP basis set [20].

Theoretical studies on the BP86 level revealed that protonation induces a severe ruffling in the case of 29c (Fig. 4.16a, left), which is planar in its neutral form but exhibits a non-planar geometry upon protonation. Protonation of LH₄ seems to orientate the nitrogen atoms toward the center of the pockets (Fig. 4.16a, right). Even though the molecule is still severely twisted the arrangement of the single heterocycles toward each other is more ordered. In NMR spectroscopy, it was observed that both NH^{Pz} protons point to one cavity which is then occupied with four protons while the remaining pocket only carries two protons. However, in the solid state structure no dissymmetry of the two pockets was observed. DFT calculations were performed for the two different pyrazole protonation possibilities of symmetric pockets each carrying three protons (gold) and asymmetric pockets with four and two protons (pink) (Fig. 4.16b). Comparison of these with the X-ray structure demonstrate a much better fit of the asymmetric protonated DFT calculation. Thus, the asymmetric protonation pattern is present in solution and the gas phase.

4.3 Chiral Resolution

Helices can be either right-handed (*P*) or left-handed (*M*) and are intrinsically chiral. Helical structures are widespread, e.g. in screws or double-stranded DNA. Screws and ordinary B-DNA exhibit right-handed helices. Upon methylation, the left-handed Z-DNA is formed [31].

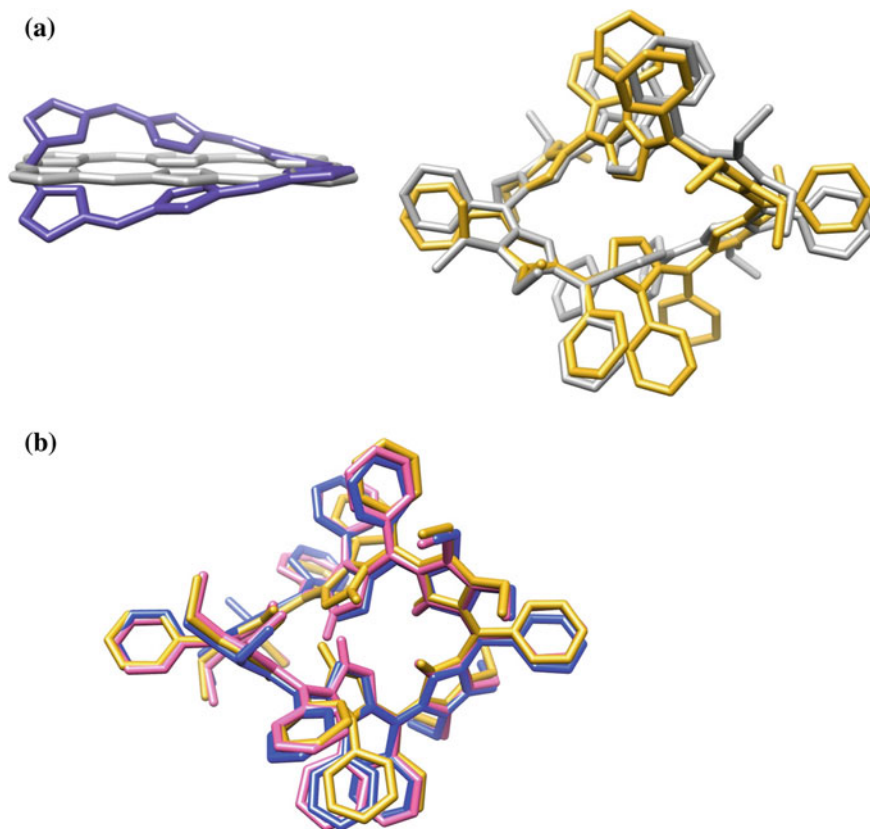


Fig. 4.16 DFT studies on the geometry effect of protonation (proton atoms were omitted for clarity). **a** $29c$ (gray) versus $29cH_2^{2+}$ (dark blue) and LH_4 (gray) versus LH_6^{2+} (gold). **b** Comparison of the crystal structure of LH_6^{2+} (blue), and the DFT calculations of LH_6^{2+} with both pyrazole protons in one pocket (pink) and the pyrazole protons in different pockets (gold)

Helical conformations are not only a characteristic property of screws and DNA, but also of expanded porphyrins. Most hepta- and octaphyrins exhibit distorted or figure-eight geometries which are intrinsically chiral, but the two present enantiomeric forms generally interconvert rapidly. Vogel and coworkers showed first in 1999 that in β -hexadecaethyl octaphyrin **XV** the dynamics are impeded. In this case, the chiral separation of the left- and right-handed helices via high pressure liquid chromatography (HPLC) with a chiral stationary phase was feasible—for the ligand and its metal complex $XVPd_2$ [32]. Also Osuka et al. demonstrated the chiral resolution of quadruply *N*-fused heptaphyrin [33]. Some porphyrins, in which ruffling was induced by ring modifications or complexation of a small Ni^{II} ion, showed helical chirality [34].

LH_4 exhibits a highly twisted geometry and its crystal structure proved the presence of a racemic mixture of right- and left-handed helices (Sect. 4.1.2).

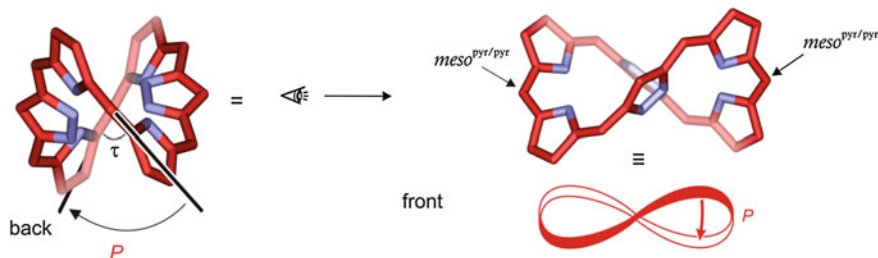


Fig. 4.17 Assignment of the stereodescriptors and definition of the angle τ . Copyright Wiley-VCH Verlag GmbH & Co. KGaA. Reproduced with permission [3]

Stereodescriptors M and P were assigned as shown in Fig. 4.17. In cooperation with Bringmann and coworkers the chiral separation was carried out. For the non-protonated Siamese-twin porphyrin **LH₄**, a separation on a chiral HPLC column was not successful after varying conditions such as flow rate and solvent system. **LH₄** was proven to be highly pH-sensitive and with protonation (species **LH₆²⁺**) a separation was observed.

A rigidification upon protonation was reported for [30]heptaphyrin and [38]nonaphyrin and was reasoned to have its origin in the hydrogen bonding interaction between counteranions and the positively charged expanded porphyrin [35]. The rigidification was proven to exist comparing the singlet excited-state lifetimes of the protonated and the non-protonated forms with longer lifetimes for the protonated form. These measurements could not be performed for **LH₄/LH₆²⁺** because specialized equipment is required. After addition of 0.05 % TFA to EtOAc the resolution of the two enantiomers P -**LH₆²⁺** and M -**LH₆²⁺** was successful with M -**LH₆²⁺** as the faster eluting enantiomer (Chiralpak[®] IA column, ethyl acetate (EtOAc) + 0.05 % TFA/*n*-hexane (v/v) 30:70) (Fig. 4.18).

Enantiomers are known to have the same chemical and physical properties in achiral environments except for their ability to rotate plane-polarized light. Plane-polarized light is composed of a superposition of right- and left circular polarized light (ϵ_{rcp} and ϵ_{lcp} , respectively) of same amplitude and phase. After interaction with enantiomerically pure material, the amplitude and phase of either the right or the left polarized component changes, resulting in an elliptic polarization. The actually measured value in circular dichroism (CD) spectroscopy is the difference of the extinction coefficients after interaction with the sample: [36]

$$CD = \Delta\epsilon = \epsilon_{lcp} - \epsilon_{rcp} \quad (4.1)$$

Even though retention times are similar and according to UV-vis detection no clear separation took place, a resolution was observed using a CD detector, once more showing the advantages of the online stereochemical investigation by HPLC-CD coupling [37]. Since CD spectra were measured online, the ellipticity values of the helimers could not be determined (axis: CD/mdeg).

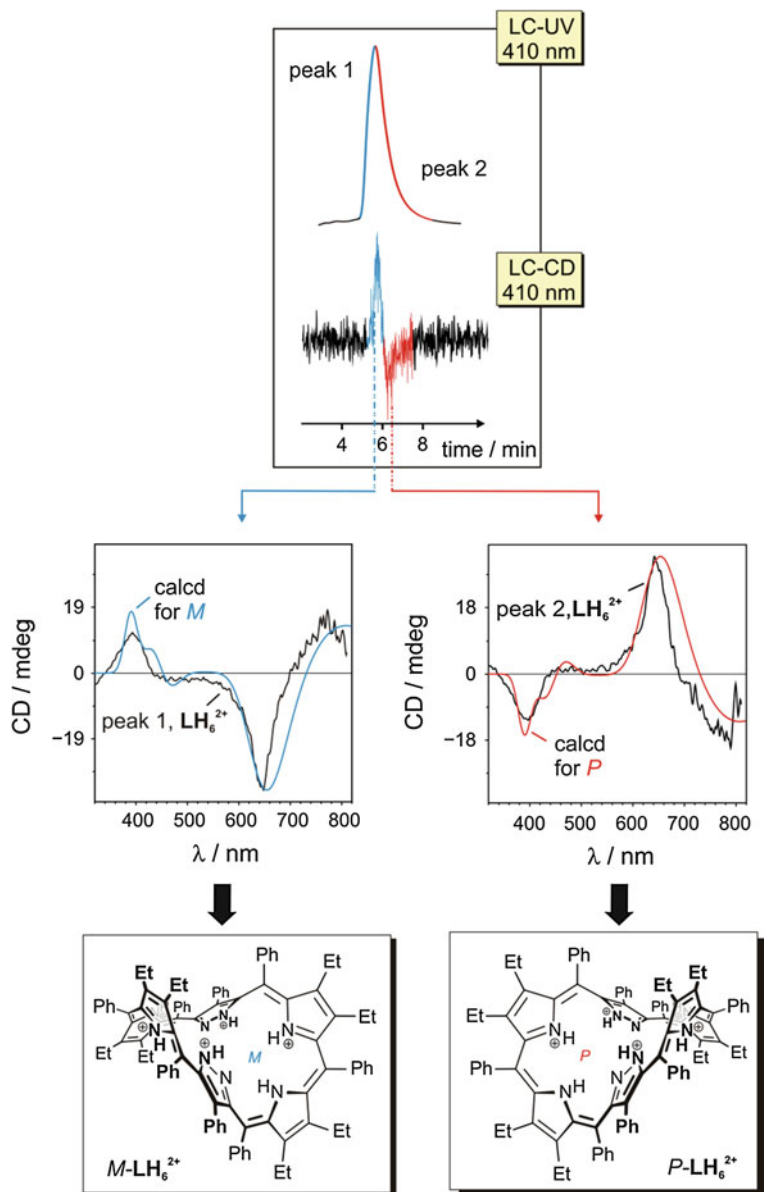


Fig. 4.18 Results of the HPLC separation of a racemic mixture of LH_6^{2+} on a chiral phase (Chiralpak[®] IA, ambient temperature, EtOAc/*n*-hexane (v/v) 30:70, isocratic flow rate: 0.8 mL·min⁻¹) and elucidation of the absolute configuration of the two helical enantiomers by comparison of the experimental CD spectra with the calculated CD curves. Copyright Wiley-VCH Verlag GmbH & Co. KGaA. Reproduced with permission [3]

Because of the novelty of the structure and, thus, no possibility for an empirical determination for the assignment of the absolute configuration, quantum-chemical UV and CD calculations were carried out [38]. Calculations within this range were performed using the Gaussian09 software package [39] and the B3LYP/6-31G(d,p) method [40, 41]. During the investigation of the conformational space of LH₆²⁺ only two strain-free backbone conformations exist of each enantiomer (Conf-1 and Conf-2). Comparative CD spectra calculations for the *M*-Conf-1 and *M*-Conf-2 were performed resulting in a significant blue shift (>40 nm) for *M*-Conf-2 revealing *M*-Conf-1 to be the present species (Fig. 4.19, left). While a change in the chromophoric backbone did not affect the CD result, ethyl orientation can be independently varied (Conf-1 and Conf-1_{anti}) (Fig. 4.19, right).

It was attempted to determine the energy barrier for racemization via NMR spectroscopy. If the two enantiomers interconvert, a transition state with a mirror plane has to be passed through such that the two diastereotopic protons on each methylene group exchange (Fig. 4.20, left). This process can be followed using

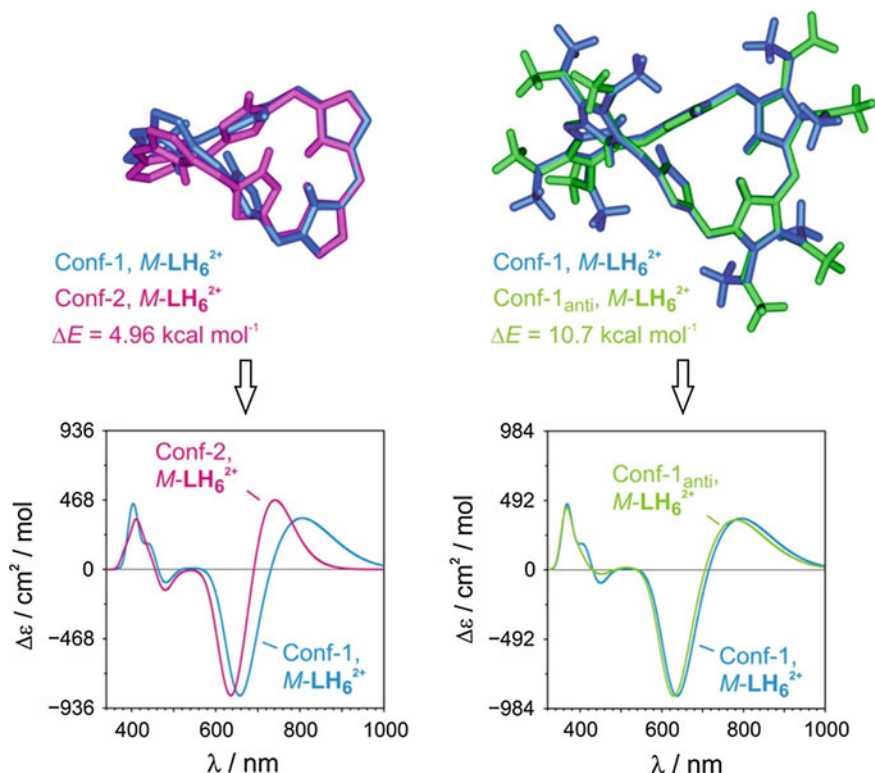


Fig. 4.19 Comparison of conformations of LH₆²⁺ of the same absolute configuration (here *M*), but with different chromophoric frameworks (*blue* and *pink*; left), and with completely opposite orientated ethyl substituents (*blue* and *green*, right) and their predicted CD spectra. Copyright Wiley-VCH Verlag GmbH & Co. KGaA. Reproduced with permission [3]

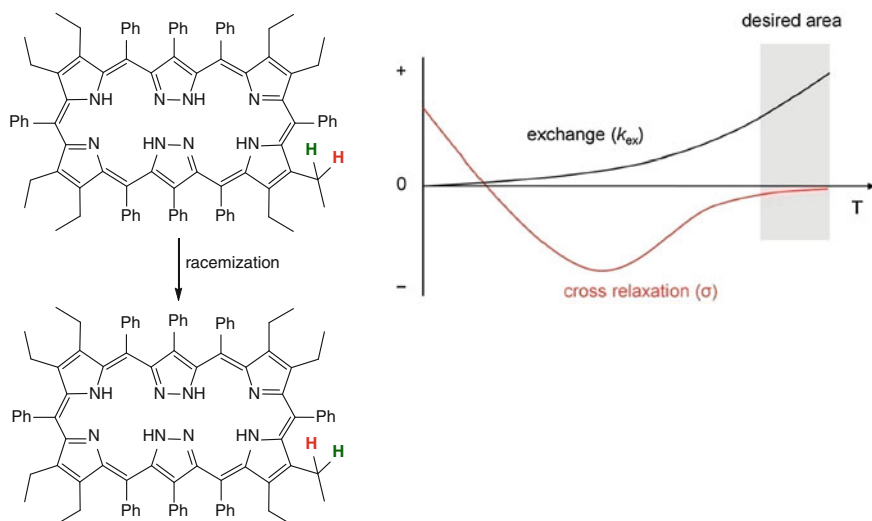


Fig. 4.20 *Left* Visualization of racemization by exchange of the diastereotopic methylene protons exemplarily demonstrated with only one CH_2 group. *Right* Temperature-dependency of the NOESY cross peaks (2) composition of the NOESY signal for small mixing times τ_m

NOESY measurements. Cross peaks in NOESY spectra are composed of cross relaxation and chemical exchange contributions (Fig. 4.20, right). The sign and magnitude of both contributions depend on temperature, additionally cross relaxation depends on the molecular size. The exchange contribution is positive and increases with temperature while for large molecules such as LH_4 cross relaxation changes its sign with temperature to negative values and after running through a minimum moves toward zero. At very high temperatures where exchange is dominant, NOESY measurements should evidence a sign change from negative to positive cross peaks and the exchange rate k_{ex} can be determined from the cross peak intensity (Fig. 4.20, Eq. 4.2). With k_{ex} known for different temperatures, the inversion barrier ΔG^\ddagger can be determined graphically using the Eyring Eq. (4.3). Variable temperature NOESY measurements were performed for LH_4 and LH_6^{2+} but the molecules decomposed at about 400 K before the desired area was reached. A lowerlimit for racemization enthalpies was estimated: Without TFA the exchange rates k_{ex} are smaller than 0.5 s^{-1} up to 393 K, which refers to a ΔG^\ddagger of $100 \text{ kJ}\cdot\text{mol}^{-1}$ and with the assumption of temperature independent ΔG^\ddagger an enantiomeric life time (k_{ex}^{-1}) of approximately 12 h at 298 K could be determined. For the protonated molecule enantiomers are stable for approximately 4 d at temperatures of 298 K. The lower limit of k_{ex} was determined to be smaller than 0.5 s^{-1} at temperatures up to 413 K, which refers to a ΔG^\ddagger of $105 \text{ kJ}\cdot\text{mol}^{-1}$. Considering the short experiment time for chiral resolution of approximately 20 min, chiral resolution should be possible for the more stable LH_6^{2+} enantiomers but as well for the

enantiomers of **LH₄**. Hence, that the two enantiomers of **LH₄** could not be isolated originates rather from a separation problem than from a fast interconversion of the two enantiomers. Besides the NMR spectroscopic determination of enantiomeric life times, this statement is supported by the weak separation of the two chiral enantiomers of **LH₆²⁺** using the UV detector.

$$\frac{I_{cross}}{I_{diagonal}}(\sigma + k_{ex})\tau_m \quad (4.2)$$

where, I = intensity, τ_m = mixing time = const., σ = cross relaxation rate, (3) Eyring equation with k_{ex} = exchange rate, k_B = Boltzmann constant, h = Planck constant, ΔG^\ddagger = racemization enthalpy, T = temperature and R = gas constant

$$\ln k_{ex} = \ln \frac{k_B T}{h} - \Delta G^\ddagger \frac{1}{RT} \quad (4.3)$$

4.4 Redox Properties

Redox activity of porphyrins is well known from naturally occurring chlorophyll and cytochrome P450. In vitro, the redox behavior can be studied using cyclic voltammetry (CV) [42], in which the current is measured when substances are getting oxidized and reduced by applying an external electric voltage. CV experiments provide information about the redox potentials of the substrate, the reversibility of the electron transfer reaction, the reactivity of intermediates, the presence of consecutive reactions and the number of transferred electrons. The solution is not stirred in CV experiments and thus redox processes are limited to the barrier layer between the electrode and the solution. Electrochemical reversibility is guaranteed, when fast electron transfer within the barrier layer is observed ($k > 10^{-1} \text{ cm}\cdot\text{s}^{-1}$) and thermodynamic laws become valid inclusive the Nernst equation.

Two common indicators of electrochemical reversibility are: [43] (1) The separation between the two peak potentials ΔE which can be used for a redox couple with

$$E^{ox} - E^{red} = \frac{0.058V}{n} \quad (4.4)$$

in which n amounts to the number of transferred electrons. With this equation insight into the number of transferred electrons is obtained. (2) Measurements at varying scan rates (v) indicate electrochemical reversibility when peak currents i_p increase linearly as a function of the square root of the scan rate:

$$i_p \propto \sqrt{v} \quad (4.5)$$

If the second indicator but not the first is proven true, redox processes are discussed as quasi-reversible and the electron transfer rate is within a range of $10^{-1} > k > 10^{-5} \text{ cm}\cdot\text{s}^{-1}$.

Besides the electrochemical reversibility, chemical reversibility is indicated when the anodic potential scan i_p^{anodic} and the cathodic potential scan i_p^{cathodic} are of the same magnitude and the same amount of substance that got oxidized is subsequently reduced. Chemical reversibility reveals information about the presence and the rate of consecutive reactions. In the case of consecutive reactions faster than the time scale of the CV experiment Eq. 4.6 is no longer valid:

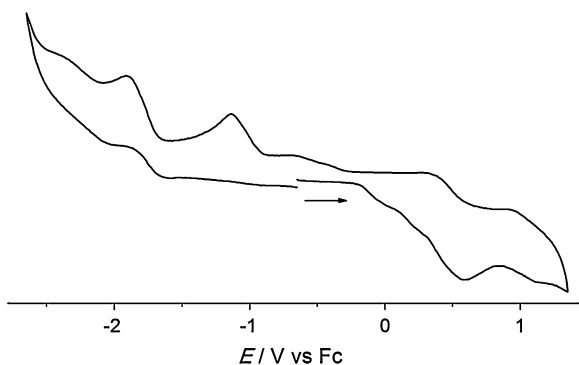
$$\frac{i_p^{\text{cathodic}}}{i_p^{\text{anodic}}} = 1 \quad (4.6)$$

The electrochemical redox behavior of porphyrins has been well studied using CV. Porphyrins usually exhibit four reversible waves in the potential range of -3 to $+3$ [44]. The assigned redox states, in tetraphenylporphyrin for example, are $\text{H}_2\text{TPP}^{2+}$, H_2TPP^+ , H_2TPP , H_2TPP^- and $\text{H}_2\text{TPP}^{2-}$ the mono-anionic and cationic species are π -radicals. Electrochemical investigations of expanded porphyrins are rare in the literature. Imahori and coworkers studied the redox chemistry of expanded porphyrins, which all have *meso*-3,5-bis(trifluoromethyl)phenyl substituents [45]. The CV curves of these do not exhibit as many reversible signals as CV curves for porphyrins but show reversibility to some extent. For our purpose it would be of interest if LH_4 indeed is a non-innocent ligand. The non-innocence of LH_4 would support the application of its metal complexes as catalysts for redox reactions.

Therefore, LH_4 was investigated by CV. If not otherwise specified the depicted CV curves were recorded at a scan rate of $100 \text{ mV}\cdot\text{s}^{-1}$ first measuring anodic scans. A 0.1 M solution of $[\text{NBu}_4]\text{PF}_6$ as the supporting electrolyte in CH_2Cl_2 was used. Decamethylferrocene [Fc^* , $E = -0.48$ vs. ferrocene (Fc) in CH_2Cl_2] [46] was used as an internal standard because the Fc signal was overlaying with redox processes for LH_4 .

Investigation of LH_4 showed all observed CV waves to be irreversible (Fig. 4.21). The signal at -1.8 V was measured separately without any indication

Fig. 4.21 CV curve of LH_4 in CH_2Cl_2 with $[\text{NBu}_4]\text{PF}_6$ as an electrolyte at a scan rate of $100 \text{ mV}\cdot\text{s}^{-1}$



of reversibility. From NMR measurements the Siamese-twin porphyrin was known to be dynamic and pH sensitive. Acidification of the reaction mixture in the CV experiment did not improve its reversibility.

References

1. M. Mori, T. Okawa, N. Iizuna, K. Nakayama, J.M. Lintuluoto, J.-I. Setsune, *J. Org. Chem.* **74**, 3579–3582 (2009)
2. E. Vogel, M. Bröring, J. Fink, D. Rosen, H. Schmickler, J. Lex, K.W.K. Chan, Y.-D. Wu, D.A. Plattner, M. Nendel, K.N. Houk, *Angew. Chem. Int. Ed.* **34**, 2511–2514 (1995)
3. L.K. Blusch, Y. Hemberger, K. Pröpper, B. Dittrich, F. Witterauf, M. John, G. Bringmann, C. Brückner, F. Meyer, *Chem. Eur. J.* **19**, 5868–5880 (2013)
4. M.H. Levitt, *Spin dynamics* (Wiley, Weinheim, 2002)
5. C. J. Medforth, in *Porphyrin Handbook*, ed. by K.M. Kadish, K.M. Smith, R. Guilard, vol 5. (Academic Press, San Diego, 2000) pp. 3–74
6. S. Mori, A. Osuka, *J. Am. Chem. Soc.* **127**, 8030–8031 (2005)
7. S. Berger, S. Braun, H.-O. Kalinowski, *NMR Spectroscopy of the Non-metallic Elements* (Wiley, New York, 1996)
8. J.L. Sessler, A. Mazaffari, M.R. Johnson, *Org. Synth.* **9**, 242 (1998)
9. T. Krygowski, M. Cyrański, in *Topics in Heterocyclic Chemistry*, vol. 19, ed. by R.R. Gupta. (Springer, Heidelberg, 2009)
10. M.A. Fox, J.K. Whitesell, *Organische Chemie* (Spektrum Akademischer Verlag, Heidelberg, 1995)
11. V.M. Albers, H.V. Knorr, *J. Chem. Phys.* **4**, 422–425 (1936)
12. H. Falk, *The chemistry of linear oligopyrroles and bile pigments* (Springer, New York, 1989)
13. J.A. Shelnut, X.-Z. Song, J.-G. Ma, S.-L. Jia, W. Jentzen, C.J. Medforth, *Chem. Soc. Rev.* **27**, 31–42 (1998)
14. S. Saito, A. Osuka, *Angew. Chem. Int. Ed.* **50**, 4342–4373 (2011)
15. F. Neese, *ORCA, an ab initio density functional and semiempirical program package* (University of Bonn, Germany, 2007)
16. M.J.S. Dewar, E.G. Zoebisch, E.F. Healy, J.J.P. Stewart, *J. Am. Chem. Soc.* **107**, 3902–3909 (1985)
17. M.J.S. Dewar, E.G. Zoebisch, E.F. Healy, J.J.P. Stewart, *J. Am. Chem. Soc.* **115**, 5348 (1993)
18. A.D. Becke, *Phys. Rev. A* **38**, 3098–3100 (1988)
19. P. Perdew, *Phys. Rev. B* **33**, 8822–8824 (1986)
20. A. Schäfer, H. Horn, R. Ahlrichs, *J. Chem. Phys.* **97**, 2571–2577 (1992)
21. T.D. Lash, A.M. Young, A.L.V. Ruden, G.M. Ferrence, *Chem. Commun.* 6309–6311 (2008)
22. M.M. Kruk, A.S. Starukhin, W. Maes, *Macroheterocycles* **4**, 69–79 (2011)
23. S. Saito, J.-Y. Shin, J.M. Lim, K.S. Kim, D. Kim, A. Osuka, *Angew. Chem. Int. Ed.* **47**, 9657–9660 (2008)
24. J.M. Lim, J.-Y. Shin, Y. Tanaka, S. Saito, A. Osuka, D. Kim, *J. Am. Chem. Soc.* **132**, 3105–3114 (2010)
25. J.-Y. Shin, J.M. Lim, Z.S. Yoon, K.S. Kim, M.-C. Yoon, S. Hiroto, H. Shinokubo, S. Shimizu, A. Osuka, D. Kim, *J. Phys. Chem. B* **113**, 5794–5802 (2009)
26. S. Hiroto, H. Shinokubo, A. Osuka, *J. Am. Chem. Soc.* **128**, 6568–6569 (2006)
27. R. Misra, R. Kumar, T.K. Chandrashekar, B. Joshi, *J. Org. Chem.* **72**, 1153–1160 (2007)
28. J.-Y. Shin, H. Furuta, K. Yoza, S. Igarashi, A. Osuka, *J. Am. Chem. Soc.* **123**, 7190–7191 (2001)
29. B. Biospin, *Almanac* (2012)

30. M. Stepień, L. Latos-Grazyński, in *Topics in Heterocyclic Chemistry*, vol. 19, ed. by R.R. Gupta. (Springer, Heidelberg, 2009), pp. 83–153
31. H. Basu, B. Feuerstein, D. Zarling, R. Shafer, L. Marton, *J. Biomol. Struct. Dyn.* **6**, 299–309 (1988)
32. A. Werner, M. Michels, L. Zander, J. Lex, E. Vogel, *Angew. Chem. Int. Ed.* **38**, 3650–3653 (1999)
33. S. Saito, A. Osuka, *Chem.-Eur. J.* **12**, 9095–9102 (2006)
34. C. Brückner, D.C.G. Götz, S.P. Fox, C. Ryppa, J.R. McCarthy, T. Bruhn, J. Akhigbe, S. Banerjee, P. Daddario, H.W. Daniell, M. Zeler, R.W. Boyle, G. Bringmann, *J. Am. Chem. Soc.* **133**, 8740–8752 (2011)
35. J.-Y. Shin, K.S. Kim, M.-C. Yoon, J.M. Lim, Z.S. Yoon, A. Osuka, D. Kim, *Chem. Soc. Rev.* **39**, 2751–2767 (2010)
36. M.K. Johnsons, in *Physical Methods in Bioinorganic Chemistry*, ed. by J. Lawrence Que. (University Science Books, Sausalito, 2000)
37. G. Bringmann, D.C.G. Götz, T. Bruhn, in *Comprehensive Chiroptical Spectroscopy*, vol 2, ed. by N. Berova, P.L. Polavarapu, K. Nakanishi, R.W. Woody. (Wiley, Hoboken, 2012) pp. 355–420
38. G. Bringmann, T. Bruhn, K. Maksimenka, Y. Hemberger, *Eur. J. Org. Chem.* 2717–2727 (2009)
39. M.J. Frisch, G.W. Trucks, H.B. Schlegel, G.E. Scuseria, M.A. Robb, J.R. Cheeseman, G. Scalmani, V. Barone, B. Mennucci, G.A. Petersson, H. Nakatsuji, M. Caricato, X. Li, H.P. Hratchian, A.F. Izmaylov, J. Bloino, G. Zheng, J.L. Sonnenberg, M. Hada, M. Ehara, K. Toyota, R. Fukuda, J. Hasegawa, M. Ishida, T. Nakajima, Y. Honda, O. Kitao, H. Nakai, T.J.A. Vreven, J. Montgomery, J.E. Peralta, F. Ogliaro, M. Bearpark, J.J. Heyd, E. Brothers, K.N. Kudin, V.N. Staroverov, T. Keith, R. Kobayashi, J. Normand, K. Raghavachari, A. Rendell, J.C. Burant, S.S. Iyengar, J. Tomasi, M. Cossi, N. Rega, J.M. Millam, M. Klene, J.E. Knox, J.B. Cross, V. Bakken, C. Adamo, J. Jaramillo, R. Gomperts, R.E. Stratmann, O. Yazyev, A.J. Austin, R. Cammi, C. Pomelli, J.W. Ochterski, R.L. Martin, K. Morokuma, V.G. Zakrzewski, G.A. Voth, P. Salvador, J.J. Dannenberg, S. Dapprich, A.D. Daniels, O. Farkas, J.B. Foresman, J.V. Ortiz, J. Cioslowski, *d* (J. Fox, Gaussian, Wallingford CT, 2010)
40. A.D. Becke, *J. Chem. Phys.* **98**, 5648–5652 (1993)
41. C. Lee, W. Yang, R.G. Parr, *Phys. Rev. B* **37**, 785–789 (1988)
42. A.J. Bard, L.R. Faulkner, *Electrochemical Methods: Fundamentals and Applications*, 2nd edn. (Wiley, Weinheim, 2000)
43. J. Heinze, *Angew. Chem. Int. Ed.* **23**, 831–847 (1984)
44. W. Kaim, A. Klein, *Spectroelectrochemistry*. (Royal Society of Chemistry, 2008)
45. S. Kang, H. Hayashi, T. Umeyama, Y. Matano, N. V. Tkachenko, H. Lemmetyinen, H. Imahori. *Chem.-Asian J.* **3**, 2065–2074 (2008)
46. N.G. Connelly, W.E. Geiger, *Chem. Rev.* **96**, 877–910 (1996)

Chapter 5

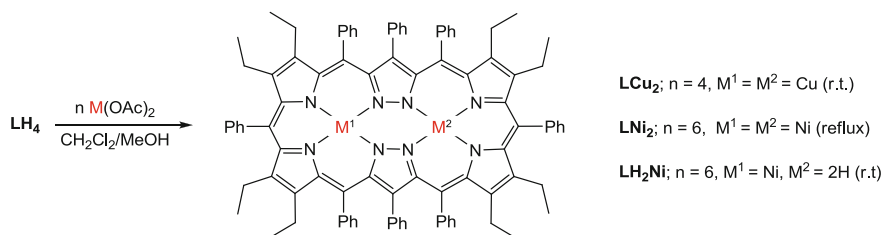
Nickel and Copper Complexes

The synthesized novel Siamese-twin porphyrin **LH₄** was designed as a chelating macrocyclic ligand to bind two metals in close proximity. The twin N₄ pockets are negatively charged twice after deprotonation. Most first row transition metals exhibit a stable oxidation state of 2 + [1]. With these M²⁺ metals, neutral complexes of the Siamese-twin porphyrin can be formed and the oxidation of neutral complexes usually is easier compared to positively charged complexes. This may facilitate the formation of high-valent species, including metal-oxo species.

Ni^{II} and Cu^{II} form the most stable complexes according to the Irving-Williams series [2, 3] and are commonly used in porphyrin chemistry to form porphyrin complexes although copper-porphyrin complexes do not occur naturally. Ni^{II} and Cu^{II} fit perfectly in the rigid porphyrinic cavity with their ionic radii in square planar coordination spheres of 0.63 Å for Ni^{II} and 0.71 Å for Cu^{II} [4]. It was reasoned that these metals might also fit in the rigid cavities of **LH₄**. While Ni^{II} complexes are diamagnetic, in the case of paramagnetic copper complexes magnetic interactions can be expected due to the two adjacent metal centers that are bridged by pyrazolates.

The incorporation of Fe^{II} would be of interest with regards to the biomimetic background, but the focus of this work lies on the synthesis and complete characterization of copper and nickel complexes. Working with nickel and copper is facilitated compared to iron, because they carry the advantage of stable M²⁺ oxidation states at ambient conditions, plus no axial ligands are required. To gather experience with capabilities of the Siamese-twin porphyrin and to obtain first impressions of its feasibility in redox processes, copper and nickel will provide a good starting point.

For the synthetic approach, Ni(OAc)₂ and Cu(OAc)₂ were used as metal salts, because they supply the metal(II) cation and a basic anion for deprotonation of **LH₄** in one. **LH₄** was stirred with an excess of Cu(OAc)₂ in a MeOH/CH₂Cl₂ mixture for 2 h to give the bimetallic dicopper complex **LCu₂** (Scheme 5.1). Subsequent purification via column chromatography with *n*-hexane/EtOAc gave pure **LCu₂** in 29 % yield. **LNi₂** was prepared in analogy using Ni(OAc)₂. However, the mixture had to be refluxed for 24 h. Separation by column chromatography with *n*-hexane/EtOAc yielded pure **LNi₂** in 62 % yield.

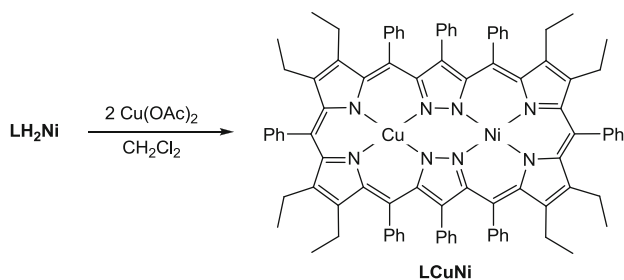


Scheme 5.1 Synthesis of homobimetallic complexes **LCu₂**, **LNi₂** and monometallic **LH₂Ni**

Besides **LNi₂**, the synthesis of the monometallated species **LH₂Ni** was successful. **LH₄** was stirred at r.t. with 6 equivalents of Ni(OAc)₂ in MeOH/CH₂Cl₂. Complexation of a second nickel ion requires additional energy to overcome an energy barrier. Hence, product control can be achieved via temperature: at high temperatures the bimetallic complex is formed while at room temperature the monometallic complex is formed. In minimal amounts, the bimetallic nickel complex is formed as a side product at room temperature but can easily be separated via column chromatography. Pure **LH₂Ni** was obtained by redissolving the crude material in a minimum amount of acetone. Short exposure to an ultra sonic bath and subsequent filtering yielded **LH₂Ni** in 83 % as a green solid.

With **LH₂Ni** in hand, it was subsequently possible to generate the heterobimetallic complex **LCuNi** (Scheme 5.2). **LH₂Ni** was dissolved in CH₂Cl₂, two equivalents Cu(OAc)₂ were added and the solution was stirred for 20 min. After column chromatography **LCuNi** could be obtained in 56 % yield. Heterobimetallic complexes are of interest in catalysis as the two metal centers supply different electronic properties and thereby the reaction can be tuned [5–10]. From the synthetic point of view it is usually a challenging task to asymmetricize the system by inserting two different metal ions.

Due to the neutral nature and the bulky organic substituents, all metal complexes are insoluble in polar solvents. First evidence for all four synthesized



Scheme 5.2 Synthesis of the heterobimetallic **LCuNi** complex

complexes was obtained via ESI-HRMS measured for solutions of the products in a mixture of CH_2Cl_2 and MeCN. The compositions of $\text{C}_{92}\text{H}_{80}\text{Cu}_2\text{N}_8$ (**LCu₂**), $\text{C}_{92}\text{H}_{80}\text{N}_8\text{Ni}_2$ (**LNi₂**), $\text{C}_{92}\text{H}_{82}\text{N}_8\text{Ni}$ (**LH₂Ni**) and $\text{C}_{92}\text{H}_{80}\text{CuN}_8\text{Ni}$ (**LCuNi**) were confirmed as peaks of a mass to charge ratio characteristic of $[\text{M}^+]$; measured data and simulations match well (Fig. 5.1). The presence of the monocationic M^+ indicates the capability to form mixed-valent species, which is already an interesting hint in terms of redox chemistry.

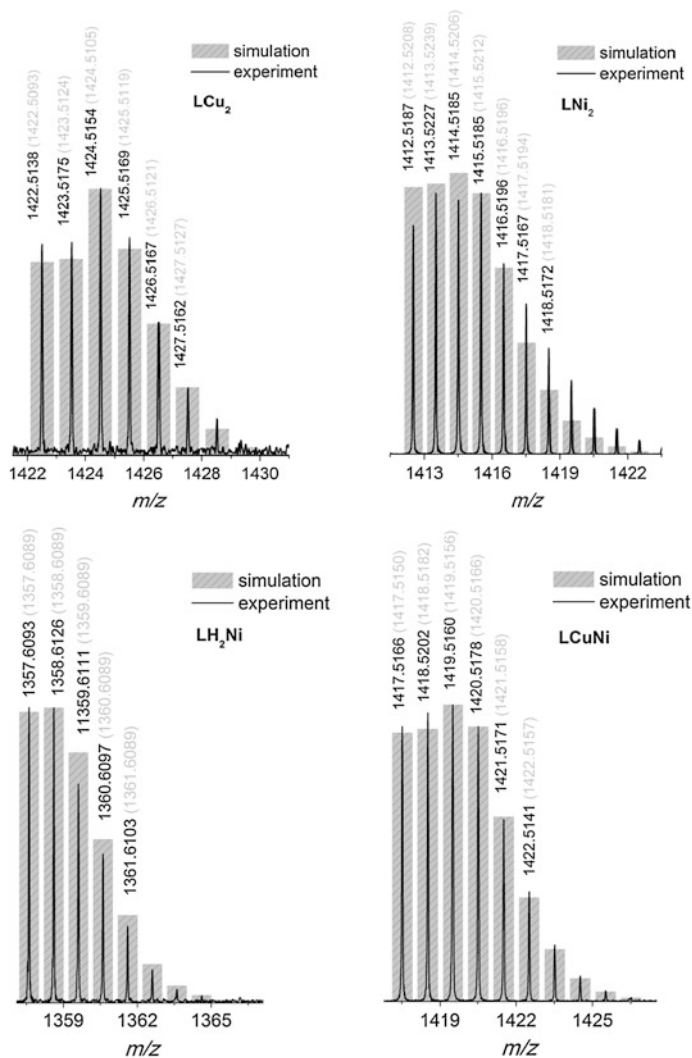


Fig. 5.1 ESI-HRMS of **LCu₂**, **LNi₂**, **LH₂Ni** and **LCuNi** overlaid with their simulated spectra

5.1 Comparison of Optical Properties

The resultant complexes are as intensively colored as the ligand itself. While **LH₂Ni** only undergoes a marginal color change and is still green, **LCu₂** is turquoise, **LNi₂** deep purple and **LCuNi** dark blue. Their characteristic UV–vis spectra were recorded in CH₂Cl₂ and in addition photographs were taken of the cuvettes (Fig. 5.2). All have high extinction coefficients of magnitudes higher than $1 \cdot 10^4 \text{ m}^{-1} \text{ cm}^{-1}$, suggestive of allowed transitions. The exact values are listed in Table 5.1. The highest absorption is found at around 380–390 nm in the UV–vis spectra of the complexes. Because the transition's intensity is only slightly affected by the variation of the metal ions it is assigned to ligand excitation which was later confirmed via magnetic circular dichroism measurements (MCD, Sect. 5.2.3). The band is reminiscent of the **LH₄** band at 390 nm (Fig. 4.6) but the extinction coefficients after complexation are smaller ($11 \cdot 10^4$ versus $5 \cdot 10^4 \text{ m}^{-1} \text{ cm}^{-1}$). This hypochromic shift can easily be explained: Metal ions in complexes are bound via coordinative bonds and electron density is pushed from the ligand toward the metal ions (Lewis acids). Thus, excitation of the electron-deficient ligand system is impeded resulting in reduced band intensities. The interrupted conjugation pathway is still preserved after complexation.

The bands between 500 and 900 nm are assumed to have at least partial metal contribution because they highly correlate with the presence of different metal ions. Most probably, they arise from metal-to-ligand charge-transfers (MLCT), as $d \leftarrow d$ transitions are Laporte-forbidden and have significantly smaller extinction coefficients. Because the ligand shows a broad absorption band in this region, overlapping of ligand and metal-induced bands are likely.

Crystalline material of **LCu₂**, **LNi₂** and **LCuNi** was obtained via slow evaporation of saturated solutions in toluene and was used for further analysis.

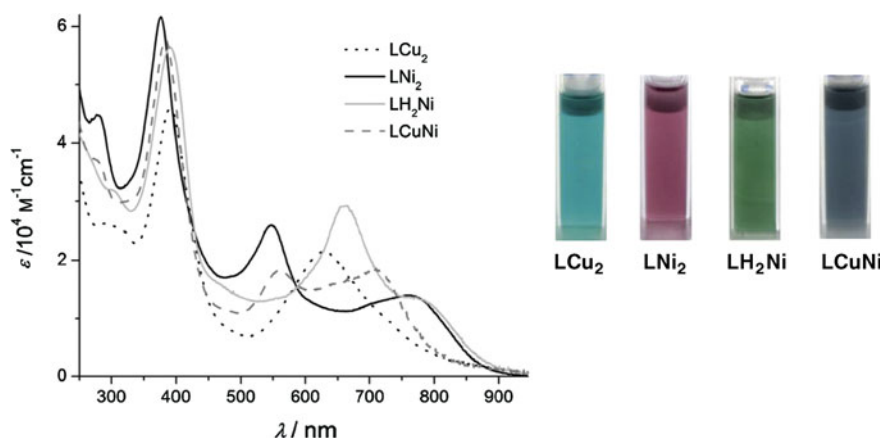


Fig. 5.2 UV–vis spectra of all four complexes measured in CH₂Cl₂

Table 5.1 Wavelengths and extinction coefficients for all four complexes

	LCu ₂	LNi ₂	LH ₂ Ni	LCuNi
λ/nm	306 (2.6)	281 (4.5)	303 (3.2)	279 (3.7)
$(\epsilon/10^4\text{m}^{-1}\text{cm}^{-1})$	391 (4.6)	377 (6.2)	394 (5.6)	385 (5.7)
	629 (2.2)	547 (2.6)	661 (2.9)	559 (1.8)
		765 (1.4)	778 (1.3)	710 (1.8)

Elemental analysis suggested a crystal composition of **LM₂** · 4 toluene. For analysis of **LH₂Ni**, the precipitated powder was used as obtained.

In the following chapters, each complex will be discussed separately. In accordance with their paramagnetic and diamagnetic ground states different methods were appropriate to investigate the complexes.

5.2 Dicopper(II) Complex LCu₂

5.2.1 Solid-State Structure

The obtained single crystals of **LCu₂** were suitable for X-ray analysis. Non-hydrogen atoms were refined anisotropically but for clarity reasons X-ray structures are depicted with the ball and stick model. **LCu₂** crystallizes in the non-chiral and monoclinic space group *C2/c* in which the second enantiomer can be generated via the glide plane (Fig. 5.3). The ligand-inherent twist is retained and thus the dicopper(II) complex is also severely distorted (Fig. 5.4). The crystal structure of **LCu₂** shows a crystallographic *C₂* axis through space making the two pockets symmetrically equivalent via the symmetry operation $1 - x, y, 0.5 - z$. Hence,

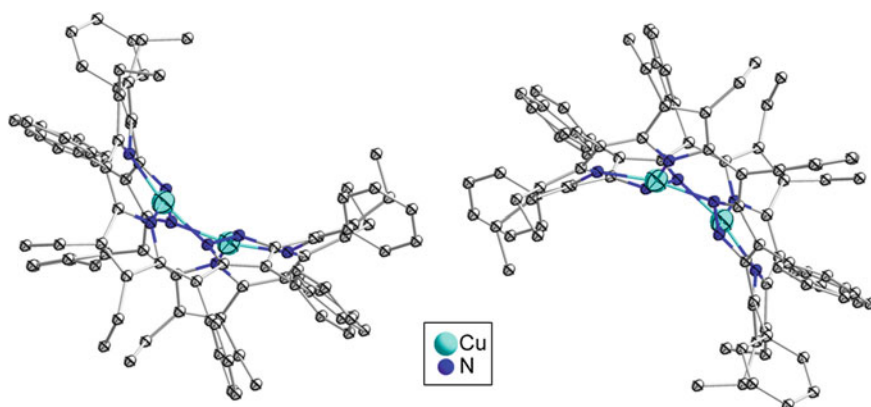


Fig. 5.3 Packing diagram of the two *P* and *M* enantiomers of **LCu₂**. Hydrogen atoms and solvent molecules were omitted for clarity

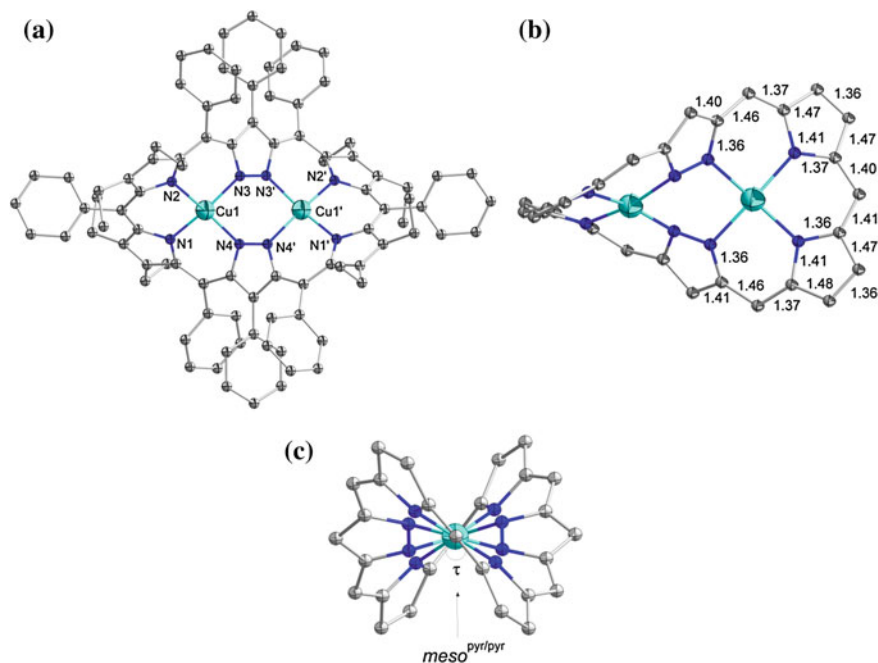


Fig. 5.4 Crystal structure of LCu_2 in its front side including labeling (a), core structure depicted in side view with selected bond lengths (b) and view along the long axis of the molecule describing τ (c); all hydrogen atoms, solvent molecules and in b and c phenyl and ethyl groups are omitted for clarity. Symmetry transformation to generate equivalent atoms (\prime): $1 - x, y, 0.5 - z$. Copyright Wiley-VCH Verlag GmbH & Co. KGaA. Reproduced with permission [38]

the asymmetric unit contains half a molecule of LCu_2 and two molecules of toluene. The composition of $\text{LCu}_2 \cdot 4$ toluene was predicted previously by elemental analysis. The toluene molecules are disordered, so are two phenyl groups. The lower populated positions of the disordered phenyl groups (0.2 versus 0.8) are omitted for clarity reasons. The absence of counterions confirms that the complex is neutral. Each copper ion is coordinated in a distorted square planar fashion with an N1-Cu1-N3 and N2-Cu1-N4 angle of 168° . But all N1-Cu1-N2, N2-Cu1-N3, N3-Cu1-N4 and N4-Cu1-N1 angles amount to 90° . Defining a mean plane through all nitrogen atoms and the copper ion of one pocket, the nitrogen atoms deviate about $\pm 0.21 \text{ \AA}$ from the mean-plane while the copper ion exactly lies within the plane. Despite the distortion of each copper pocket a square planar coordination sphere is anticipated as the basis of d orbital splitting [11].

The Cu-N distances range from $1.96\text{--}2.01 \text{ \AA}$ with the longer bonds to the N^{pz} . The metal-metal separation of 3.88 \AA lies well within the range of reported Cu-Cu separations in pyrazolate-bridged binuclear complexes ($3.5\text{--}4.0 \text{ \AA}$) [12, 13]. Besides the distorted copper environment itself, the orientation of the two copper coordination planes toward each other is almost orthogonal. The dihedral angles

following the $\text{Cu-N}^{\text{PZ}}\text{-N}'^{\text{PZ}}\text{-Cu}'$ bonds are 78° (via N4 and $\text{N4}'$) and 80° (via N3 and $\text{N3}'$). The torsion can further be defined by τ , which also amounts to 78° . Thus, helical chirality with a helical pitch of 10.61 \AA arises. The angle between the N1-N2-N3-N4-Cu1 and $\text{N1'-N2'-N3'-N4'-Cu1}'$ mean planes amounts to 49° . The crystal structure of LCu_2 shows that the twist inherent to LH_4 is retained upon complexation. Cu^{II} with its d^9 configuration has one unpaired electron. The two crystallographic symmetrical “Cu pockets” are almost orthogonal toward each other, which will most likely influence the magnetic interactions of the two unpaired spins.

5.2.2 Magnetic Properties

Magnetic properties of LCu_2 were studied with susceptibility measurements using a SQUID magnetometer and electron paramagnetic resonance (EPR) spectroscopy. While EPR yields information about the localization of the unpaired electron(s) and its surrounding, SQUID reveals the number of unpaired spins and their magnetic interaction in the case of $S > 1/2$. In principle one distinguishes between two different magnetic interactions: The dipole–dipole interaction is anisotropic and mediated through space and the exchange interaction is isotropic and mediated via bonds.

Having a two-spin system as LCu_2 , exchange interaction of the two unpaired electrons gives rise to an energy splitting in a triplet state with total spin $S_t = 1$

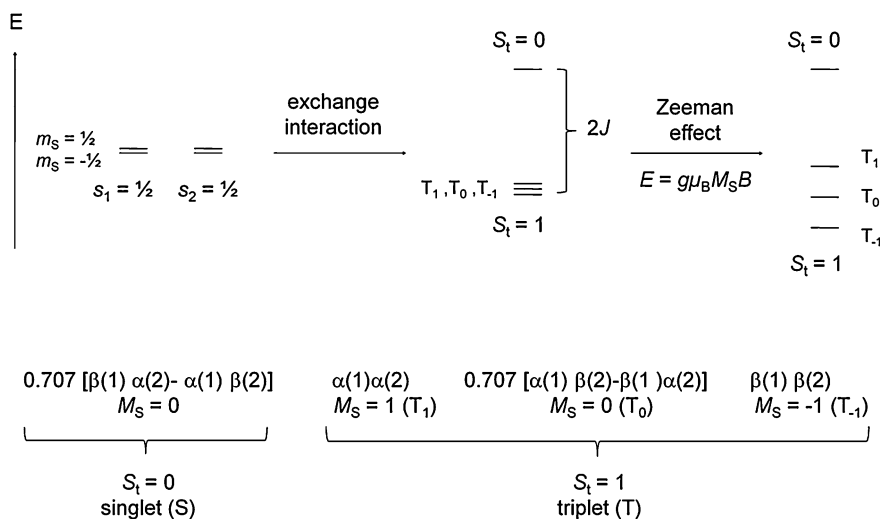


Fig. 5.5 Ferromagnetic exchange interaction of a two-spin system: representation of singlet and triplet states with total spins $S_t = 0$ and $S_t = 1$, respectively, in the basis of local spins s_1 and s_2 with magnetic quantum $m_s = +1/2$ (α) and $m_s = -1/2$ (β)

and a singlet state with $S_t = 0$, for which the local spins are oriented parallel and anti-parallel, respectively. The two states are eigen solutions of the isotropic Heisenberg – Dirac – VanVleck Hamiltonian ($\hat{H} = -2J\hat{S}_1 \cdot \hat{S}_2$), and their energy separation is given by two times the exchange coupling constant, $|2J|$ (Fig. 5.5). Ferromagnetic coupling ($J > 0$) renders the triplet ground state, whereas antiferromagnetic coupling ($J < 0$) yields the singlet ground state [14]. Population of the two total spin states is temperature-dependent according to Boltzmann's equation. In the absence of magnetic fields the triplet state, as the name suggests, is threefold degenerated. The triplet magnetic substates can be described on the basis of local spins s_1 and s_2 with magnetic quantum numbers $m_s = +1/2$ (α) and $m_s = -1/2$ (β) as given in Fig. 5.5 [15]. At high temperature, $kT \gg 2J$, where singlet and triplet states approach equal population, the magnetic susceptibility (χ) of a spin-coupled system approaches the value of completely uncoupled spins (spin-only value), which means the susceptibility equals the sum of susceptibilities of individual spins. The values can be determined applying the Eq. 5.1, whereas μ_{eff} is the effective magnetic moment, μ_B the

$$\mu_{\text{eff}} = g\sqrt{s_1(s_1 + 1) + s_2(s_2 + 1)} = 2.828\sqrt{\chi T}\mu_B \quad (5.1)$$

Bohr magneton and g the Landé factor. The g value represents a proportionality constant relating the magnetic moment (μ) with the angular momentum of the electron ($\mu = g\mu_B m_s$) and has a magnitude of 2.0023 for the free electron. This g value for most organic radicals is close to the free-electron value whereas it differs for transition metal ions because of a larger spin-orbit coupling [16].

The temperature dependency of the effective magnetic moment of **LCu₂** shows a roughly constant value of $2.73 \mu_B$ in the temperature range 150–300 K (Fig. 5.6). This value is close to the spin-only value of two uncoupled $s = 1/2$ systems of $\mu_{\text{eff}} = 2.66 \mu_B$ for a g value of 2.17. The effective moment of **LCu₂** increases at lower temperatures and reaches a maximum of $3.06 \mu_B$ at 8 K. This behavior is indicative of ferromagnetic exchange interaction and a triplet ground

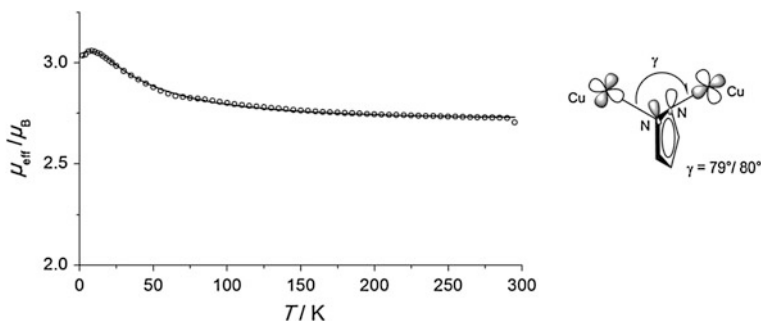


Fig. 5.6 Left Plot of μ_{eff} versus T for **LCu₂** (magnetic field of 0.5 T from 295 to 2.0 K); experimental data (○) and calculated curve fit (—). Right: Illustration of the Cu-N^{pz}-N^{pz}-Cu dihedral angle γ . Copyright Wiley-VCH Verlag GmbH & Co. KGaA. Reproduced with permission [16]

state. Below 8 K the effective moment decreases again due to the usual saturation behaviour at low temperatures.

The experimental data could be well simulated by using the isotropic Heisenberg–Dirac–Van Vleck Hamiltonian amended with the corresponding Zeeman term $\hat{H} = -2J\hat{S}_1 \cdot \hat{S}_2 + g\mu_B(\hat{S}_1 + \hat{S}_2)B$ (Fig. 5.5) [17]. The equation considers both effects, with B being the externally applied magnetic field, and gives the corresponding J and g values. Thus, the theoretical fit confirms the ferromagnetic behaviour and determines a sizeable positive coupling constant of $J = +16.3 \text{ cm}^{-1}$ and a g value of 2.17.

The possibility of ferromagnetic coupling in pyrazolate bridged dinuclear complexes was predicted to exist [17], but all complexes reported so far showed antiferromagnetic coupling in the typical range of $-245 \leq J \leq -70 \text{ cm}^{-1}$ [19–23]. However, the pyrazolate-bridged complex reported here is the first example exhibiting ferromagnetic coupling. This can be explained by the presence of orthogonal magnetic orbitals—one out of three established concepts to explain the phenomena of exchange coupling [17, 22]. Orthogonality of the magnetic orbitals (singly occupied orbitals) causes a zero overlap integral. Hence antiferromagnetic exchange contribution ($J_{\text{antiferro}}$) to the overall coupling term of $J = J_{\text{ferro}} + J_{\text{antiferro}}$ vanishes such that only ferromagnetic coupling remains. This orthogonality can be strict and inherent to the symmetry of the magnetic orbitals or coincidental and introduced via geometry.

Searching the Cambridge Structural Database shows that the common γ angle (Fig. 5.6, right) for pyrazolate bridged dicopper complexes is smaller than 32° . The maximal torsion angle ever reported in literature was 41° , but magnetic investigations are lacking [23]. The extraordinary behaviour of **LCu₂** seems to be related to the pronounced torsion. Assuming a d orbital splitting in a square planar ligand field, the two unpaired electrons are located in $d_{x^2-y^2}$ orbitals. X-ray analysis revealed a torsion angle between Cu–N^{Pz}–N^{Pz}–Cu of 79° or 80° . The two $d_{x^2-y^2}$ orbitals are not orthogonal without torsion of the two molecule halves, but due to the distorted geometry they are coincidentally close to orthogonal, resulting in a minimal overlap integral and ferromagnetic coupling.

EPR spectroscopy is a technique similar to NMR spectroscopy. For both, the Zeeman effect is fundamental (Fig. 5.5). While in NMR spectroscopy the splitting of e.g. the two degenerated spin states of the hydrogen nuclei with $m_I = 1/2$ and $m_I = -1/2$ by an external magnetic field is relevant, in EPR spectroscopy in the case of a triplet state the degeneracy of T_1 , T_0 and T_{-1} states is lifted. According to the selection rule for EPR of $\Delta M_s = \pm 1$ and $\Delta M_I = 0$, transitions between these states resulting from spin flips can be induced if matching the resonance frequency. This is given with $\Delta E = g\mu_B B$ and the absorption of this energy is the origin of the EPR signal. Resonance is technically realized by applying microwave radiation of constant frequency to the sample and sweeping the magnetic field (constant wave method). This is why the EPR device is named after its constant frequency, such as the most commonly used X band (9.5 GHz) or Q band (35 GHz) devices.

Evaluation of the EPR spectra reveals information about the localization of the unpaired electron and the electronic geometry around the radical. Coupling of the unpaired electron(s) to the nuclear spin(s) (I) is referred to as hyperfine coupling (a) and gives rise to further splitting of EPR lines. Information about the electronic structure of the system can be derived from the g value and its anisotropic splitting, leading to isotropic, axial or rhombic spectra. In the first case, the three g values according to the three local magnetic principal axes are identical, in axial spectra only two g values are the same while the third is different, whereas in rhombic systems all three values, g_x , g_y and g_z differ [22]. Usually the first derivative of the EPR signal is measured and depicted.

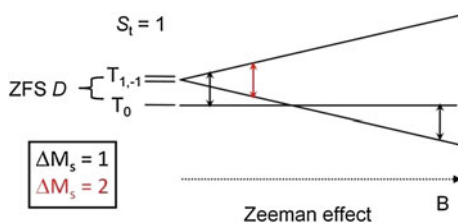
The effective magnetic field experienced by each electron is a sum of internal magnetic interactions and the external field. The exchange coupling as an internal interaction and the Zeeman effect as an external influence on magnetic microstates has already been discussed. For EPR spectroscopy a further internal electron–electron interaction is relevant—the zero field splitting (ZFS) [15, 24]. This behaviour can only occur for spin systems with $S > 1/2$, as given in the present case. The degeneracy of the triplet substates can already be lifted without an external magnetic field (zero field!) if ZFS affects the system. ZFS results from dipolar spin–spin coupling, which is mediated through space (Fig. 5.7).

The EPR spectrum of LCu_2 was measured at X band in a frozen glass of CH_2Cl_2 at 10 K and 143 K and is quite complicated, but did not show any temperature dependency. Following common convention, the first derivative of the EPR absorption is depicted. It shows a broad main signal in the range of 260 mT to 410 mT and a half field signal between 130 and 190 mT (Fig. 5.8). For understanding this complex spectrum, simulations are required.

The simulation was performed with the Bruker program X-SOPHE. Only the triplet state is EPR active. Because the triplet-singlet separation is larger than the Zeeman-induced separation of the M_S states (about 0.3 cm^{-1} in X-band), the triplet-singlet mixing is vanishing, and the singlet state can be neglected in the simulation. Thus, the spectrum of LCu_2 can be simulated using one set of g values and ZFS. In this way, information already known cannot be fine-tuned and are hidden in ZFS parameters, as the anisotropy of the hyperfine coupling. Also the fact, that the two ‘Cu pockets’ show a distortion of 80° can only be considered indirectly.

Thus, a simulation approach with two spin pairs was chosen and all coupling effects were considered using a J matrix. The trace contains all isotropic and anisotropic coupling contributions, and the exchange part can be determined

Fig. 5.7 Influence of ZFS and subsequent Zeeman effect on the triplet state ($S_t = 1$) [26]



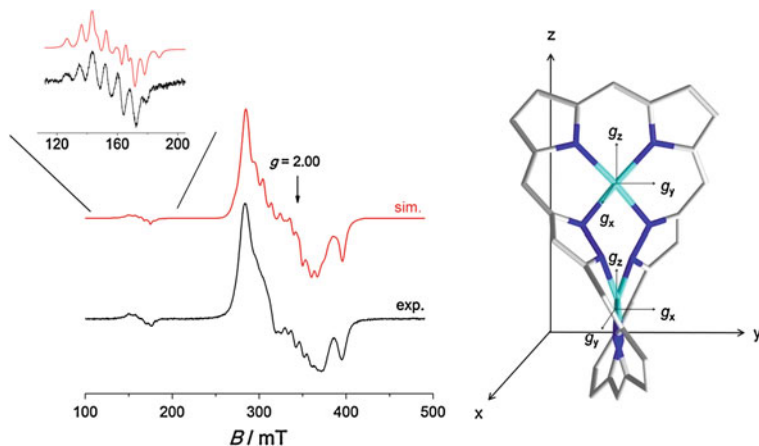


Fig. 5.8 *Left*: EPR spectrum and simulation of LCu_2 measured in CH_2Cl_2 as a frozen glass at 10 K at X-band in perpendicular and parallel mode (zoom); *Right*: local g tensors and the linking of g_x and g_y . Reproduced with permission [42]. Copyright (2013) American Chemical Society

calculating the mean value of the diagonal elements because the anisotropic dipole coupling is traceless. Such a description is much more accurate.

The LCu_2 system is rhombic and three different g values were defined. As the two ‘Cu-pockets’ in the structure are equal (related by crystallographic C_2 symmetry) the same g values for the two copper ions were anticipated. Because the two copper coordination planes are almost orthogonal with respect to each other, the g_x and g_y value were switched (rotation about 90°), when z is set to the long axis of the molecule, along which the g values for Cu1 and Cu1’ are supposed to be equal (Fig. 5.8, right). The attempt was proven to be correct with $g_x = 2.13$, $g_y = 2.07$ and $g_z = 2.03$ for Cu1 and $g_x = 2.07$, $g_y = 2.13$ and $g_z = 2.03$ for Cu1’. The switch of the g values represents a twist of exactly 90° because the axes in coordinate systems enclose 90° angles; yet the simulation was not perfectly matching. Additionally the z axis was tilted about 10 % to end up with a distortion of both copper coordination planes of approximately 80° as revealed from X-ray data. A strong hyperfine coupling to Cu1 ($I = 3/2$) of $a = 22.7$ mT was observed in x direction. Hyperfine coupling to Cu1’ was first defined to the y axis of the same magnitude as for Cu1 but became partially splitted upon the tilt of the z axis in $a_x = 9.1$ mT, $a_y = 13.3$ mT and $a_{xy} = 23.1$ mT. The coupling was introduced with values of $J_x = 1.03$, $J_y = 1.04$ and $J_z = 0.93$ cm^{-1} . X-SOPHE uses a different Hamiltonian and thus defined J to $\hat{H} = J\hat{S}_1 \cdot \hat{S}_2$ instead of $\hat{H} = -2J\hat{S}_1 \cdot \hat{S}_2$ [25]. The obtained J values from EPR simulation have the opposite sign and amount to twice the size of J obtained using the Heisenberg-Dirac Hamiltonian. As mentioned the actual J value can then be calculated by taking the mean value of the diagonal matrix elements and multiply it by two which leads to $J = 8$ cm^{-1} . This differs from the SQUID measurements determined coupling constant of $J = 16$ cm^{-1} but

is of same magnitude. The final simulated spectrum was obtained by setting a line width of $40 \cdot 10^{-4} \text{ cm}^{-1}$ in all directions and use Lorentz line shapes.

Despite the anisotropic dipole coupling is traceless, its amount can be calculated by simplifying the two rhombic spin centers to dipoles. Applying a dipole-dipole model, a metal-metal distance of 3.8 Å can be determined. This value agrees well with the metal-metal separation of 3.88 Å obtained from X-ray data analysis.

Besides the normal signal, a half-field signal between 130 and 190 mT was observed. Usually, the EPR selection rule only allows transitions with $\Delta M_s = 1$, but this rule is relaxed at low magnetic fields [26]. The zero field interactions such as ZFS and spin-orbit coupling dominate over the effect of the external magnetic field and the spin states of T_1 , T_0 and T_{-1} are not well defined anymore. Weak transitions with $\Delta M_s = 2$ become visible at exactly half the field explaining their name. To study the measured half field signal in more detail, the cavity mode was changed from perpendicular to parallel. With that, the $\Delta M_s = 2$ becomes allowed and a more intense and better resolved signal was detected (zoom in Fig. 5.8, left). For the simulation of the half field signal, X-SOPHE was set to parallel mode as well and besides that the same parameter set was used as for the simulation run in the perpendicular mode.

5.2.3 MCD Spectroscopy

MCD spectroscopy is experimentally similar to CD spectroscopy: In both cases the differential extinction of left and right circularly polarized light is measured as a function of the energy of the incident light. The main difference in the experimental set up is the applied external magnetic field in the case of MCD spectroscopy. While for CD spectroscopy an inherent structural dissymmetry (chirality) is required, MCD is a universal property because its origin lies in the Faraday effect. Lcp and rcp light propagates at different speed when passing through a longitudinal magnetic field. This effect was discovered by and named after Faraday [24].

The selection rule for an optical transition is different for lcp and rcp light: $\Delta m_{\text{lcp}} = +1$ and $\Delta m_{\text{rcp}} = -1$ (Fig. 5.9, right). The intensity difference of the absorption between lcp and rcp light is reported as $\Delta \epsilon$ [$\text{M}^{-1} \text{cm}^{-1} \text{T}^{-1}$] and can be mathematically described by the fundamental equation of MCD spectroscopy in (Fig. 5.9):

It is apparent that three different intensity mechanisms contribute to the observed MCD intensity: the A-, B- and C-term. The A-term arises when the excited state is degenerate. B-term intensity results from the field-induced mixing of either the ground and/or the excited state with a nearby auxiliary state. Because this is always given within a magnetic field (although often very weak), the B-term demonstrates the universality of the Faraday effect. The C-term contribution requires ground state degeneracy and is specifically observed for paramagnetic systems. While the A- and B-terms are temperature independent, the C-term intensity is inversely proportional to temperature and therefore requires measurements at very low temperatures [27].

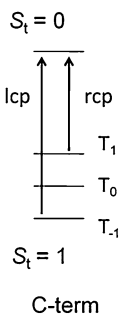
$$I \propto \Delta\varepsilon \propto \text{const} \cdot \left[A_1 \left(\frac{-\partial f(E)}{\partial E} \right) + \left(B_0 + \frac{C_0}{kT} \right) f \right] \mu_B B$$


Fig. 5.9 Fundamental equation for MCD spectroscopy: at low temperatures the C-term becomes dominant. The C-term intensity is proportional to the population differences of T_{-1} and T_1

At liquid helium temperatures, the C-term becomes the dominant intensity mechanism for paramagnetic substances. The C-term intensity at low temperatures is a direct consequence of the Boltzmann population distribution over the Zeeman-split sublevels of the ground state (T_1 , T_0 , T_{-1} , Fig. 5.9, right). At high temperatures these magnetic sublevels are still equally populated, thus not showing any differences in the transition probability for lcp and rcp light and thus no C-term intensity arises. However, at low temperatures, there is a higher population of the energetically lower sublevels and the transitions of lcp and rcp light lead to different absorption intensities (Fig. 5.9), and hence, a C-term signal becomes visible. An increase of the magnetic field shows the same qualitative effect as a temperature decrease, leading to a larger population of the lower sublevels, and hence a further increase in the C-term intensity.

Thus at very low temperatures or very strong magnetic fields only the lowest energy level is populated, which allows the C-term intensity to reach its maximum and to be saturated. The temperature- and field-dependent C-term intensity (VT VH = variable temperature variable field) contains the complete information of the ground state of the complex, and is particularly sensitive to ZFS and exchange interactions [28].

LCu₂ is paramagnetic with its threefold degenerated triplet ground state, thus the C-term is the most relevant intensity mechanism in this case. For this reason, only the dominant C-term was measured for **LCu₂** by recording a spectrum from 10,000 to 40,000 cm^{-1} at 4.1 K in a polystyrene (PS) film in collaboration with Lehnert (Fig. 5.10). Due to the complexity of MCD spectra, individual transitions are best identified by a fit of the MCD spectrum and the absorption spectrum. Here, the optical spectra of **LCu₂** were deconvoluted using the program PeakFit. The C-term spectrum of **LCu₂** allows one to resolve the broad bands observed in the UV-vis spectrum into 16 different electronic transitions within the measured region. It is eye-catching that the two main absorption bands in the UV-vis spectrum, 4 and 11, do not show much MCD intensity. That points to pure ligand-derived electronic transitions, most likely $\pi^* \leftarrow \pi$ transitions, that lack any

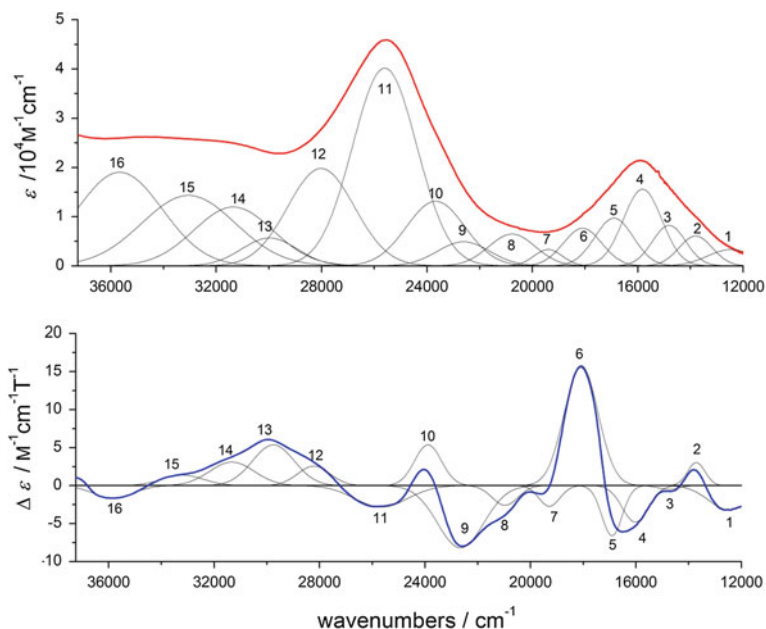
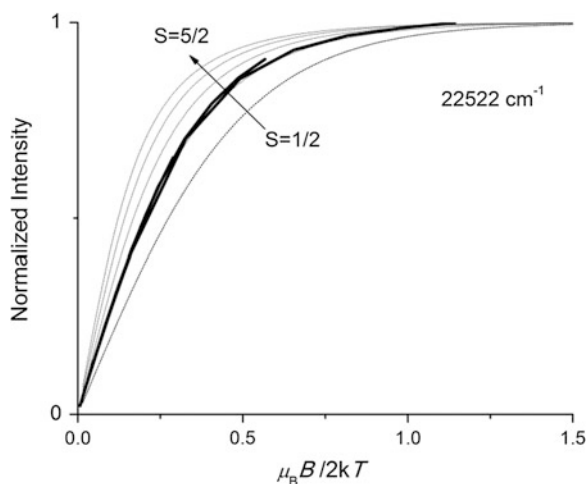


Fig. 5.10 *Top*: UV-vis spectrum of LCu_2 (red line) and the calculated contributions to the overall absorption spectrum (black lines 1–16); *Bottom*: MCD C-term spectrum measured in polystyrene (PS) at 4.1 K. The solid black lines represent a correlated fit of these data. Reproduced with permission [42]. Copyright (2013) American Chemical Society

degeneracy in the excited state and any significant metal contribution, which is in stark contrast to the Soret bands of porphyrins [29].

By varying the magnetic field and the temperature, magnetic saturation curves were further measured for LCu_2 (Fig. 5.11, bold). Figure 5.11 shows the

Fig. 5.11 VTVH saturation curves of the C-term intensity at $22,522 \text{ cm}^{-1}$ of LCu_2 . Reproduced with permission [42]. Copyright (2013) American Chemical Society



saturation curve for band 9, measured at 22,522 cm⁻¹ as example, together with the theoretically calculated Brillouin curves.

The Brillouin equation (5.2) predicts the temperature and field depending curves for different spin systems, but assumes no ZFS [30]. Here, the Brillouin curves were calculated for spin systems varying from $S = 1/2$ to $S = 5/2$ (Fig. 5.11, light black lines). The experimental curve is exactly that of $S = 1$ for the VTVH data determined for band 9 (and other bands, not shown). Hence a ferromagnetic ground state with $S = 1$ can clearly be assigned also with MCD spectroscopy.

$$I = I_{(\text{satlimit})} \cdot \tanh\left(\frac{g\mu_B B}{2kT}\right) \quad (5.2)$$

5.2.4 Chiral Resolution

The twisted geometry of LCu₂ not only gives rise to the ferromagnetic coupling, but also to helical chirality. X-ray analysis showed the presence of enantiomers in the solid state structure. As metal complexation rigidifies the system, separation was successful with a 1:1 ratio of EtOAc and *n*-hexane on a Chiralpak[®] IB column. In contrast to LH₆²⁺, a clear separation was already observed in the LC-UV band (Fig. 5.12). DFT-optimization of the global minima of LCu₂ as well as the subsequent CD spectra calculations were carried out with the B3LYP functional in combination with the 6-31(d,p) basis set for all elements except the copper ions for which the larger 6-311G* [31, 32] basis set was applied. Comparison of the experimental CD data with the calculated CD curves for the enantiomers of both bimetallic complexes revealed a good match for the CD spectrum with the *P*-enantiomer being the faster eluting isomer (peak 1, blue).

5.3 Mono- and Di-Nickel(II) Complexes LH₂Ni and LNi₂

5.3.1 Solid-State Structures

Crystals of LH₂Ni were grown via slow evaporation of a saturated solution of LH₂Ni in acetone. LH₂Ni crystallizes in the space group $P\bar{1}$ and exhibits no crystallographic symmetry (Fig. 5.13, a). Interestingly, the C–C bond lengths of LH₂Ni along with its two distinct pockets are similar for both pockets. Crystal data were good enough to locate H atoms in LH₂Ni at the two pyrrole nitrogen atoms, while the pyrazole nitrogen atoms are deprotonated. The Lewis acidic nickel ion binds to two N^{Pz} atoms and withdraws electron density. The increased acidity of all N^{Pz} atoms introduces a proton shift from pyrazole to pyrrole and the overall neutral state of LH₂Ni was confirmed by the absence of any counterions.

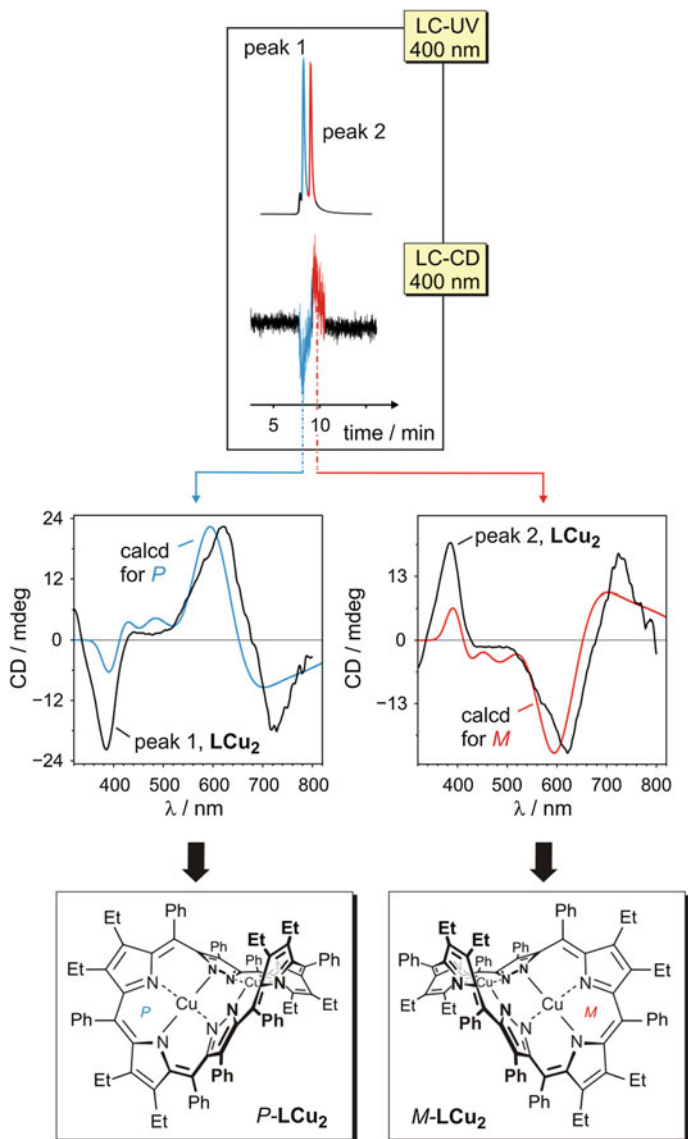


Fig. 5.12 Results of the HPLC separation of a racemic mixture of LCu_2 on a chiral phase (Chiralpak[®] IB, ambient temperature, EtOAc/*n*-hexane (v/v) 1:1, isocratic flow rate: $0.5 \text{ mL}\cdot\text{min}^{-1}$) and elucidation of the absolute configuration of the two helimeric enantiomers by comparison of the experimental CD spectra with the calculated CD curves resulting from TD DFT calculations using B3LYP/6-31G(d,p) and 6-311G* for both Cu atoms. The more rapidly eluting compound (peak 1, blue) possesses the *P*-configuration while the more slowly eluting enantiomer (peak 2, red) consequently is *M*-configured. Copyright Wiley-VCH Verlag GmbH & Co. KGaA. Reproduced with permission [38]

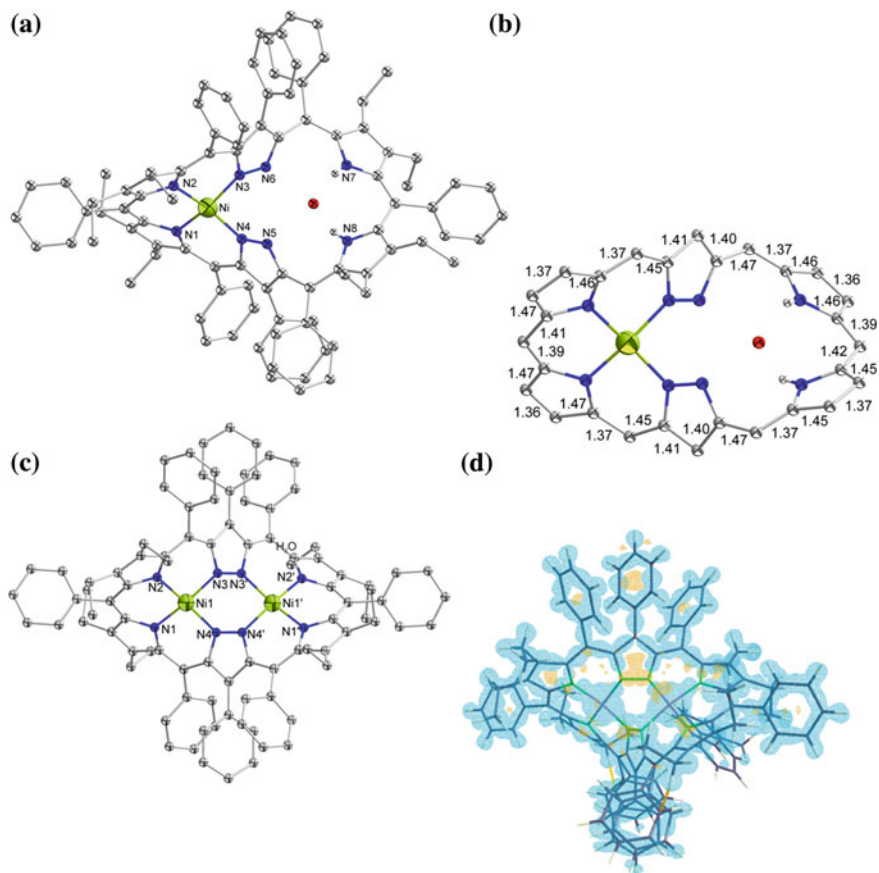


Fig. 5.13 X-ray structures of LH_2Ni (top) and LNi_2 (bottom) in front view including labeling (a and c). **b** shows a side view with bond lengths of the core, **d** shows a side view with multipole deformation density map. Symmetry equivalents were used to generate all atoms: $0.5 - x$, $0.5 + y$, $1.5 - z$. Copyright Wiley-VCH Verlag GmbH & Co. KGaA. Reproduced with permission [38]

Furthermore, the metal-free cavity accommodates one hydrogen-bonded water molecule. The dihedral angle τ which was defined as in Fig. 5.4 amounts to 78° and 90° for the two sides and a helical pitch of 10.65 \AA is observed (Table 5.2). The nitrogen atoms of theazole rings of LH_2Ni in its metal-free cavity do not point toward the cavity's center, because their orientation is not fixed via bonding to metal ions. This results in a distorted arrangement of theazole rings with a dihedral angle between N6-N3-N4-N5 of 83° which reveals an almost perpendicular orientation of the two pyrazoles toward each other.

Crystals of LNi_2 suitable for X-ray analysis were obtained as described for LCu_2 . The solid-state structure of LNi_2 is reminiscent of the LCu_2 solid-state

Table 5.2 Comparison of all obtained X-ray crystal structures listing selected angles and distances in degrees and Å, respectively

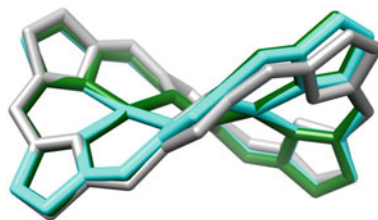
	LH_6^{2+}	LH_2Ni	LNi_2	LCu_2	$[\text{LCu}_2](\text{BF}_4)_2$
τ	$\pm 86^\circ/-87^\circ$	$\pm 78^\circ/-90^\circ$	± 73	± 78	± 76
sh/l C–C	1.36/1.48	1.36/1.47	1.36/1.47	1.36/1.48	1.36/1.46
Pitch	10.73	10.65	10.48	10.61	10.52
N1–M–N3	–	160°	166°	168	163
$\text{N}^{\text{pyr}}\text{-M}$ (av)	–	1.88	1.90	1.96	1.98
$\text{N}^{\text{pz}}\text{-M}$ (av)	–	1.87	1.92	1.99	1.99
M– $\text{N}^{\text{pz}}\text{-N}^{\text{pz}}\text{-M}$	–	–	$\pm 80/\pm 82$	$\pm 79/\pm 80$	$\pm 75/\pm 85$
M–M	–	–	3.81	3.88	3.88

For further comparison see Appendix
av average, *sh* shortest, *l* longest

structure: Both crystallize in the monoclinic space group $C2/c$ with four toluene molecules per LM_2 and show a similar crystallographic twofold symmetry (Fig. 5.13c). The refinement of the crystal structure for LNi_2 was first performed using the common independent atom model (IAM). This resulted in a crystallographic R factor of 3.86 %. As the data were of good quality after the IAM refinement, the invariom method, namely non-spherical scattering factors, was applied [33, 34]. The invariom method is usually used for small molecules to precisely determine the electron density. It was never used for inorganic molecules with such a large molecular mass. Only positional and displacement parameters of non-hydrogen atoms were adjusted in invariom refinement, so that the number of parameters was not increased in comparison to the IAM. Bond distances to H atoms were set to values of model compounds of the invariom database [35]. Figure 5.13d shows the additional valence electron density included in the model that is ignored in conventional IAM refinements. Due to this approach it was possible to reduce the R factor of LNi_2 to 2.96 %.

The crystal structure of LNi_2 is discussed by comparing the measured angles and distances to the obtained data of LCu_2 and LH_6^{2+} , which all have two similar pockets. Besides Table 5.2 that lists selected angles and distances, an overlay of the three cores was created to visualize the structural differences (Fig. 5.14). The $\text{meso}^{\text{pyr/pyr}}$ distance is more relaxed in LH_6^{2+} than in both dinuclear metal complexes. Hence, metal complexation induces a steric switch toward a higher degree of square planarity within the cavities, which results in an overall more distorted

Fig. 5.14 Overlay of the cores of LH_6^{2+} (gray), LCu_2 (cyan blue) and LNi_2 (green)



molecule. Distortion comes along with decreasing metal ion size (ionic radii of Ni^{II} : 0.63 and Cu^{II} : 0.71 Å) [4]. The smaller the metal radii are, the shorter is the pitch, the shorter is the observed metal-metal separation and the shorter are the M – N bonds. A higher distortion due to nickel complexation was also observed in porphyrin chemistry and was listed as one out of four fundamental factors that originated distortion (Sect. 4.1.3). Although the ligand gets deformed upon metal complexation, the bond lengths within the ligand scaffold remain the same. The higher distortion in LNi_2 is indicative of an enhanced strain and explains why heating is required during its preparation.

5.3.2 pH Dependency

LH_2Ni includes one metal-free pocket with two non-protonated nitrogen atoms and thus protonation studies were performed similar to the free ligand LH_4 . To ensure a neutral starting material, LH_2Ni was stirred over Na_2CO_3 in a mixture of MeOH and CH_2Cl_2 over night to isolate the neutral form after column chromatography. Ni^{II} with its d^8 configuration, bound in a square planar fashion, is diamagnetic, thus allowing NMR spectroscopic investigations. UV-vis and NMR spectroscopy were chosen to study the pH dependency of LH_2Ni via titration with TFA.

Changes in the UV-vis spectrum during the TFA titration of LH_2Ni were observed up to one equivalent of TFA (Fig. 5.15). Thus UV-vis spectroscopy suggests a species of LH_3Ni^+ . With time, decomposition was observed and the sample turned orange/brown.

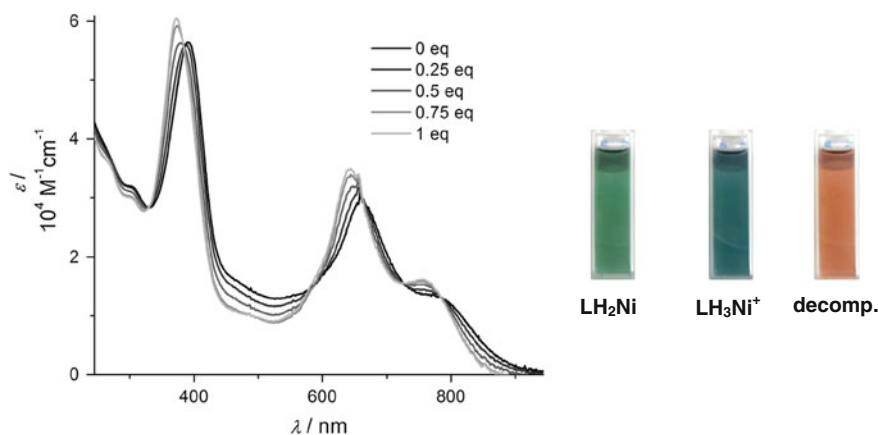


Fig. 5.15 *Left:* pH titration of LH_2Ni in CH_2Cl_2 with TFA followed by UV-vis spectroscopy. *Right:* Photographs of cuvettes filled with solutions of LH_2Ni , LH_3Ni^+ and their decomposition product

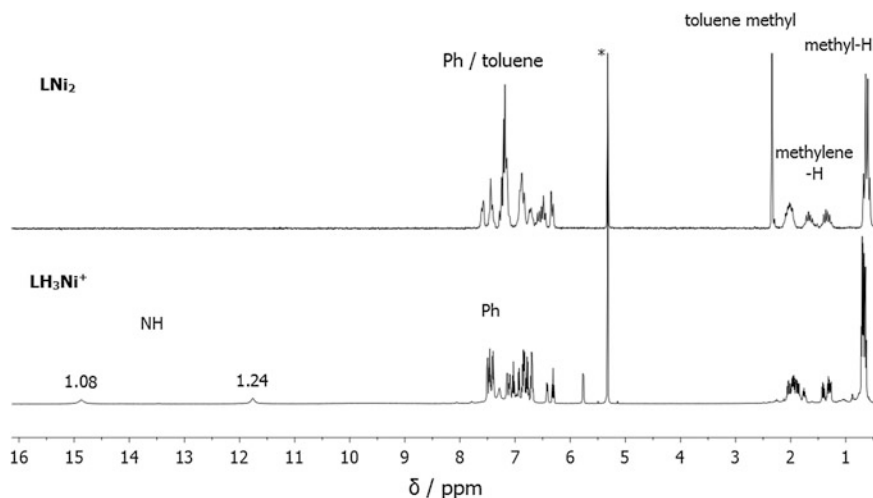


Fig. 5.16 *Top:* ¹H NMR spectrum (200 MHz, CD₂Cl₂) of LNi₂; *bottom:* ¹H NMR spectrum (500 MHz, CD₂Cl₂) of LH₃Ni⁺. The asterisk marks the residual proton signals of CD₂Cl₂

Following the titration experiment with NMR spectroscopy, changes were observed up to an addition of two equivalents of TFA and the final spectrum is depicted in Figs. 4.10 and 5.16. For NMR spectroscopic investigation, a drop of TFA/CD₂Cl₂ stock solution was added to the sample in the NMR tube, but the moment the TFA solution reached the surface of the LH₂Ni sample, LH₂Ni decomposed due to the local acidic excess and turned orange/brown as observed in UV-vis spectroscopy.

The need of two equivalents in the titration reaction using NMR spectroscopy is contradictory to one required TFA equivalent using UV-vis spectroscopy as the detection method. UV-vis measurements were not as strongly affected by decomposition reactions as NMR measurements, because UV-vis is a faster detection technique and local TFA excess was reduced because cuvettes were shaken immediately after addition of the TFA stock solution. Thus, data collected from UV-vis experiments are more reliable and LH₃Ni⁺ is assumed to be the species in NMR spectroscopic investigations as well.

The NMR spectrum of LH₃Ni⁺ shows C₂ symmetry (Fig. 5.16) which is proven by two NH signals in the downfield region but more significantly in its ¹³C NMR spectrum. A two-fold symmetry of LH₃Ni⁺ can solely exist, when the pyrazole proton scrambles to make both sides chemically equivalent on the NMR time scale. In contradiction with the assumed scrambling is the observed temperature-independency of the spectrum. ¹H¹⁵N-NMR spectroscopy could not be performed due to extreme broadening of the NH resonances. Attempts to obtain line sharpening at higher or at lower temperatures failed. Hence, the exact assignment of the NH signals is lacking. Integration of the two NH resonances proves a ratio of 1.08:1.24 which is neither in accordance with a 1:1 nor a 1:2 ratio but broadening is known to impede a correct integration.

The recorded spectra of LNi_2 are similar to the ones recorded of LH_6^{2+} with an excess of TFA (Fig. 5.16). Both molecules exhibit D_2 symmetry in solution and hence only two distinct triplet signals at 0.60 and 0.64 ppm are observed. While in LH_6^{2+} with an excess of TFA, the pseudo D_2 symmetry derives from the fast exchange rate of the NH^{Pz} protons with TFA dependent on the amount of TFA and on temperature, LNi_2 is intrinsically D_2 symmetric. For NMR measurements crystals were taken with proven analytical purity. The singlet at 2.34 ppm and the multiplet between 7.07 and 7.25 ppm result from toluene molecules incorporated in the crystal lattice (four molecules per molecule LNi_2).

In both cases, LNi_2 and LH_3Ni^+ , NMR spectra underline the twisted geometry. A stacked representation of the two spectra demonstrates the higher symmetry of LNi_2 . In the downfield region of the spectrum of LNi_2 , the NH resonances vanished upon metal complexation.

5.3.3 MCD Spectroscopy

Due to the universality of the Faraday effect, LNi_2 complex shows MCD intensity, but much weaker than LCu_2 . The measured MCD spectrum fits well to its absorption spectrum which seems to consist of overall 11 bands (Fig. 5.17).

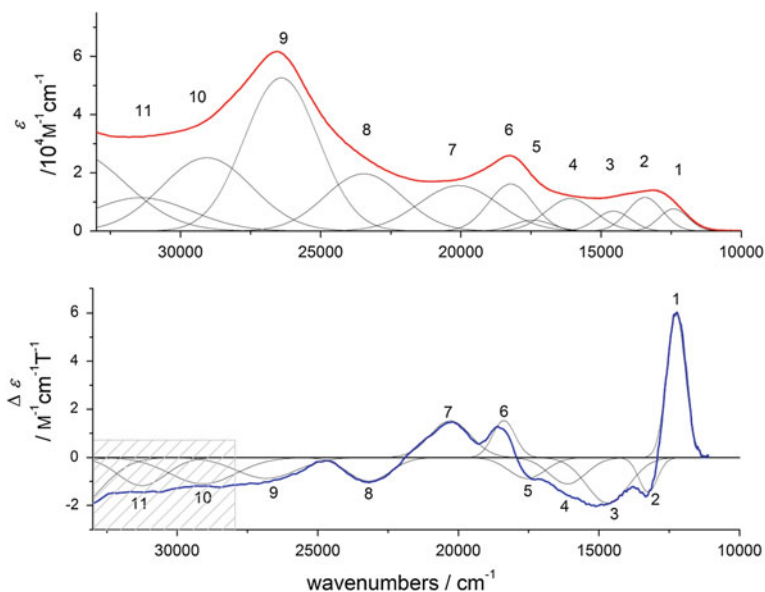


Fig. 5.17 Top: UV-vis spectrum of LNi_2 plotted against wavenumbers. Bottom: MCD spectrum measured in PS at 5.1 K. The gray box highlights inconclusive MCD data due to baseline shifting. The solid black lines represent a correlated fit of these data

The UV–vis absorption and MCD spectra were deconvoluted using PeakFit. As in **LCu₂**, band 9 does not show any metal-induced contribution, and it does not contribute to a pseudo A-term signal (zero crossing), which is a sign of a non-degenerate excited state. This is further in agreement with the non-aromatic nature of the ligand itself and its complexes. In porphyrins, the Soret- and Q-band excited states that originate from $\pi^* \leftarrow \pi$ transitions of the delocalized π -system are usually two-fold degenerate with E_u symmetry (in approximate D_{4h} symmetry). The gray box in Fig. 5.17 indicates a spectral region in the MCD data that is somewhat less reliable due to problems with baseline shifting. Band 1 is too intense to originate from a $d \leftarrow d$ transition but cannot be assigned a priori. No change of intensity was observed in temperature-dependent MCD measurements. This clearly mirrors the diamagnetic properties of **LNi₂** and with that, MCD spectroscopy is in line with all other applied methods.

5.3.4 Chiral Resolution

The attempt to separate the two helical enantiomers of **LH₂Ni** was abandoned and it was focused on **LNi₂**. For the chiral separation of **LNi₂** the same conditions were applied and the same function and basis sets used for calculations as for **LCu₂**. **LCu₂** and **LNi₂** show almost the same CD curves. The main difference is reduced to the *P*-enantiomer being the faster eluting enantiomer for **LCu₂** but slower in the case of **LNi₂**. Furthermore, the UV and CD detectors were set to slightly different wavelengths with 375(UV) and 388(CD) nm for the **LNi₂** and 400 nm for **LCu₂** (Fig. 5.18).

5.4 Heterobimetallic Copper(II) Nickel(II) Complex LCuNi

Crystals of **LCuNi** were obtained according to the described procedure but good X-ray data are pending. Many crystals were not monocrystalline. For those which scattered well it was impossible to distinguish between copper and nickel ions due to a statistical population of the two pockets.

5.4.1 Magnetic Properties

The crystals were still useful to guarantee the purity of the samples. Especially in susceptibility measurements this is a requirement, as the magnetic moment μ correlates with the amount of paramagnetic substance.

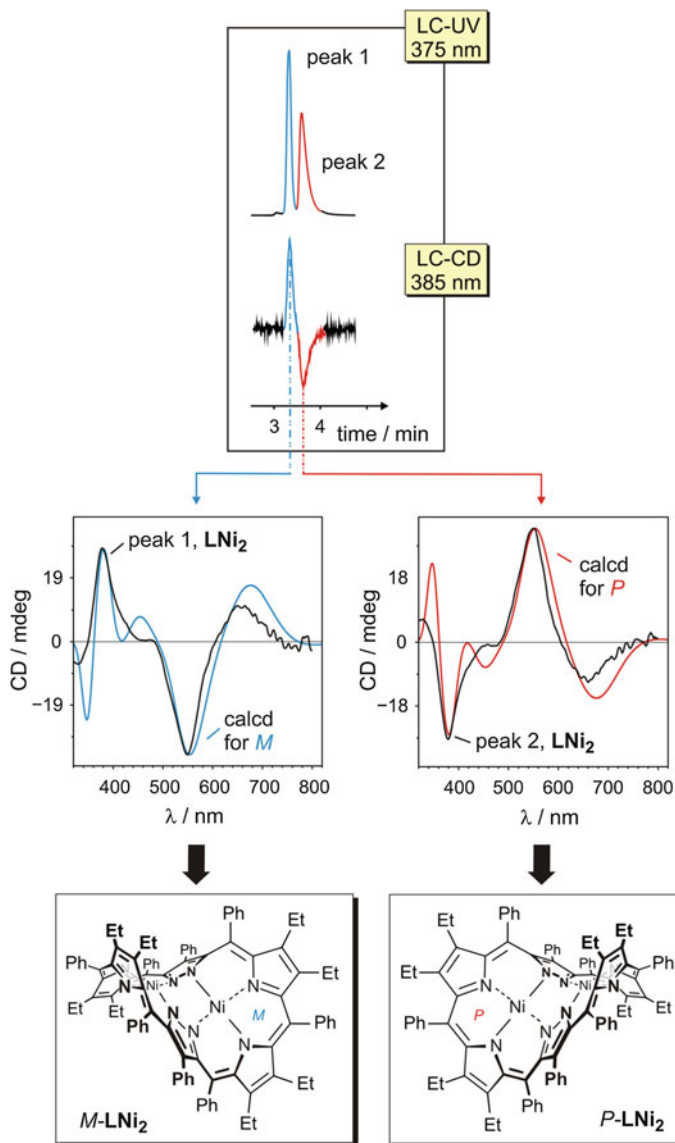
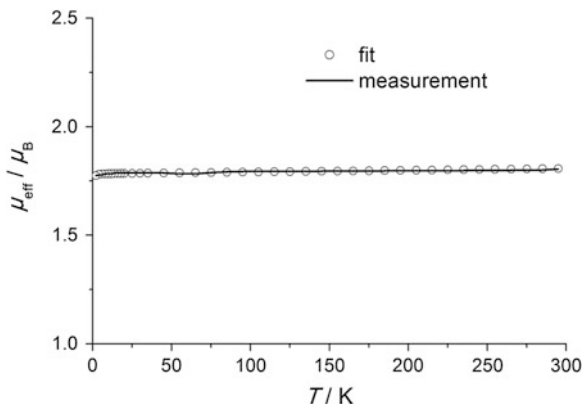


Fig. 5.18 Results of the HPLC separation of a racemic mixture of LNi_2 on a chiral phase (Chiralpak® IB, ambient temperature, ethyl acetate/*n*-hexane (v/v) 1:1, isocratic flow rate: $1.5 \text{ mL} \times \text{min}^{-1}$) and stereochemical assignment of the two enantiomers by comparison of the experimental CD spectra with the computed curves. Copyright Wiley-VCH Verlag GmbH & Co. KGaA. Reproduced with permission [38]

The SQUID measurement gave the theoretical value of $1.73 \mu_{\text{B}}$ for the effective magnetic moment according to Eq. 5.1 and thereby the presence of only one unpaired electron is proven (Fig. 5.19). Elemental analysis revealed the

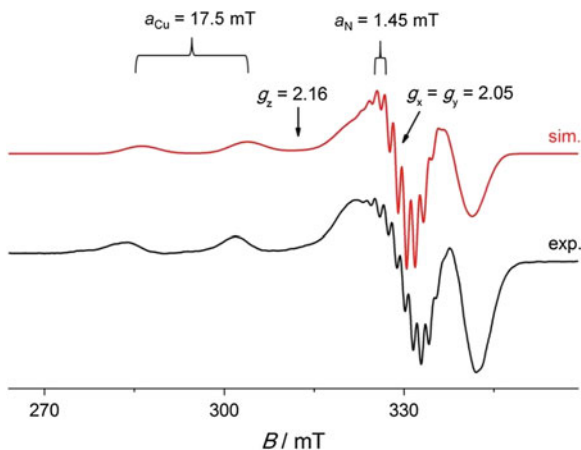
Fig. 5.19 Plot of μ_{eff} versus T for **LCuNi** (magnetic field of 0.5 T from 295 to 2.0 K); experimental data (○) and calculated curve fit (—)



incorporation of four toluene molecules per **LCuNi** molecule. The low magnetic moment but high molecular weight required a relatively large amount of material and additionally an accurate diamagnetic correction to obtain reliable values. Diamagnetic correction was performed applying the increment method using the tables of Pascal constants [17, 36, 37].

EPR spectroscopy showed a classic axial copper-centered signal with $g_x = g_y < g_z$. The spectrum was measured at 150 K in CH_2Cl_2 as a frozen glass. An electron localized on one copper nucleus results in a four line spectrum due to coupling to the nuclear spin of $I = 3/2$ for both copper isotopes ^{63}Cu and ^{65}Cu ($2nI + 1$ lines, $n =$ number of nuclei). The hyperfine coupling resolution to the copper nucleus is limited to z direction and amounts to 17.5 mT. The nine super hyperfine signals in x and y direction state a super hyperfine coupling to four nitrogen atoms ($I_{\text{N}} = 1$) located in the x, y plane and reveal the unpaired electron to sit in the $d_{x^2-y^2}$ orbital with a coupling constant of 1.45 mT. The simulation was run with g values of 2.05 for g_x and g_y and 2.16 for g_z (Fig. 5.20).

Fig. 5.20 EPR spectrum (experimental and simulation) of **LCuNi** at 150 K in CH_2Cl_2 as a frozen glass



References

1. N.N. Greenwood, A. Earnshaw, *Chemistry of the Elements*, 2nd edn. (Butterworth-Heinemann, Amsterdam, 1997)
2. H. Irving, R.J.P. Williams, *Nature* **162**, 746–747 (1948)
3. H. Irving, R.J.P. Williams, *J. Am. Chem. Soc.* **1953**, 3192–3210
4. A.F. Holleman, N. Wiberg, *Lehrbuch der Anorganischen Chemie*, 102nd edn. (Walter de Gruyter, Berlin, 2007)
5. N. Wheatley, P. Kalck, *Chem. Rev.* **99**, 3379–3420 (1999)
6. E.K. van den Beuken, B.L. Feringa, *Tetrahedron* **54**, 12985–13011 (1998)
7. P.A. Shapley, N. Zhang, J.L. Allen, D.H. Pool, H.-C. Liang, *J. Am. Chem. Soc.* **122**, 1079–1091 (2000)
8. K. Severin, *Chem. Eur. J.* **8**, 1514–1518 (2002)
9. D.W. Stephan, *Coord. Chem. Rev.* **95**, 41–107 (1989)
10. Y. Yang, K.A. Abboud, L. McElwee-White, *Dalton Trans.* **22**, 4288–4296 (2003)
11. E. Riedel, *Moderne Anorganische Chemie*, 3rd edn. (de Gruyter, Berlin, 2009)
12. J. Klingele, S. Dechert, F. Meyer, *Coord. Chem. Rev.* **253**, 2698–2741 (2009)
13. A.L. Gavrilova, B. Bosnich, *Chem. Rev.* **104**, 349–384 (2004)
14. N.M. Atherton, *Principles of Electron Spin Resonance* (Ellis Horwood PTR Prentice Hall, New York, 1993)
15. K. A. Sandberg, Ph.D. thesis, *Theoretical Investigations of Spin-Spin Interactions: Semiempirical Estimations of the Exchange Parameter for Diradical Metalloporphyrin Cations and Zero Field Splitting Parameter for Conjugated Diradicals* (NC State University, 1998)
16. P.W. Atkins, *Physikalische Chemie*, 3rd edn. (WILEY-VCH, Weinheim, 2001)
17. O. Kahn, *Molecular Magnetism* (Wiley-VCH, Weinheim, 1993)
18. L.K. Frensch, K. Pröpper, M. John, S. Demeshko, C. Brückner, F. Meyer, *Angew. Chem. Int. Ed.* **50**, 1420–1424 (2011)
19. D. Ajo, A. Bencini, F. Mani, *Inorg. Chem.* **27**, 2437–2444 (1988)
20. V.P. Hanot, T.D. Robert, J. Kolnaar, J.P. Haasnoot, J. Reedijk, H. Kooijman, A.L. Spek, *J. Chem. Soc. Dalton Trans.* **22**, 4275–4281 (1996)
21. H. Matsushima, H. Hamada, K. Watanabe, M. Koikawa, T. Tokii, *J. Chem. Soc., Dalton Trans.* 971–977 (1999)
22. W. Plass, *Chem. Unserer Zeit* **32**, 323–333 (1998)
23. T.-L. Hu, J.-R. Li, C.-S. Liu, X.-S. Shi, J.-N. Zhou, X.-H. Bu, J. Ribas, *Inorg. Chem.* **45**, 162–173 (2005)
24. J. Teichgräber, G. Leibelng, S. Dechert, F. Meyer, *Z. Anorg. Allg. Chem.* **631**, 2613–2618 (2005)
25. R.S. Drago, *Physical Methods for Chemists*, 2nd edn. (Saunders College Publishing, New York, 1992)
26. T. Ohnishi, *Biochimica et Biophysica Acta (BBA) - Bioenergetics* **1364**, 186–206 (1998)
27. X. Liu, J.A. McAllister, M.P. de Miranda, E.J.L. McInnes, C.A. Kilner, M.A. Halcrow, *Chem. Eur. J.* **10**, 1827–1837 (2004)
28. M. Heichel, P. Höfer, A. Kamlowski, M. Griffin, A. Muys, C. Noble, D. Wang, G.R. Hanson, C. Eldershaw, K.E. Gates, K. Burrage, *Bruker Report* **148**, 6–9 (2000)
29. D. Meschede, *Gerthsen Physik*, 23rd edn. (Springer, Berlin, 2006)
30. M.K. Johnsons, in *Physical Methods in Bioinorganic Chemistry*, ed. by J. Lawrence Que (University Science Books, Sausalito, 2000)
31. M.G.I. Galinato, T. Spolitat, D.P. Ballou, N. Lehnert, *Biochemistry* **50**, 1053–1069 (2010)
32. J. Mack, M.J. Stillman, N. Kobayashi, *Coord. Chem. Rev.* **251**, 429–453 (2007)
33. J.-J. Girerd, Y. Journaux, ed. by J. Lawrence Que (University Science Books, Sausalito, 2000)
34. R. Krishnan, J.S. Binkley, R. Seeger, J.A. Pople, *J. Chem. Phys.* **72**, 650–654 (1980)
35. K. Raghavachari, G.W. Trucks, *J. Chem. Phys.* **91**, 2457–2460 (1989)

36. B. Dittrich, T. Koritsánszky, P. Luger, *Angew. Chem. Int. Ed.* **43**, 2718–2721 (2004)
37. C.J. O'Connor, *Prog. Inorg. Chem.* **29**, 203–283 (1982)
38. G.A. Bain, J.F. Berry, *J. Chem. Educ.* **85**, 532 (2008)
39. L.K. Blusch, Y. Hemberger, K. Pröpper, B. Dittrich, F. Witterauf, M. John, G. Bringmann, C. Brückner, F. Meyer, *Chem. Eur. J.* **19**, 5868–5880 (2013)
40. B. Dittrich, C.B. Hübschle, M. Messerschmidt, R. Kalinowski, D. Girnt, P. Luger, *Acta Crystallogr. Sect. A Found. Crystallogr.* **A61**, 314–320 (2005)
41. B. Dittrich, C.B. Hübschle, P. Luger, M.A. Spackman, *Acta Crystallogr. Sect. D Biol. Crystallogr.* **D62**, 1325–1335 (2006)
42. L.K. Blusch, K.E. Craigo, V. Martin-Diaconescu, E. Bill, A. B. McQuarters, S. Dechert, S. DeBeer, N. Lehnert, F. Meyer, *J. Am. Chem. Soc.* DOI:[10.1021/ja406176e](https://doi.org/10.1021/ja406176e)

Chapter 6

Redox Properties

Inspired by nature, the Siamese-twin porphyrin system was designed to comprise unique redox properties. The free ligand itself does not show any reversible redox processes as was investigated in Sect. 4.4. In this Chapter, the redox chemistry of the synthesized metal complexes is presented, which turned out to be much more promising. First, a short comparative overview is given, then detailed redox properties of each complex are discussed.

Redox properties were electrochemically investigated using CV measurements. The same experimental setup as in Sect. 4.4 was used. Upon complexation, well defined voltammograms were obtained (Fig. 6.1). While the CV curve for **LCu₂** reveals overall six redox waves between -2.5 and 1.3 V, for **LCuNi** and **LNi₂** only five redox waves are observed with a broad band at highest potential. For all three bimetallic complexes only the signals in the region marked with the red rectangles (Fig. 6.1) appear electrochemically reversible according to the reversibility criteria defined in Sect. 4.4. In the blue highlighted region only the half wave potentials for the homobimetallic complexes seem to be electrochemically reversible. **LCu₂** is oxidized more easily than **LNi₂** according to the redox half wave potentials of -0.26 versus -0.05 V, respectively (Fig. 6.1, red highlighted region). Comparing the red highlighted region of the spectrum of **LCuNi** with the ones for the homobimetallic complexes, the first oxidation wave occurs at similar potential as in **LCu₂** ($E_{1/2} = -0.23$ V vs. $E_{1/2} = -0.26$ V) whereas the half wave potential of the second oxidation resembles the second observed half wave potential in the red highlighted region for **LNi₂** ($E_{1/2} = 0.35$ vs. 0.41 V).

Further electrochemical methods including differential pulse voltammetry such as square wave voltammetry (SWV) and bulk electrolysis were carried out, which are discussed in the following sections but general information is placed here. In SWV a square wave is superimposed on the potential staircase sweep, which minimizes capacitive charging currents. Thus SWV is more sensitive than CV and the comparison of peak areas offers valuable information about the relative number of transferred electrons. Bulk electrolysis is not limited to the barrier layer but the complete solution is oxidized or reduced. To enhance the surface, the glassy carbon electrode is replaced by a platinum net electrode and the solution is stirred. Bulk electrolysis reveals the absolute number of transferred electrons when the

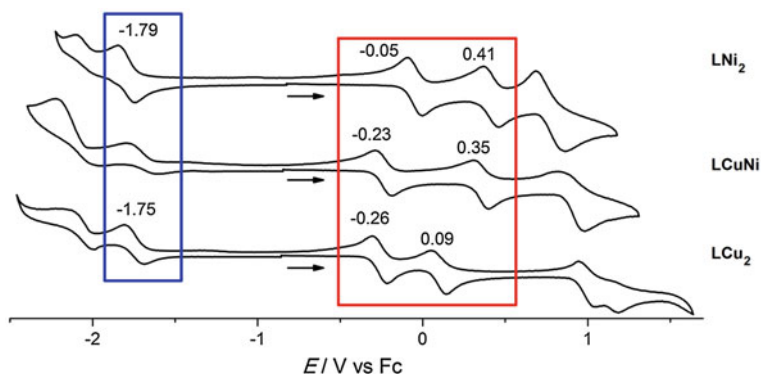


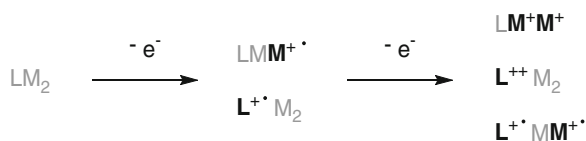
Fig. 6.1 CV curves of the synthesized bimetallic complexes **LNi₂**, **LCuNi** and **LCu₂** were measured in CH₂Cl₂ with [NBu₄]PF₆ as an electrolyte and plotted versus Fc as an internal standard. The zone with reversible processes is highlighted in red and blue. Half-wave potentials ($E_{1/2}$) are indicated in Volts

accurate amount of substance is known. Additionally, bulk electrolysis is a useful electrochemical method for preparation of the different redox species in small scale, which then can be investigated using spectroscopic methods. The reaction was monitored by UV–vis spectroscopy with a quartz immersion probe, which was inserted in the electrochemical cell. Chemical reversibility can be checked in bulk electrolysis experiments, in which the time scale is longer than in CV experiments and redox processes are not limited to the barrier layer. In the case of chemical reversibility, oxidation and subsequent reduction or vice versa of the sample solution should give the initial UV–vis spectrum.

Assuming the non-innocence of the Siamese-twin porphyrin, each redox process can either be metal or ligand-centered (Scheme 6.1). To determine the site of oxidation or reduction, EPR spectroscopy is a helpful tool by evaluating the g values and hyperfine coupling parameters. Great caution is needed in interpreting the data, because neglected antiferromagnetic coupling might be misleading concerning the localization of unpaired electrons. Labelling of the oxidized or reduced species will be written as **LM₂^{charge}**, which is descriptive of the redox state but does not evoke information about the localization of the redox process.

For example the oxidation chemistry of nickel(II) β -diketiminato (NacNac) was investigated by Khusniyarov and Wieghardt et al. First assuming a metal-centered oxidation process, neat evaluation of EPR and SQUID data of the oxidized state revealed the existence of a NacNac radical ($S = 1/2$) and a nickel(II), which are strongly antiferromagnetically coupled [1].

Scheme 6.1 General visualization of different oxidation possibilities. The particular oxidation center is marked in *black* and *bold*

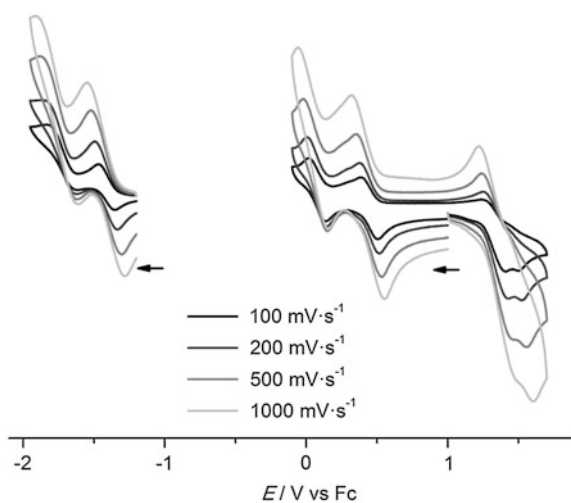


A chemical synthetic approach to the oxidized or reduced species is desirable to obtain quantitative amounts of pure substance. With more material in hand, additional experiments can be conducted to finally answer the question of redox site. Next to the already introduced techniques such as UV-vis, NMR, EPR spectroscopy, X-ray diffractometry and susceptibility measurements, also X-ray absorption spectroscopy should provide information about the oxidation level of the metal ions itself. DFT calculations performed by our collaborator Lehnert at the University of Michigan are still pending.

6.1 Dicopper Complex

The dicopper(II) complex of the Siamese twin porphyrin shows six redox waves in its voltammogram at half wave potentials of $E_{1/2} = -1.75, -0.26$ and 0.09 V for the three electrochemical reversible redox steps and half waves at $E_p^{ox} = -2.00, 1.04$ and 1.18 V and $E_p^{red} = -2.14, 0.95$ and 1.15 V (Figs. 6.1 and 6.3). The CV curve of **LCu₂** was recorded at different scan rates of 100, 200, 500 and 1000 $\text{mV}\cdot\text{s}^{-1}$ (Fig. 6.2). While it is confirmed, that half waves at $E_p^{ox} = -2.00, 1.04$ and 1.18 V and $E_p^{red} = -2.14, 0.95$ are electrochemically irreversible, waves at $E_{1/2} = -1.75, -0.26$ and 0.09 V are electrochemically reversible. SWV measurements show that the signals between 0.95 and 1.18 V merge into one large wave with a small shoulder. This peak area is slightly larger than each of the other four peak areas, which are of approximately the same magnitude and are assumed to be one-electron redox processes. Thus, the merged signal refers most likely to a one electron redox process with a consecutive decomposition reaction. Contamination with impurities can be ruled out because crystalline material was used and

Fig. 6.2 CV curves of **LCu₂** in CH_2Cl_2 with $[\text{NBu}_4]\text{PF}_6$ as an electrolyte at scan rates of 100, 200, 500 and 1000 $\text{mV}\cdot\text{s}^{-1}$. Reproduced with permission [45]. Copyright (2013) American Chemical Society



its purity was confirmed by elemental analysis. Furthermore, these results were reproducible with different batches. Overall five one-electron redox processes are observed. The first one-electron oxidation would lead to LCu_2^+ and further oxidation to LCu_2^{2+} and LCu_2^{3+} . Reduction on the opposite would lead to LCu_2^- and LCu_2^{2-} . For reasons of clarity a color code is used for the different redox species, which does not reflect the authentic colors: The starting material LCu_2 is light blue, LCu_2^+ dark blue, LCu_2^{2+} purple and LCu_2^{3+} pink, while LCu_2^- is green and LCu_2^{2-} black (Fig. 6.3, top, left). The authentic colors are too similar to use these for assignment. The comproportionation constant K_c for LCu_2^+ was calculated as $9.5 \cdot 10^5$ from half wave potentials according to: [2, 3]

$$K_c = \exp\left[\frac{n \cdot F}{RT} \cdot (E_2 - E_1)\right] \quad (6.1)$$

with F as Faraday constant, R as gas constant, T as temperature, n as the number of transferred electrons and E_2 and E_1 as half-wave potentials. The magnitude of K_c refers to the thermodynamic stability and thus, LCu_2^+ is supposed to be

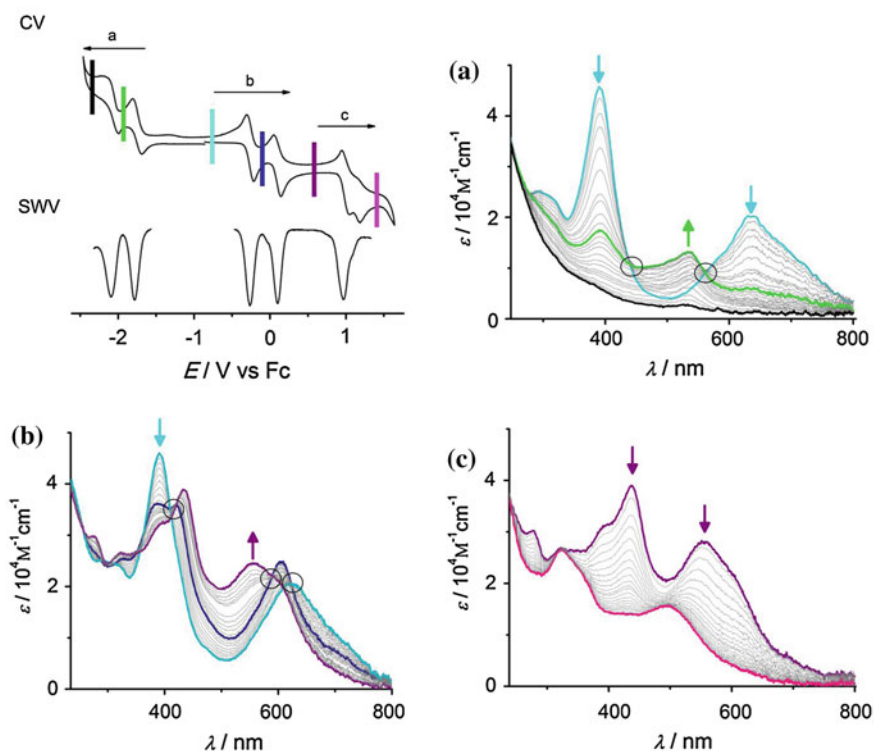


Fig. 6.3 Top left CV curve and SWV of LCu_2 in CH_2Cl_2 with $[\text{NBu}_4]\text{PF}_6$ as an electrolyte. The electrochemistry was followed using UV-vis spectroscopy (a–c). Black circles indicate isosbestic points. Reproduced with permission [45]. Copyright (2013) American Chemical Society

thermodynamically stable. Any kind of electronic coupling in LCu_2 is assured, as otherwise the two symmetrical centers would undergo oxidation at approximately the same potential.

6.1.1 Electrochemical Oxidation/Reduction

Redox processes were examined using bulk electrolysis and are labelled with (a), (b) and (c). The spectroelectrochemical investigations showed enormous changes in the UV–vis spectra upon reduction or oxidation (Fig. 6.3 and Table 6.1).

- (a) The one-electron reduction (light blue to green) leads to a decrease in the absorption bands at 391 and 629 nm, while a band at 535 nm appears. Isosbestic points are apparent indicative of a direct conversion [4]. The second reduction to LCu_2^{2-} (black) resulted in an almost complete extinction of absorption to featureless bands and no isosbestic points were observed. The fact of an almost non-absorbing featureless spectrum is most likely an evidence of decomposition reactions.
- (b) The one-electron oxidation (light blue to dark blue, LCu_2 to LCu_2^+) shows a decrease of λ_{max} and a new band is formed at 421 nm. A shift in the absorption bands at 629–605 nm and at 306–325 nm is observed. The substance is still greenish colored. Isosbestic points are suggestive of a direct conversion. The following oxidation (dark blue to purple, LCu_2^+ to LCu_2^{2+}) shows isosbestic points as well. A blue shift of the band at 605–556 nm with a remaining shoulder at 593 nm is observed. λ_{max} is located at 433 nm with a shoulder at 395 nm. The substance turns brown-black upon the second oxidation.
- (c) In the UV–vis spectra for the transformation from LCu_2^{2+} to LCu_2^{3+} (purple to pink) no obvious intermediate is formed in line with SWV measurements. The existing signals disappear and new signals arise at 324 and 495 nm. No isosbestic points are observed.

Besides the application of electrochemical reversibility criteria, chemical reversibility was tested by oxidizing and subsequent reducing the solution. Ending up with the initial UV–vis spectrum points to a reversible reaction. To obtain a complete reduction or oxidation, the supply of an overpotential is recommended,

Table 6.1 Wavelengths and extinction coefficients of all LCu_2 species in CH_2Cl_2

	LCu_2^{2-}	LCu_2^-	LCu_2	LCu_2^+	LCu_2^{2+}	LCu_2^{3+}
	Descending	391 (1.7)	306 (2.6)	325 (2.5)	276 (2.9)	324 (2.2)
	From	535 (1.5)	391 (4.6)	388 (3.6)	322 (2.6)	495 (1.3)
λ/nm	262 (2.8)		629 (2.2)	421 (3.6)	395 (3.2)	
$(\epsilon/10^4\text{M}^{-1}\text{cm}^{-1})$	to 620 (0)			605 (2.5)	433 (3.9)	
					556 (2.4)	
					593 (2.2)	

as this would shift the redox equilibrium completely toward the desired products [5]. With overpotentials of 0.118, 0.236, and 0.354 V stoichiometric ratios of 10:1, 100:1, and 1000:1 respectively are obtained.

- (a) First the reduction reaction toward LCu_2^+ was examined. Bulk electrolysis was performed as described and the potential set to -1.9 V. The peak separation does not allow the use of an overpotential. However, the CV signal matches the criteria for electrochemical and chemical reversibility on the CV time scale, oxidation and subsequent reduction did not merge in the initial UV-vis spectrum, and thus was proven to be chemically irreversible. With that chemical reversibility investigations on the second reduction became unnecessary.
- (b) The two-electron oxidation reaction from LCu_2 to LCu_2^{2+} (light blue to dark blue to purple) was tested in one step. The potential was set to 0.5 V and the oxidation and subsequent reduction led to the initial UV-vis spectrum of LCu_2 . Several cycles of oxidation and re-reduction verified a complete chemical reversibility. A reduction of LCu_2^{2+} back to LCu_2 was observed to occur upon long-time exposure to ambient conditions. What acted as the reductant in this case, remained unclear.
- (c) The last oxidation step (purple to pink) was chemically irreversible on the time scale of bulk electrolysis and in line with CV and SWV data.

In summary, the proposed electrochemically reversible one-electron waves highlighted in red in Fig. 6.1 are also chemically reversible processes in the case of LCu_2 . Large peak separation shows a thermodynamically stable compound with $K_c = 9.5 \cdot 10^5$ observed for LCu_2^+ . Samples of each redox species were taken from the reaction mixture of bulk electrolysis, in which the inevitable electrolyte is still present and immediately frozen in liquid nitrogen. EPR spectroscopy is not affected by the presence of an electrolyte and was chosen as the method for first spectroscopic investigation. LCu_2 was proven to have a paramagnetic ground state with two unpaired electrons. Thus, LCu_2^- , LCu_2^+ and LCu_2^{3+} are predicted to be EPR active. LCu_2^{2+} was proven to be EPR silent, and unexpectedly, LCu_2^- and LCu_2^{3+} were EPR silent as well, most likely due to decomposition. The EPR spectrum of LCu_2^+ is discussed later in Sect. 6.1.3.

6.1.2 Chemical Oxidation

For spectroscopic investigation using other methods besides EPR, it is advantageous to avoid using an electrolyte. Thus, a chemical oxidant is favorable to generate pure samples in reasonable amounts. Because the reversibility is most attractive, the isolation of the oxidized species LCu_2^+ and LCu_2^{2+} is aspired.

Formal standard potentials of oxidizing agents are tabulated versus. Fc [5]. The most convenient synthetic strategy toward LCu_2^+ is to use an oxidizing agent of a potential between -0.26 and 0.09 V and one between 0.35 V and 0.90 V to

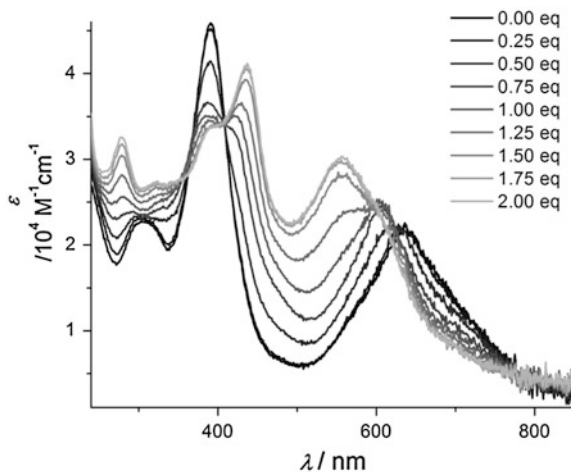
synthesize LCu_2^{2+} . The oxidizing agent should be easy to remove after the completion of the oxidation reaction and commercial availability is advantageous. With a formal potential of -0.14 mV for I_2 and of 0.0 mV for Fc^+ these oxidants were tested. Their reduced products are soluble in aqueous solution and due to the non-polarity of LCu_2 their removal is uncomplicated. The oxidation toward LCu_2^+ failed using I_2 or Fc^+ , therefore the stronger oxidant AgBF_4 was used to obtain the first and second oxidized species. The redox potential of Ag^+ drastically depends on the solvent. While in acetonitrile its oxidative power is low ($E = 0.04$ V), it increases in acetone ($E = 0.18$ V), THF ($E = 0.41$ mV) and CH_2Cl_2 ($E = 0.65$ V) [5]. Acetonitrile would match perfectly for the synthesis of LCu_2^+ , but LCu_2 is insoluble in polar solvents including acetonitrile. Thus, the oxidation reaction had to be controlled via stoichiometry instead of potential.

A titration of LCu_2 in CH_2Cl_2 with a 0.1 M stock solution of AgBF_4 in nitroethane was followed using UV–vis spectroscopy (Fig. 6.4). AgBF_4 dissolves in nitroethane, which is soluble with CH_2Cl_2 . The recorded UV–vis spectra were compared to the UV–vis spectra obtained by electrochemical oxidation and are similar. Differences in the region from 230 to 380 nm result from the intrinsic absorption of nitroethane (380 nm). The titration of exactly two equivalents AgBF_4 toward LCu_2^{2+} confirms that waves in the CV and SWV represent two one-electron oxidations.

To synthesize quantitative amounts, the reaction was scaled up to 40 mg of the starting material LCu_2 . LCu_2^+ was found to be stable at ambient conditions and the solvent was removed under reduced pressure. The substance was redissolved in CH_2Cl_2 and filtered using a membrane filter to remove the formed silver particles. For synthesis of LCu_2^{2+} an excess of AgBF_4 in CH_2Cl_2 was used followed by the same work-up.

A second route toward LCu_2^+ was realized via comproportionation of equimolar amounts of LCu_2 and LCu_2^{2+} . Following the second route did not reveal any

Fig. 6.4 Titration of LCu_2 in CH_2Cl_2 with a 0.1 M stock solution of AgBF_4 in nitroethane followed by UV–vis spectroscopy. The addition of one equivalent AgBF_4 gave LCu_2^+ , while the addition of two equivalents AgBF_4 gave LCu_2^{2+} . Reproduced with permission [45]. Copyright (2013) American Chemical Society

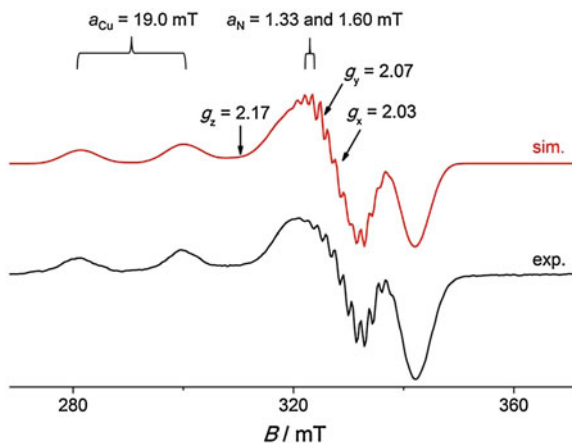


advantage as stoichiometry was required as well. Both, LCu_2^+ and LCu_2^{2+} have to be stored under inert conditions because reduction initiates with time at ambient conditions.

6.1.3 Localization of the Redox Center in LCu_2^+

LCu_2^+ was oxidized from LCu_2 with its two d^9 copper centers and the question of ligand versus metal-centered oxidation should be disclosed. Metal oxidation would introduce a switch from a d^9 to a d^8 configuration on one copper center leaving the system with one copper having a localized unpaired electron. Favoring the ligand-centered oxidation, the ligand turns into a radical. In the case of strong antiferromagnetic coupling of the ligand radical to one unpaired electron on the metal site, the system would also show one metal-centered unpaired electron. The EPR signal of the two discussed systems would be identical. Analysis of EPR samples generated from bulk electrolysis revealed the expected copper-localized unpaired electron (Fig. 6.5). The depicted EPR spectrum was recorded at 166 K and resembles the EPR spectrum recorded for LCuNi (Sect. 5.4.1). The unpaired electron couples to the nuclear spin of copper with a coupling constant of 19.0 mT, which results in a splitting in four lines. Only two out of four are well resolved. Due to anisotropy of the g values $g_x = 2.03$, $g_y = 2.07$, $g_z = 2.17$, the EPR signal is rhombic but appears axial because g_x and g_y are similar. Super hyperfine coupling was observed to four nitrogen atoms surrounding one copper center exhibiting coupling constants of $a_x = a_y = 1.33$ mT and $a_z = 1.60$ mT. The nine lines are well resolved in the x and y direction pointing to a localization of the unpaired electron in the $d_{x^2-y^2}$ orbital. A line width of 0.45 mT in x and y direction and 1.8 mT in z direction are anticipated. The simulation was fitted with Gaussian line shape. Thus, EPR spectroscopy established the success of the one electron oxidation.

Fig. 6.5 EPR spectrum of LCu_2^+ measured in CH_2Cl_2 at 166 K and its simulation in red. Reproduced with permission [45]. Copyright (2013) American Chemical Society



Mixed valence complexes carry two centers in different redox states such as $LM^{\text{II}}M^{\text{III}}$. In mixed valence compounds the unpaired electron can be localized (class I) or delocalized over both centers (class II or III) [6]. Most class II and III complexes are $Ru^{\text{II}}/Ru^{\text{III}}$ based dinuclear complexes [7] which are bridged via conjugated bidentate ligands [8, 9]. Besides dinuclear ruthenium-based complexes, delocalization was observed in dinuclear mixed valence iron, cobalt, osmium, rhenium, manganese and molybdenum complexes [10–14]. Among the many reported mixed valence dicopper complexes ($Cu^{\text{I}}Cu^{\text{II}}$) [15] some show delocalization as well [16–19]. Pyrazole is a suitable aromatic bidentate ligand to mediate the communication between two metal centers and thus some class II and class III dinuclear mixed valence pyrazolate bridged complexes were reported [20, 21]. An inter-valence charge transfer (IVCT) can be observed, which is a characteristic feature generally present in the near-IR region of the electronic absorption spectrum for class II and III mixed valence complexes [6, 22, 23]. Besides the photoinduced excitation, the IVCT can also be thermally induced and temperature-dependent EPR spectroscopy is a common tool to detect the phenomenon of electron delocalization between the two metal centers [17, 18]. Apart from the discussed metal to metal charge transfer (MMCT) IVCT are also observed for $L_1^+ \leftarrow L_2^+$ transitions when two differently oxidized ligands or ligand sites are present (LLCT) [24, 25].

In the product of ligand-centered oxidation of the dicopper complex $L^+Cu^{\text{II}}Cu^{\text{II}}$ a LLCT could be observed and in the case of metal-centered oxidation $LCu^{\text{II}}Cu^{\text{III}}$ a MMCT could be observed. The observation of an IVCT would neither point to a ligand- nor a metal-centered oxidation. A UV–vis spectrum covering the near-IR region was recorded (Fig. 6.6), but no defined IVCT band was observed. Additionally, variable-temperature EPR spectroscopy was performed to detect the thermally induced electron delocalization. In the case of delocalization, the electron switches from one copper ion to the other and would therefore couple to both copper ions on an EPR time scale and give a seven-line

Fig. 6.6 UV–vis–NIR spectrum of LCu_2^+ in CH_2Cl_2 . Typical IVCT region is highlighted. Reproduced with permission [45]. Copyright (2013) American Chemical Society

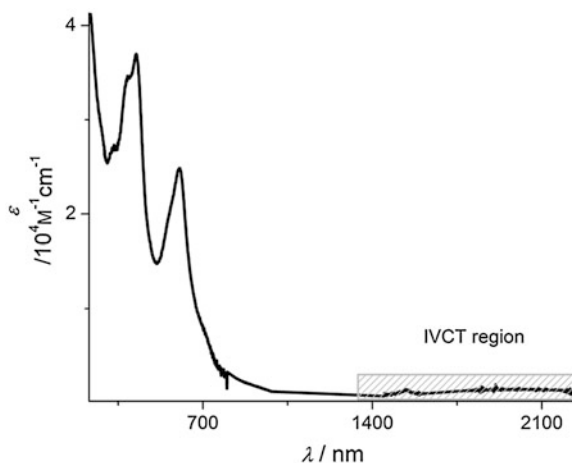
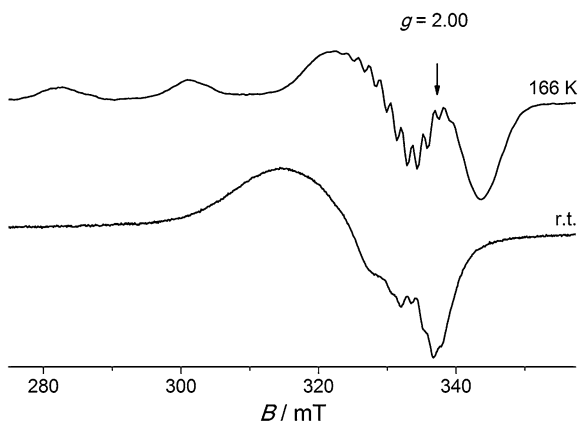


Fig. 6.7 EPR spectra of LCu_2^{2+} at r.t. and at 166 K in CH_2Cl_2 . Reproduced with permission [45]. Copyright (2013) American Chemical Society



copper hyperfine spectrum. While at low temperatures in many systems a localization is stated, with increasing temperature the intervalence electron transfer can be excited. An EPR spectrum at r.t. was recorded, but in line with UV–vis–NIR spectroscopy, no seven-line spectrum was observed (Fig. 6.7). The absence of an IVCT evidences a class I mixed valence compound. Due to the twisted geometry a communication between the two pockets is limited which is consistent with the spin localization. Despite much effort, neither UV–vis nor EPR spectroscopy could solve the mystery of redox localization in LCu_2^+ . X-ray absorption spectroscopy (XAS) experiments were not performed because absorption energies arising from Cu^{II} and Cu^{III} may overlap. Solely the pending DFT calculations are able to highlight the redox state of the ligand and its metal centers for LCu_2^+ .

6.1.4 Localization of the Redox Center in LCu_2^{2+}

The second oxidation toward LCu_2^{2+} can again be ligand- or metal-centered. Four different products are conceivable: $\text{LCu}^{\text{III}}\text{Cu}^{\text{III}}$, when one-electron oxidations occurred on both metal ions; $\text{L}^+\text{Cu}^{\text{III}}\text{Cu}^{\text{II}}$, when one one-electron oxidation was located on the ligand and the other on the metal center or $^{2+}\text{LCu}^{\text{II}}\text{Cu}^{\text{II}}$, or $^+\text{L}^+\text{Cu}^{\text{II}}\text{Cu}^{\text{II}}$ in the case of two ligand-centered oxidations, where $^{2+}\text{LCu}^{\text{II}}\text{Cu}^{\text{II}}$ represents the ligand, which is oxidized twice at the same position. While $^{2+}\text{LCu}^{\text{II}}\text{Cu}^{\text{II}}$ and $\text{LCu}^{\text{III}}\text{Cu}^{\text{III}}$ are intrinsically diamagnetic, $\text{L}^+\text{Cu}^{\text{III}}\text{Cu}^{\text{II}}$ and $^+\text{L}^+\text{Cu}^{\text{II}}\text{Cu}^{\text{II}}$ can only be diamagnetic upon strong antiferromagnetic coupling. The absence of any detected signal by EPR spectroscopy of samples generated from bulk electrolysis could be due to a diamagnetic sample or a large ZFS ($S \geq 1$).

NMR spectroscopy confirmed the diamagnetic nature of LCu_2^{2+} (Fig. 6.8). The NMR spectrum of LCu_2^{2+} is well-resolved and exhibits D_2 symmetry as only one quarter of the molecule is chemically inequivalent. The methyl proton resonances are visible at 0.67 and 0.69 ppm and the methylene protons at 1.63 and 2.15 ppm.

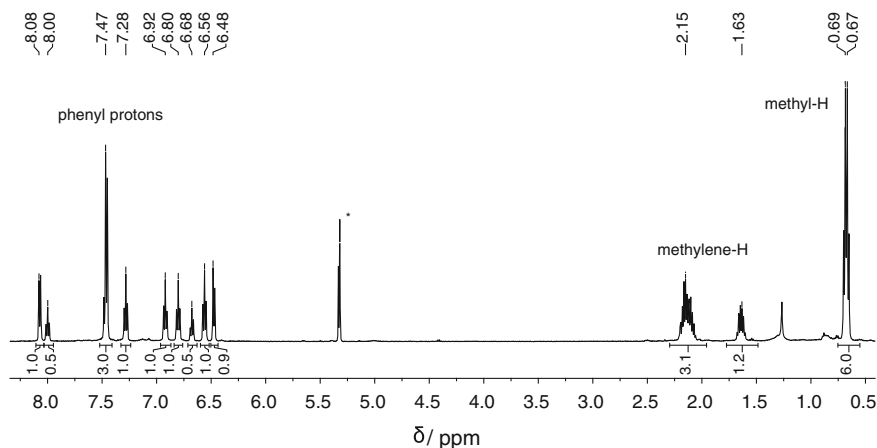
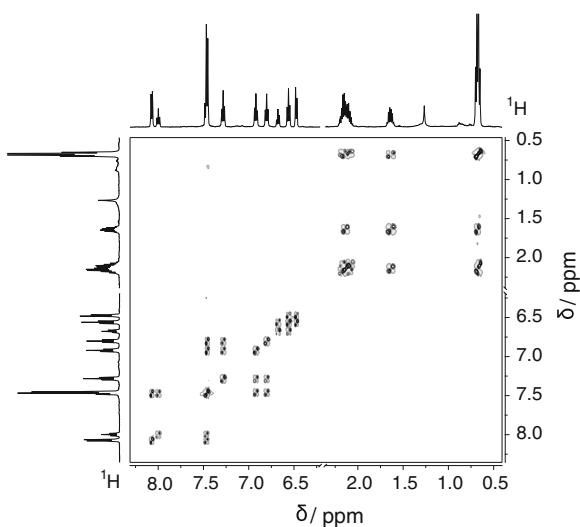


Fig. 6.8 ^1H NMR spectrum (500 MHz, CD_2Cl_2 , r.t.) of LCu_2^{2+} . The residual solvent signal is marked with an *asterisk*. Reproduced with permission [45]. Copyright (2013) American Chemical Society

Diastereotopicity for the methylene protons is anticipated, based on the above discussion of NMR spectra (Sect. 4.1.1) but it has not been proven because chemical shifts of the methyl protons are too similar to observe distinct cross peaks in the $^1\text{H}^1\text{H}$ -COSY (Fig. 6.9). The nonappearance of signals in the downfield region evidences the deprotonation of the NH protons due to complexation of the two metal ions. Two signals among the phenyl protons at 6.68 and 8.00 ppm just integrate to 0.5 indicative of the *para* phenyl protons lying on the C_2 axes. This is further confirmed by the $^1\text{H}^1\text{H}$ -COSY spectrum (Fig. 6.9), because these

Fig. 6.9 $^1\text{H}^1\text{H}$ -COSY spectrum (500 MHz, CD_2Cl_2) of LCu_2^{2+} . Unsignificant region between 2.5 and 6 ppm was cut off. Reproduced with permission [45]. Copyright (2013) American Chemical Society



resonances only couple to one another's neighbouring proton. LCu_2^{2+} is isoelectronic to LNi_2 and NMR data resemble each other (Fig. 5.16 for LNi_2 vs. Fig. 6.8 for LCu_2^{2+}). Further comparison shows that only two methylene signals instead of three are separated and symmetry aspects are alike. Assuming a ligand-centered oxidation, the NMR signals should be affected and the symmetry reduced, which is not observed. Thus, NMR spectroscopy points to a metal-centered oxidation.

Crystals suitable for X-ray diffraction were grown by slow diffusion of a saturated solution of $[\text{LCu}_2](\text{BF}_4)_2$ in acetone into toluene under inert conditions. Two toluene and two acetone molecules are present per $[\text{LCu}_2(\text{acetone})_2](\text{BF}_4)_2$ and besides the four coordinative bonds to copper from the four nitrogen atoms, also a fifth coordinative bond is exhibited by the oxygen atom of one acetone molecule with a bond lengths of 2.39 Å. The axially bound acetone renders the system in a square-pyramidal coordination geometry. The presence of two BF_4^- anions confirms an overall charge of 2^+ of the complex cation (Fig. 6.10). The BF_4^- anions are disordered [the minor population (0.295 vs. 0.705) is not depicted]. The BF_4^- counterions are relatively far away from the positive charge-carrying centers. The crystallographic C_2 axis within the molecule is obvious and similar to the one observed in the solid-state structures of LCu_2 and LNi_2 . $[\text{LCu}_2(\text{acetone})_2](\text{BF}_4)_2$ also crystallizes in the space group $C2/c$. The symmetry equivalent atoms are generated via the symmetry transformation $1-x, y, 1.5+z$.

Comparison of the solid-state structures of $[\text{LCu}_2(\text{acetone})_2](\text{BF}_4)_2$ with the isoelectronic structure of LNi_2 reveals that the Ni–N bond lengths are much shorter than the Cu–N bond lengths. While the Ni–N^{PZ} and Ni–N^{PYR} amount to 1.90 and 1.92 Å average, the values of the Cu–N^{PZ} and Cu–N^{PYR} are about 0.08 Å longer (1.99 and 1.98 Å) (Table 5.2). LNi_2 is still more distorted than $[\text{LCu}_2(\text{acetone})_2](\text{BF}_4)_2$ ($\pm 73^\circ$ vs. $\pm 76^\circ$).

Comparison of the structures of LCu_2 and $[\text{LCu}_2(\text{acetone})_2](\text{BF}_4)_2$ (Fig. 6.10) shows almost same Cu...Cu distances. Overall the torsion (compare Fig. 4.5) increases upon oxidation: while in LCu_2 torsion angles of about $\pm 78^\circ$ are observed, the torsion for $[\text{LCu}_2(\text{acetone})_2](\text{BF}_4)_2$ amounts to $\pm 76^\circ$. No change in the Cu–N^{PZ} bond lengths is observed but the Cu–N^{PYR} bond lengths are about 0.02 Å shorter for the unoxidized species. As an oxidation-state change would severely affect the Cu–N bond lengths, the similarity of the Cu–N bond lengths for LCu_2 and $[\text{LCu}_2(\text{acetone})_2](\text{BF}_4)_2$ points to a ligand-centered oxidation. The alternating bond length pattern for the ligand scaffold remains. Differences among the C–C bond lengths of LCu_2 and $[\text{LCu}_2(\text{acetone})_2](\text{BF}_4)_2$ are negligible and within measuring inaccuracy. A ligand-centered oxidation of LCu_2 should evoke some kind of change in the C–C bond lengths. In conclusion, neither significant bond lengths changes in the Siamese-twin scaffold nor in the Cu–N bond lengths are observed, thus X-ray analysis gives no hint to the actual oxidation site.

To clarify the so far ambiguous results concerning the oxidation site, XAS measurements at the Cu K-edge were run for LCu_2^{2+} in collaboration with DeBeer and coworkers. In these XAS measurements, the sample is exposed to X-ray radiation whereupon K-electrons get excited [26]. The experimental XAS spectrum is divided into three significant parts: The pre-edge, the edge and the

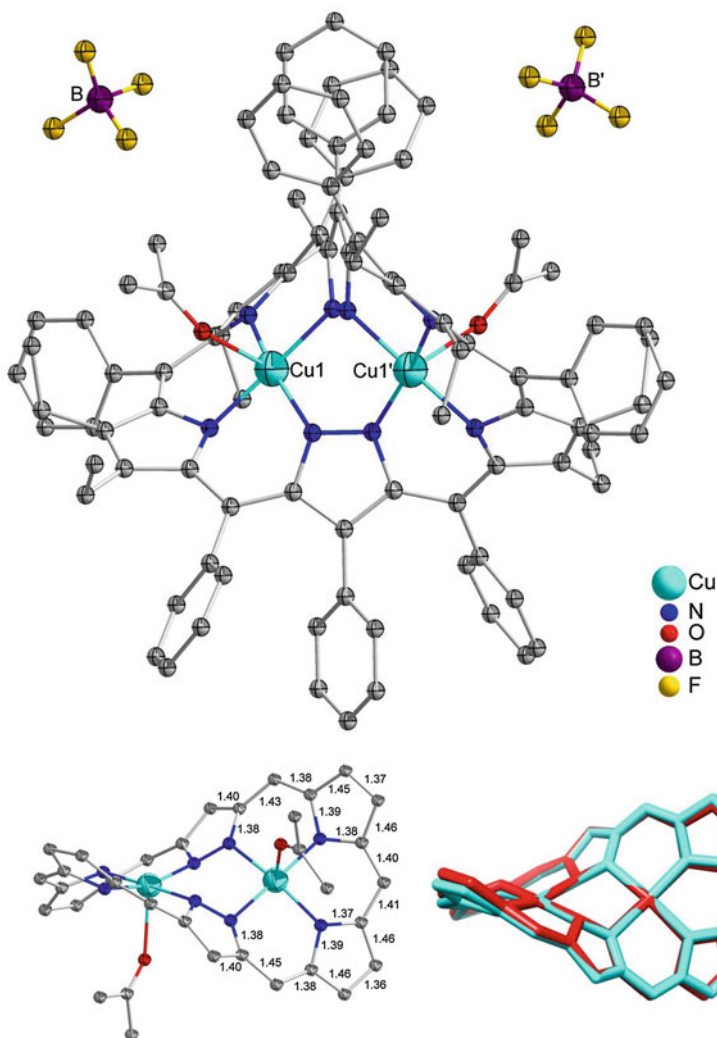


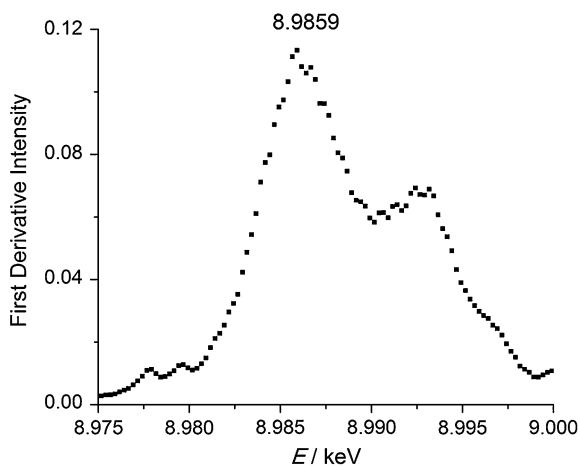
Fig. 6.10 *Top* Crystal structure of $[\text{LCu}_2(\text{acetone})_2](\text{BF}_4)_2$. Symmetry transformation to generate equivalent atoms ($'$): $1-x, y, 1.5-z$. *Bottom* Overlay of the core units of LCu_2 (cyan blue) and $[\text{LCu}_2(\text{acetone})_2](\text{BF}_4)_2$ (red). Reproduced with permission [45]. Copyright (2013) American Chemical Society

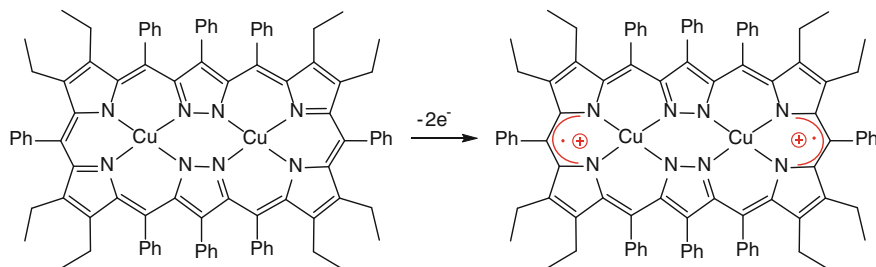
extended-X-ray absorption fine structure (EXAFS). The pre-edge reveals information about the oxidation state of the metal ion and local geometry, the edge hints at the oxidation state of the metal ion and the EXAFS region reveals information about the type, number and distances of neighbouring atoms.

In order to analyze the XAS measurements of LCu_2^{2+} , Cu K-edge energies of LCu_2^{2+} were compared to those found in model complexes. XAS-measurements of LCu_2 and subsequent comparison of the K-edge energies with LCu_2^{2+} would reveal much more comprehensive and reliable statements about the oxidation state. Analysis can further be confirmed using DFT calculations which are still pending. LCu_2^{2+} shows an absorption edge at ~ 8.9859 keV with two pre-edge features at ~ 8.9778 and ~ 8.9802 keV (Fig. 6.11). An absorption edge between 8.986 and 8.988 keV is consistent with a Cu^{II} oxidation state [27] and a pre-edge at ~ 8.9778 keV is indicative of a Cu^{II} $3d \leftarrow 1s$ transition which generally occurs at ~ 8.9786 keV [28, 29]. The presence of a second pre-edge feature is somewhat surprising, but would be consistent with a low-lying partially occupied ligand orbital (L). In contrast to that, Cu^{III} species generally have $3d \leftarrow 1s$ features at ~ 8.9808 keV with a very intense feature at ~ 8.986 keV due to $4p \leftarrow 1s$ transitions [29]. The rather featureless spectrum is consistent with a predominantly Cu^{II} species. Thus, XAS measurements suggest a ligand-centered oxidation.

In conclusion, the answer to the question of the redox site is a tough task. While investigations on LCu_2^+ only revealed that a class I compound is present, neat spectroscopic investigation of LCu_2^{2+} do not direct to a definite solution. XAS measurements suggest a ligand-centered oxidation because the copper oxidation state could be assigned to 2+. This observation is in line with X-ray because no change in the Cu–N bonds upon oxidation was observed but simultaneously no significant C–C bond lengths changes of the Siamese-twin scaffold were observed comparing LCu_2 and $[\text{LCu}_2(\text{acetone})_2](\text{BF}_4)_2$. However, NMR spectra point to a metal-centered oxidation or a severe antiferromagnetic coupling to obtain a diamagnetic species.

Fig. 6.11 First derivative of the XAS spectrum measured at the Cu K-edge for LCu_2^{2+}





Scheme 6.2 Oxidation reaction from LCu_2 toward LCu_2^{2+} and visualization of the assumed location of oxidation (*red radical*)

The only solution consistent with all recorded data is presented in Scheme 6.2, where each *meso*^{pyr/pyr} carbon atom was oxidized. Under the circumstance of strong antiferromagnetic coupling of the resulted radicals to the neighboring copper d^9 centers, the system would be diamagnetic. The antiferromagnetic coupling could be mediated by spinpolarization [30], which is a second concept for exchange coupling next to the concept of orthogonal orbitals (Sect. 5.2.2). Spinpolarization mediates exchange coupling by antiparallel alignment of the spins of neighboring atoms. If the oxidation takes place as pronounced, LCu_2^{2+} would exhibit D_2 symmetry as was found in its NMR spectra. With this solution also the second pre-edge feature in XAS measurements is reasonable.

6.2 Mono- and Di-Nickel Complexes

The CV curve of LH_2Ni is similar to that of LH_4 in the sense that no electrochemically reversible redox processes could be observed, even after addition of TFA (Fig. 6.12). Thus, LH_2Ni was not further investigated.

Fig. 6.12 CV curve of LH_2Ni and $\text{LH}_3\text{Ni}^{2+}$ in CH_2Cl_2 with $[\text{NBu}_4]\text{PF}_6$ as an electrolyte. The voltammogram was measured at a scan rate of $100 \text{ mV}\cdot\text{s}^{-1}$ and plotted versus Fc

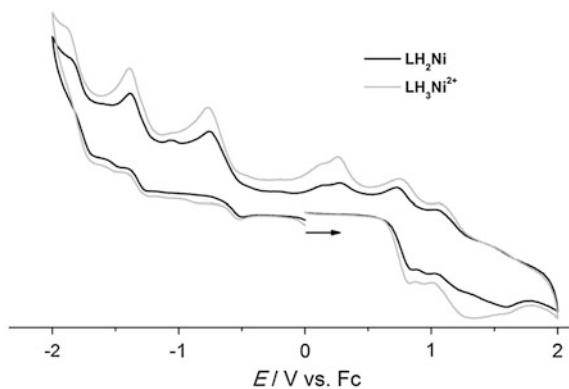
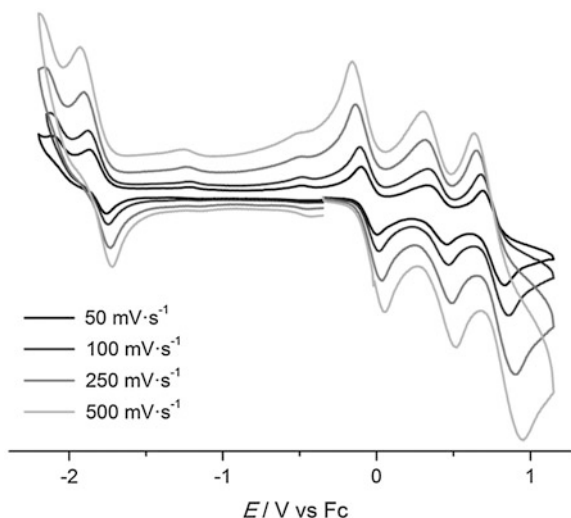


Fig. 6.13 CV curves of LNi_2 measured in CH_2Cl_2 with $[\text{NBu}_4]\text{PF}_6$ as an electrolyte at scan rates of 50, 100, 250 and 500 $\text{mV}\cdot\text{s}^{-1}$



The voltammogram of LNi_2 showed three electrochemically reversible processes with half wave potentials at $E_{1/2} = -1.79, -0.05, 0.41$ V and electrochemically irreversible half waves at $E_p^{\text{ox}} = -2.00$ and 0.86 V and $E_p^{\text{red}} = -2.10$ and 0.68 V (Figs. 6.1 and 6.14). Measuring the CV curves at differing scan rates of 50, 100, 250 and 500 $\text{mV}\cdot\text{s}^{-1}$, and considering the second criterion in Sect. 4.4 confirms this (Fig. 6.13). Integration of SWV peaks leads to equal areas for the three electrochemically reversible redox processes. If these refer to one-electron processes, the SWV curve at -2.10 V refers to much less than one electron, thus only parts of the Siamese-twin porphyrin get reduced. In opposite, the area of the signal at the highest potential refers to more than an one-electron oxidation, but does not integrate to double the peak area which would indicate a two-electron process. Against the background of this finding, the electrochemically reversible signals at $-1.79, -0.05$ and 0.41 are the most interesting to investigate with spectroelectrochemical methods. K_c for LNi_2^+ was determined as $7.2 \cdot 10^7$ and thus LNi_2^+ is thermodynamically stable [2].

6.2.1 Electrochemical Oxidation/Reduction

Spectroelectrochemical investigations were carried out under the same conditions as in Sect. 6.1. A color code is used, which does not relate to the authentic colors, to ascribe the different UV–vis spectra of the electrochemically generated species (Fig. 6.14 and Table 6.2): LNi_2^- (orange), LNi_2 (dark red), LNi_2^+ (yellow), LNi_2^{2+} (rose) and LNi_2^{3+} (green). The conversions are marked with (a), (b), (c) and (d).

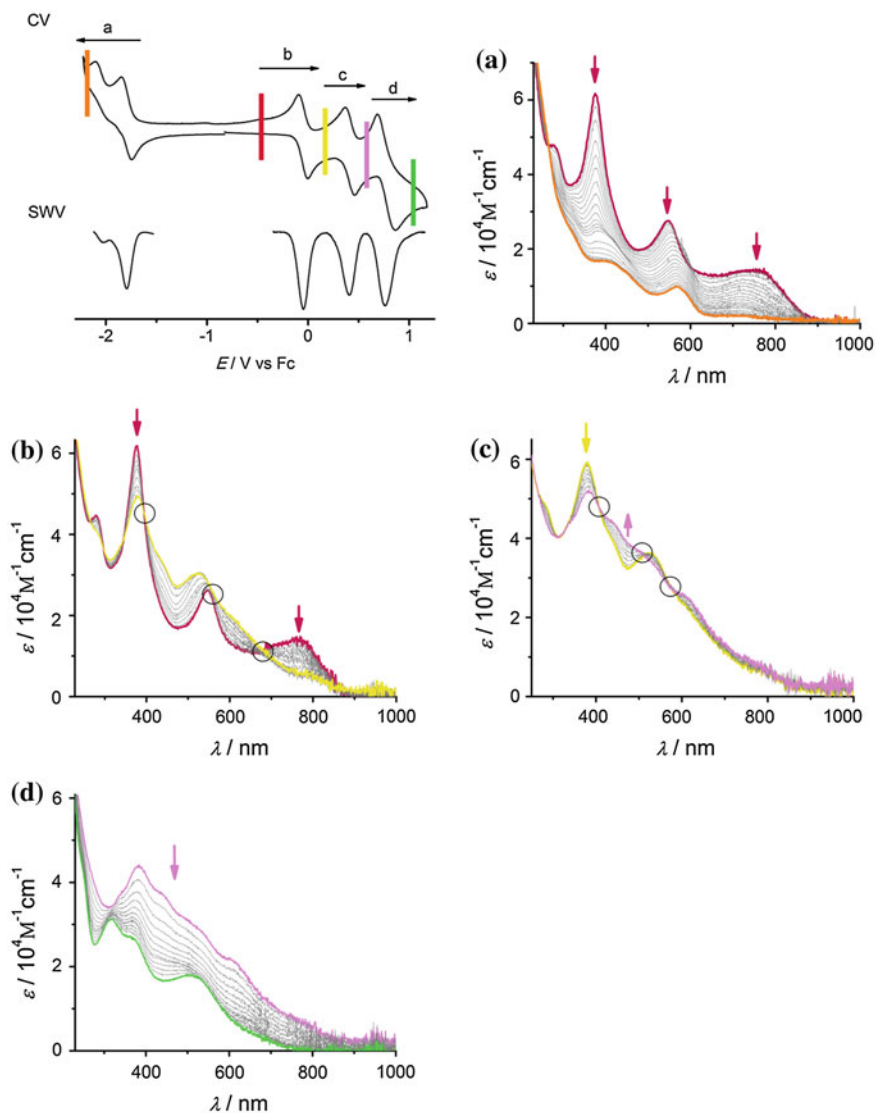


Fig. 6.14 Top left CV and SWV of LNi_2 . The electrochemistry was followed using UV-vis spectroscopy. Black circles highlight isosbestic points

- (a) Initial measurements toward the anodic potential, the starting material LNi_2 (dark red) is reduced (orange spectrum), and no isosbestic points appear. In general, all signals decrease and a featureless spectrum is observed with bands at 409 and 569 nm.

Table 6.2 Wavelengths and extinction coefficients of all redox species of LNi_2 in CH_2Cl_2

	LNi_2^-	LNi_2	LNi_2^+	LNi_2^{2+}	LNi_2^{3+}
λ/nm	409 (1.7)	281 (4.5)	281 (4.1)	366 (3.7)	316 (3.1)
$(\epsilon/10^4\text{M}^{-1}\text{cm}^{-1})$	569 (1.0)	377 (6.2)	377 (5.9)	383 (4.4)	372 (2.7)
		547 (2.6)	437 (3.4)	437 (3.8)	515 (1.8)
		765 (1.4)	524 (3.0)	506 (3.1)	607 (2.2)

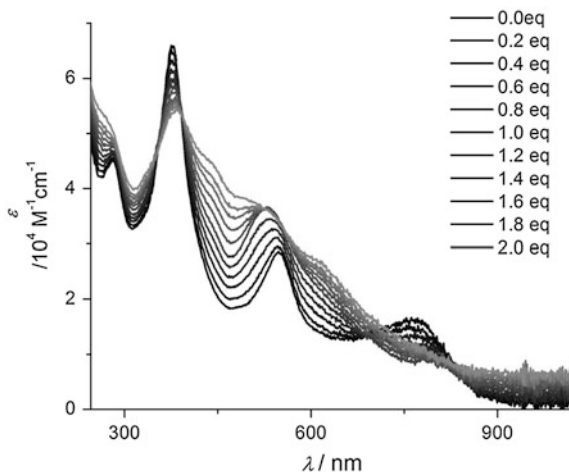
- (b+c) The one-electron oxidation to LNi_2^+ (yellow) results in a decrease of the band at 377 nm with a slight shoulder at 437 nm, while the band at 765 nm disappears. The band at 547 nm is blue-shifted to 524 nm. Further oxidation caused an upward trend of the spectrum, starting at 900 nm and reaching its maximum at 383 nm with a smaller extinction coefficient than LNi_2 or LNi_2^+ . Several shoulder peaks at 366, 437, 506 and 607 nm are present. Isosbestic points indicate direct conversions.
- (d) Further oxidation results in a decrease of intensity of the complete spectrum, finally exhibiting three maxima at 316, 372 and 515 nm (green spectrum).

Oxidation and re-reduction reveal that only the half wave potentials at -0.05 and 0.41 V are chemically reversible on the time scale of bulk electrolysis, in contrast to the half wave at $E_{1/2} = -1.79$ V, which appears to be solely reversible on CV time scale (Fig. 6.1). As observed for LCu_2^{2+} , LNi_2^{2+} gets slowly reduced first to LNi_2^+ , then to LNi_2 when it is longer exposed to ambient conditions. Initial examination of the different redox steps was done by sample generation from the bulk electrolysis experiment. The reaction was monitored via UV-vis spectroscopy and EPR samples were taken from the spectroelectrochemical sample mixture and immediately frozen in liquid nitrogen. The diamagnetic ground state of the starting material LNi_2 is advantageous. The EPR samples of the singly reduced and oxidized products LNi_2^- and LNi_2^+ were obtained without complete conversion. LNi_2^- and LNi_2^+ are predicted to be EPR active. Especially, information about the monoreduced form is of interest as any insight in reductive processes in LCu_2 and LNi_2 is still lacking. Unfortunately, the monoreduced species is extremely sensitive and decomposes immediately. Due to the sensitivity of LNi_2^- an anodic potential of -1.9 V was shortly applied and an EPR sample was taken. Although one-electron reduction of a diamagnetic state must be EPR active, no signal was detected. Repetition of the same experiment did not reveal any different results. All taken samples were EPR silent except for the monooxidized species LNi_2^+ , which will be discussed later in more detail.

6.2.2 Chemical Oxidation

As the two reversible redox waves at $E_{1/2} = -0.05$ and 0.41 V are of great interest, experiments were run in order to obtain the oxidized species LNi_2^+ and LNi_2^{2+} by chemical oxidation. Profiting from the experience gathered with LCu_2 ,

Fig. 6.15 Titration of LNi_2 in CH_2Cl_2 with a 0.1 M stock solution of AgBF_4 in Nitroethane followed by means of UV-vis spectroscopy



AgBF_4 was used as the oxidizing agent. The titration of LNi_2 with a 0.1 M solution of AgBF_4 in nitroethane (Fig. 6.15) proved the assumption of one-electron waves in the CV curve to be correct, as after the addition of two equivalents of the oxidizing agent LNi_2^{2+} was obtained.

The scale-up of this reaction allowed the synthesis of quantitative amounts of LNi_2^+ at ambient conditions. After the removal of the reaction solvents, CH_2Cl_2 and nitroethane, the remaining substance was dried in vacuum and then redissolved in CH_2Cl_2 . The suspension was filtered using a membrane filter in air to remove any silver particles. The solvent was removed using rotary evaporation and the substance was stored under inert conditions.

The synthesis of LNi_2^{2+} proved difficult. Besides the problem of facile irreversible overoxidation of LNi_2^{2+} to LNi_2^{3+} , re-reduction at ambient conditions initiated immediately and thus the reaction was repeated in the glove box. Besides the sensitivity of LNi_2^{2+} , reaction monitoring via UV-vis spectroscopy was impeded due to minimum observable changes between LNi_2^+ , LNi_2^{2+} and LNi_2^{3+} and similar absorption maxima of LNi_2^+ and LNi_2^{3+} . In situ reaction control with the immersion probe could not be performed in the glove box.

6.2.3 Localization of the Redox Center in LNi_2^+

Initially, first samples of LNi_2^+ were obtained from bulk electrolysis experiments and investigated by EPR spectroscopy (Fig. 6.16, left). The spectrum of LNi_2^+ consists of three sub-spectra with two having rhombic symmetry and one axial symmetry. Sub-spectrum 1 (sub1, Fig. 6.16, right, green) has rhombic symmetry with g values of $g_x = 2.10$, $g_y = 2.33$ and $g_z = 2.37$. A slightly different line width was anticipated for the different directions with $W_x = W_y = 68.57$, $W_z = 68.17$.

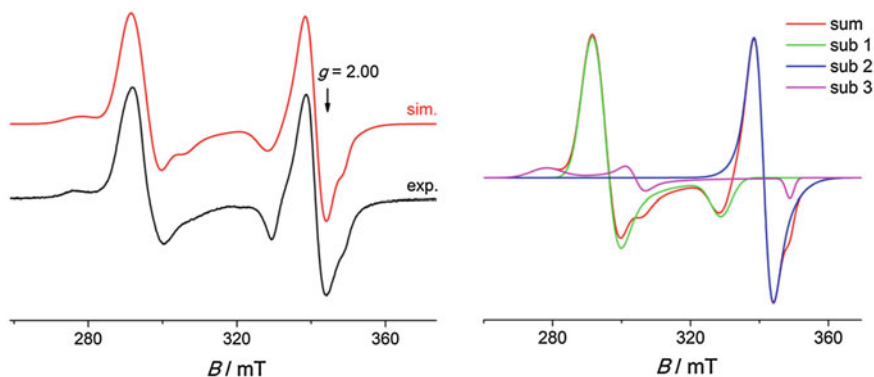


Fig. 6.16 *Left* Measured EPR spectra at 10 K in CH_2Cl_2 of the electrochemically generated LNi^{2+} and its simulation; *Right* Composition of the simulated spectrum divided in its three subspectra

Sub spectrum 2 (sub2, Fig. 6.16, right, blue) exhibits axial symmetry with g values of $g_x = g_y = 2.02$ and $g_z = 2.01$ and line widths of $W_x = W_y = 52.27$ and $W_z = 165.60$. The third sub-spectrum (sub3, Fig. 6.16, right, green) has largely separated g values of $g_x = 2.48$, $g_y = 2.27$ and $g_z = 1.98$. The ratio of sub1:sub2:sub3 is 59 %:19 %:22 % and sub-spectra 2 and 3 are equally represented in the mixture. The presence of impurities can be ruled out because crystalline material was used as starting material, where purity was confirmed via elemental analysis and the data were reproducible.

In literature, chemically synthesized nickel(II) porphyrins were investigated with respect to their redox properties [31]. Oxidation gave nickel(II) π -cation radicals and nickel(III) porphyrin complexes in a manner highly dependent on the reaction conditions. Wolberg and Manassen reported on a nickel(III)TPP complex, which was stable at 77 K in benzonitrile, but decomposed via a nickel(II)TPP π -radical at room temperature [32, 33]. Dolphin succeeded in characterizing a nickel(II)TPP π -radical using CH_2Cl_2 as the solvent [34, 35]. The coexistence of a nickel(III) complex and a nickel(II) π -radical and their temperature-dependent valence tautomerism was described as well [24, 36–39]. Nickel(II) π -radicals showed an isotropic signal at g_{av} values of 2.00, nickel(III) complexes showed axial symmetry with g_{av} values of 2.22–2.24 [40, 41]. The average g value of 2.015 of sub2 in the measured EPR spectrum most likely indicates a ligand-centered radical, while g_{av} for sub1 of 2.27 supports the presence of a nickel(III) complex. Sub3 is hard to interpret and could not be assigned.

The main factors that influence the localization of oxidation are the nature of the counterion and the solvent system, primarily because counterions or solvents with donor functions can be involved in complexation at the vacant axial position [31]. Axial coordination raises the energy of the d_{z^2} orbital and leaves the system with an unpaired electron located in the d_{z^2} orbital. Figure 6.17 illustrates the present case of an equilibrium of a nickel(III) complex and a ligand-centered radical species. If nickel(III) and nickel(II) π -radicals can coexist, the energy of the ligand and nickel

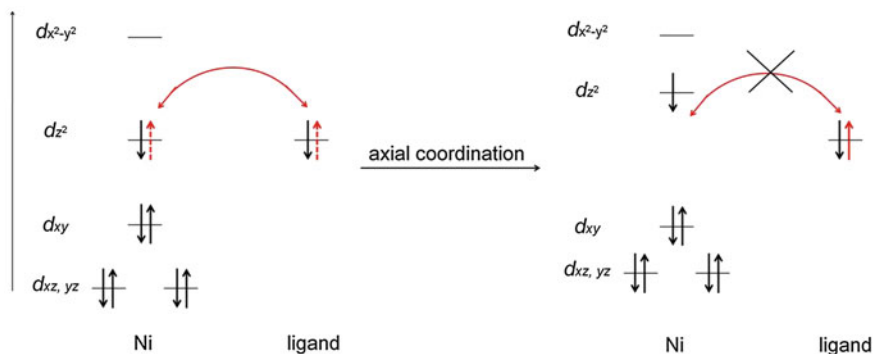
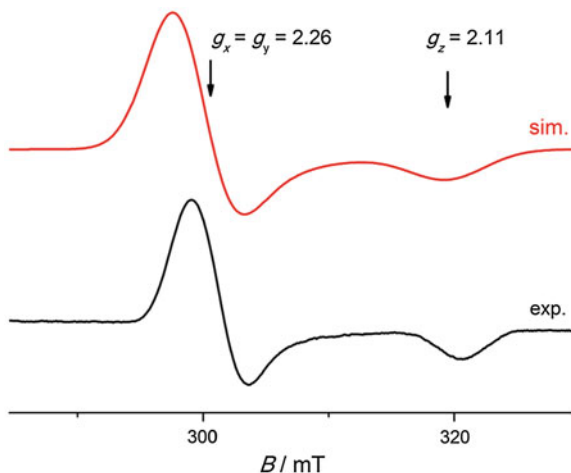


Fig. 6.17 Square planar d orbital splitting before and after the addition of an axial ligand

orbital have to be roughly equal. Thus, the unpaired spin can flip from one to another. In literature, pyridine was added as an axial ligand with resulting hyperfine coupling to the pyridine nitrogen atom(s) in the z direction, because the spin carrying d_{z^2} orbital points exactly to the pyridine nitrogen atoms [41, 42]. Here, addition of pyridine to the electrochemically produced samples resulted in an axial spectrum (Fig. 6.18) with g values of $g_x = g_y = 2.26$ and $g_z = 2.11$, which are slightly higher than reported in literature but of the same magnitude. The hyperfine coupling to the axially bound nitrogen atoms was not resolved. However, this experiment confirms the possibility of a ligand- and metal-centered oxidation and the coexisting spectra merge to one metal centered signal after addition of pyridine.

EPR investigation of the chemically oxidized sample LNi_2^+ differed from the electrochemically generated sample and only showed two subspectra, namely sub1 and sub2, with sub2 being the main species (Fig. 6.19). Sub1 and sub2 are similar to sub1 and sub2 observed for the electrochemically generated sample (Fig. 6.16) but were simulated with slightly different g values of $g_x = 2.14$, $g_y = 2.32$ and

Fig. 6.18 EPR spectrum of $[\text{LNi}_2]\text{BF}_4$ after addition of pyridine in CH_2Cl_2



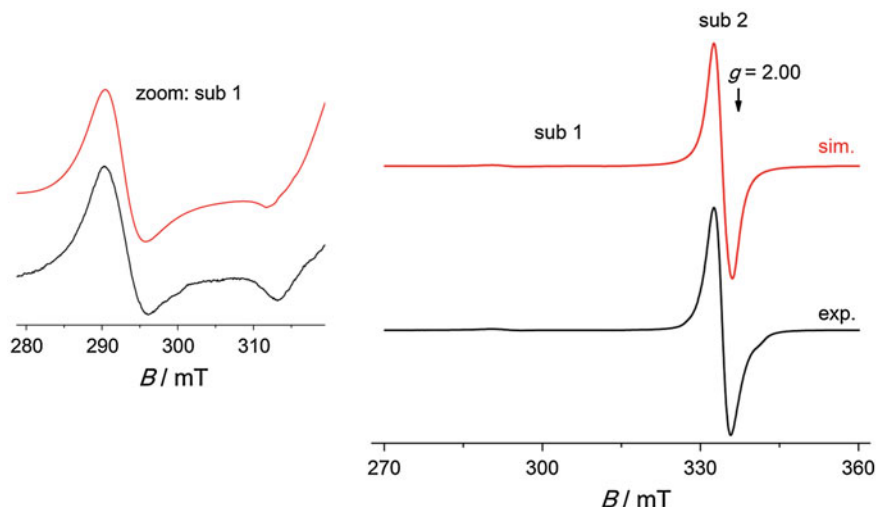


Fig. 6.19 EPR spectrum of LNi_2^+ chemically oxidized with AgBF_4 , recorded at 150 K and its simulation with two different subspectra. In order to visualize sub1, an expansion of the region between 280 and 320 mT is shown on the *left*

$g_z = 2.31$ and line widths of $W_x = 50.7$, $W_y = 90.0$ and $W_z = 35.7$ for sub1 and $g_x = 2.02$, $g_y = 2.03$ and $g_z = 2.01$ for sub2. Sub1 was simulated using Gaussian line shapes and sub2 using Lorentzian line shapes with isotropic line widths of 40. The ratio of sub1:sub2 is 4:96. Thus, in the chemically generated sample the ligand-centered radical is dominant.

The various parameters that influence the equilibrium of ligand radicals and Ni^{III} complexes in nickel porphyrin EPR spectra were further investigated by modifying reaction conditions step-by-step. The most obvious difference in chemically and electrochemically generated samples is the kind of counterion, BF_4^- and PF_6^- respectively, and thus samples were chemically generated with AgPF_6 as oxidant. An EPR sample using AgPF_6 was produced analogous to procedures using AgBF_4 . The EPR spectrum of the sample chemically generated with AgPF_6 do not resemble the spectrum obtained after electrochemical sample generation (Fig. 6.16 vs. 6.20) even though in both samples the species $[\text{LNi}_2]\text{PF}_6$ should be present. The spectrum of the chemically oxidized $[\text{LNi}_2]\text{PF}_6$ resembles more the spectrum of the chemically synthesized $[\text{LNi}_2]\text{BF}_4$, because in both cases the ligand-centered radical is the main species. Comparing the spectra of chemically generated $[\text{LNi}_2]\text{BF}_4$ and $[\text{LNi}_2]\text{PF}_6$, a stronger rhombicity of sub2 with g values of $g_x = 2.04$, $g_y = 2.03$ and $g_z = 1.97$ was observed for $[\text{LNi}_2]\text{PF}_6$ and line widths of $W_x = 44.7$, $W_y = 23.4$ and $W_z = 30.7$. The ratio of sub1 and sub2 is 17:83 %.

The influence of the counterion was further investigated by addition of a large excess of the electrolyte $[\text{NBu}_4]\text{PF}_6$ to the chemically generated sample using AgBF_4 , but no change was observed. Additionally, temperature and concentration effects of the sample itself did not affect the ratio of the three sub spectra.

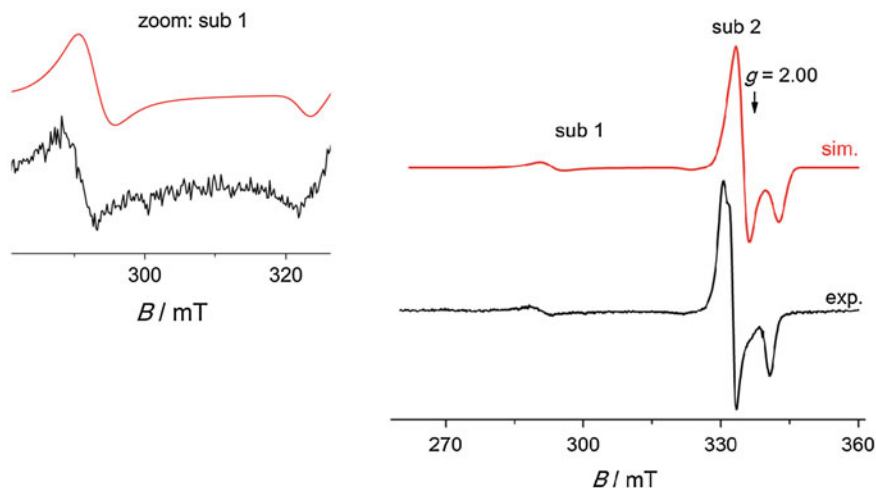


Fig. 6.20 EPR spectrum of $[\text{LNi}_2]\text{PF}_6$ generated chemically measured in CH_2Cl_2 and 173 K as a frozen glass

The solvent influence was investigated by utilizing non-coordinating solvents which produce good glasses, such as CH_2Cl_2 , CHCl_3 and toluene. All so far reported EPR spectra were measured in CH_2Cl_2 . While toluene gave undefined spectra, the spectrum measured in CHCl_3 (Fig. 6.21) resembles the rhombicity observed in the spectrum of the chemically generated $[\text{LNi}_2]\text{PF}_6$. Furthermore sub spectrum 3 became present.

The variable appearance of the EPR spectra of LNi_2^+ cannot be explained and no trend emerged. An overview of all used conditions is given in Table 6.3.

Fig. 6.21 EPR spectrum of $[\text{LNi}_2]\text{BF}_4$ in CHCl_3 at 135 K

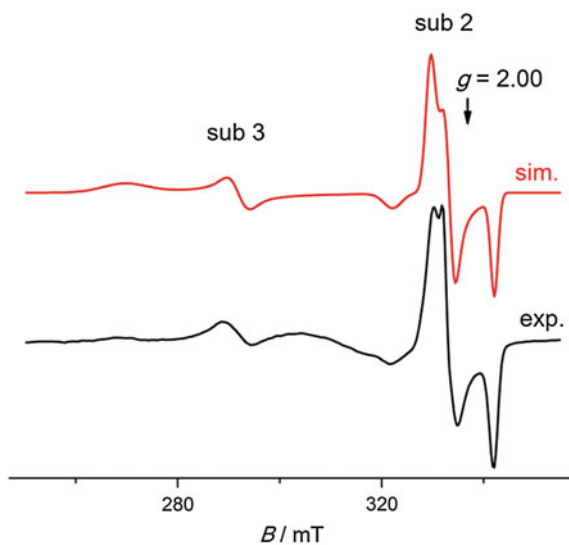


Table 6.3 Different conditions applied for EPR measurements of sample LNi_2^+

	Preparation	Temperature	Counterion	Solvent	Concentration
LNi_2^+	Electro-chemically, chemically	10 K – 160 K	BF_4^- and PF_6^-	CH_2Cl_2 , CHCl_3	10^{-3} and 10^{-5} M
	Chem. prep.: ligand-centered radical dominant	No influence	No trend	No trend	No influence

Nevertheless, EPR spectroscopy revealed the presence of a nickel(III) complex and a coexisting ligand-centered radical. Upon addition of pyridine as an axial donor, the equilibrium shifts toward the nickel(III) complex. With this experiment it was shown that the different sub spectra all originate from LNi_2^+ and not from impurities.

For $\text{LNi}^{\text{II}}\text{Ni}^{\text{III}}$ or a ligand-centered radical in $\text{L}^+\text{Ni}^{\text{II}}\text{Ni}^{\text{II}}$, IVCT can occur. A UV-vis-NIR spectrum was recorded at r.t. in CH_2Cl_2 (Fig. 6.22) and exhibits a broad band between 950 and 2000 nm, which most likely originates from an IVCT. Variable-temperature EPR spectroscopy already demonstrated the temperature-independency of the signal.

XAS measurements were performed for LNi_2^+ at the Ni K-edge (Fig. 6.23). The measured absorption energy of 8.3438 keV hardly directs to a distinct redox state because K-edge energies for Ni^{II} and Ni^{III} only differ in -0.5 eV. DFT calculations to corroborate the spectroscopic data are still pending. Additionally evaluation might be impeded because of the presence of a mixed valence compound, which could lead to overlapping signals. The pre-edge feature at 8.3315 keV arising from a $3d \leftarrow 1s$ transition is more in accordance with a Ni^{I} or Ni^{II} center (8.3315 and 8.3320 keV respectively) than a Ni^{III} where this transition is observed at energies of ~ 8.3326 keV [43, 44]. This absorption is in general much more intense for Ni^{III} than that presented herein [44]. The presence of two pre-edge features due to $3d \leftarrow 1s$ and $4p \leftarrow 1s$ transitions indicates a square planar geometry for the nickel ions.

Fig. 6.22 UV-vis-NIR spectrum of $[\text{LNi}_2]\text{BF}_4$ recorded at r.t. in CH_2Cl_2

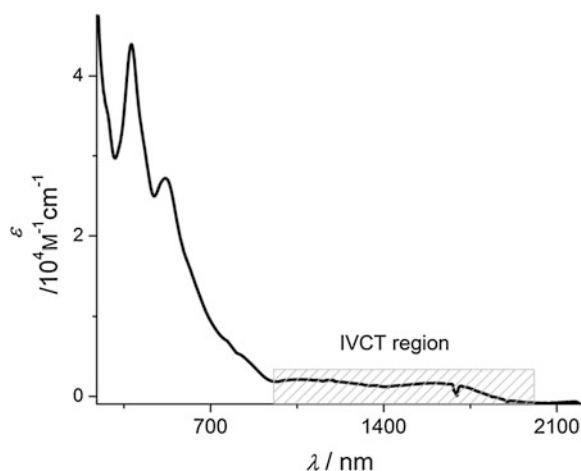
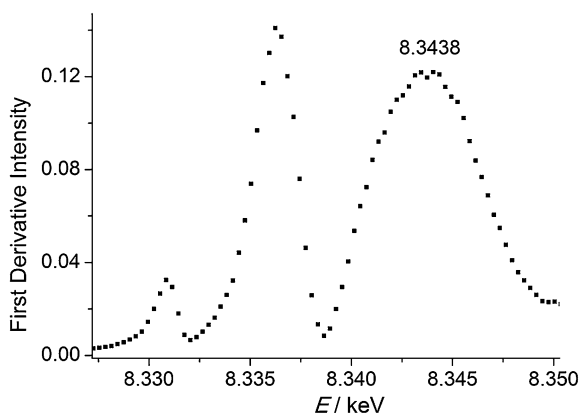


Fig. 6.23 First derivative spectrum of the XAS absorption for LNi_2^+ measured at the Ni K-edge

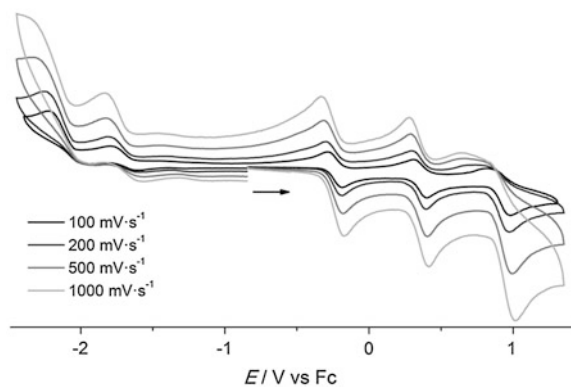


In summary, oxidation of LNi_2 to LNi_2^+ can be ligand- or metal-centered according to EPR spectroscopy depending on a not yet discovered factor. XAS measurements point to a ligand-centered oxidation in the solid state. The high sensitivity of LNi_2^{2+} hindered the full characterization of this compound.

6.3 Copper Nickel Complex

The voltammogram of LCuNi shows five redox waves with two electrochemically reversible half wave potentials of $E_{1/2} = -0.23$ and 0.35 V and electrochemically irreversible half waves at $E_p^{\text{ox}} = -1.97, -1.61$ and 0.98 V and $E_p^{\text{red}} = -2.22, -1.79$ and 0.83 V (Fig. 6.25). For measurements conducted at different scan rates (100, 200, 500 and $1000 \text{ mV}\cdot\text{s}^{-1}$) the expected linear increase of the current according to equation 4.5 was observed only for the two reversible redox processes (Fig. 6.24). SWV analysis revealed that in all redox processes the same

Fig. 6.24 CV curve of LCuNi measured in CH_2Cl_2 with $[\text{NBu}_4]\text{PF}_6$ as an electrolyte with varying scan rates of 100, 200, 500 and $1000 \text{ mV}\cdot\text{s}^{-1}$



number of electrons are transferred, except for the one at highest potential (0.90 V). This peaks' area is marginally larger, which has been previously reported for the homobimetallic complexes. K_c was calculated for LCuNi^+ as $8.1 \cdot 10^9$ and thus LCuNi^+ is thermodynamically stable. Due to the asymmetric pockets of LCuNi three different redox sites now exist: the nickel ion, the copper ion and the Siamese-twin porphyrin.

6.3.1 Electrochemical Oxidation/Reduction

Bulk electrolysis investigations were performed according to the procedure applied for LCu_2 and LNi_2 . A color code was used as follows, LCuNi^{2-} (black), LCuNi^- (green), LCuNi (red), LCuNi^+ (ocher), LCuNi^{2+} (blue) and LCuNi^{3+} (orange). The transitions from LCuNi to LCuNi^{2-} are described in (a), the ones for LCuNi to LCuNi^{2+} in (b), and from LCuNi^{2+} to LCuNi^{3+} in (c) (Fig. 6.25).

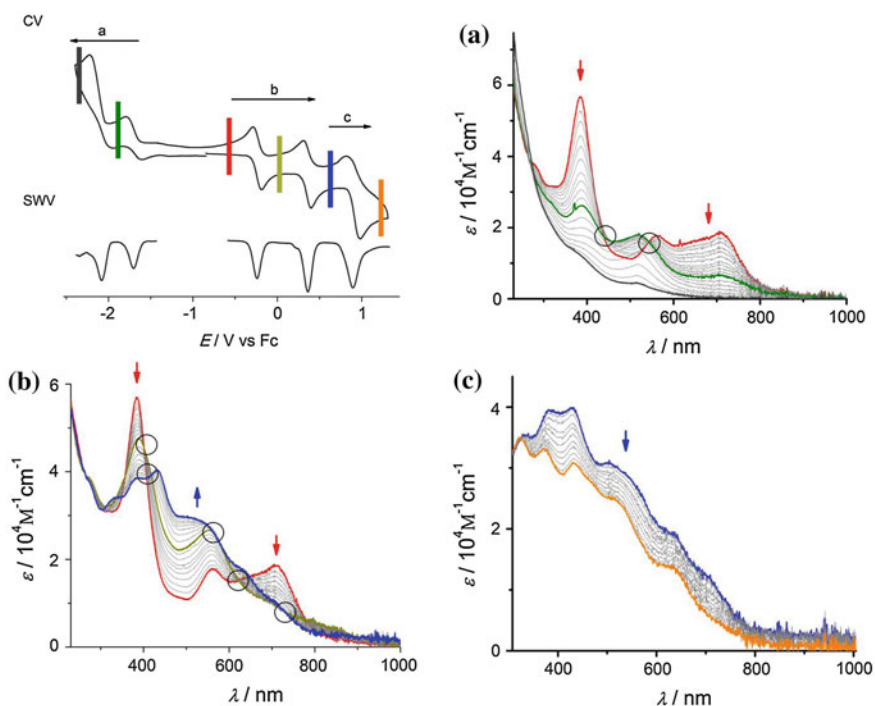


Fig. 6.25 Top left CV and SWV of LCuNi . The electrochemistry was followed using UV-vis spectroscopy. Black circles are indicating isosbestic points

Table 6.4 Wavelengths and extinction coefficients of all redox species of LCuNi in CH₂Cl₂ at r.t

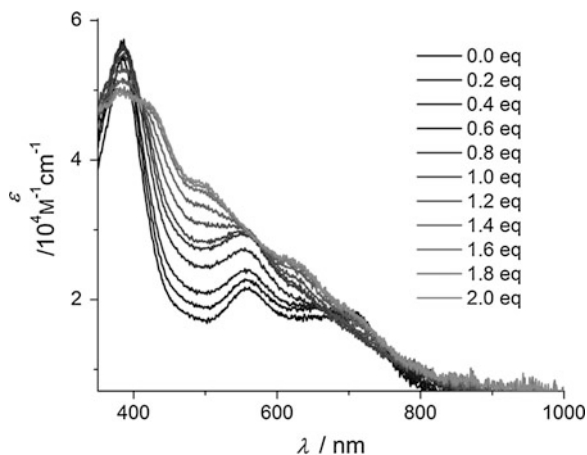
	LCuNi ²⁻	LCuNi ⁻	LCuNi	LCuNi ⁺	LCuNi ²⁺	LCuNi ³⁺
	382 (1.2)	386 (2.6)	279 (3.7)	271 (3.9)	271 (3.8)	323 (3.5)
		518 (1.8)	385 (5.7)	389 (4.8)	331 (3.4)	373 (3.3)
λ/nm	517 (0.4)	708 (0.7)	559 (1.8)	556 (2.7)	381 (3.8)	433 (3.1)
$(\epsilon/10^4\text{M}^{-1}\text{cm}^{-1})$			710 (1.8)	685 (1.1)	432 (4.0)	513 (2.5)
					526 (2.9)	630 (1.4)
					632 (1.8)	

- (a) Initial reduction induces a decrease of the absorption bands at 385 and 710 nm until a minimum is reached. The absorption band at 559 nm experiences a strong blue shift to 518 nm but preserves its intensity. Ongoing reduction leads to an almost complete extinction except in the UV region, where an increase is observed. In the first reductive conversion isosbestic points are evident, but are absent in the second.
- (b) Upon oxidation, the λ_{max} of **LCuNi** at 385 nm decreases. The band at 710 nm loses intensity and the one at 559 nm rises. In the UV region a negligible shoulder appears. With the second oxidation, the former λ_{max} of **LCuNi** at 385 nm decreases further. The maximum of the curve is found at a wavelength of 432 nm. Following the curve from this point to higher wavelengths, it steadily decreases but shows shoulders at 526 and 632 nm to finally reach its complete extinction at 950 nm. Toward smaller wavelengths, several local maxima are present at 271, 331 and 381 nm. Each conversion shows several isosbestic points.
- (c) For the last oxidation process the UV–vis spectrum follows a continuous downward trend of all absorption bands to leave the spectrum with three predominant absorption maxima at wavelengths of 323, 373 and 433 nm and shoulders at 513 and 630 nm. No isosbestic points are observed (Table 6.4).

Chemical reversibility was tested following the UV–vis spectra during oxidation/reduction and subsequent re-reduction/re-oxidation. This showed, that only the two waves at potentials of -0.23 and 0.35 V were chemically reversible. Repetition of the bulk experiment delivered first EPR samples of each redox species. Because the ground state of **LCuNi** with one unpaired electron is paramagnetic (Sect. 5.4), the mono-oxidized and -reduced products **LCuNi⁺** and **LCuNi⁻**, respectively, are supposed to be diamagnetic. The second oxidized and reduced forms, **LCuNi²⁺** and **LCuNi²⁻** respectively, are assumed to be EPR active and **LCuNi³⁺** to be EPR silent.

As predicted, **LCuNi⁻**, **LCuNi⁺** and **LCuNi³⁺** did not show any EPR activity. Contradictory to expectations, **LCuNi²⁻** was found to be EPR silent, most likely due to irreversible decomposition reactions. EPR spectra of **LCuNi²⁺** will be discussed in Sect. 6.3.4.

Fig. 6.26 Titration of **LCuNi** in CH_2Cl_2 with a 0.1 M stock solution of AgBF_4 in Nitroethane followed by means of UV-vis spectroscopy



6.3.2 Chemical Oxidation

LCuNi was oxidized chemically using AgBF_4 , firstly by performing a titration (Fig. 6.26). The reaction was scaled up and the oxidized species **LCuNi⁺** and **LCuNi²⁺** were isolated by first removing the solvent mixture under reduced pressure and then redissolving the solid in CH_2Cl_2 . Subsequent filtering of the obtained suspension yielded the desired compounds in quantitative amounts. For **LCuNi⁺** and **LCuNi²⁺**, the work-up was done under ambient conditions. The product was stored under inert atmosphere, because otherwise a reduction to the starting material was observed.

6.3.3 Localization of the Redox Center in **LCuNi⁺**

In the case of a metal-centered oxidation, **LCuNi⁺** is a hetero mixed valent compound of **LCu^{III}Ni^{II}** or **LCu^{II}Ni^{III}** with d^8d^8 or d^9d^7 configurations, respectively. The electronic ground state after a ligand-centered oxidation is **L⁺Cu^{II}Ni^{II}**. A strong antiferromagnetic coupling of the two unpaired spins in **LCu^{II}Ni^{III}** and **L⁺Cu^{II}Ni^{II}** would result in an EPR silent ground state. Due to their diamagnetic character, NMR spectroscopy was thus attempted on the chemically synthesized samples. The inability to obtain solely **LCuNi⁺** resulted in broadened spectra due to a paramagnetic contribution. These did not reveal any information about the localization of the first oxidation. The sample was studied with UV-vis-NIR spectroscopy (Fig. 6.27) and a broad band emerged between 1400 and 2100 nm from the background. Absorption bands within this region can only originate from IVCT. Because the electronic configurations in the case of metal-centered

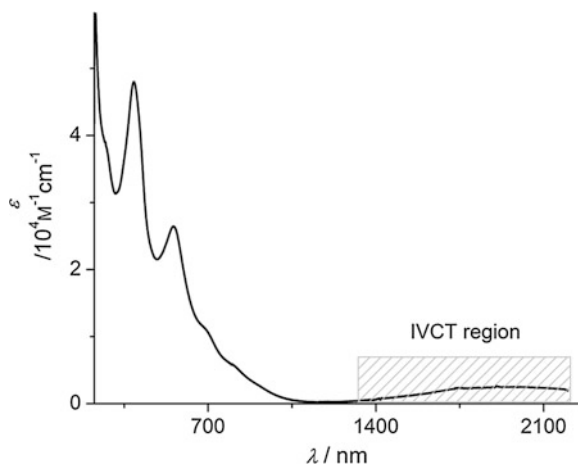


Fig. 6.27 UV-vis-NIR of LCuNi^+ measured in CH_2Cl_2 at r.t. IVCT band marked in red

oxidation show no mixed valency a LLCT occurs, which points to a ligand-centered oxidation.

To answer the ongoing question of the localization of the oxidation reaction, XAS measurements were performed. The monooxidized species is suitable for investigation with XAS because the two distinct copper and nickel ions have different absorption energies of about 0.6 keV for their M^{II} states. LCuNi^+ samples were measured at the Cu and Ni K-edge to determine the redox states of both incorporated metal ions (Fig. 6.28). These data are compared to the Ni K-edge spectrum of LNi_2^+ and to the Cu K-edge spectrum of LCu_2^{2+} , where the introduced color code is used throughout. The $3d \leftarrow 1s$ Ni pre-edge transition energy of 8.3315 keV and the Cu-K-absorption edge at 8.9859 keV indicate M^{II} redox states. The high degree of spectral overlap suggests that the nickel centers in

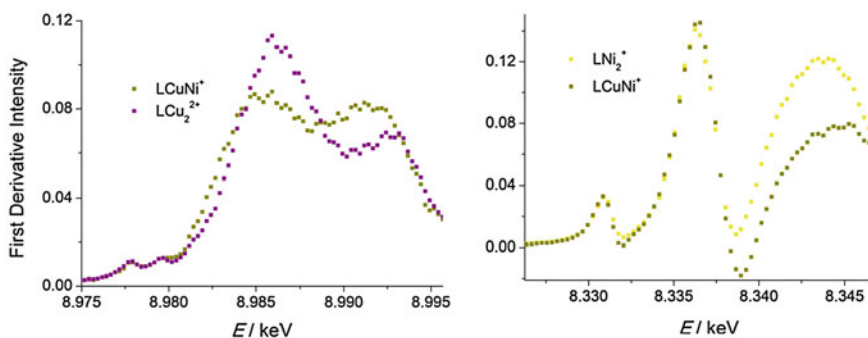


Fig. 6.28 First derivative spectra of the XAS absorption: Cu-K-edge measurement of LCuNi^+ compared with LCu_2^{2+} (left) and Ni-K-edge measurement of LCuNi^+ compared with LNi_2^+ (right)

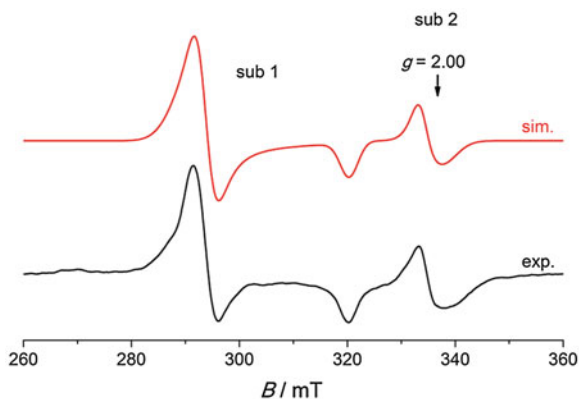
LCuNi^+ and LNi_2^+ and the copper centers in LCuNi^+ and LCu_2^{2+} have similar oxidation states. The presence of well resolved $3d \leftarrow 1s$ and $4p \leftarrow 1s$ features in the Ni K-edge measurements is consistent with a square planar nickel center. The lower absorption intensity in the pre-edge $4p \leftarrow 1s$ transition at ~ 8.3377 keV for LNi_2^+ points to a more distorted square planar geometry for the nickel center in LNi_2^+ than in LCuNi^+ [43]. Even though crystallographic characterization for the oxidized species LNi_2^+ , LCuNi and LCuNi^+ is lacking, it was observed that nickel complexation induced a higher degree of distortion in the Siamese-twin scaffold than copper. This finding is in line with XAS conclusions.

Thus, XAS and UV-vis-NIR measurements suggest a ligand-centered oxidation.

6.3.4 Localization of the Redox Center in LCuNi^{2+}

Assuming first a ligand-centered oxidation the twice-oxidized LCuNi^{2+} can have the following four ground states: $\text{L}^+\text{Cu}^{\text{III}}\text{Ni}^{\text{II}}$ and $\text{L}^+\text{Cu}^{\text{II}}\text{Ni}^{\text{III}}$ if the second oxidation is metal-based or $^+\text{L}^+\text{Cu}^{\text{II}}\text{Ni}^{\text{II}}$ and $^{2+}\text{LCu}^{\text{II}}\text{Ni}^{\text{II}}$ if the second oxidation is ligand-based as well, where $^{2+}\text{LCu}^{\text{II}}\text{Ni}^{\text{II}}$ represents the species with the ligand oxidized twice at the same position. Thus, LCuNi^{2+} was investigated by EPR spectroscopy and EPR samples were obtained by electrochemical synthesis. LCuNi^{2+} is EPR active and gives a spectrum similar to LNi_2^+ . Again two sub-spectra are present, where sub1 exhibits axial and sub2 isotropic symmetry (Fig. 6.29). Sub1 shows resonances at g values of $g_x = 2.10$, $g_y = 2.30$ and $g_z = 2.32$ and sub2 shows signals at $g_x = 2.02$ and $g_y = g_z = 2.00$ but can still be discussed as isotropic. Gaussian line shapes were used and line widths of $W_x = 38.0$, $W_y = 35.1$ and $W_z = 80.0$ for sub1 and of $W_x = 25.0$, $W_y = 68.0$ and $W_z = 70.0$ for sub2 were used. That the simulated and experimental curves differ slightly derives primarily from the low intensity of the EPR signal and the

Fig. 6.29 EPR spectrum of LCuNi^{2+} generated via electrochemical oxidation and measured in frozen CH_2Cl_2 at 150 K



insufficient baseline correction. Additionally, trace amounts of sub3 might be present. As observed for the electrochemically synthesized LNi_2^+ , the main species here is sub1 with 97 %.

The recorded spectrum resembles the spectrum observed for LNi_2^+ . Hence, the copper ion has to be EPR silent, which can only be realized by either a copper-centered oxidation to Cu^{III} or a strong antiferromagnetic coupling of Cu^{II} to a ligand-based radical. Due to that and because of the absence of any hyperfine coupling to a copper core, the oxidation possibility of ${}^2\text{LCu}^{\text{II}}\text{Ni}^{\text{II}}$ with its diamagnetic ligand scaffold and a Cu^{II} core can be ruled out. The similarity of EPR spectra of LNi_2^+ and LCuNi^{2+} additionally reveals that the same oxidative processes occurred in both compounds.

The g values are indicative of sub1 representing a nickel(III) complex and sub2 of representing a ligand-centered radical. These two species coexist. The presence of an equilibrium of a nickel(III) complex and a ligand-centered radical always includes, that an intramolecular redox reaction between the ligand and the nickel ion occurred. Thus, ${}^+\text{L}^+\text{Cu}^{\text{II}}\text{Ni}^{\text{II}}$ and $\text{L}^+\text{Cu}^{\text{II}}\text{Ni}^{\text{III}}$ can be understood as resonance structures, in which the unpaired electron is either located on the ligand or on the nickel ion. The two remaining species $\text{L}^+\text{Cu}^{\text{III}}\text{Ni}^{\text{II}}$ and ${}^+\text{L}^+\text{Cu}^{\text{II}}\text{Ni}^{\text{II}} \leftrightarrow \text{L}^+\text{Cu}^{\text{II}}\text{Ni}^{\text{III}}$ (in case of a strong antiferromagnetic coupling between one ligand radical and the unpaired electron located on the copper center) might be the origin for the observed EPR spectrum. Which of the two solution models the present state best cannot be determined and needs further investigation.

Upon chemical oxidation using AgBF_4 , the EPR spectrum of LCuNi^{2+} consists of three subspectra, with a ratio of sub1:sub2:sub3 of 50:30:20 (Fig. 6.30). Thus, the metal-centered radical remains as the main species, in contrast to observations made for LNi_2^+ , where the ligand-centered radical became dominant in the

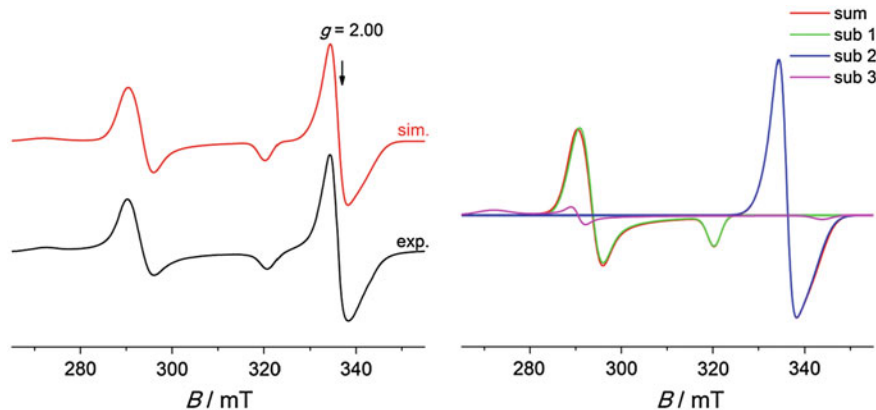
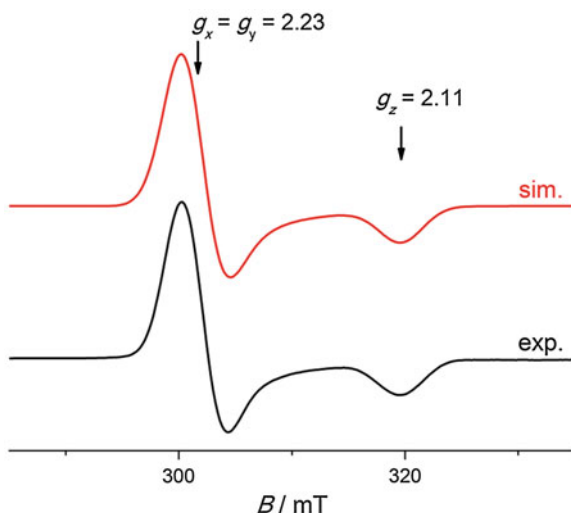


Fig. 6.30 *Left* Experimental and simulated spectrum of LCuNi^{2+} measured in CH_2Cl_2 as a frozen glass at 150 K. *Right* Composition of the simulation (sum) with sub1, sub2 and sub3

Fig. 6.31 EPR spectrum of LCuNi^{2+} after addition of pyridine and its simulation



chemically oxidized sample. Addition of pyridine to a sample of LCuNi^{2+} resulted in the formation of an axial spectrum with g values of $g_x = g_y = 2.23$ and $g_z = 2.11$ due to axial coordination (Fig. 6.31 and Sect. 6.2.3, Fig. 6.18).

References

1. M.M. Khusniyarov, E. Bill, T. Weyhermüller, E. Bothe, K. Wieghardt, *Angew. Chem. Int. Ed.* **50**, 1652–1655 (2011)
2. J. Heinze, *Angew. Chem. Int. Ed.* **23**, 831–847 (1984)
3. W. Kaim, A. Klein, M. Glöckle, *Acc. Chem. Res.* **33**, 755–763 (2000)
4. R.S. Drago, *Physical Methods for Chemists*, 2nd edn. (Saunders College Publishing, New York, 1992)
5. N.G. Connelly, W.E. Geiger, *Chem. Rev.* **96**, 877–910 (1996)
6. D.M. D'Alessandro, F.R. Keene, *Chem. Soc. Rev.* **35**, 424–440 (2006)
7. R.J. Crutchley, *Adv. Inorg. Chem.* **41**, 273–325 (1994)
8. S.F. Nelsen, *Chem.-Eur. J.* **6**, 581–588 (2000)
9. M.D. Ward, *Chem. Soc. Rev.* **24**, 121–134 (1995)
10. K.D. Demadis, C.M. Hartshorn, T.J. Meyer, *Chem. Rev.* **101**, 2655–2686 (2001)
11. D. Unseld, V.V. Krivykh, K. Heinze, F. Wild, G. Artus, H. Schmalle, H. Berke, *Organometallics* **18**, 1525–1541 (1999)
12. W. Kaim, W. Bruns, S. Kohlmann, M. Krejčík, *Inorg. Chim. Acta* **229**, 143–151 (1995)
13. T.-Y. Liu, Y.J. Chen, C.-C. Tai, K.S. Kwan, *Inorg. Chem.* **38**, 674–679 (1999)
14. T.T. Chin, R.N. Grimes, W.E. Geiger, *Inorg. Chem.* **38**, 93–99 (1998)
15. M. Dunaj-Jurčo, G. Ondrejovič, M. Melník, J. Garaj, *Coord. Chem. Rev.* **83**, 1–28 (1988)
16. R.R. Gagne, C.L. Spiro, T.J. Smith, C.A. Hamann, W.R. Thies, A.D. Shiemke, *J. Am. Chem. Soc.* **103**, 4073–4081 (1981)
17. R.C. Long, D.N. Hendrickson, *J. Am. Chem. Soc.* **105**, 1513–1521 (1983)
18. R.R. Gagne, C.A. Koval, T.J. Smith, M.C. Cimolino, *J. Am. Chem. Soc.* **101**, 4571–4580 (1979)

19. M. Gennari, J. Pécaut, S. DeBeer, F. Neese, M.-N. Collomb, C. Duboc, *Angew. Chem. Int. Ed.* **50**, 5662–5666 (2011)
20. S. Roeser, M.Z. Ertem, C. Cady, R. Lomoth, J. Benet-Buchholz, L. Hammarström, B. Sarkar, W. Kaim, C.J. Cramer, A. Llobet, *Inorg. Chem.* **51**, 320–327 (2011)
21. S. Baitalik, S. Dutta, P. Biswas, U. Flörke, E. Bothe, K. Nag, *Eur. J. Inorg. Chem.* **2010**(4), 570–588 (2010)
22. G.C. Allen, N.S. Hush, *Prog. Inorg. Chem.* **8**, 357–390 (1967)
23. P. Day, N.S. Hush, R.J.H. Clark, *Phil. Trans. R. Soc. A* **366**, 5–14 (2008)
24. Y. Wang, B.T. Hauser, M.M. Rooney, R.D. Burton, K.S. Schanze, *J. Am. Chem. Soc.* **115**, 5675–5683 (1993)
25. A. Vogler, H. Kunkely, *Comments Inorg. Chem.* **9**, 201–220 (1990)
26. B. K. Teo, *EXAFS Spectroscopy: principles and applications* (Plenum Publishing Corporation, New York, 1981)
27. L.S. Kau, D.J. Spira-Solomon, J.E. Penner-Hahn, K.O. Hodgson, E.I. Solomon, *J. Am. Chem. Soc.* **109**, 6433–6442 (1987)
28. J.L. DuBois, P. Mukherjee, T.D.P. Stack, B. Hedman, E.I. Solomon, K.O. Hodgson, *J. Am. Chem. Soc.* **122**, 5775–5787 (2000)
29. R. Sarangi, N. Aboeella, K. Fujisawa, W.B. Tolman, B. Hedman, K.O. Hodgson, E.I. Solomon, *J. Am. Chem. Soc.* **128**, 8286–8296 (2006)
30. W. Plass, *Chem. unserer Zeit* **32**, 323–333 (1998)
31. M.W. Renner, J. Fajer, *J. Biol. Inorg. Chem.* **6**, 823–830 (2001)
32. A. Wolberg, J. Manassen, *J. Am. Chem. Soc.* **92**, 2982–2991 (1970)
33. A. Wolberg, J. Manassen, *Inorg. Chem.* **9**, 2365–2367 (1970)
34. D. Dolphin, T. Niem, R.H. Felton, I. Fujita, *J. Am. Chem. Soc.* **97**, 5288–5290 (1975)
35. E.C. Johnson, T. Niem, D. Dolphin, *Can. J. Chem.* **56**, 1381–1388 (1978)
36. D. Chang, T. Malinski, A. Ulman, K.M. Kadish, *Inorg. Chem.* **23**, 817–824 (1984)
37. D. Kim, L.A. Miller, T.G. Spiro, *Inorg. Chem.* **25**, 2468–2470 (1986)
38. P.A. Connick, K.A. Macor, *Inorg. Chem.* **30**, 4654–4663 (1991)
39. J. Seth, V. Palaniappan, D.F. Bocian, *Inorg. Chem.* **34**, 2201–2206 (1995)
40. A. B. Goodman, J. B. Raynor, in *Advances in Inorganic Chemistry and Radiochemistry*, vol. 13, ed. by H.J. Emeléus, A.G. Sharpe (Academic Press, New York, 1970)
41. T. Storr, E.C. Wasinger, R.C. Pratt, T.D.P. Stack, *Angew. Chem. Int. Ed.* **46**, 5198–5201 (2007)
42. T. Storr, P. Verma, Y. Shimazaki, E.C. Wasinger, T.D.P. Stack, *Chem. -Eur. J.* **16**, 8980–8983 (2010)
43. G.J. Colpas, M.J. Maroney, C. Bagyinka, M. Kumar, W.S. Willis, S.L. Suib, P.K. Mascharak, N. Baidya, *Inorg. Chem.* **30**, 920–928 (1991)
44. R. Sarangi, M. Dey, S.W. Ragsdale, *Biochemistry* **48**, 3146–3156 (2009)
45. L.K. Blusch, K.E. Craig, V. Martin-Diaconescu, E. Bill, A. B. McQuarters, S. Dechert, S. DeBeer, N. Lehnert, F. Meyer, *J. Am. Chem. Soc.* doi:[10.1021/ja406176e](https://doi.org/10.1021/ja406176e)

Chapter 7

Summary and Outlook

During this thesis research, the synthesis of a long-sought Siamese-twin porphyrin was achieved with the chemical structure depicted in Fig. 7.1. Characterization of the deep-greenish compound by NMR spectroscopy and X-ray analysis revealed a severely twisted geometry, which originates from the steric hindrance in its backbone. LH_4 is neither aromatic nor anti-aromatic applying Hückel's and Möbius' concepts of aromaticity. As the pyrazole units disrupt the conjugation pathway. The two-electron oxidation of LH_4 which would yield [26] Siamese-twin porphyrin, a Möbius anti-aromatic analog, was not feasible. As (expanded) porphyrins are known to be highly pH sensitive, protonation studies were performed and followed using NMR and UV-vis spectroscopy. In accordance with its non-aromatic character, only subtle color changes were observed upon protonation, and titration revealed the macrocycle to be dibasic. The twisted geometry implies helical chirality and first evidence of the presence of a racemic mixture was found in the crystal packing. Chiral resolution of the *P* and *M* enantiomers was realized with a chiral stationary phase and their absolute stereostructures could be assigned using quantum chemical calculations.

With this well-studied ligand in hand, several nickel(II) and copper(II) complexes could be synthesized by reaction with the corresponding metal acetate salts. Besides the two homobimetallic complexes, LCu_2 and LNi_2 , the monometallic nickel(II) complex LH_2Ni could also be synthesized which was used as a precursor to accomplish the synthesis of the heterobimetallic compound LCuNi . Solid-state structures were obtained for LCu_2 , LNi_2 and LH_2Ni . Each metal ion is bound in a square planar fashion, while the two pockets are severely twisted. The overall torsion is largest in LNi_2 . The electronic ground state of these complexes was thoroughly studied taking advantage of a multitude of spectroscopic methods, including ESI-MS, NMR, EPR, UV-vis, CD and MCD spectroscopy, SQUID measurements and X-ray diffraction. The twisted geometry generated unexpected and unprecedented findings, such as the observed ferromagnetic coupling for the two pyrazolate-bridged unpaired spins of the copper(II) ions of LCu_2 . Chiral resolution of the two homobimetallic complexes was also successful.

Inspired by the naturally enzymes cytochrome P450 and methane monooxygenase, the complexes of the Siamese-twin porphyrin were designed to exhibit

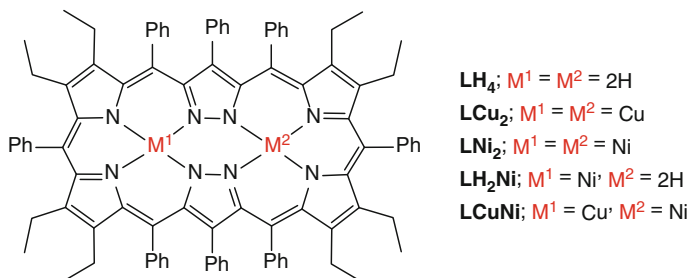


Fig. 7.1 Overview of the synthesized ligand and its mono and bimetallic nickel(II) and copper(II) complexes

striking redox properties. Electrochemical studies were performed upon each presented compound. While the free-base ligand LH_4 and the monometallic nickel(II) complex LH_2Ni showed mostly irreversible redox features, the redox properties of the bimetallic complexes proved to show greater potential. Overall, five single electron redox steps were observed for each bimetallic complex of which two were chemically reversible. SWV measurements and bulk electrolysis were used to further investigate the bimetallic complexes.

The two oxidation products LM_2^+ and LM_2^{2+} could be synthesized chemically using silver(I) salts and the isolation of pure quantitative amounts helped to investigate the oxidized species. NMR, EPR, UV-vis and XA spectroscopy and X-ray diffraction were used to answer the question of the location of the oxidation reactions. Though the obtained data are somewhat ambiguous, they point to ligand-centered oxidation processes for LCu_2 . In LNi_2^+ and LCuNi^{2+} a ligand-centered radical and a nickel(III) complex seem to coexist in solution according to EPR spectroscopy. With these experiments, the non-innocence of the Siamese-twin porphyrin is unequivocally evidenced.

With the knowledge and understanding of the ground states of the Siamese-twin porphyrin and its complexes, as well as first information about its redox chemistry, synthetic procedures can now be expanded to metal ions capable of exhibiting more versatile redox states, such as manganese, iron and ruthenium. Especially against the biomimetic background, iron complexes of the Siamese-twin porphyrin are desirable. These complexes should be investigated with respect to their oxygen activating potential and their ability to act as catalysts in oxidation or oxygenation reactions of small organic molecules.

Chapter 8

Experimental Section

8.1 Instruments and Materials

NMR Spectroscopy. ^1H and ^{13}C NMR spectra were recorded on Bruker Avance 300, 400 or 500 MHz spectrometers. ^{13}C NMR spectra were generally measured in proton-decoupled mode. Chemical shifts are reported in ppm relative to residual proton signals of CD_2Cl_2 at 5.32 ppm or DMSO at 2.50 ppm. Respectively the chemical shifts in ^{13}C NMR refer to the CD_2Cl_2 carbon atom at $\delta = 53.8$ ppm or to the DMSO carbon atoms at $\delta = 39.5$ ppm [1].

UV-vis Spectroscopy. UV-vis spectra were recorded at room temperature with a Varian Cary 50 spectrometer using quartz cuvettes ($d = 1$ cm) or equipped with a glass fiber-optics-cable and a Hellma quartz immersion probe. UV-vis-NIR spectra were recorded on a Varian Cary 5,000 spectrophotometer. If not mentioned otherwise, CH_2Cl_2 was used as solvent.

Infrared Spectroscopy. IR spectra were recorded on a Digilab Excalibur FTS 3,000 spectrometer (KBr pellets). The given intensity in the experimental section is abbreviated as follows: vs (very strong), s (strong), m (medium), w (weak).

Mass Spectrometry. ESI-MS measurements were recorded on Applied Biosystems *API 2,000* spectrometer. HRMS measurements were recorded on a Bruker FTICR-MS APEX IV. The Bruker program XMass was used for simulations.

Susceptibility Measurements. Susceptibility measurements were carried out with a Quantum-Design MPMS-5S SQUID magnetometer equipped with a 5 Tesla magnet. The powdered sample was contained in a Teflon bucket and fixed in a non-magnetic sample holder. Each raw data file for the measured magnetic moment was corrected for the diamagnetic contribution of the sample holder and the Teflon bucket. The molar susceptibility data were corrected for the diamagnetic contribution. Simulation of the experimental data with a full-matrix diagonalization of exchange coupling and Zeeman splitting was performed with the *JulX* program (E. Bill: Max-Planck Institute for Bioinorganic Chemistry, Mülheim/Ruhr, Germany)

Magnetic Circular Dichroism (MCD). The MCD setup employs an OXFORD SM4000 cryostat and a JASCO J-815 CD spectrometer. The SM4000 cryostat

consists of a liquid helium-cooled superconducting magnet providing horizontal magnetic fields of 0–7 T. The J-815 spectrometer uses a gaseous nitrogen-cooled xenon lamp and a detector system consisting of two interchangeable photomultiplier tubes in the UV–vis and NIR range. The samples were loaded into a 1.5–300 K variable temperature insert (VTI), which offers optical access to the sample via four optical windows made from Suprasil B quartz. The MCD spectra were measured in $[\Theta] = \text{mdeg}$ and manually converted to $\Delta\epsilon$ ($\text{M}^{-1}\text{cm}^{-1}\text{T}^{-1}$) using the conversion factor $\Delta\epsilon = \Theta/(32980.3 \text{ cdB})$, where c is the concentration, B the magnetic field, and d the path length. The product cd can be substituted by $A_{\text{MCD}}/\epsilon_{\text{UV-vis}}$, where A is the absorbance of the sample measured by the CD spectrometer. Complete spectra were recorded at different temperatures (2, 5, 10, 20, and 100 K) and magnetic fields (0–7 T) to obtain the VTVH data for all unambiguous MCD bands. This was done by varying the field at a specific temperature. The optical spectra were deconvoluted using the program PeakFit. All measurements were carried out at the University of Michigan in cooperation with N. Lehnert and coworkers.

Electron Paramagnetic Resonance (EPR) Measurements. X-band EPR derivative spectra in the temperature range of 120–298 K were recorded on a Bruker ELEXSYS E500 spectrometer, equipped with a ER 049 X microwave bridge, an ER 083 CS magnet, and a digital temperature control system ER 4131 VT using liquid nitrogen as coolant. The microwave frequency of 9.4 GHz was modulated with 5–9 G field modulation amplitude, 100 kHz field modulation frequency, and around 10 mW microwave power. Measurements at lower temperatures using liquid helium were run on Bruker E500 ELEXSYS X-band EPR spectrometer with the Bruker dual-mode cavity (ER4116DM) or a standard cavity (ER4102ST) and an Oxford Instruments helium flow cryostat (ESR 910). Microwave frequencies were measured with a Hewlett-Packard frequency counter (HP5352B), and the field control was calibrated with a Bruker NMR field probe (ER035 M).

EPR spectra without hyperfine coupling contributions were simulated with ESIM which was developed by Bill (E. Bill: Max-Planck Institute for Bioinorganic Chemistry, Mülheim/Ruhr, Germany), all others were simulated using the XSope-Sophe-XeprView [2, 3] software. Usually full matrix diagonalization was applied with the SOPHE interpolation scheme for field and angular space; two field segments and an angular grid of 40 bands have been sufficient for reproducible smooth results.

Electrochemical Measurements. Redox properties have been studied by CV, SWV and bulk electrolysis in $\text{CH}_2\text{Cl}_2/0.1 \text{ M} [\text{NBu}_4]\text{PF}_6$ (electrochemical grade) solutions. Measurements were performed using a PerkinElmer 263A potentiostat controlled by electrochemistry powersuit software. For CV and SWV a glassy carbon electrode was used as working electrode, platinum as counter electrode and silver as reference electrode. Bulk electrolysis measurements were carried out using a platinum net as working electrode, reference and counter electrode remained the same. CV and SWV spectra were measured versus $\text{Cp}^*\text{Fe}/\text{Cp}^*\text{Fe}^+$ as internal standard.

High Pressure Liquid Chromatography-Circular Dichroism (HPLC-CD).

Analytical enantiomeric resolution was performed on Jasco HPLC systems (pump PU1580, gradient unit LG-980-025 or LG-2080-04, degasser DG-2080-53 or DG-2080-54, UV detector MD-2010Plus or Erma Cr. Inc. Erc-7215) equipped with Chiralpak[®] IA or Chiralpak[®] IB (Chiral Technologies Europe) columns (4.6 × 250 mm) as the chiral phases and coupled to a Jasco 715 spectropolarimeter for the online-CD investigations scanning rate: 200 nm/min, bandwidth: 1.0 nm, response time: 0.25 s, accumulations: 3. All enantiomeric resolutions were carried out at room temperature with a constant flow rate using an isocratic solvent system consisting of EtOAc and *n*-hexane. Measurements were performed at the University of Würzburg in cooperation with G. Bringmann, Y. Hemberger and F. Witterauf.

X-ray Absorption Spectroscopy (XAS). Solid samples diluted with boron nitride were run at SSRL (Stanford Synchrotron Radiation Lightsource, 3 GeV ring) beam line 7-3 equipped with a Si(220) $\phi = 90^\circ$ double crystal monochromator. Data were collected using a PIPS detector with a Z-1 filter. Data averaging and energy calibration were performed using SixPack [4]. The first inflection points from the XANES spectral regions were set to 8980.3 eV for Zn foil (Cu samples) and to 8331.6 eV for Ni foil (Ni samples). The AUTOBK algorithm available in the Athena software package was employed for data reduction and normalization [5]. Measurements were performed in cooperation with V. Martin-Diaconescu and S. DeBeer.

Elemental Analysis. Standard CHN elemental analyses were measured on an Elementar 4.1 vario EL 3. Analytical determination of the metal content was done with an AAS 5FL Analytik Jena. The measurements were performed by the “Analytical Laboratory” of the Chemistry Department at the University of Göttingen.

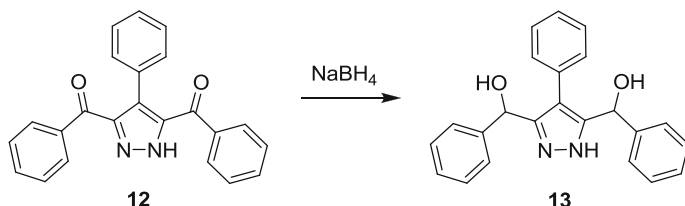
Column Chromatography. Silica gel column chromatography was performed on Machery-Nagel MN60 (0.063–0.2 mm/70–230 mesh ASTM) silica gel. Thin layer chromatography (TLC) was carried out on fluorescence active polyester sheets coated with silica gel Machery-Nagel MN60 (Polygram[®] SIL G/UV₂₅₄). For size exclusion chromatography GE Healthcare Sephadex[™] LH-20 soaked with CH₂Cl₂ was used.

Chemicals. Compounds 3,5-dibenzoyl-4-phenyl-1*H*-pyrazole (**3**) [6], 3,4-dihydropyrrole (**14b**) [7, 8], dipyrromethane **26** and dipyrromethene **27** [9] were synthesized according to reported methods. Unless otherwise noted, materials obtained from commercial suppliers (Aldrich, Deutero, Fluka and Grüssing) were used without further purification, except CH₂Cl₂, acetone and toluene. Anhydrous CH₂Cl₂ was obtained by drying over and distilling from CaH₂, and acetone and nitroethane were dried using molecular sieves of pore size 3 Å and subsequent distillation. Toluene was dried with sodium and then distilled [10].

Reactions were carried out under ambient conditions unless otherwise noted. For reactions under inert argon atmosphere Schlenk techniques with appropriate glassware were applied.

8.2 Ligand Synthesis

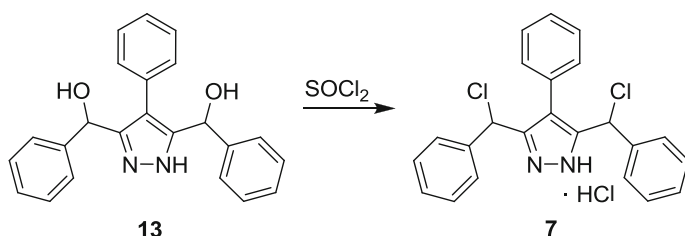
8.2.1 3,5-Bis-(hydroxy(phenyl)methyl)-4-phenyl-1H-pyrazole (13)



Under ice cooling, NaBH₄ (0.64 mg, 17.0 mmol, 2 eq) was added slowly to a solution of 3,5-dibenzoyl-4-phenyl-1H-pyrazole (**12**) (3.00 g, 8.51 mmol, 1 eq) in CHCl₃ (10 mL) and MeOH (5 mL), and stirred for 4 h. The reaction progress was controlled by TLC. After addition of MeOH (30 mL) the solution was washed twice with aqueous NH₄Cl solution (50 mL, 100 mM), and the organic phase was dried over MgSO₄. The solvent was removed under reduced pressure and the crude material purified by column chromatography (silica, *n*-hexane/EtOAc 1:2) yielding a white powder (2.41 g, 79 %). The non-chromatographed product could be used for the conversion to **7**.

Yield	2.41 g, 79 %
Empirical formular	C ₂₃ H ₂₀ N ₂ O ₂
Molecular weight/g/mol	356.42
R _f (silica, <i>n</i> -hexane/EtOAc 1:2)	0.35
¹ H NMR (300 MHz, CD ₂ Cl ₂)	δ/ppm = 5.77 (s, 1H, CH), 5.79 (s, 1H, CH), 7.02–7.29 (m, 15H, Ph)
¹³ C NMR (75 MHz, CD ₂ Cl ₂)	δ/ppm = 69.2 (COH), 69.5 (COH), 127.2 (Ph), 127.3 (Ph), 127.6 (Ph), 127.7 (Ph), 128.3 (Ph), 128.7 (Ph), 128.8 (Ph), 128.9 (Ph), 130.0 (C4), 142.5 (C3/5)
MS (ESI ⁺ , MeCN): <i>m/z</i> (%)	420 (100) [M + Na + MeCN] ⁺ , 379 (72) [M + Na] ⁺ , 339 (36) [M-OH] ⁺
MS (ESI ⁻ , MeCN): <i>m/z</i> (%)	355 (100) [M-H] ⁻
m.p.	158 °C
HRMS (ESI ⁺ , MeOH): <i>m/z</i> (%)	357.1597 (calc. 357.1598) [M + H] ⁺
IR (KBr): $\tilde{\nu}$ /cm ⁻¹	3221 (w), 2963 (w), 1714 (w), 1261 (s), 1089 (s), 1022 (s), 901 (vs), 696 (m)

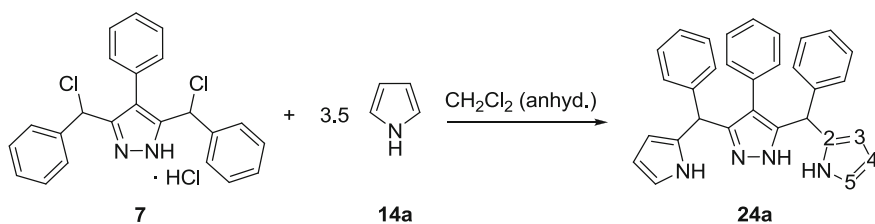
8.2.2 3,5-Bis-(chloro(phenyl)methyl)-4-phenyl-1H-pyrazole hydrochloride (7)



Under inert conditions, a molar excess of freshly distilled SOCl_2 was added to 3,5-bis-(hydroxy(phenyl)methyl)-4-phenyl-1H-pyrazole (**13**) (3.00 g, 8.42 mmol) and the mixture was stirred at r.t. for 3 d. Excessive SOCl_2 was removed under reduced pressure at r.t. and the residue was dissolved in anhydrous toluene. This was subsequently also removed under reduced pressure at r.t. The resulting yellowish, moisture sensitive solid (3.20 g, 95 %) was stored under anhydrous nitrogen atmosphere. Despite it turned red upon standing, no decomposition was detectable.

Yield	3.20 g, 95 %
Empirical formular	$\text{C}_{23}\text{H}_{19}\text{Cl}_3\text{N}_2$
Molecular weight/g/mol	429.77
^1H NMR (300 MHz, CD_2Cl_2)	$\delta/\text{ppm} = 6.15$ (s, 1H, CH), 6.17 (s, 1H, CH), 7.12–7.45 (m, 15H, Ph), 10.66 (s, 2H, NH)
^{13}C NMR (75 MHz, CDCl_3)	$\delta/\text{ppm} = 52.2$ (CCl), 120.0 (C4), 127.5 (Ph [']), 127.6 (Ph ^{''}), 128.5 (Ph), 128.6 (Ph), 128.8 (Ph), 129.0 (Ph), 129.2 (Ph), 130.9 (Ph ^{'''}), 131.0 (Ph [']), 136.3 (Ph), 145.5 (C3/5), 145.6 (C3/5)
MS (ESI ⁺ , MeCN): <i>m/z</i> (%)	393 (5) [M + H] ⁺ , 357 (36) [M-Cl] ⁺ , 338 (100) [M + OH-Cl] ⁺ , 321 (32) [M-HCl-Cl]
IR (KBr) $\bar{\nu}/\text{cm}^{-1}$	1493 (w), 1261 (m), 1013 (m), 696 (vs)

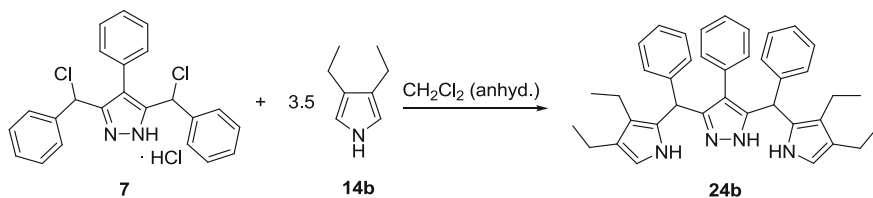
8.2.3 3,5-Bis-(1H-pyrrole-2-yl-benzyl)-1H-pyrazole (24a)



Under inert conditions, pyrrole (**14a**) (0.549 g, 8.18 mmol, 3.5 eq) was added dropwise to a solution of 3,5-bis-(chloro(phenyl)methyl)-4-phenyl-1*H*-pyrazole hydrochloride (**7**) (1.00 g, 2.33 mmol, 1 eq) in anhydrous CH₂Cl₂ (60 mL), and the mixture was stirred for 2 h at r.t. The reaction progress was controlled via TLC. The mixture was washed with H₂O (50 mL), and the organic phase separated. The aqueous phase was extracted with CH₂Cl₂ (2 × 20 mL). The combined organic phases were dried over Na₂SO₄ and the solvent was removed using rotary evaporation. The crude material was purified by column chromatography (silica, *n*-hexane/EtOAc 2:1), and isolated as a white-orange solid (0.211 g, 19.9 %). The product is sensitive to decomposition.

Yield	2.41 g, 79 %
Empirical formular	C ₃₁ H ₂₆ N ₄
Molecular weight/g/mol	454.56
R _f (silica, <i>n</i> -hexane/EtOAc 2 :1)	0.43
¹ H NMR (400 MHz, DMSO- <i>d</i> ₆)	δ/ppm = 5.32 (s, 2H, C [*] H), 5.82 (m, 2H, C3H), 5.91 (s, 4H, C4H), 6.61 (s, 2H, C5H), 7.15–7.38 (m, 15H, Ph), 6.38 (s, 2H, CH ^{pyr}), 10.51 (br, 2H, NH ^{pyr}), 12.55 (br, 1H, NH ^{pz})
¹³ C NMR (100 MHz, DMSO- <i>d</i> ₆)	δ/ppm = 29.9 (C [*]), 41.5 (C [*]), 107.3 (C3), 108.4 (C4), 117.6 (C5), 126.9 (Ph), 127.2 (Ph), 128.2 (Ph), 128.6 (Ph), 128.8 (Ph), 130.2 (Ph), 131.6 (Ph), 142.5 (Ph)
MS (ESI ⁺ , MeCN): <i>m/z</i> (%)	301.2 (100) [M-2Ph + H] ⁺ , 388.4 (30) [M-pyr] ⁺ , 455.4 (18) [M + H] ⁺ , 477.2 (68) [M + Na] ⁺
HRMS (ESI ⁺ , CH ₂ Cl ₂): <i>m/z</i> (%)	477.2079 (calc. 477.2055) [M + Na] ⁺
IR (KBr) $\tilde{\nu}$ /cm ⁻¹	1612 (w), 1468 (w), 1452 (w), 1250 (w), 1072 (w), 1013(w), 768 (m), 718 (s), 701(vs)

8.2.4 3,5-Bis-(3,4-diethyl-1*H*-pyrrole-2-yl-benzyl)-1*H*-pyrazole (**24b**)

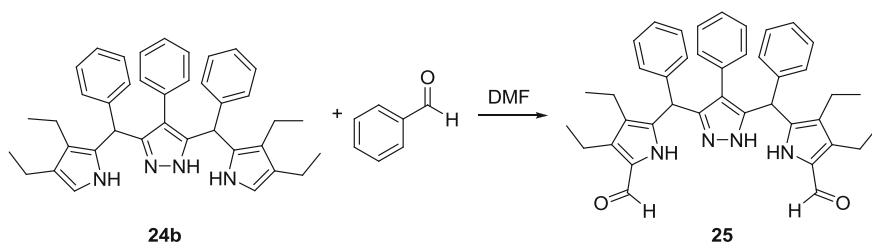


To a solution of 3,5-bis-(chloro(phenyl)methyl)-4-phenyl-1*H*-pyrazole hydrochloride (**7**) (1.00 g, 2.33 mmol, 1 eq) in anhydrous CH₂Cl₂ (60 mL) 3,4-diethylpyrrole (**14b**) (0.95 g, 7.71 mmol, 3.5 eq) was added dropwise under inert conditions, and the reaction mixture was stirred for 2 h at r.t. Reaction progress

was controlled by TLC. The mixture was washed with H₂O (50 mL), and the organic phase separated. The aqueous phase was extracted with CH₂Cl₂ (2 × 20 mL). The combined organic phases were dried over Na₂SO₄ and the solvent was removed under reduced pressure. The crude material was purified by column chromatography (silica, *n*-hexane/EtOAc 5:1) yielding a brown-orange solid (0.50 g, 41 %). The product is sensitive to decomposition and has to be stored under inert conditions and cool temperatures.

Yield	50 mg, 41 %
Empirical formular	C ₃₉ H ₄₂ N ₄
Molecular weight/g/mol	566.78
R _f (silica, <i>n</i> -hexane/ EtOAc 4:1)	0.36
¹ H NMR (400 MHz, CD ₂ Cl ₂)	δ/ppm = 0.81 (t, ³ J (H,H) = 7.6 Hz, 6H, CH ₃), 1.15 (t, ³ J (H,H) = 7.6 Hz, 6H, CH ₃), 2.25 (q, ³ J (H,H) = 7.6 Hz, 4H, CH ₂), 2.41 (q, ³ J (H,H) = 7.6 Hz, 4H, CH ₂), 5.43 (s, 2H, C [*] H), 6.38 (s, 2H, CH ^{pyr}), 7.04–7.31 (m, 15H, Ph), 8.13 (br, 1H, NH)
¹³ C NMR (75 MHz, CD ₂ Cl ₂)	δ/ppm = 15.0 (CH ₃), 15.9 (CH ₃), 17.9 (CH ₂), 19.0 (CH ₂), 39.8 (C [*]), 113.6, 113.7, 121.0, 121.1, 125.7, 126.9, 127.2, 127.5, 128.5, 128.6, 128.9, 129.1, 129.2, 130.5, 133.0, 143.0 (C _{3/5})
MS (ESI ⁺ , MeCN): <i>m/z</i>	567 (85) [M + H] ⁺ , 444 (23) [M-C ₈ H ₁₂ N] ⁺ , 353 (100) [M-C ₁₅ H ₁₉ N] ⁺ (%)
MS (ESI ⁻ , MeCN): <i>m/z</i>	565 (100) [M-H] ⁻ (%)
m.p.	126 °C
HRMS (ESI ⁺ , CH ₂ Cl ₂) <i>m/z</i> (%)	589.291 (calc. 589.3302) [M + H] ⁺
IR (KBr): $\tilde{\nu}$ /cm ⁻¹	2961 (vs), 2927 (m), 1700 (m), 1456 (m), 1077 (w), 699 (vs)

8.2.5 3,5-Bis-(3,4-diethyl-5-formyl-1H-pyrrole-2-yl-benzyl)-1H-pyrazole (25)

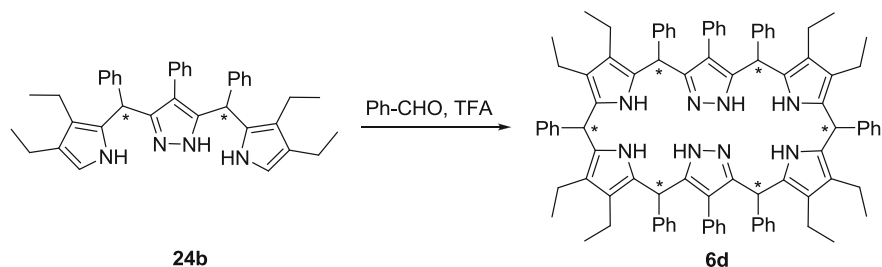


3,5-Bis-(3,4-diethyl-1H-pyrrole-2-yl-benzyl)-1H-pyrazole **24b** (200 mg, 0.35 mmol) was dissolved in DMF (313 mg, 4.28 mmol, 12.5 eq) and cooled down to

0 °C using an ice bath. Benzoylchloride (484 mg, 3.44 mmol, 10 eq) was added. After stirring the reaction mixture for 2 h at 0 °C the temperature was raised to r.t. followed by additional stirring for 3 h. A saturated sodium carbonate solution (4 mL) and ethanol (4 mL) were added and the reaction mixture was stirred overnight. The addition of CH₂Cl₂ led to a phase separation, the organic phase was extracted with water. The aqueous phase was washed twice with CH₂Cl₂ and the combined organic phases were dried over MgSO₄. The crude product was purified via column chromatography (silica, *n*-hexane/EtOAc 2 :1) and **25** was isolated as a brown solid (50 mg, 23 %).

Yield	50 mg, 23 %
Empirical formular	C ₄₁ H ₄₂ N ₄ O ₂
Molecular weight/g/mol	622.8
R _f (silica, <i>n</i> -hexane/EtOAc 1:1)	0.52
¹ H NMR (200 MHz, CD ₂ Cl ₂)	δ/ppm = 0.79 (t, 6H, CH ₃), 1.22 (t, 6H, CH ₃), 2.22 (q, 4H, CH ₂), 2.69 (q, 4H, CH ₂), 5.59 (s, 2H, CH), 6.88–7.63 (m, 15H, ph), 9.34 (s, 2H, CHO), 10.18 (s, 2H, NH)
¹³ C NMR (75 MHz, CD ₂ Cl ₂)	δ/ppm = 15.8 (CH ₃), 17.0 (CH ₃), 17.5 (CH ₂), 17.8 (CH ₂), 39.3 (C*), 125.2, 127.4, 127.9, 128.3, 129.0, 130.6, 177.0 (CHO)
MS (ESI ⁺ , MeCN): <i>m/z</i> (%)	623.4 (12) [M + H] ⁺ , 645.4 (100) [M + Na] ⁺
MS (ESI ⁻ , MeCN): <i>m/z</i> (%)	621.3 (71) [M-H] ⁻
IR (KBr): $\tilde{\nu}$ /cm ⁻¹	3264 (w), 2930 (s), 2929 (s), 1626 (vs), 1444 (m), 1359 (w), 1260 (m), 1080 (m), 1013 (m), 814 (w), 428 (vs)

8.2.6 Siamese-twin Porphyrinogen **6d**

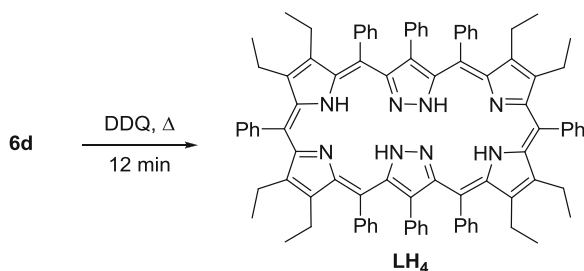


Benzaldehyde (1.79 mL of a 100 mM solution in CH₂Cl₂; 19.1 mg, 0.18 mmol, 1 eq) and TFA (180 μL of a 1 M in CH₂Cl₂; 20.5 mg, 0.18 mmol, 1 eq) were

diluted with CH_2Cl_2 (14.9 mL) and shielded from light. 3,5-Bis-(3,4-diethyl-1*H*-pyrrole-2-yl-benzyl)-1*H*-pyrazole (**24b**) (1.79 mL of a 100 mM solution in CH_2Cl_2 ; 100 mg, 0.18 mmol, 1 eq) was added and stirred for 2 h. Reaction progress was controlled by TLC. The solvent was removed using rotary evaporation and the obtained violet solid was purified by column chromatography (silica, *n*-hexane/*EtOAc* 5:1). The product was obtained as a yellow solid (67.5 mg, 57 %).

Yield	67.5 mg, 57 %
Empirical formula	$\text{C}_{92}\text{H}_{92}\text{N}_8$
Molecular weight/g/mol)	1309.77
R_f (silica, <i>n</i> -hexane/ <i>EtOAc</i> 2:1)	0.79
^1H NMR (500 MHz, CD_2Cl_2)	$\delta/\text{ppm} = 0.60\text{--}1.04$ (m, 24H, CH_3), 1.94–2.53 (m, 16H, CH_2), 5.20–5.57 (m, 6H, CH), 6.70–7.43 (m, 40H, Ph)
^{13}C NMR (125 MHz, CD_2Cl_2)	$\delta/\text{ppm} = 14.2\text{--}18.4$ (CH_3), 38.5–41.5 (CH_2), 118.7–123.1, 127.6–133.1, 142.0–144.3
MS (ESI ⁺ , MeCN) m/z (%)	1309.7 [$\text{M} + \text{H}$] ⁺
HRMS (ESI ⁺ , MeCN) m/z (%)	1309.7514 (calc. 1309.7518) [$\text{M} + \text{H}$] ⁺
IR (KBr); $\tilde{\nu}/\text{cm}^{-1}$	2959 (m), 2926 (w), 2866 (w), 1493 (s), 1450 (s), 1216 (vw), 700 (vs)
UV–vis/nm ($\epsilon/\text{M}^{-1}\text{cm}^{-1}$)	436 nm (1183), 379 (1274)

8.2.7 Siamese-twin Porphyrin LH_4

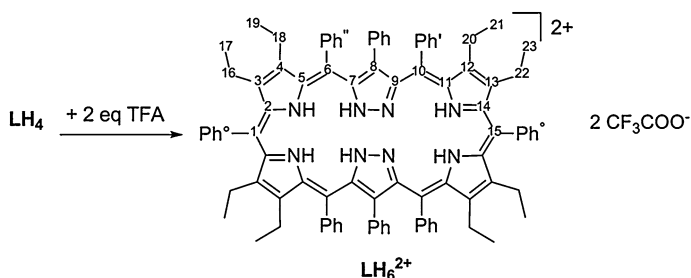


To a solution of the porphyrinogen **6d** (0.40 g, 0.31 mmol) in toluene (60 mL) was added DDQ (0.28 g, 1.22 mmol, 4 eq) all at once, and the mixture was heated to 80 °C for 12 min using a preheated oil bath. Reaction progress was monitored by TLC. The solvent was removed under reduced pressure. The crude solid

material was purified by column chromatography (silica, *n*-hexane/EtOAc 2:1). The dark green fraction was collected to provide **LH₄**. Minimal amounts of acetone were added and the suspension filtered to yield pure **LH₄** (0.18 mg, 45 %).

Yield	0.18 g, 45 %
Empirical formular	C ₉₂ H ₈₄ N ₈
Molecular weight/g/mol)	1301,70
R _f (silica, <i>n</i> -hexane/EtOAc 2:1)	0.67
¹ H NMR (500 MHz, CD ₂ Cl ₂ , 248 K)	δ/ppm = 0.40 (t, 6H, CH ₃), 0.44 (t, 6H, CH ₃), 0.54 (t, 6H, CH ₃), 0.55 (t, 6H, CH ₃), 0.77–0.93 (m, 2H, CH ₂), 1.14–1.26 (m, 2H, CH ₂), 1.34–1.46 (m, 4H, CH ₂), 1.47–1.61 (m, 4H, CH ₂), 1.81–1.93 (m, 2H, CH ₂), 1.93–2.05 (m, 2H, CH ₂), 6.17 (d, 2H, Ph), 6.29 (t, 2H, Ph), 6.56 (t, 2H, Ph), 6.73–6.83 (m, 4H, Ph), 6.84 (d, 2H, Ph), 6.97 (t, 2H, Ph), 7.01 (d, 2H, Ph), 7.05 (d, 2H, Ph), 7.15–7.37 (m, 18H, Ph), 7.47–7.57 (m, 4H, Ph), 11.40 (s, 2H, NH ^{pyr}), 13.36 (s, 2H, NH ^{pzc})
¹³ C NMR (125 MHz, CD ₂ Cl ₂ , 248 K)	δ/ppm = 14.5 (CH ₃), 15.4 (CH ₃), 15.7 (CH ₃), 16.0 (CH ₃), 17.8 (CH ₂), 17.9 (CH ₂), 18.2 (CH ₂), 18.7 (CH ₂), 105.8 (Ph), 1114.0 (Ph), 123.8 (Ph), 124.1 (Ph), 124.2 (Ph), 125.9 (Ph), 126.2 (Ph), 126.3 (Ph), 126.8 (Ph), 126.9 (Ph), 127.0 (Ph), 127.1 (Ph), 127.4 (Ph), 127.5 (Ph), 127.6 (Ph), 127.7 (Ph), 130.5 (Ph), 131.4 (Ph), 132.2 (Ph), 132.4 (Ph), 132.9 (Ph), 133.0 (Ph), 133.7 (Ph), 135.1 (Ph), 137.9 (Ph), 138.8 (Ph), 139.1 (Ph), 140.3 (Ph), 141.1 (Ph), 141.3 (Ph), 144.9 (Ph), 147.4 (Ph), 147.9 (Ph), 150.8 (Ph), 151.2 (Ph), 167.2 (Ph)
MS (ESI ⁺ , MeCN): <i>m/z</i> (%)	651.4 [M + 2H] ²⁺ , 1301.5 [M + H] ⁺
HRMS (ESI ⁺ , MeCN): <i>m/z</i> (%)	1301.6895 (calc. 1301.6892) [M + H] ⁺
IR (KBr): $\tilde{\nu}$ /cm ⁻¹	2963 (vw), 2926 (vw), 1673 (vw), 1506 (m), 1206 (s), 1155 (vs), 525 (w)
UV–vis/nm (ϵ /M ⁻¹ cm ⁻¹)	734 (17381), 639 (48939), 390 (110803), 307 (38583)

8.2.8 Siamese-twin Porphyrin LH₆²⁺

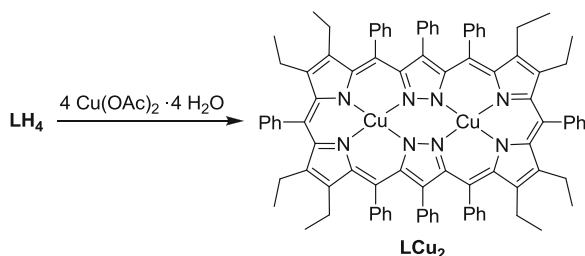


To a solution of **LH₄** (0.05 g, 0.038 mmol) in CH₂Cl₂ (5 mL) was added TFA (153.6 μL of a 0.5 M in CH₂Cl₂, 2 eq) and the solvent removed under reduced pressure.

Yield	0.05 g, 100 %
Empirical formular	C ₉₂ H ₈₆ N ₈
Molecular weight/g/mol)	1303,70
R _f (silica, <i>n</i> -hexane/EtOAc 2:1)	0.63
¹ H NMR (500 MHz, CD ₂ Cl ₂ , 248 K)	δ/ppm = 0.57 (t, 6H, C21H ₃), 0.67 (t, 12H, C19/23H ₃), 0.74 (t, 6H, C17H ₃), 1.08 (m, 2H, C16H ₂), 1.30 (m, 2H, C22H ₂), 1.69 (m, 2H, C18H ₂), 1.79 (m, 6H, C18/20H ₂), 1.93 (m, 2H, C22H ₂), 2.03 (m, 2H, C16H ₂), 5.96–7.03 (m, 30H, Ph, Ph', Ph''), 7.27–7.47 (m, 10H, Ph ^o), 11.52 (s(br), 2H, NH ^{pyr}), 13.24 (s (br), 2H, NH ^{pyr}), 15.32 (s(br), 2H, NH ^{pz})
¹³ C NMR (125 MHz, CD ₂ Cl ₂ , 248 K)	δ/ppm = 14.2 (C21), 14.3 (C23), 15.1 (C19), 15.33 (C17), 18.3 (C16), 18.5 (C22), 18.8 (C20), 19.2 (C18), 103.0 (C1), 103.7 (C15), 117.4 (q, CF ₃ (TFA)), 122.6 (C10), 124.9 (Ph), 126.1 (Ph), 126.5 (Ph), 126.6 (Ph'), 126.7 (Ph''), 127.5 (Ph'), 127.7 (Ph''), 127.9 (Ph'), 128.2 (Ph ^o), 128.5 (Ph'', Ph ^o), 128.8 (Ph ^o), 129.1 (C8), 130.3 (Ph'), 130.8 (Ph), 131.4 (Ph), 131.6 (Ph''), 132.4 (Ph''), 132.6 (Ph'), 132.9 (Ph), 133.5 (Ph ^o , Ph ^o), 135.1 (Ph''), 136.9 (Ph ^o), 138.1 (Ph'), 138.2 (C9), 139.5 (C5), 142.4 (C3), 143.3 (C6), 144.1 (C13), 144.5 (C11), 147.8 (C7), 148.6 (C12), 150.1 (C4), 156.0 (C2), 159.5 (q, CF ₃ C (TFA)), 160.4 (C14)
UV-vis/nm (ε/M ⁻¹ cm ⁻¹)	795 (17509), 668 (86481), 400 (104133), 298 (40683)

8.3 Complex Synthesis

8.3.1 Siamese-twin Porphyrin Dicopper(II) Complex LCu₂

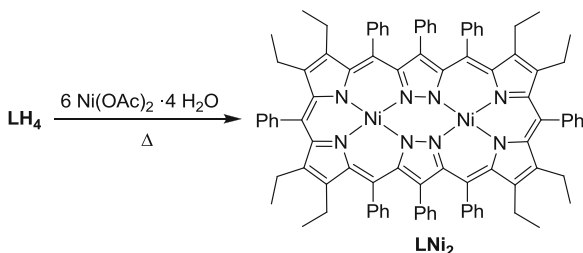


LH₄ (0.11 g, 0.08 mmol) was dissolved in a mixture of CH₂Cl₂ (5 mL) and methanol (15 mL) to which Cu(OAc)₂ · H₂O (0.07 g, 0.34 mmol, 4 eq) was added. The mixture was stirred for two hours. Then, the solvent was removed

under reduced pressure and the crude solid product was purified by column chromatography (silica, *n*-hexane/EtOAc 9:1). The dark-blue fraction was isolated and the solvent removed under reduced pressure. Analytically pure crystals were obtained by slow evaporation of a saturated toluene solution of **LCu₂**.

Yield	35 mg, 29 %
Empirical formular	C ₉₄ H ₈₀ Cu ₂ N ₈
Molecular weight (g/mol)	1448.79
R _f (silica, <i>n</i> -hexane/EtOAc 6:1)	0.90
MS (ESI ⁺ , MeCN): <i>m/z</i> (%)	1422.3 [M] ⁺
HRMS (ESI ⁺ , MeCN): <i>m/z</i> (%)	1422.5138 (calc. 1422.5093) [M] ⁺
IR (KBr): $\tilde{\nu}$ /cm ⁻¹	2965 (vw), 2926 (vw), 1629 (w), 1433 (vs), 1113 (w), 1015 (w), 694 (w)
UV-vis/nm (ϵ /M ⁻¹ cm ⁻¹)	628 (21567), 391 (45952)
Elemental Analysis	Found (Calcd.) for C ₉₂ H ₈₀ Cu ₂ N ₈ · 4 toluene in %: C 79.36 (80.37), H 6.30 (6.29), N 6.21 (6.25)

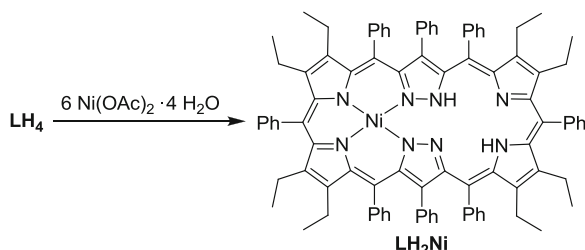
8.3.2 Siamese-twin Porphyrin Dinickel(II) Complex **LNi₂**



To a solution of the Siamese-twin porphyrin **LH₄** (0.10 g, 77.0 μmol) in a mixture of CH₂Cl₂ (5 mL) and MeOH (10 mL) Ni(OAc)₂ · 4 H₂O (382 mg, 1.54 mmol, 20 eq) was added. The mixture was heated to reflux for 24 h and the reaction was monitored via TLC. The solvent was removed under reduced pressure and the crude solid product purified by column chromatography (silica, *n*-hexane/EtOAc 4:1). The red–purple fraction was isolated and evaporated to dryness. Analytically pure crystals were obtained by slow evaporation of a saturated toluene solution of **LNi₂**.

Yield	67.5 mg, 62 %
Empirical formular	C ₉₂ H ₈₀ N ₈ Ni ₂
Molecular weight/g/mol	1415.06
R _f (silica, <i>n</i> -hexane/EtOAc 2:1)	0.83
¹ H NMR (500 MHz, CD ₂ Cl ₂)	δ/ppm = 0.60 (t, 12H, CH ₃), 0.64 (t, 12H, CH ₃), 1.29–1.43 (m, 4H, CH ₂), 1.58–1.73 (m, 4H, CH ₂), 1.92–2.10 (m., 8H, CH ₂), 6.28–7.64 (m, 40H, Ph)
¹³ C NMR (125 MHz, CD ₂ Cl ₂)	δ/ppm = 15.4, 16.0, 19.1, 19.6, 125.2, 126.6, 126.9, 127.4, 127.5, 128.0, 128.2, 146.3, 148.7
MS (ESI ⁺ , CH ₂ Cl ₂ /MeCN): <i>m/z</i> (%)	1413.5 (100) [M] ⁺
HRMS (ESI ⁺ , CH ₂ Cl ₂ /MeCN): <i>m/z</i> (%)	1412.5187 (calc. 1412.5208) [M] ⁺
IR (KBr): $\tilde{\nu}$ /cm ⁻¹	2963 (w), 1635 (w), 1457 (m), 1261 (m), 1110 (vs), 1018 (vs), 801 (s), 694 (m)
UV–vis/nm (ϵ /M ⁻¹ cm ⁻¹)	766 (14043), 547 (26107), 376 (61491)
Elemental Analysis	Found (Calcd.) for C ₉₂ H ₈₀ Ni ₂ N ₈ · 4 toluene in %: C 80.54 (80.81), H 6.08 (6.33), N 6.32 (6.28)

8.3.3 Siamese-twin Porphyrin Mononickel(II) Complex **LH₂Ni**



Ni(OAc)₂ · 4H₂O (114 mg, 0.46 mM, 6 eq) was added to a solution of **LH₄** (100 mg, 0.08 mmol) in CH₂Cl₂ (10 mL) and MeOH (10 mL). The mixture was stirred for 15 min at r.t. and the reaction was monitored via TLC. After removing the solvent under reduced pressure the purification was done using column chromatography (*n*-hexane/EtOAc 4:1). The obtained dark green product **LH₂Ni** was recrystallized in acetone to yield 87 mg. Crystals suitable for X-ray crystallography could be obtained via slow evaporation of a saturated solution of **LH₂Ni** in acetone.

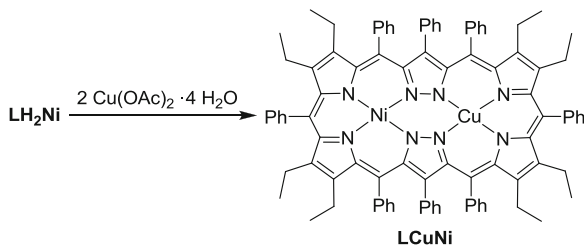
Yield	87 mg, 83 %
Empirical formular	C ₉₂ H ₈₂ N ₈ Ni
Molecular weight/g/mol	1358.38

(continued)

(continued)

Yield	87 mg, 83 %
R_f (silica, <i>n</i> -hexane/EtOAc 4:1)	0.61
^1H NMR (500 MHz, CD_2Cl_2)	$\delta/\text{ppm} = 0.63\text{--}0.73$ (m, 24H, CH_3), 1.25–1.46 (m, 6H, CH_2), 1.70–2.09 (m, 12H, CH_2), 5.67–7.59 (m, 40H, Ph), 11.76 (s, 1H, NH), 14.88 (s, 1H, NH)
^{13}C NMR (125 MHz, CD_2Cl_2)	$\delta/\text{ppm} = 14.7$ (CH_3), 14.8 (CH_3), 15.9 (CH_3), 16.3 (CH_3), 19.1 (CH_2), 19.4 (2 CH_2), 20.3 (CH_2), 105.6, 111.0, 120.4, 122.1, 124.0, 126.0, 126.3 (Ph), 127.0 (Ph), 127.2 (Ph), 127.3, 127.6 (Ph), 128.3 (Ph), 128.4 (Ph), 128.5 (Ph), 128.6 (Ph), 129.0 (Ph), 129.1 (Ph), 129.4, 130.9, 131.7 (Ph), 131.8 (Ph), 131.9, 132.5, 132.7 (Ph), 134.0 (Ph), 134.2 (Ph), 135.4, 137.5, 138.0, 138.6, 145.2, 145.4, 146.7, 147.1, 147.4, 147.9, 149.9, 151.5, 159.9, 160.4
MS (ESI^+ , $\text{CH}_2\text{Cl}_2/\text{MeCN}$): m/z (%)	1357.4 (100) $[\text{M}]^+$, 679.5 (54) $[\text{M}^{2+}]$
HRMS (ESI^+ , $\text{CH}_2\text{Cl}_2/\text{MeCN}$): m/z (%)	1357.6093 (calc. 1357.6089) $[\text{M}]^+$
IR (KBr): $\tilde{\nu}/\text{cm}^{-1}$	2970 (w), 1635 (m), 1507 (s), 1437 (m), 1113 (w), 1056 (w), 1016 (w), 697 (m)
UV-vis/nm ($\epsilon/\text{M}^{-1}\text{cm}^{-1}$)	778 (13392), 661 (29223), 394 (56455), 303 (31921)

8.3.4 Siamese-twin Porphyrin Copper(II) Nickel(II) Complex LCuNi



To addition of LH_2Ni (100 mg, 0.07 mM) in CH_2Cl_2 (10 mL) was added $\text{Cu}(\text{OAc})_2 \cdot 4\text{H}_2\text{O}$ (14.7 mg, 0.07 mM, 1 eq) and the mixture was stirred for 10 min. The reaction was monitored via TLC. The solvent was removed under reduced pressure and the crude product was then purified via column chromatography (*n*-hexane/EtOAc 2:1) to give LCuNi (90.1 mg, 87 %). Slow evaporation of a saturated solution of LCuNi in toluene yielded pure crystals.

Yield	90.1 mg, 87 %
Empirical formular	C ₉₂ H ₈₀ N ₈ CuNi
Molecular weight/g/mol	1419.91
R _f (silica, <i>n</i> -hexane/EtOAc 2:1)	0.83
MS (ESI ⁺ , CH ₂ Cl ₂ /MeCN): <i>m/z</i> (%)	1419.3 (100) [M] ⁺
HRMS (ESI ⁺ , CH ₂ Cl ₂ /MeCN): <i>m/z</i> (%)	1417.5166 (calc. 1417.5150) [M] ⁺
IR (KBr): $\tilde{\nu}/\text{cm}^{-1}$	2963 (m), 1635 (w), 1457 (m), 1261 (m), 1100 (vs), 1018 (vs), 801 (s), 694 (m)
UV-vis/nm ($\epsilon/\text{M}^{-1}\text{cm}^{-1}$)	279 (36804), 385 (57367), 559 (18319), 710 (18485)

8.3.5 General Procedure Toward LM₂⁺

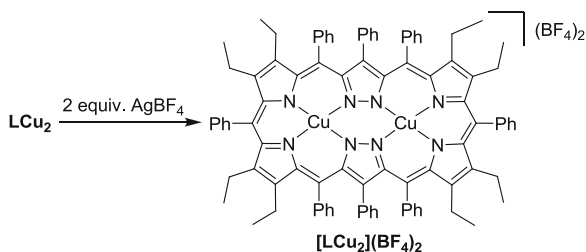
To a solution of LM₂ (20 μmol) in CH₂Cl₂ (15 mL) 1 equiv. of AgBF₄ (200 μL, 0.1 M stock solution in EtNO₂) was added and the reaction monitored via UV-vis spectroscopy. The solvent was removed under reduced pressure and the solid redissolved in 10 mL CH₂Cl₂. The suspension was filtered at air using a membrane filter. The solvent was removed under reduced pressure and the product LM₂⁺ had to be stored under inert conditions.

8.3.6 General Procedure Toward LM₂²⁺

To a solution of LM₂ (20 μmol) in CH₂Cl₂ (15 mL) 2 equiv. of AgBF₄ (400 μL, 0.1 M stock solution in EtNO₂) were added and the reaction monitored via UV-vis spectroscopy. The solvent was removed under reduced pressure and the solid redissolved in 10 mL CH₂Cl₂. The suspension was filtered at air using a membrane filter. The solvent was removed under reduced pressure and the product LM₂²⁺ had to be stored under inert conditions.

Solely for LNi₂²⁺, the reaction was performed under inert conditions using anhydrous solvents.

8.3.6.1 [LCu₂](BF₄)₂



The synthesis and isolation of [LCu₂](BF₄)₂ followed the general procedure described in 8.3.6. Except for X-ray diffraction, [LCu₂](BF₄)₂ was used as obtained after filtering off the silver particles. Crystals were obtained via slow diffusion of a saturated solution of [LCu₂](BF₄)₂ in anhydrous acetone into anhydrous toluene under inert conditions.

Empirical formula	C ₉₂ H ₈₂ B ₂ Cu ₂ F ₈ N ₈
Molecular weight/g/mol	1598.37
¹ H NMR (500 MHz, CD ₂ Cl ₂)	δ/ppm = 0.67 (t, 12H, CH ₃), 0.69 (t, 12H, CH ₃), 1.58–1.73 (m, 4H, CH ₂), 2.02–2.24 (m, 12H, CH ₂), 6.48 (d, 4H, Ph), 6.56 (t, 4H, Ph), 6.68 (t, 2H, Ph), 6.80 (t, 4H, Ph), 6.92 (t, 4H, Ph), 7.28 (t, 4H, Ph), 7.41–7.52 (m, 12H, Ph), 8.00 (t, 2H, Ph), 8.08 (d, 4H, Ph)
¹³ C NMR (125 MHz, CD ₂ Cl ₂)	δ/ppm = 15.7 (CH ₃), 15.8 (CH ₃), 19.2 (CH ₂), 19.7 (2 CH ₂), 124.8 (Ph), 126.8 (Ph), 127.1 (Ph), 127.2, 128.3 (Ph), 128.4 (Ph), 128.6 (Ph), 129.2 (Ph), 129.3 (Ph), 129.7 (Ph), 129.9 (Ph), 130.1 (Ph), 132.1 (Ph), 136.2 (Ph), 140.5 (Ph), 144.6 (Ph), 151.7 (Ph), 157.3 (Ph), 170.0 (Ph), 174.6 (Ph), 179.5 (Ph)
UV-vis/nm (ε/M ⁻¹ cm ⁻¹)	593 (21639), 556 (24413), 433 (38846), 395 (32259), 322 (26429), 276 (29439)

References

1. G.R. Fulmer, A.J.M. Miller, N.H. Sherden, H.E. Gottlieb, A. Nudelman, B.M. Stoltz, J.E. Bercaw, K.I. Goldberg, *Organometallics* **29**, 2176–2179 (2010)
2. M. Heichel, P. Höfer, A. Kamlowski, M.M. Griffin, C. A. Noble, D. Wang, G. R. Hanson, C. Eldershaw, K. E. Gates, K. Burrage, *Bruker Report* **148**, 6–9 (2000)
3. G.R.G. Hanson, K. E. Noble, C. J. Griffin, M. Mitchell, A. Benson, S. J. Inorg. Biochem. **98**, 903–916 (2004)
4. S.M. Webb, *Phys. Scripta*, T115 **2005**, 1011–1014
5. B. Ravel, M. Newville, *J. Synchrotron Radiat.* **12**, 537–541 (2005)

6. A. Sachse, L. Penkova, G. Noel, S. Dechert, O.A. Varzatskii, I.O. Fritsky, F. Meyer, *Synthesis* **5**, 800–806 (2008)
7. J.L. Sessler, A. Mazaffari, M.R. Johnson, *Org. Synth.* **9**, 242 (1998)
8. G.D. Hartman, L.M. Weinstock, *Org. Synth.* **6**, 620 (1988)
9. K.M. Kadish, K.M. Smith, R. Guilard, *The Porphyrin Handbook*, vol. 1 (Academic Press, San Diego, USA, 2000)
10. H.G.O. Becker, R. Beckert, G. Domschke, E. Fanhänel, W.D. Habicher, P. Metz, D. Pavel, K. Schwetlick, *Organikum*, 21st edn. (WILEY-VCH, Weinheim, 2001)

Appendix

Crystallographic Details

Crystals of compound **LCu₂·4 toluene**, **LNi₂·4 toluene** and **LH₂Ni·acetone**, **LH₆²⁺·acetone** and TFA were mounted on a Bruker three circle diffractometer equipped with a SMART 6000 detector and with monochromated Cu-K_α radiation ($\lambda = 1.54 \text{ \AA}$). Integration was performed with SAINT [1], absorption and intensity data were corrected with the SADABS program [2]. The structure was solved using direct methods and refined by full-matrix least-squares procedures against F^2 with SHELX [3]. Non-hydrogen atoms were refined anisotropically and hydrogen atoms were added using the riding model.

X-ray data for **[LCu₂(acetone)₂](BF₄)₂ · 2 toluene · 2 acetone** were collected on a STOE IPDS II diffractometer (graphite monochromated Mo-K_α radiation, $\lambda = 0.711 \text{ \AA}$) by use of ω scans. The structure was solved by direct methods and refined on F^2 using all reflections with SHELX [3]. Most non-hydrogen atoms were refined anisotropically. Hydrogen atoms were placed in calculated positions and assigned to an isotropic displacement parameter of 1.2/1.5 Ueq(C). Counterions and solvent molecules were found to be disordered. SADI (d_{B-F} , d_{F-F}) restraints were used to model the disorder of the counterions.

In the case of **LCu₂·4 toluene**, **LNi₂·4 toluene** the asymmetric unit contains half a molecule and two toluene molecules. The two disordered toluene solvent molecules could be refined. FLAT, DFIX, and DANG as well as SIMU, DELU, and ISOR restraints were used, because of complex ligand and solvent disorder. The asymmetric unit of **[LCu₂](BF₄)₂** contains half a molecule and one acetone. For **LH₂Ni·acetone**, **LH₆²⁺·acetone** the refinement was challenging due to several incorporated disordered solvent molecules and in the case of **LH₆²⁺** the presented result is preliminary.

	LH ₆ ²⁺	LH ₂ Ni
Empirical formula	C _{395.62} H _{366.64} F _{21.45} N ₃₂ O _{37.90}	C _{207.90} H _{220.60} N ₁₆ Ni ₂ O _{12.60}
Formula weight	6583.22	3262.41
Temperature	100(2) K	100(2) K
Crystal system	Triclinic	Triclinic
Space group	<i>P</i> 1	<i>P</i> $\bar{1}$
Unit cell dimensions	<i>a</i> = 19.4383(3) Å <i>α</i> = 66.0039(2)° <i>b</i> = 22.0280(6) Å <i>β</i> = 89.2671(2)° <i>c</i> = 23.8899(7) Å <i>γ</i> = 88.4771(2)°	<i>a</i> = 14.9415(4) Å <i>α</i> = 98.1120(10)° <i>b</i> = 17.0016(4) Å <i>β</i> = 96.8950(10)° <i>c</i> = 19.0343(5) Å <i>γ</i> = 109.7450(10)°
Volume/Å ³	9341.9(5)	4431.9(2)
<i>Z</i>	1	2
Density (calculated)/Mg/m ³	1.164	1.222
Absorption coefficient/mm ⁻¹	0.672	0.789
<i>F</i> (000)	3443	1737
Crystal size/mm ³	0.02 × 0.01 × 0.01	0.125 × 0.125 × 0.125
<i>θ</i> range for data collection	2.2 to 70.3°	2.384 to 68.245°
Index ranges	-23 ≤ <i>h</i> ≤ 23 -39 ≤ <i>k</i> ≤ 38 -16 ≤ <i>l</i> ≤ 14	-18 ≤ <i>h</i> ≤ 18 -21 ≤ <i>l</i> ≤ 19 -20 ≤ <i>k</i> ≤ 20
Reflections collected	57916	97557
Independent reflections	57916 [<i>R</i> (int) = 0.039]	15835 [<i>R</i> (int) = 0.0393]
Data/restraints/parameters	57913/6336/4618	15835/1523/1284
Goodness-of-fit on <i>F</i> ²	2.63	1.078
Final <i>R</i> indices [<i>I</i> > 2σ(<i>I</i>)]	<i>R</i> 1 = 0.1298, <i>wR</i> 2 = 0.3220	<i>R</i> 1 = 0.0602, <i>wR</i> 2 = 0.1667
<i>R</i> indices (all data)	<i>R</i> 1 = 0.1559, <i>wR</i> 2 = 0.3514	<i>R</i> 1 = 0.0657, <i>wR</i> 2 = 0.1794
Res. el. dens/e/Å ³	-0.66 and 1.73	0.671 and -0.858

	LNi ₂	LCu ₂
Empirical formula	C ₁₂₀ H ₁₁₂ N ₈ Ni ₂	C ₁₂₀ H ₁₁₂ Cu ₂ N ₈
Formula weight	1783.74	1793.26
Temperature	100(2) K	100(2) K
Crystal system	Monoclinic	Monoclinic
Space group	<i>C</i> 2/ <i>c</i>	<i>C</i> 2/ <i>c</i>
Unit cell dimensions	<i>a</i> = 19.5208(9) Å <i>α</i> = 90° <i>b</i> = 21.9198(1) Å <i>β</i> = 109.601(2)° <i>c</i> = 23.3495(1) Å <i>γ</i> = 90°	<i>a</i> = 19.594(3) Å <i>α</i> = 90° <i>b</i> = 22.051(3) Å <i>β</i> = 90° <i>c</i> = 23.455(4) Å <i>γ</i> = 90°
Volume/Å ³	9412.1(3)	9523(3)

(continued)

(continued)

	LNi ₂	LCu ₂
Z	4	4
Density (calculated)/Mg/m ³	1.259	1.251
Absorption coefficient/mm ⁻¹	0.925	0.974
F(000)	3777	3784
Crystal size/mm ³	0.25 × 0.02 × 0.01	0.05 × 0.05 × 0.02
θ range for data collection	3.1 to 73.8°	3.13 to 68.24°
Index ranges	-24 ≤ h ≤ 24 -27 ≤ l ≤ 26 -28 ≤ k ≤ 29	-23 ≤ h ≤ 23 -26 ≤ k ≤ 26 -27 ≤ l ≤ 28
Reflections collected	108147	241142
Independent reflections	9699 [R(int) = 0.030]	8631 [R(int) = 0.0424]
Data/restraints/parameters	8638/400/602	8631 / 2183 / 780
Goodness-of-fit on F ²	3.84	1.05
Final R indices [I > 2σ(I)]	R1 = 0.0296	R1 = 0.0472, wR2 = 0.1334
R indices (all data)	wR2 = 0.038	R1 = 0.0537, wR2 = 0.1425
Res. el. dens/e/Å ³	-0.228 and 0.287	1.157 and -0.447
<hr/>		
[LCu₂(acetone)₂](BF₄)₂		
Empirical formula	C ₁₁₈ H ₁₂₀ B ₂ Cu ₂ F ₈ N ₈ O ₄	
Formula weight	2014.92	
Temperature	133(2) K	
Crystal system	Monoclinic	
Space group	C 2/c	
Unit cell dimensions	a = 18.8185 (1) Å α = 90° b = 22.3182 (1) Å β = 97.898 (4)° c = 24.6188 (1) Å γ = 90°	
Volume/Å ³	10241.7 (9)	
Z	4	
Density (calculated)/Mg/m ³	1.307	
Absorption coefficient/mm ⁻¹	0.488	
F(000)	4224	
Crystal size/mm ³	0.25 × 0.17 × 0.12	
θ range for data collection	1.42 to 24.69°	
Index ranges	-21 ≤ h ≤ 22 -26 ≤ k ≤ 26 -27 ≤ l ≤ 28	
Reflections collected	45112	

(continued)

(continued)

	[LCu ₂ (acetone) ₂](BF ₄) ₂
Independent reflections	8614 [<i>R</i> (int) = 0.1311]
Data/restraints/parameters	8614/257/701
Goodness-of-fit on <i>F</i> ²	1.138
Final <i>R</i> indices [<i>I</i> > 2σ(<i>I</i>)]	<i>R</i> 1 = 0.0849, <i>wR</i> 2 = 0.1590
<i>R</i> indices (all data)	<i>R</i> 1 = 0.1300, <i>wR</i> 2 = 0.1760
Res. el. dens/e/Å ³	0.434 and -0.409

Details on DFT Calculations

DFT Optimizations

DFT calculations were carried out with the ORCA software package [4]. Atom coordinates were obtained from first guess structures drawn with ChemDraw3D. First, coordinates were optimized with the semi-empirical Austin Model 1 (AM1) [5, 6] and then refined using the Becke-Perdew-1986 functional (BP86) [7, 8]. Compounds **LH₄**, **LH₆²⁺** (symmetric and asymmetric protonation motif), **29a**, **29b**, **29c** and **29cH₂²⁺** readily converged.

TDDFT Calculations

Conformational analyses for **LH₆²⁺**, **LCu₂** and **LNi₂** were done using Gaussian09 software package.[96] The geometry optimization for **LH₆²⁺** was repeated using the B3LYP [9, 10] functional and performed for **LCu₂** and **LNi₂** as well. The 6-31G(d,p) basis set [11, 12] was chosen for all first-row elements and the larger 6-311G* [13, 14] basis set for the transition metals Cu and Ni. The TDDFT excited states calculations of the global minima were also performed using Gaussian09. The UV and CD spectra were also simulated with B3LYP/6-31G(d,p) for **LH₆²⁺** (nstates = 50), **LCu₂** (nstates = 40), and **LNi₂** (nstates = 40) while for the transition metals the 6-311G* basis set was used. The UV and CD curves of all compounds were calculated as sums of Gauss functions centered at the wavelength of the corresponding excitations and multiplied by the respective oscillator and rotational strength values (length formalism), with an empirically chosen exponential half width of 0.16 eV. Calculated rotational strength values were multiplied by -1 to get the enantiomeric CD curves. Before comparison of the computational CD curve with the experiments, a UV correction of 5 nm for **LH₆²⁺**, -10 nm for **LNi₂** and -30 nm for **LCu₂** was performed. SpecDis was used for Gauss curve generation, UV correction, plotting and comparison with experimental data [15–17].

References

1. Bruker, *APEX2, SAINT, SHELXTL*, Madison, Wisconsin, USA, 2009
2. G.M. Sheldrick, *SADABS* (University of Göttingen, Germany, 2009)
3. G.M. Sheldrick, *Acta Crystallogr. Sect. A: Found. Crystallogr.* **A64**, 112–122 (2008)
4. F. Neese, *ORCA, an ab initio density functional and semiempirical program package* (University of Bonn, Germany, 2007)
5. M.J.S. Dewar, E.G. Zoebisch, E.F. Healy, J.J.P. Stewart, *J. Am. Chem. Soc.* **115**, 5348 (1993)
6. M.J.S. Dewar, E.G. Zoebisch, E.F. Healy, J.J.P. Stewart, *J. Am. Chem. Soc.* **107**, 3902–3909 (1985)
7. A.D. Becke, *Phys. Rev. A* **38**, 3098–3100 (1988)
8. P. Perdew, *Phys. Rev. B* **33**, 8822–8824 (1986)
9. A.D. Becke, *J. Chem. Phys.* **98**, 5648–5652 (1993)
10. C. Lee, W. Yang, R.G. Parr, *Phys. Rev. B* **37**, 785–789 (1988)
11. W.J. Hehre, R. Ditchfield, J.A. Pople, *J. Chem. Phys.* **56**, 2257–2261 (1972)
12. P.C. Hariharan, J.A. Pople, *Theor. Chim. Acta* **28**, 213–222 (1973)
13. R. Krishnan, J.S. Binkley, R. Seeger, J.A. Pople, *J. Chem. Phys.* **72**, 650–654 (1980)
14. K. Raghavachari, G.W. Trucks, *J. Chem. Phys.* **91**, 2457–2460 (1989)
15. G. Bringmann, S. Busemann, in *Natural Product Analysis: Chromatography, Spectroscopy, Biological Testing*, eds. by P. Schreier, M. Herderich, H.-U. Humpf, W. Schwab (Vieweg, Wiesbaden, 1998), pp. 195–211
16. G. Bringmann, T. Bruhn, K. Maksimenka, Y. Hemberger, *Eur. J. Org. Chem.*, 2717–2727 (2009)
17. T. Bruhn, A. Schaumlöffel, Y. Hemberger, G. Bringmann, *SpecDis* (Würzburg, Germany, 2012)

List of Scientific Contributions

Publications

“*The Siamese-Twin Porphyrin: A Pyrazole-Based Expanded Porphyrin Providing a Bimetallic Cavity*” L. K. Frensch, K. Pröpper, M. John, S. Demeshko, C. Brückner, F. Meyer, *Angew. Chem.* **2011**, *123*, 1456–1460; *Angew. Chem. Int. Ed.* **2011**, *50*, 1420–1424.

“*Siamese-Twin Porphyrin: A Pyrazole-Based Expanded Porphyrin of Persistent Helical Conformation*” L. K. Blusch, Y. Hemberger, K. Pröpper, B. Dittrich, F. Witterauf, M. John, G. Bringmann, C. Brückner, and F. Meyer, *Chem. Eur. J.* **2013**, *19*, 5868–5880.

“*Hidden Non-Innocence in an Expanded Porphyrin: Electronic Structure of the Siamese-Twin Porphyrin’s Dicopper Complex in Different Oxidation States*” L. K. Blusch, K. E. Craigo, V. Martin-Diaconescu, E. Bill, A. B. McQuarters, S. Dechert, S. DeBeer, N. Lehnert, F. Meyer, DOI:[10.1021/ja406176e](https://doi.org/10.1021/ja406176e)

Oral Presentations

“*Homo- and Heterobimetallic Complexes of the Siamese-Twin Porphyrin: Story of a Non-Innocent Twist*” Coordination Chemistry Conference (Zing conferences), Cancun, Mexico, December, **2011**.

“*The Siamese-Twin Porphyrin and its Copper Complex: Synthesis, Magnetic and Redox Properties*” Jung-Chemiker Forum (sponsored by GDCh), Göttingen, Germany, July **2011**.

“*The Siamese-Twin Porphyrin and its Copper Complex: Synthesis, Magnetic and Redox Properties*” Koordinationschemie-Treffen, Stuttgart, Germany, March **2011**.

“*Bioinorganic Molecules and Beyond: The Siamese-Twin Porphyrin as an Example*” ISER Pune - Georg-August University Göttingen workshop, Göttingen, Germany, October **2010**.

Poster Presentations

“Persistent Chiral Twists: Protonation Studies and Chiral Resolution of the Siamese-twin Porphyrin and its Homobimetallic Complexes” 16. Vortragstagung der Wöhlerversammlung 2012; Göttingen, September **2012**.

“The Siamese-Twin Porphyrin” International Symposium on Molecular Coordination Chemistry, MPI Mülheim, Germany, November **2010**.

“Synthesis of a Doubleporphyrin: A New Scaffold for Bimetallic Complexes” Summer School: Computational Chemistry and Spectroscopy; Essen, Germany, September **2009**.

Curriculum Vitae

Personal data

Name	Lina Katharina Blusch, née Frensch
Date of Birth	4 th September 1983
Place of Birth	Moers
Nationality	German
Marital Status	Married

Academic career

since 02/2013	Postdoctoral Fellow at the University of British Columbia, Vancouver, Canada, “ <i>Self-Assembling Zinc Acetate Based Metal-Organic Block Copolymers</i> ” with Prof. M. MacLachlan
11/2012–01/2013	Scientific Assistant at the Georg-August University, Göttingen with Prof. F. Meyer
02/2009–10/2012	PhD in the Department of Inorganic Chemistry, Georg-August University Göttingen, “ <i>The Siamese-Twin Porphyrin and Its Copper and Nickel Complexes: A Non-Innocent Twist</i> ” with Prof. F. Meyer
01/2009	“Diplom” in Chemistry
05/2008–10/2008	Thesis: “ <i>Synthesis of Pyrrole/Pyrazol-Hybridblocks as Precursors for the Doubleporphyrin</i> ” with Prof. F. Meyer and Prof. C. Brückner
10/2005	Intermediate “ <i>Chemistry</i> ”
10/2003–01/2009	Chemistry Major at the Georg-August University, Göttingen

Pre-Academic career

- 6/1/2003 “Abitur” Secondary School Leaving Certificate required for admission to university (Major subjects: Chemistry, Biology)
- 1994–2003 Secondary School: “*Gymnasium Adolfinum*”, Moers, Germany
- 1990–1994 Elementary School: “*Eichendorfschule*”, Moers, Germany

Index

A

AgBF₄, 99, 111, 120
Anion recognition, 15
Aromaticity, 1, 11, 13, 43, 47

B

Bohr magneton, 74
Brillouin equation, 81
Bulk electrolysis.
 See Spectroelectro experiment

C

Catalysis, 24
Chirality, 28, 35, 46
 chiral resolution LCu₂, 81
 chiral resolution LH₄, 56
 chiral resolution LNi₂, 88
Chlorophyll, 3
Circular dichroism, 58
 instrument data, 131
Comproportionation constant, 96, 108, 118
Cooperativity, 4, 18, 73, 75
Core-modified expanded porphyrins, 11
Cryptand-type ligand, 18
Cyclic voltammetry
 general information, 62
 instrument data, 130
 LCu₂, 95
 LCuNi, 117
 LH₂Ni, 107
 LNi₂, 108
Cytochrome P450, 5, 16, 23

D

DFT calculation
 CD spectra, 59, 81, 89
 details, 150

 protonation, 56
 twisted geometry, 47
Dipyrrrometha(ε)ne, 32

E

Electron paramagnetic resonance
 general information, 75
 instrument data, 130
LCu₂, 76
LCu₂⁺, 100
LCuNi, 90
LCuNi⁺, 122
LNi₂⁺, 111

F

Faraday effect, 78, 87
Fischer, 6

H

Hemoglobin, 4
Hexaphyrin, 10, 12, 14
HOMO-LUMO gap, 8

I

Invariom method, 84

K

Katsiaouni, 25

L

Landé factor, 74
Lind, 25
Lindsey, 6

M

- Macdonald, 7, 11, 25
- Magnetic circular dichroism
 - general information, 78
 - instrument data, 129
 - LCu₂, 79
 - LNi₂, 87
- Magnetic moment, 74, 90, 129
- Mass spectrometry, 34
 - high resolution, 35, 36, 69
 - instrument data, 129
- Methane monooxygenase, 16, 23
- Mixed valency, 101, 121
- Monooxygenase, 16

N

- NMR spectroscopy
 - 24a-b, 31
 - 6d, 37
 - aromaticity, 12
 - general information, 75
 - instrument data, 129
 - [LCu₂](BF₄)₂, 102
 - LH₂Ni, 85
 - LH₄, 41, 50, 60
 - LNi₂, 87
- Non-innocence, 3, 63
- Non-linear optical properties, 15

O

- Oxidative coupling, 11

P

- Photodynamic therapy, 15
- Porphyrin
 - general introduction, 1
 - octaethylporphyrin (OEP), 7
 - synthesis, 6
 - tetraphenylporphyrin (TPP), 7
- Protonation, 28, 32, 58
 - LH₂Ni, 85
 - LH₄, 49
- Pyrazole, 17, 27
- Pyrrrole, 29
- Pyrrrole/pyrazole hybrid, 30

R

- Rothmund, 6, 11

S

- Schiff-base ligand, 18
- Solid-state structure
 - details, 147
 - instrument data, 131
 - LCu₂, 71
 - [LCu₂](BF₄)₂, 104
 - LH₂Ni, 81
 - LH₄, 45
 - LNi₂, 83
- Soret band, 8, 46, 80
- Spectroelectro experiment
 - general information, 93
 - LCu₂, 97
 - LCuNi, 118
 - LNi₂, 108
- Square wave voltammetry
 - general information, 93
 - LCu₂, 95
 - LCuNi, 117
 - LNi₂, 108
- Susceptibility
 - general information, 73
 - instrument data, 129
 - LCu₂, 74
 - LCuNi, 89
- Symmetry, 41, 46, 52, 71, 81, 102

T

- Tyrosinase, 16

U

- UV-vis spectroscopy
 - 6d, 36
 - instrument data, 129
 - LH₄, 45, 54
 - metal complexes, 70

X

- X-ray absorption
 - general information, 104
 - [LCu₂](BF₄)₂, 106
 - LCuNi⁺, 122
 - LNi₂⁺, 116